THE UNIVERSITY OF CHICAGO

MECHANISMS UNDERLYING MOTION DISCRIMINATION IN THE MAMMALIAN RETINA

A DISSERTATION SUBMITTED TO

THE FACULTY OF THE DIVISION OF THE PHYSICAL SCIENCES

AND

THE FACULTY OF THE DIVISION OF THE BIOLOGICAL SCIENCES

AND THE PRITZKER SCHOOL OF MEDICINE

IN CANDIDACY FOR THE DEGREE OF

DOCTOR OF PHILOSOPHY

GRADUATE PROGRAM IN BIOPHYSICAL SCIENCES

BY

HÉCTOR E. ACARÓN LEDESMA

CHICAGO, ILLINOIS

AUGUST 2020

Table of Contents

List of Figures

Acknowledgements

I would like to begin by thanking my advisors, Wei Wei and Bozhi Tian, since none of this work would have been possible without their mentorship, guidance, and expertise. I came to graduate school with the intention of exploring new fields of study and challenging myself both intellectually and technically. Both Wei and Bozhi provided me with the tools I needed to succeed while at the same time giving me the space to grow and learn from my own mistakes. I was lucky enough to receive different and complementary training from my two advisors. Wei taught me how to think critically and thoroughly as a scientist and Bozhi showed me how to be creative in my scientific approach and think outside the box.

I am extremely grateful for the guidance I have received from Ruth Anne Eatock, John Maunsell, and Mark Sheffield. Thank you all for being part of my thesis committee. In particular, I want to thank John Maunsell for chairing the committee and co-sponsoring my NRSA F31 application. I want to also acknowledge Nicolas Brunel and David Biron for providing advice early on in my PhD. I had the pleasure of being a teaching assistant for Ruth Anne Eatock, John Maunsell, Murray Sherman, Aaron Fox, and Steve Shevell throughout my stay at UChicago, thank you all for the wonderful discussions in and out of the classroom.

I must credit the numerous lab members who contributed directly and indirectly to this work and my graduate school experience. I want to thank Xiaolin “Lindsay” Huang, Qiang “Chris” Chen, David Koren, Jennifer Ding, and Chen Zhang for being exceptional colleagues and providing support throughout the years. Chen Zhang has been instrumental in our lab, I specially thank her for maintaining our mouse colony and for performing the intravitreal injections in Chapter 4. I also want to acknowledge David Koren since his dissertation identified the importance of mGluR2

signaling in SACs which provided the basis for Chapter 2. Yin Fang, Yuanwen Jiang, and Menahem Rotenberg were key collaborators from the Tian lab who made Chapters 8 and 9 possible.

Many of the experiments described in this dissertation would not have been possible without the help and guidance of the greater retina and visual processing community. First, I would like to thank Jianhua "JC" Cang and his lab members for being long-time collaborators, colleagues, and friends. Marla Feller and David Feldheim provided transgenic mouse lines that were important for many chapters of this dissertation. Michael Lin and Sui Wang supplied the voltage sensors and viral vectors used in Chapter 2.

The Biophysical Sciences (BPHYS) graduate program has been very supportive of me during my time at UChicago. I want to thank Michele Wittels and Julie Feder for always being there when I needed someone to talk to. I am grateful for having Adam Hammond, Greg Engel, and Tobin Sosnick as our BPHYS leaders and for being proactive on ways to improve our graduate program. I also want to give special thanks to Adam Hammond for supporting both my NSGFRP and NRSA F31 applications and for being an exceptional mentor since my arrival at UChicago.

Lastly, I want to thank my family for making my education a top family priority and for encouraging me to pursue my dreams. My mother taught me how to challenge myself and how to push through difficult times. I want to thank my father for always being there to uplift my spirit and reminding me of my potential. To my partner, Gary Kafer, thank you for holding my hand throughout the rollercoaster that is graduate school. I have been extremely lucky to share this experience with you and I am beyond excited to see our careers take off to new heights.

Abstract

Information processing in the brain is orchestrated by neural circuits that are optimized to extract relevant features from the environment. In particular, visual circuits sensitive to contrast, texture, color, motion, and orientation help create internal representations of our visual world and guide animal behavior. Visual motion enhances saliency of perceived objects and is critical for coordinating animal reflexes and more complicated behaviors, such as flight-or-fight responses. This dissertation is divided in two parts. Part I focuses on visual processing in the mammalian retina, particularly visual feature selectivity across different biological length scales. As it will be described in further detail in Chapter 1, motion sensitivity if first computed in the retina by dedicated circuits that give rise to direction and axial-selective responses. Understanding the mechanisms underlying motion detection in the mammalian retina can provide a foundation for describing complex neural computations in higher order brain areas.

In the mammalian retina, the detection of motion direction, or direction selectivity, is first observed in the dendrites of starburst amacrine cells (SACs). Individual dendritic sectors of SACs exhibit centrifugal preference for the direction of motion, meaning that they are maximally activated by objects moving from soma to tip and only weakly activated by motion in opposite direction, tip to soma. This remarkable dendritic computation can be achieved in such a compact neuron because dendritic sectors in SACs are eletrotonically isolated from each other; however, the mechanisms orchestrating this fine balance between integration and isolation is not completely understood. In Chapter 2, we look into the contributions of cell-intrinsic properties and voltage-dependent mechanisms to compartmentalized signaling in SACs. Our results highlight how metabotropic glutamate receptor II (mGluR2) and voltage-gated potassium channels of subfamily 3 (Kv3)

regulate dendritic excitability and the initiation of non-linear calcium events along the dendrites of SACs.

The direction selective signals in the dendrites of SACs are relayed to direction-selective ganglion cells, which transform inhibitory and excitatory inputs into a direction-selective spiking output that is transmitted to downstream visual nuclei, including the superior colliculus and visual thalamus. Asymmetric GABAergic inhibition from SACs to DSGCs is considered the central mechanism for direction selectivity in DSGCs; although, SACs also release acetylcholine which activate nicotinic acethylcholine receptors DSGCs and represents a significant fraction of total excitatory charge in these neurons. In Chapter 3, we look into parallel mechanisms for retinal direction selectivity by using conditional transgenic strategies to manipulate individual synapses in the direction selective circuit. Results from this study highlight how excitatory mechanisms contribute to direction selectivity and expands on the roles of SACs in visual processing. In Chapter 4, I worked together with external collaborators to determine the extent of which retinal direction selectivity influences signaling in a major retinorecipient target, the superior colliculus.

Then, I characterized transgenic methods to express GCaMP6 in retinal ganglion cells (RGCs) in effort to improve and streamline functional imaging in the output neurons of the retina (Chapter 5). Using the *Vglut2-IRES-Cre* mouse line to express GCaMP6 in RGCs, I monitored the abundance of motion sensitive receptive fields across development and characterized the response properties of On-Off orientation sensitive, or axis selective, receptive fields in Chapter 6.

Part II of this dissertation focuses on next-generation devices and tools for the interrogation of neural circuits. Currently, biological systems are interrogated with bulky electrodes, which tend to be highly invasive because of their large-scale dimensions and mechanical mismatch with targeted tissue. As described in Chapter 7, recent advances in nanoscale technologies have facilitated the development of novel materials that are well suited for biological applications, including flexible alternatives to rigid and invasive probes. In Chapter 8, I discuss the fabrication of porous silicon nanowires and their application as optical tools for neuronal stimulation. Lastly, in Chapter 9 we describe a carbon-based supercapacitor and demonstrate efficient stimulation in neural and cardiac tissues.

Part I

Motion processing in the early visual system

Chapter 1

The retina as a model system

This chapter contains adapted sections from the publication "Chapter 9 - Synapse formation in the developing vertebrate retina" for the 2nd edition of *Synapse Development and Maturation* in which I was a contributing author along with Xiaolin Huang and Wei Wei. This work is included with permission from all authors.

Since the discovery of the neuron as the basic signaling unit of the nervous system (Ramón y Cajal, 2011), a major goal in neuroscience has been to understand how individual neurons organize into neural circuits that process information and guide animal behavior. Neurons enable rapid intercellular communications due to the spread of electrical impulses along their excitable membranes (Hodgkin & Huxley, 1945). During development, the concerted action of both molecular (Yamagata & Sanes, 2008) and activity-dependent mechanisms (Ackman & Crair, 2014) direct neurons to form specific synaptic connections and assemble into distinct functional networks. This precise organization of excitatory and inhibitory neurons within local brain circuits instruct the algorithmic operations of synapses in the execution of complex tasks. For instance, circuit-level interactions between neurons and signal transformations within individual neurons allow these functional networks to compute and extract relevant information from the environment.

Over the last century, numerous discoveries have contributed to our current understanding of synaptic transmission and bioelectric signaling in neurons. However, how interactions between neurons coordinate the progression from sensation to perception to behavior is not completely understood, in part due to the complexity of the human brain. Despite the vast diversity of neuronal cell types that exist in the brain, neurons operate under a similar set of working principles. These include changes to the resting membrane potential upon a sequence or combination of synaptic inputs, the ability to initiate all-or-none electrical events, and intercellular communication through chemical and/or electrical synapses.

Information processing has been largely studied in the context of sensory systems, such as the visual system, in which neuronal receptive fields transduce physical stimuli into chemical and electrical patterns. The visual system has been particularly attractive since illumination parameters (intensity, location, duration, etc.) can be easily controlled in the lab and its components span across multiple brain regions. Furthermore, the discovery of selective visual receptive fields in the earlier part of the 20th century initiated large momentum in visual neuroscience research (Hubel & Wiesel, 1959; KUFFLER, 1953).

In most vertebrates, the eyes are the gateway for visual information to reach the brain. Light enters the eye through the cornea and is focused by the lens onto the retina, a thin sheet of neural tissue that sits at the back of the eye, where photosensitive neurons convert light into chemical and electrical signals that the brain can understand. These signals are then used to create internal representations of the outside visual world. Early retina experiments in the 1950s demonstrated that retinal neurons exhibit preference to small spots of light and moving stimuli over large

diffused illumination. These experiments presented the notion that visual processing begins in the retina and that retinofugal signals carry more information than just light intensity levels (Barlow & Hill, 1963; KUFFLER, 1953). Work over the last several decades has demonstrated that salient visual features are extracted by retinal circuits (Baden et al., 2016) and these complex receptive fields have significant contributions to behavior (Yonehara et al., 2009, 2016; Yoshida et al., 2001) and processing in downstream nuclei (Cruz-Martín et al., 2014; Shi et al., 2017).

As one of the most approachable parts of the central nervous system (CNS), the retina is an excellent model system to study neural circuits owing to its highly ordered architecture, well-defined cell types, and experimental accessibility. Additionally, most of the circuit motifs found in the retina are widespread throughout the brain, thus the network interactions and physiology underlying visual response properties in retinal neurons can provide insight into mechanisms involved in higher order processing. The first part of this dissertation will focus on retinal visual feature selectivity, particularly direction and orientation selectivity.

1.1 Anatomical organization and neuronal cell types

The vertebrate retina contains five main neuronal classes: photoreceptors, horizontal cells, bipolar cells, amacrine cells, and retinal ganglion cells (RGCs) (Jeon et al., 1998). Their cell bodies and neuronal processes are segregated into three cellular or nuclear layers and two intercalating synaptic or plexiform layers (**Figure 1.1**). Photoreceptors reside in the outer nuclear layer (ONL) and extend their pedicles into the outer plexiform layer (OPL) where they form glutamatergic ribbon synapses with horizontal cell and bipolar cell dendrites (Bachman & Balkema, 1993). Horizontal cells are activated by photoreceptor glutamate release, and mediate inhibition of

photoreceptor-bipolar cell signaling through their laterally extending neurites. In the inner plexiform layer (IPL), bipolar cells synapse onto the dendrites of RGCs and amacrine cells and are the main source of excitatory drive in the inner retina. Subsequently, amacrine cells form feedforward lateral connections onto RGCs and other amacrine cells and in some cases they form feedback connections onto bipolar cell terminals in a cell-type specific manner. Finally, RGC axons bundle together to form the optic nerve, through which they target one or more retinorecipient brain regions (Berson, 2008; Gauvain & Murphy, 2015; Martersteck et al., 2017; Yonehara & Roska, 2014).

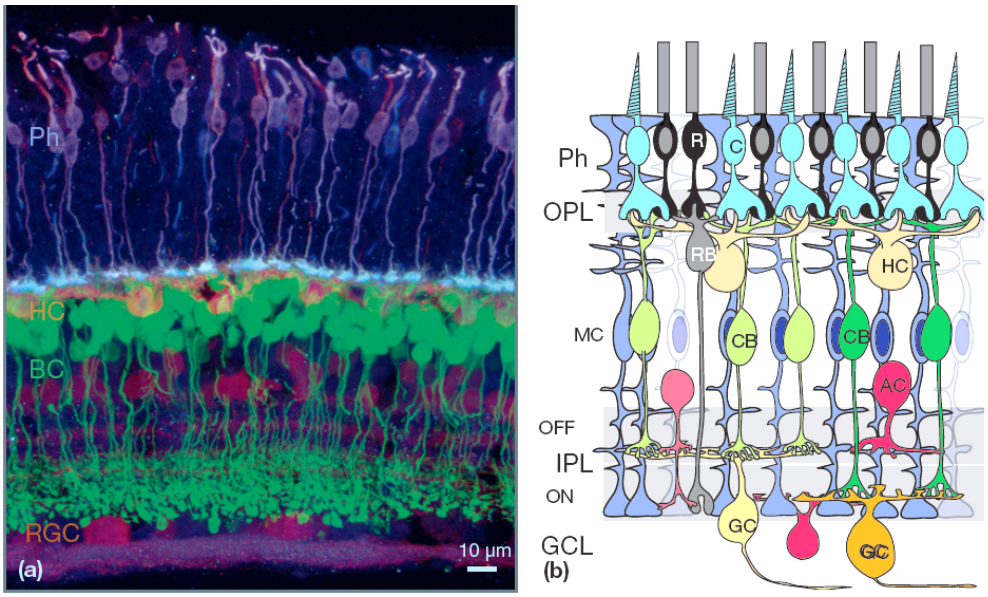

Figure 1.1: Anatomical organization of the mammalian retina. (a) Cross section of an adult mouse retina in which a subclass of bipolar cells expresses green fluorescent protein. The section was immunostained for photoreceptors (Ph) using anti-cone arrestin, horizontal cells (HC), amacrine cells (AC), and retinal ganglion cells (RGC) using anti-calbindin. (b) Schematic of the laminar organization of retinal neurons. OPL, IPL: outer and inner plexiform layers; GCL: ganglion cell layer; Ph, photoreceptor; MC: Muller glial cell; R, rod; C, cone; RB, rod bipolar cell; CB, cone bipolar cell; AC, amacrine cell; GC, ganglion cell. On, On sublamina; Off, Off sublamina. ** Adapted from Yoshimatsu et al. Chapter 36 in Rubenstein, J. L. R., & Rakic, P. 2013. Cellular Migration and Formation of Neuronal Connections: Comprehensive developmental neuroscience. Volume 2 http://dx.doi.org/10.1016/B978-0-12-397266-8.00114-9 Amsterdam: Elsevier/AP.2013)]*

The five retinal cell classes described above can be further divided into approximately 100 cell types based on their morphology, stratification patterns, light response, and molecular signatures. For instance, four types of photoreceptors can be found in the mouse retina: rods, short-wavelength (S-) cones, and medium-wavelength (M-) cones (Nikonov et al., 2006). Humans have an additional cone-type that is sensitive to long-wavelengths (L-).Visual-evoked responses for most diurnal animals are mediated by cones, which are sensitive to different portions of the visible light spectrum (350 – 750 nm). On the other hand, rods are optimized for dim light vision (scotopic) and become saturated during daylight. The number of horizontal cell types varies from one to three depending on the animal species, but the vast majority of animals have two types (Richard H Masland, 2012).

Bipolar cells can be broadly categorized into cone bipolar cells (CBCs) and rod bipolar cells (RBCs) based on the origin of their synaptic inputs. CBCs are subdivided into 13 cell types according to their light response properties, glutamate receptor expression, and axon terminal stratification in the IPL (Euler & Masland, 2000). On CBCs have depolarizing responses to light onset and express metabotropic glutamate receptor 6 (mGluR6), while Off CBCs have depolarizing responses to light offset and express ionotropic glutamate receptors (iGluRs). When light intensity increases, both rods and cones hyperpolarize and reduce their pedicle glutamate release. mGluR6 in On CBCs becomes less active, leading to enhanced activity of the effector cation channel Trpm1 (Koike et al., 2010; Morgans et al., 2009; Shen et al., 2009) and membrane depolarization. Light onset on the other hand reduces the activation of iGluRs in Off CBCs and thus hyperporlarizes the Off bipolar cell membrane. Therefore, sign-reversing mGluR6 signaling in On bipolar cell dendrites and sign-conserving iGluR signaling in Off bipolar cell dendrites

initiate the segregation of bright and dark signals at the first visual synapse. Rod bipolar cells also express mGluR6, and thus are activated by light onset like On cone bipolar cells (Nomura et al., 1994).

Although a clear consensus on the number of amacrine types has not been reached, it is estimated that 40 – 50 types exist in the mouse retina. Most amacrine cells are either GABAergic or glycinergic, with the exceptions of an amacrine cell type that is non-GABAergic and non-glycinergic (nGnG AC) (Kay, Voinescu, et al., 2011) and a glutamatergic monopolar interneuron (GluMI) (Della Santina et al., 2016). Additionally, there are dual-neurotransmitter releasing amacrine cells such as starburst amacrine cells (co-releasing GABA and acetylcholine) (O'Malley & Masland, 1989; Vaney & Young, 1988) and VGluT3 amacrine cells (co-releasing glycine and glutamate) (Haverkamp & Wässle, 2004; S. Lee et al., 2014). Subsets of GABAergic amacrine cells have also been shown to contain neuromodulators such as serotonin, catecholamines, or neuropeptides (Karten & Brecha, 1983)

All postsynaptic neurons of bipolar cells, including amacrine cells and RGCs, use iGluRs (AMPA/KA receptors and/or NMDA receptors) to transform bipolar cell-mediated glutamatergic inputs into excitatory postsynaptic potentials (EPSPs). Amacrine cells, once activated by CBCs, provide conventional feedforward synapses to RGCs and/or feedback synapses to bipolar cell axons. Therefore, amacrine cell signaling profoundly shapes the retinal outputs both by directly synapsing onto RGCs and by shaping the excitatory inputs to RGCs. Recent surveys of light response patterns estimate that there are ~ 30 – 35 functionally distinct RGC types in the mouse retina, each encoding a specific feature of the visual scene (Baden et al., 2016). These are broadly

categorized as On, Off, and On-Off based on their responses to light increments and decrements. RGCs are further classified by their stratification patterns (mono-, bi-, multi-stratified), response kinetics (transient or sustained), and by their motion sensitivity (local edge detectors, direction selective, orientation sensitive). Lastly, RGCs are recognized as an individual subtypes if they have consistent dendritic morphology, exhibit a specific light response pattern, and follow a mosaic distribution throughout the retina. For example, posterior preferring On-Off direction selective ganglion cells (DSGCs) responds to both light onset and offset, are maximally activated by motion in one particular direction (preferred direction), exhibit symmetric bistratified (S2 and S4 sublaminae in the IPL) dendritic morphology, and have an active D4 dopamine receptor (Drd4+) promoter (Huberman et al., 2009).

1.2 Neural computations by retinal circuits

The organization of synaptic inputs along dendritic trees and the biophysical properties of dendrites determine the distinct firing patterns of RGCs. The passive cable properties of dendrites dictate the degree of spatiotemporal attenuation of inputs as they travel towards the soma, where action potentials are fired (Rall, 1964). As it will become evident throughout this dissertation, neural computations arise from the individual or combined contributions of synaptic, network, and postsynaptic mechanisms. Throughout the visual system, subsets of neurons are maximally activated by motion along a particular direction, termed direction-selective neurons, and others are selectively activated during motion along a particular orientation, termed orientation- or axis-selective neurons. These visual features are highly conserved across species and widely observed throughout multiple visual brain areas (Albright, 1984; Chapman & Stryker, 1993; Livingstone & Conway, 2003; Niell & Stryker, 2008; C. W. Oyster, 1968; Piscopo et al., 2013; Rochefort et al.,

2011; Zhao et al., 2013). Both direction and axis selectivity are first encoded by distinct retinal circuits (Antinucci & Hindges, 2018; Weng et al., 2005) whose output neurons, RGCs, carry direction and axis sensitive information to downstream visual nuclei.

1.2.1 Retinal direction selectivity

The direction of motion is computed in the retina by the direction-selective circuit (**Fig. 1.2A**), whose output neurons, direction-selective ganglion cells (DSGCs), are maximally activated by motion in their preferred direction and strongly suppressed by motion in the opposite, or null direction (**Fig. 1.2B-C**) (Barlow & Hill, 1963; Barlow & Levick, 1965). Studies on retinal motion processing have mostly focused on two types of DSGCs: On-Off DSGCs and On DSGCs. On-Off DSGCs have medium-size, bistratified dendritic arbors and respond to both light increments and light decrements. In contrast, On DSGCs have larger, mono-stratified dendritic arbors and respond preferentially to light increments (E. V. Famiglietti, 1992). In both mice and rabbit, On-Off DSGCs consist of four subtypes based on their preferred directions along posterior, anterior, superior, and inferior directions in the visual field (Clyde W. Oyster & Barlow, 1967). On DSGCs have traditionally been categorized into three subtypes (C. W. Oyster, 1968); however, a recent study uncovered that preferred directions On DSGCs align with the cardinal optic flow along the forward-backward motion axis and the up-down gravitational axis (Sabbah et al., 2017).

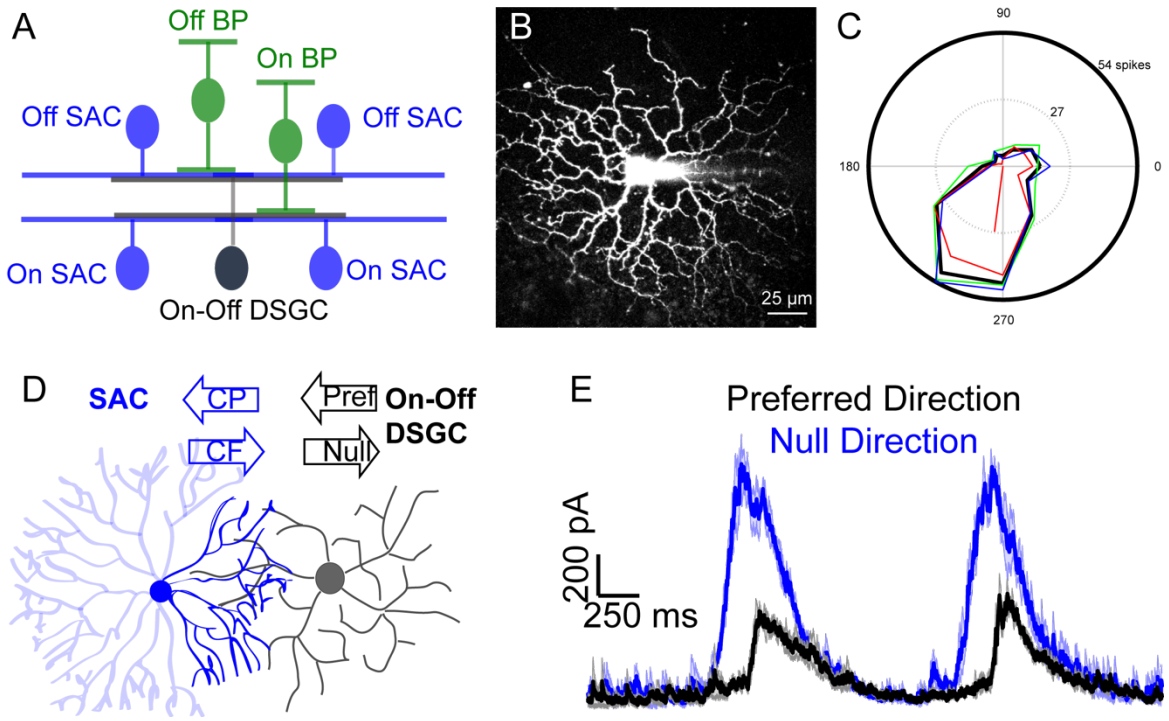

Figure 1.2: Retinal direction selectivity. (A) Schematic of the On-Off retinal direction selective circuit. Bipolar cells (green) synapses onto both SACs (blue) and DSGCs (black). SACs form inhibitory connections onto neighboring SACs (not shown) and DSGCs. (B) Maximum intensity projection of On-Off DSGC filled with Alexa 594. (C) Example tuning curve of the cell in B in response to a moving bar in 12 directions. Red, blue, and green curves correspond to individual trials and black curve to the average across all three trials. Red line represents the resultant vector sum of the average responses. Angle of the vector sum indicates the preferred direction (D) Schematic illustrating anti-parallel wiring between SACs and DSGCs. (E) Inhibitory postsynaptic currents recorded from an On-Off DSGC showing stronger inhibition during null direction motion compared to preferred direction motion.

The directional spiking responses of DSGCs are coordinated by distinct spatiotemporal patterns of synaptic inputs in the preferred and null directions that are further processed in the dendrites of DSGCs. Whole-cell recordings from DSGCs demonstrated stronger and faster inhibitory inputs during motion along the null direction and weaker and delayed inhibition along the preferred direction (**Fig. 1.2E**) (Fried et al., 2002; Taylor & Vaney, 2002). Further studies identified starburst amacrine cells (SACs) as the cellular basis for asymmetric inhibition onto DSGCs. SACs are radially symmetric, axonless interneurons that co-release GABA and acetylcholine from

varicosities located at distal sites in their dendritic arbors (Vaney & Young, 1988). Two fundamental properties mediate directionally tuned inhibition from SACs to DSGCs. First, the dendrites of SACs are direction selective themselves with preference for centrifugal motion (soma to tip) (**Fig. 1.3A**) (Euler et al., 2002). Second, DSGCs receive GABAergic inputs from SAC dendrites orientated along the DSGC's null direction indicating an antiparallel relationship between postsynaptic preferred direction and presynaptic dendritic anatomical orientation (**Fig. 1.2D**) (Briggman et al., 2011; Wei et al., 2011a). Therefore, motion along the DSGC's null direction corresponds to centrifugal direction of the presynaptic SAC dendrites which results in maximal activation and significant GABA release. On the other hand, motion along the preferred direction corresponds to the centripetal direction of the presynaptic SAC dendrites which leads to little to no GABA release (**Fig. 1.2E**).

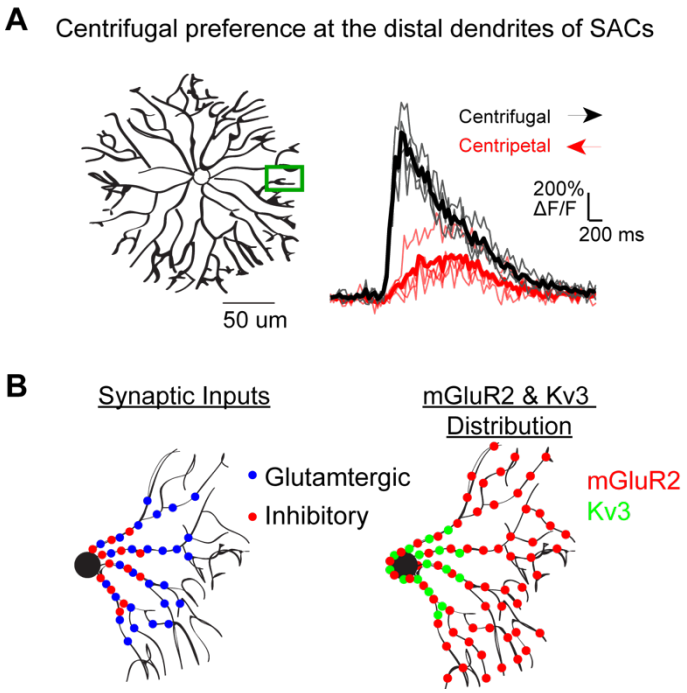

Figure 1.3: Centrifugal preference in the dendrites of SACs. (A) Left: Illustration of SAC radially symmetric morphology. Green square indicates imaging window for calcium imaging on the right. Right: Calcium transients at the distal dendrites during centrifugal and centripetal motion. (B) Left: Synaptic input distribution along the dendrites of SACs, adapted from (Ding et al., 2016b). Right: Distribution of mGluR2 and Kv3 along dendrites of SACs according to data from Chapter 2 and (Ozaita et al., 2004).

DSGCs receive excitatory cholinergic and glutamatergic inputs from SACs and bipolar cells, respectively. Numerous studies have reported direction selective excitatory synaptic currents in DSGCs that are eliminated upon wash-in of inhibitory blockers (Fried et al., 2005; S. Lee et al., 2010). Technical limitations of patch-clamp techniques and off-target effects of GABA-A receptor antagonists have hindered progress in the investigation of direction selective excitation in the direction selective circuit. In Chapter 3, I will revisit this question utilizing synapse specific genetic manipulations to eliminate improper space-clamp artefacts (Poleg-Polsky & Diamond, 2011) and pharmacological side-effects.

Furthermore, direction selective responses in the dendrites of SACs revealed a potential link between dendritic computation and visual motion processing (**Fig. 1.3A**). SAC dendrites are capable of transforming untuned glutamatergic excitatory inputs into a directional output (S. Lee & Zhou, 2006). Despite robust and highly directional distal calcium responses, SAC somatic responses are small and exhibit weak directionality (Euler et al., 2002). Electrotonic isolation is a remarkable feature of SACs that is important for centrifugal direction selectivity. In this scenario, dendritic compartmentalization prevents backpropagation of centrifugal responses into other dendritic sectors, which would otherwise render them non-directional. For this reason, SAC dendritic sectors have been traditionally considered as independent computational subunits; however, linear motion sequentially activates dendritic compartments implicating a potential role for global dendritic integration (Tukker et al., 2004). Synaptic and cell-intrinsic mechanisms are believed to concertedly contribute to centrifugal direction selectivity of SAC dendrites (**Fig. 1.3B**) (Hausselt et al., 2007; J. S. Kim et al., 2014; Koren et al., 2017; S. Lee & Zhou, 2006; Vlasits et al., 2016). Particularly, mGluR2 signaling in SACs is involved in regulating dendritic

compartmentalization (Koren et al., 2017). In Chapter 2, I will elaborate how mGluR2 signaling and cell-intrinsic properties coordinate a fine balance between dendritic isolation and integration in SACs.

1.2.2 Retinal orientation selectivity

Another prominent visual feature that is first computed is the retina is orientation or axis selectivity. Orientation selective neurons exhibit enhanced responses to a narrow range of stimulus orientations and a suppression of firing when presented with orientations that are 90 degrees from that of their preferred axis. These neurons were first identified in the cat's visual cortex by Hubel and Wiesel and have been described as simple or complex cells depending on the origin of their synaptic inputs and their receptive field properties (Hubel & Wiesel, 1959; Skottun et al., 1991). Since then, orientation selective responses have been observed across many visual areas (R. H. Masland et al., 1971; Zhao et al., 2013) including the retina (Nath & Schwartz, 2016, 2017). Orientation selective ganglion cells (OSGCs) have been reported in cat (Levick & Thibos, 1982), macaque (Passaglia et al., 2002), pigeon (Maturana & Frenk, 1963), rabbit (Venkataramani & Taylor, 2010), and mouse (Nath & Schwartz, 2016) retinas.

Cortical orientation selectivity has been attributed to elongated and overlapping receptive fields (Priebe & Ferster, 2012) and cell-intrinsic nonlinearities (Priebe et al., 2004). In contrast, retinal orientation sensitivity is less understood despite comprising a significant fraction (~ 15%) of responses from RGCs (Baden et al., 2016). Three types of orientation sensitive ganglion cells (OSGCs) have been reported in the mammalian retina using calcium imaging, patch clamp recording, and multi-electrode array recording: On, Off and On-Off types. OSGCs tuned to the

two cardinal axes (horizontal- and vertical-preferring) have been identified in the mouse (Baden et al., 2016; Nath & Schwartz, 2016, 2017) and rabbit retinae (Amthor et al., 1989; Levick, 1967; Venkataramani & Taylor, 2010, 2016), while those tuned to oblique orientations have been found in mouse (Baden et al., 2016), cat (Levick & Thibos, 1980, 1982), macaque (Passaglia et al., 2002), and zebrafish (Antinucci et al., 2016; Nikolaou et al., 2012).

Inhibitory inputs play a crucial role in shaping orientation tuning in rabbit OSGCs since blocking GABA-A receptors with picrotoxin eliminated selectivity in both On and Off OSGCs (Caldwell & Daw, 1978; Venkataramani & Taylor, 2010, 2016) suggesting that inhibitory inputs onto OSGCs resulted in an asymmetric antagonistic surround receptive field. In fact, both On and Off OSGC types in rabbits exhibit asymmetric inhibitory currents. In comparison, only horizontal-preferring On OSGCs in mouse exhibit asymmetric inhibitory currents. Vertical-preferring On OSGCs and both horizontal- and vertical-preferring Off OSGC types in mouse do not show selective tuning of their inhibitory inputs (Nath & Schwartz, 2016, 2017; Venkataramani & Taylor, 2010).

Furthermore, dendritic morphology has been shown to influence selectivity for oriented stimuli in retinal neurons. Asymmetric arbors create elongated receptive fields which are maximally activated by inputs along an oriented axis. Both mouse and rabbit horizontal-preferring On OSGCs display asymmetric, elongated dendritic arbors (**Fig. 1.4B**) biased along the preferred orientation of their spiking responses (Nath & Schwartz, 2016; Venkataramani & Taylor, 2016). These dendritic biases enable asymmetric spatiotemporal integration of excitatory inputs from bipolar cells. However, this is unlikely the only mechanism for orientation tuning in On OSGCs since they

also receive selective inhibitory inputs (**Fig. 1.4C**). Blocking GABAergic transmission with GABA-A receptor antagonists has been shown to abolish orientation tuning of spiking responses in On OSGCs in rabbit (Venkataramani & Taylor, 2016), but not in mice (Nath & Schwartz, 2016).

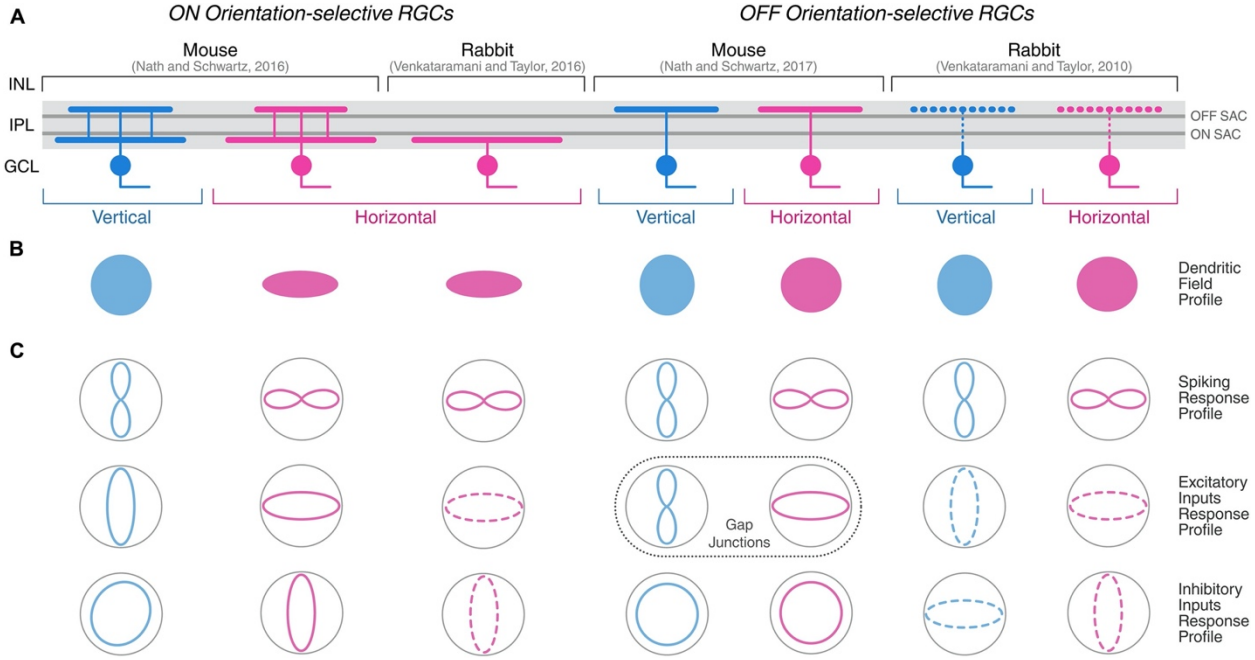

Figure 1.4: Mechanisms underlying On and Off retinal orientation selectivity. Summary of morphological and physiological findings from horizontal- and vertical-preferring OSGCs in mouse and rabbit retinas. (A) Dendritic stratification in the IPL with On (S4) and Off (S2) ChAT bands highlighted in dark gray. (B) Dendritic profiles of On and Off OSGCs. (C) Response profiles of OSGC spiking (top), excitatory inputs (middle), and inhibitory inputs (bottom). Dotted lines for excitatory and inhibitory input profiles are interpolated profiles from preferred and null data. *Adapted from (Antinucci & Hindges, 2018).*

In Chapter 6, we identify OSGCs in the mouse retina exhibiting both On and Off responses using two-photon calcium imaging and track the development of these complex receptive fields after the onset of visual experience.

1.3 Development of neural circuits in the vertebrate retina

The formation and refinement of synapses within neural circuits entwine several related developmental processes and hallmarks in the vertebrate retina. First, the time course of synapse

formation is closely linked to that of dendritic and axonal development (**Fig 1.5**). Second, before the onset of light response, the developing retina is not silent but exhibits both sporadic neurotransmission at developing synapses and coordinated spontaneous activity termed "retinal waves". Third, the development of retinal synaptic circuitry continues after the onset of light response, and is shaped by visual experience. Given the focus of this dissertation, this section will focus on development of the IPL and maturation of motion sensitive responses.

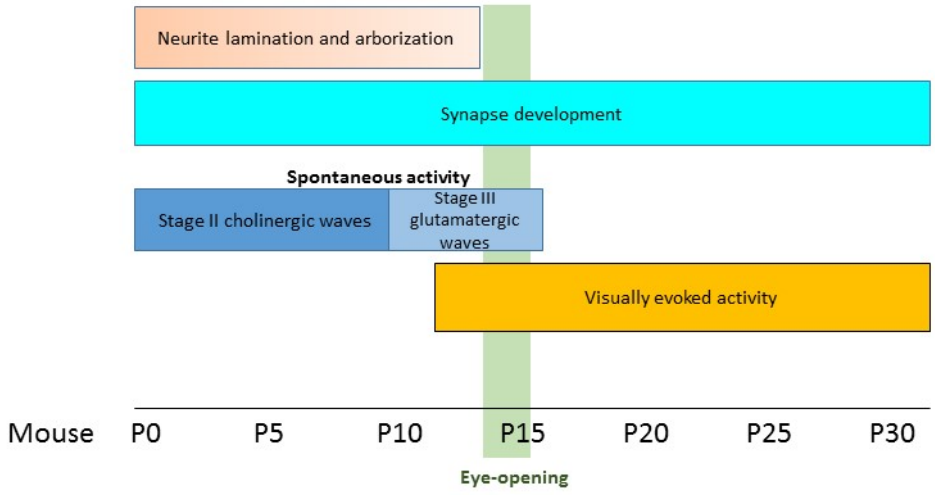

Figure 1.5: Timeline of synaptic development and patterned activity in the mouse retina. Synaptic development starts at birth and continues through the first postnatal month. In the first postnatal week, synapse development coincides with neurite growth and stage II retinal waves. In the second and third postnatal week, synapse refinement overlaps with stage III retinal waves and visually driven neural activity.

In most vertebrate retinas, the IPL matures before the OPL and conventional synapses originating from amacrine cells appear earlier than bipolar cell ribbon synapses (Hoon et al., 2014). In the mouse retina, amacrine synapses are evident in electron microscopy at P3, and continue to increase in number during the first two postnatal weeks (Fisher, 1979). In contrast, bipolar cell axons elaborate in the IPL at P7 (Morgan et al., 2006) and their ribbon synapses form between P11 to P15 (Fisher, 1979). The onset time of VGluT1 expression in BC axonal terminals is different between cone and rod bipolar cells, and between On and Off CBCs in the mouse retina. Expression

of VGluT1 in CBC terminals (P6-P10) precedes that in RBC terminals (P12) (Sherry et al., 2003). Spontaneous excitatory postsynaptic currents (EPSCs) in RGCs are detectable ~ P7 (Johnson et al., 2003; Morgan et al., 2008), which matches the maturation of CBC glutamate release. Within CBCs, VGluT1 expresses in the Off sublamina at P6-P8 before the On sublamina at P10 (Sherry et al., 2003), indicating an earlier maturation of the Off bipolar cell terminals.

Within each sublamina of the IPL, co-stratified neurons show remarkable specificity in their connectivity patterns. A well-documented example is the inhibitory connections between SACs and On-Off DSGCs. Functional GABAergic synapses between SACs and On-Off DSGCs can be detected by paired patch clamp recording at P4 in about half of the SAC-DSGC pairs with overlapping dendritic fields (Wei et al., 2011b). During the second postnatal week, the SAC sector oriented in the null direction of the DSGC show an increase of synaptogenesis with the DSGC, while the SAC sectors oriented in the preferred direction remain weakly connected to the DSGC without detectable pruning (Morrie & Feller, 2015; Wei et al., 2011b; Yonehara et al., 2011). This selective synaptogenesis between null-side SACs and DSGCs is independent of dendritic development, since SACs on both sides of the DSGC show comparable levels of dendritic overlap and densities of dendritic crossovers (Wei et al., 2011b). SAC GABAergic synapses onto On-Off DSGCs are critical for the retinal direction selectivity; however, blocking neural activity pharmacologically does not prevent the formation of asymmetric inhibitory synapses between these cells and does not affect the direction-selective spiking activity of On-Off DSGCs (Elstrott et al., 2008; L. Sun et al., 2011; Wei et al., 2011b).

The developing retina exhibits distinct forms of neural activity at different developmental stages. During the first postnatal week of the mouse, spontaneous bursts of action potentials spread across the retina in the GCL as propagating waves (Meister et al., 1991; Wong et al., 1993). These retinal waves are mediated by acetylcholine release from SACs (Feller et al., 1996; Ford & Feller, 2012). During the first ten postnatal days, SACs transiently express nicotinic acetylcholine receptors and thereby form a dense interconnected network to propagate excitation to neighboring SACs and nicotinic receptor-expressing RGCs. A few days before light response onset, cholinergic retinal waves are downregulated as SACs decrease their excitability and downregulate their nicotinic receptor expression (Ford & Feller, 2012). Between P10 and P14, glutamatergic retinal waves, which is thought to be mediated by bipolar cell glutamate spillover to extrasynaptic regions, replace cholinergic waves (Blankenship & Feller, 2010). Retinal waves are important for the refinement of retinal projections in the brain (Blankenship & Feller, 2010). However, disrupting waves causes minimal perturbations of IPL circuitry, which may be partially due to the appearance of compensatory activity in the retina mediated by gap junctions.

After the onset of light response, visually driven activity is concurrent with continuing synaptic development even though receptive field mosaics and plexiform layers of the retina have attained adult-like appearance. Visual experience has been shown to influence further On/Off segregation of synaptic inputs into RGCs (Bodnarenko & Chalupa, 1993; Tian & Copenhagen, 2003), and regulate bipolar cell synapse maturation in the OPL. In the direction-selective circuit, dark rearing does not affect the initial establishment of the direction selectivity of On-Off DSGCs (Elstrott et al., 2008; Wei et al., 2011b), but prevents the tight clustering of their preferred directions along the four cardinal directions (Bos et al., 2016). Further studies are needed to test if other aspects of

IPL circuit development are dependent on spatiotemporal characteristics of natural visual inputs. In Chapter 6, I will discuss the development of orientation sensitive receptive fields following the onset of visual experience and look into potential mechanisms underlying their development.

Chapter 2

Dendritic mechanisms underlying motion detection in starburst amacrine cells

Qiang Chen contributed to current-clamp recordings in wildtype and Vgat KO mice. Xiaolin Huang provided spontaneous EPSC recordings from SACs and DSGCs. Adam Zabner performed immunostaining for mGluR2 and Kv3.1.

2.1 Abstract

Neuronal dendrites impose specific transformations of spatiotemporally patterned synaptic inputs into outputs. The starburst amacrine cell (SAC), a key interneuron of the retinal direction-selective circuit, is an exemplary model of compartmentalized dendritic signaling. A visual stimulus moving across the SAC dendritic field strongly activates the SAC dendritic sector oriented to the direction of motion, but minimally activates the sector oriented to the opposite direction. How does the SAC integrate motion-evoked synaptic signals across its dendrites yet maintain independent direction tuning of individual dendritic sectors? Here, using a combination of electrophysiology and two-photon imaging of calcium and voltage sensors, we found that the dendritic arbor of the SAC is equipped with voltage-dependent mechanisms that are differentially distributed in the radial direction. In the SAC's proximal dendritic compartment, motion evokes a non-directional but highly stable subthreshold membrane depolarization due to enriched expression of voltage-gated potassium channels. This perisomatic motion signal nonlinearly integrates with local synaptic

inputs within each dendritic sector in a direction-selective manner via the activation of mGluR2-modulated voltage-gated calcium channels. As a result, SAC distal dendrites exhibit direction-selective calcium signals and provide direction-selective inhibitory inputs to direction-selective ganglion cells. Our findings highlight that functionally distinct dendritic compartments do not necessitate a highly isolated mode of synaptic integration, but leverage concerted intra- and cross-compartmental signal integration for compartment-specific dendritic computations.

2.2 Introduction

During neuronal signaling, synaptic signals undergo various transformations along dendrites by virtue of cell-type specific dendritic morphology and non-uniform subcellular distribution of inputs and ion channels. Therefore, the intrinsic biophysical properties of neuronal dendrites profoundly shape the input-output relationship of a neuron. Local computations in dendritic subregions, or compartments, are widespread throughout the brain and play important role in information processing (Hagai Agmon-Snir et al., 1998; Euler et al., 2002; Polsky et al., 2004) This is exemplified in starburst amacrine cells (SACs), whose individual dendritic sectors are independently tuned to distinct motion directions (Euler et al., 2002). SACs are axon-less, non-spiking interneurons in the mammalian retina whose radially symmetric dendritic arbors form a monolayer that narrowly stratifies in either the On or Off sublaminae of the inner plexiform layer (IPL) (E. V. Famiglietti, 1992; Edward V. Famiglietti, 1983). SACs receive non-directional synaptic inputs along their proximal dendrites (Ding et al., 2016b; Hanson et al., 2019; S. Lee & Zhou, 2006; Vlasits et al., 2016) and release neurotransmitters from varicosities located in their distal dendrites preferentially during visual stimuli moving in the centrifugal (soma-to-tip) direction (Qiang Chen et al., 2016; Euler et al., 2002). Therefore, the dendrites of SACs transform

untuned synaptic inputs into a directional output and are the sites where direction selectivity first emerges along the visual pathway. Centrifugal directional selectivity in SAC dendritic sectors is critical for generating directional signals in the output neurons of the retinal direction-selective circuit (He & Masland, 1997; Wässle, 2001; Yoshida et al., 2001), the direction-selective ganglion cells (DSGCs), because DSGCs receive asymmetric GABAergic inputs primarily from the SAC sectors oriented to the null direction DSGC (Briggman et al., 2011; Wei et al., 2011b). Together, direction-selective GABA release from distal SAC dendrites and the specific wiring between SAC dendritic sectors and DSGCs form a key mechanism underlying direction selectivity in the spiking responses of DSGCs.

Upon a visual stimulus moving across the entire SAC receptive field, the dendritic sector oriented opposite to the direction of motion is first stimulated by centripetal motion which leads to little or no response; but, as the stimulus continues to traverse the SAC receptive field it then stimulates the dendritic sector oriented in the direction of motion in the centrifugal direction which elicits a robust calcium response only in the distal varicosities of the centrifugally stimulated sector. How are SAC distal dendrites preferentially activated by light moving in their centrifugal direction? A useful approach is to consider individual dendritic sectors as “independent” computational units (Koren et al., 2017; Miller & Bloomfield, 1983; Tukker et al., 2004). Extensive studies on the direction-selective integration of synaptic inputs within a sector have identified multiple network mechanisms, including spatially segregated inputs and outputs along the dendrites (Vlasits et al., 2016), differential distributions of excitatory inputs with different temporal kinetics (J. S. Kim et al., 2014), lateral inhibition of SACs in the centripetal direction(Qiang Chen et al., 2016; S. Lee & Zhou, 2006), and cell-intrinsic contributions, such as patterned distribution of voltage-gated

channels (Kaneda et al., 2007; N. W. Oesch & Taylor, 2010; Ozaita et al., 2004) and passive cable properties of SAC dendrites (Poznanski, 1992). These mechanisms collectively account for strong and fast calcium transients detected in the centrifugally activated dendrites that result in strong GABA release from distal dendrites onto DSGCs.

While individual SAC dendritic sectors are independently tuned to different linear motion directions, they are nevertheless connected by the soma. Less studied are mechanisms that prevent the propagation of the strong dendritic activation in the centrifugally activated dendritic sector into other sectors. The SAC dendritic morphology, which features long, thin dendrites extending radially from the soma, contributes to the passive attenuation of signals along the dendritic arbor (Poznanski, 2005; Tukker et al., 2004). In addition, SACs express Kv3 type voltage-gated potassium channels in the perisomatic dendritic compartment that could function as a voltage-dependent shunt to limit the trans-somatic spread of depolarization from a centrifugally activated sector to other sectors (Ozaita et al., 2004). Furthermore, mGluR2 signaling in SACs modulates the activity of voltage-gated calcium channels, which is required for independent directional tuning of individual sectors (Koren et al., 2017). However, how these passive and active properties in SACs interact to regulate inter- and intra-dendritic signaling and preserve direction selectivity of individual sectors is not clear.

In this study, we focus on synaptic integration across the entire radial dendritic arbor of the SAC and examine how motion-evoked synaptic inputs across the dendritic tree are sequentially integrated and transformed by multiple dendritic compartments during the course of the motion trajectory. We combine two-photon subcellular calcium and voltage imaging, and patch clamp

recording to monitor activity patterns in soma and dendritic subregions under normal conditions and under conditions when mGluR2 signaling or Kv channels are blocked. We found that these two mechanisms concertedly modulate cross-compartmental synaptic integration that is necessary for the direction selectivity of SAC dendrites. Together, our findings highlight that the synergic action of voltage-dependent mechanisms across different dendritic compartments is critical for maintaining the functional independence of SAC dendritic sectors.

2.3 Results

2.3.1 Cross-compartmental integration of global and local dendritic signals lead to robust centrifugal responses in SACs

In this study, we focus on On SACs given their accessibility in the ganglion cell layer, similarities between On and Off SACs, and their contributions to both On and On-Off retinal direction selectivity (Edward V. Famiglietti, 1983; O'Malley et al., 1992). The receptive field profile of On SACs consists of an inhibitory surround and an excitatory center as a result of lateral inhibition and the proximal skew of vertical bipolar cell inputs (Ankri et al., 2020; Taylor & Wässle, 1995; Vlasits et al., 2016). Regardless of motion direction, full-field stimulation with a bright bar moving across the entire receptive field sequentially activates the surround and then the center triggering an initial hyperpolarization followed by a depolarization that plateaus at a membrane potential of -48.31 ± 4.30 mV (mean ± s.e.m), or 19.80 ± 0.97 mV (mean ± s.e.m) above rest (**Figure 2.1A**). The onset of depolarization occurs when the leading edge of the moving bar is located 44.28 ± 8.37 μm (mean ± s.e.m) prior to the soma and peaks when the bar is located 129.90 ± 7.11 (mean ± s.e.m) after the soma (**Figure 2.1A**). Therefore, activation of the perisomatic region is initiated while the centripetal oriented sector, or the sector oriented opposite to the direction of motion, is

being stimulated and continues to increase while the centrifugal sector, or sector oriented in the direction of motion, is stimulated.

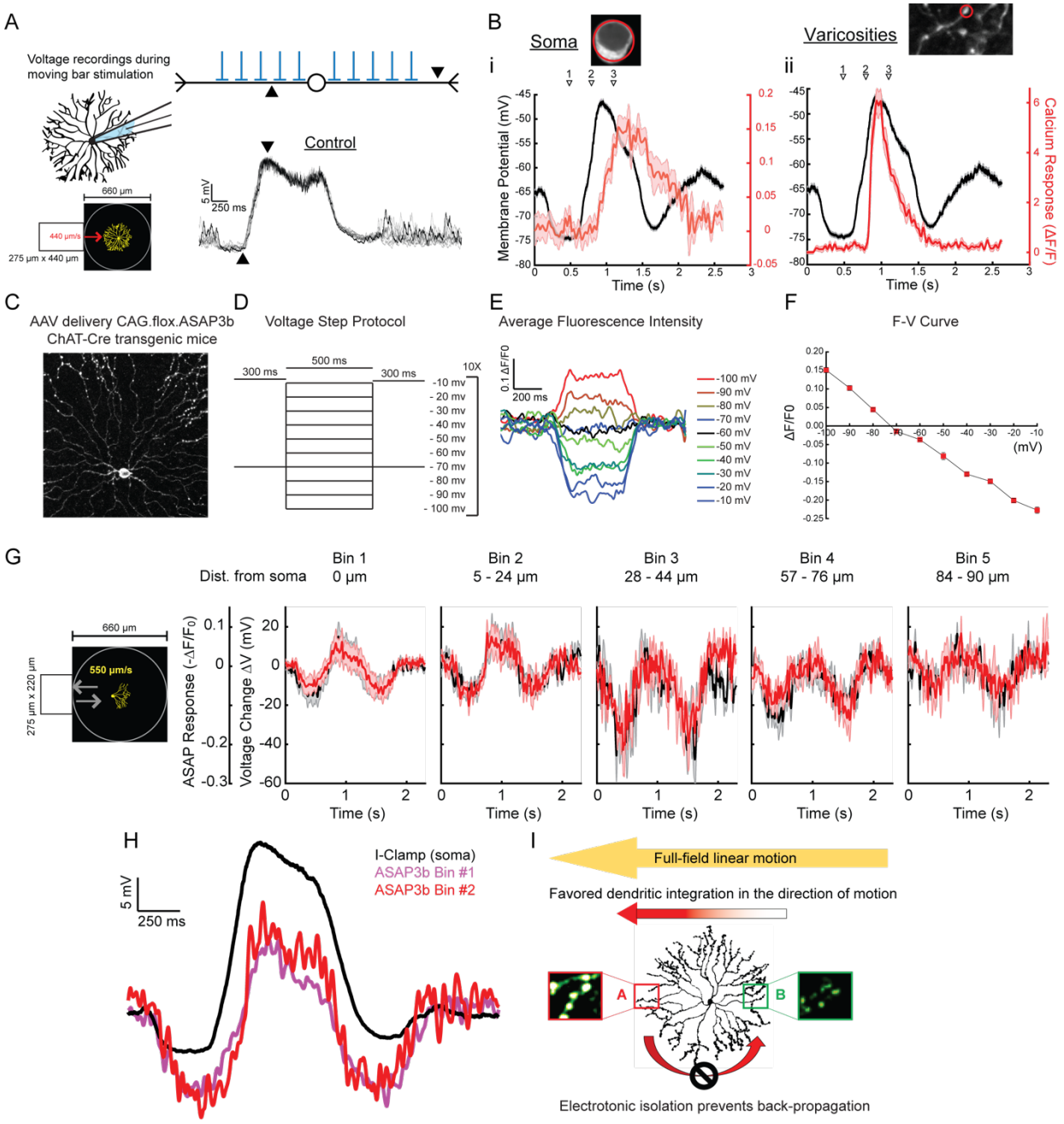

Figure 2.1: Cross-compartmental signal integration in SACs. A) Left: Schematic depicting experimental setup for current-clamp recordings. Top, right: Schematic illustrating spatial separation between SAC depolarization onset (up-triangle) and peak (down-triangle) during moving bar stimulation in relation to glutamatergic bipolar cell inputs (blue). Bottom, right: Representative traces of current-clamp recording during moving bar visual stimulation. Depolarization onset and peak marked by up and down triangles, respectively. B) Correlation of GCaMP6f signals at the (i) soma and (ii) distal dendrites with perisomatic depolarization. Open

Figure 2.1 (cont.). triangles correspond to timing of leading edge of moving bar (1 = leading edge enters SAC dendritic field, 2 = leading edge at the soma, 3 = leading edge exits dendritic field). C) Example SAC expressing GEVI ASAP3b. D) Schematic of applied voltage step protocol used to characterize F-V relationship in E and F. E) Representative average ASAP3b fluorescence traces across 10 trials. F) Fluorescence versus voltage curve shown as mean ± s.e.m. (n = 4 SACs). G) Visual-evoked ASAP3b responses shown as mean ± s.e.m at increasing distances from the soma. Red – centrifugal direction, black – centripetal direction. Bin #1 (n = 5 SACs), Bin #2 (n = 7 SACs), Bin #3 (n = 3 SACs), Bin #4 (n = 5 SACs), Bin #5 (n = 2 SACs). H) Overlay of current-clamp recording with average ASAP3b traces from Bin #1 (soma) and Bin #2. I) Summary illustrating how favorable integration and electronic mechanisms regulate activity in SACs.

Robust, fast-rising calcium responses in the distal dendrites of SACs have been reported with organic calcium dyes and genetically encoded indicators (Qiang Chen et al., 2016; Euler et al., 2002; Koren et al., 2017; S. Lee & Zhou, 2006; Poleg-Polsky et al., 2018); yet, whole-cell voltage recordings with K^+-based internal show that the perisomatic depolarization is void of any non-linear events (**Figure 2.1A-B**). Using two-photon laser scanning calcium imaging, we compared GCaMP6f signals in the soma and distal dendrites to the voltage waveform recorded at the soma. Calcium imaging at the soma revealed relatively small and slow-rising transients (average maximal response of 0.15 ± 0.04 $\Delta F/F_0$ and rise time of 454.3 ± 105.4 ms, mean ± s.e.m) whose rise and decay onset correlated well with the plateau electrical potential recorded at the soma and the kinetics of the GCaMP6f sensor (T. W. Chen et al., 2013) (**Figure 2.1B**). In contrast, we observed large, fast-rising fluorescence calcium transients (average maximal response of 5.48 ± 0.89 $\Delta F/F_0$ and rise time of 159.6 ± 31.8 ms, mean ± s.e.m) at distal dendritic locations upon stimulation with a visual stimulus moving in the centrifugal direction of the imaged dendrite. The amplitude and kinetics of the centrifugal calcium responses in the distal dendrites of SACs are indicative of a non-linear calcium event likely recruiting both N- and P/Q-types of high-voltage activated calcium channels (Cohen, 2001). The onset timing of the centrifugal calcium response aligns well with the peak of the perisomatic depolarization. Together, the somatic voltage and calcium signals shown here highlight the extent of attenuation that happens from tip to soma.

Additionally, the relative timing of perisomatic depolarization and dendritic calcium responses support the possibility coincidence detection or temporal integration of perisomatic and local dendritic signals lead to favorable dendritic integration in dendritic sectors oriented in the direction of motion; however, the extent that perisomatic signals influence dendritic responses is less known.

To explore how subthreshold voltage signals spread across dendritic compartments, we expressed the genetically encoded voltage indicator (GEVIs) ASAP3b (Lin & Schnitzer, 2016; Villette et al., 2019) in SACs (**Figure 2.1C**). ASAP-family GEVIs consist of a circularly permutated green fluorescent protein (GFP) inserted into a voltage-sensitive domain (Villette et al., 2019). In this configuration, protein conformations induced by depolarization of membrane potential dim GFP fluorescence, while those resulting from membrane hyperpolarization increase GFP fluorescence. This allows us to visualize bidirectional changes to the resting membrane potential along SAC dendrites. We first characterized the fluorescence-voltage (F-V) relationship of ASAP3b in SACs by measuring fluorescence changes ($\Delta F/F_0$) in response to applied discrete voltage steps in voltage-clamp mode (**Figure 2.1D-E**). This revealed a linear F-V curve with a slope of -0.0042 $\Delta F/F_0$ per mV within the -100 mV to -10 mV range (**Figure 2.1F**). This conversion factor was then used to convert ASAP3b $\Delta F/F_0$ signals into voltage changes from rest.

To image visual-evoked voltage responses, we equipped our custom-built two-photon microscope with a gallium arsenide phosphide (GaAsP) detector for improved photon sensitivity during time-lapse fluorescence voltage imaging and measured ASAP3b responses from 3 μm × 5 μm fields of view located at increasing distances from the soma while presenting a bright bar moving in the centripetal and centrifugal directions of the imaged dendrite (**Figure 2.1G**). ASAP3b fluorescence

transients were transformed into $\Delta F/F_0$ signals, resampled to 1000 Hz, and smoothed over 12 ms time window. Finally, ASAP3b signals were sorted by centripetal versus centrifugal direction of motion, binned and averaged by dendritic location, and converted into voltage change from rest using the slope of the F-V curve previously described. Averaging across trials and cells improves signal-to-noise ratio at the cost of high-frequency information; therefore, this dataset is not representative of non-linear voltage events that could be happening in the distal dendrites but is informative about low-frequency subthreshold depolarization. Analysis of low-frequency signals revealed a similar ASAP3b voltage waveform across all dendritic locations regardless of the direction of motion stimulation (**Figure 2.1G**). Furthermore, ASAP3b voltage waveforms from the perisomatic regions correlate well with current-clamp recordings during moving bar visual stimulation (**Figure 2.1H**). The enhanced hyperpolarization observed in bin 3 (28 – 44 μm away from the soma) can be explained by the proximal clustering local inhibitory synapses at these dendritic distances (Ding et al., 2016). Together, this data shows moving bar visual stimulation creates a subthreshold global signal that spreads well throughout the SAC.

During a full-field moving bar, the onset of the subthreshold global activation occurs while the centripetal oriented sector is being stimulated and spreads to opposing dendritic sectors prior to the arrival of local glutamatergic inputs (**Figure 2.1A**). Therefore, local inputs onto the centrifugal oriented sector can build on top of the global signal to generate a robust calcium response. Despite efficient cross-compartmental propagation of voltage from soma to tip, dendritic signals are attenuate as they propagate towards the soma since the perisomatic depolarization is non-directional and limited to 19.80 ± 0.97 mV (mean ± s.e.m) above rest (**Figure 2.1A-B,I).** Furthermore, the amplitude and kinetics of the voltage waveform recorded at the soma are highly

consistent across visual stimulation conditions, including contrast, speed, and dimensions of the moving bar suggesting there are mechanisms in place to ensure a reliable characteristic subthreshold response (Lipin et al., 2015). Synaptic mechanisms (Qiang Chen et al., 2016; Ding et al., 2016a; Fransen & Borghuis, 2017; J. S. Kim et al., 2014; Koren et al., 2017) and biophysical properties of SAC dendrites (Gavrikov et al., 2006; Ozaita et al., 2004; Tukker et al., 2004) have been postulated to contribute to centrifugal direction selectivity; but, a mechanistic understanding of how these orchestrate a fine balance between dendritic integration and isolation remains to be elucidated.

SAC dendrites are highly enriched in voltage-gated potassium channels containing subfamily 3.1 subunits (Kv3.1) (Ozaita et al., 2004). To investigate the role Kv3 plays in motion processing in SACs, we first visualized dendritic distributions of Kv3.1 by staining against the intracellular portion of the channel with a monoclonal primary antibody (Invitrogen #MA5-27684 Mouse monoclonal anti-Kv3.1 antibody) and using fluorescence microscopy (**Figure 2.2A**). Results from these experiments confirmed Kv3.1 expression exhibits a proximal-to-distal gradient since strong Kv3.1 immunofluorescence was detected in the soma and proximal regions while little to no signal was observed in the dendritic plexus layers (**Figure 2.2A**). Kv3 exhibits enhanced sensitivity to TEA compared to other voltage-gated K channels, and can be primarily blocked with 1 mM extracellular TEA (Rudy et al., 1999; Ozaita et al., 2004). Experiments before and after Kv3 block revealed that these channels mediate large outward currents in SACs (**Fig. 2.2B,D)** and prevent somatic depolarization above -45 mV (**Fig. 2.2C,E**). Unlike their traditional role in high-frequency firing neurons, Kv3 in SACs is believed to maintain a subthreshold low-noise perisomatic signal and orchestrate voltage attenuation from tip to soma (Ozaita et al., 2004).

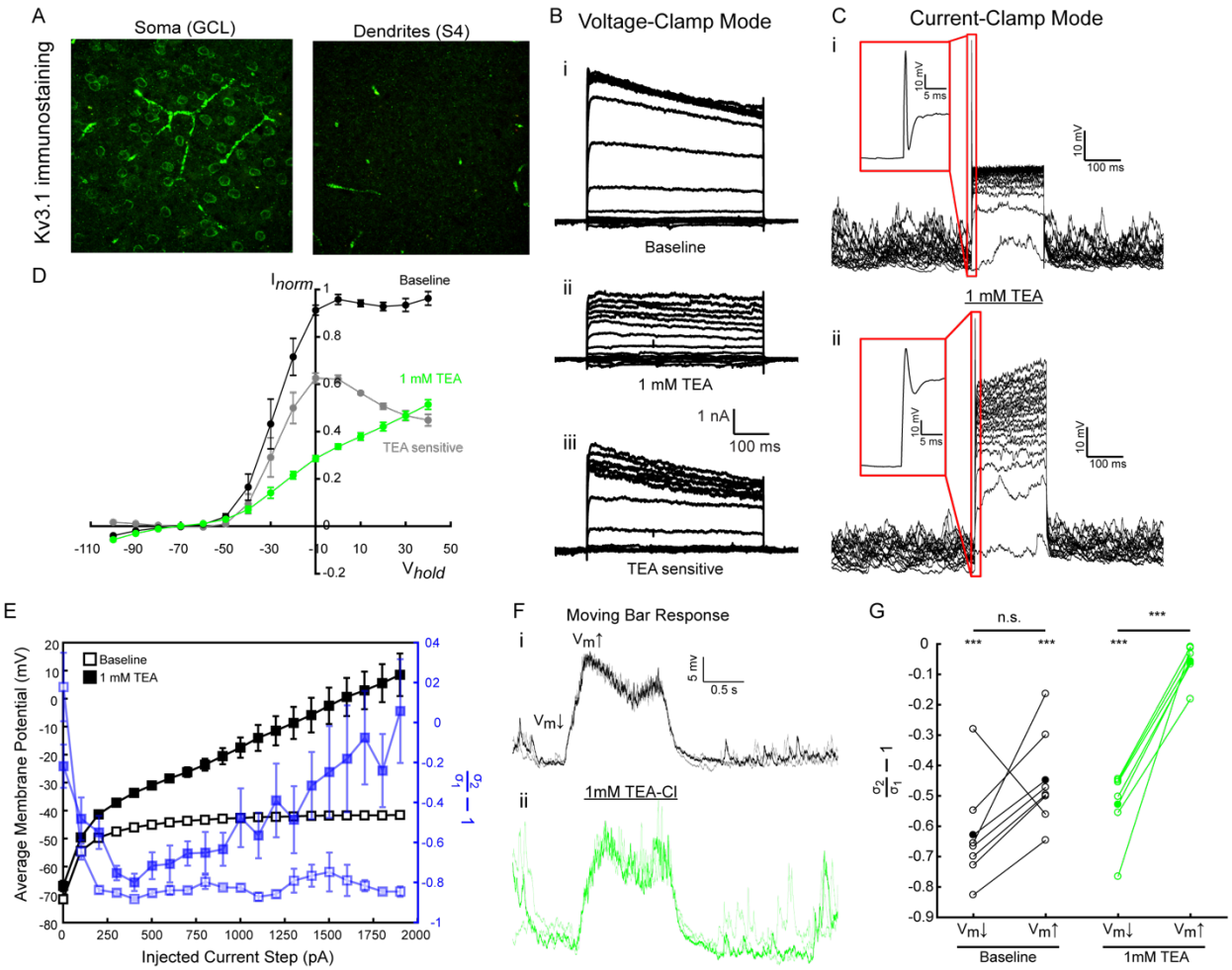

Figure 2.2: Kv3 channels in SACs limit perisomatic depolarization and reduce noise during motion stimulation. A) Example Kv3.1 immunostaining fluorescence images from the GCL (left) and S4 plexus layer (right). B) Representative traces of outward currents (K internal) in SACs under i) baseline condition and ii) application of 1 mM TEA. iii) Subtraction of ii) from i). C) Representative traces of membrane potential during applied current steps (K internal) in SACs i) before and ii) after application of 1 mM TEA. D) Current-voltage relationship of outward currents under baseline (black) and 1 mM TEA (green) conditions. Gray represents the subtracted TEA sensitive component (n = 5 SACs). E) Average membrane potential (black) and change in noise levels (blue) upon applied current steps. Open squares and closed squares correspond to baseline and 1 mM TEA conditions, respectively (n = 7 SACs). F) Representative traces of current-clamp recordings during moving bar visual stimulation under i) baseline and ii) 1 mM TEA conditions. G) Changes in noise levels during initial hyperpolarization and depolarization phases of moving bar response before (black) and after (green) application of 1 mM TEA. Open circles and closed circles correspond to individual cells and average calculation.

SACs have a highly fluctuating resting membrane potential (**Figure 2.2**C) due to tonic excitatory inputs from bipolar cells. However, at depolarized states the membrane potential becomes more

stable with less fluctuations across time (**Figure 2.2C,E**). Following bath application of 1 mM TEA, SACs experienced stronger depolarization and enhanced voltage fluctuations compared to baseline upon applied current steps (**Figure 2.2E**). Additionally, during moving bar visual stimulation SACs experience an initial hyperpolarization followed by a depolarized plateau as previously described (**Figure 2.2F**). In both of these phases, the membrane potential experiences significantly less voltage fluctuation across time compared to the resting membrane potential (**Figure 2.2G**, black). The surround inhibitory inputs likely shunt the resting tonic glutamatergic inputs and quiet the membrane voltage prior to the onset of depolarization (Chen et al., 2020 under review). Upon Kv3 blockade with 1 mM TEA, we observed an increase in voltage fluctuations during the depolarized phase of the moving bar response suggesting that outward currents mediated by Kv3 play a role in creating a stable low-noise subthreshold signal in the perisomatic region (**Figure 2.2G**, green). The data presented so far demonstrates that SACs experience a global signal during moving bar visual stimulation that is regulated by Kv3 to ensure a reliable, steady subthreshold depolarization.

2.3.2 Blockade of mGluR2 signaling differentially affects SAC somatic and dendritic responses to motion

Cross-compartmental signal integration leads to robust calcium responses in the distal dendrites of SACs; however, a mechanistic understanding on how dendritic integration is favored in the centrifugal direction is not fully understood. SACs express high levels of metabotropic glutamate receptor II (mGluR2), which has been shown to modulate both N- and P/Q-types of voltage-gated calcium channels (VGCCs) (Koren et al., 2017). Pharmacological blockade of mGluR2 results in reduced centrifugal preference in distal varicosities (**Figure 2.3A-B**) and aberrant GABAergic

transmission from SACs to DSGCs during motion stimuli (Koren et al., 2017). Nevertheless, the extent that mGluR2 regulates compartmentalized signaling and visual responses along dendritic subdomains of SACs remains to be explored.

One possibility is that enhanced VGCC availability in the dendrites of SACs following mGluR2 blockade could facilitate trans-somatic propagation of signaling from one dendritic sector to another. If proper mGluR2 signaling prevents cross-sector propagation in SACs, we would expect enhanced calcium activity in the somatic region upon mGluR2 blockade. Using two-photon laser scanning calcium imaging, we compared calcium transients at the soma and the distal dendrites during bright moving bar visual stimulation before and after pharmacological blockade of mGluR2 (**Figure 2.3A-B**). As previously demonstrated, calcium imaging under baseline conditions revealed large, fast-rising fluorescence transients (average maximal response of 5.48 ± 0.89 $\Delta F/F_0$ and rise time of 159.6 ± 31.8 ms, mean ± s.e.m) in the distal dendrites; whereas, responses at the soma were relatively small and slow-rising (average maximal response of 0.15 ± 0.04 $\Delta F/F_0$ and rise time of 454.3 ± 105.4 ms, mean ± s.e.m) (**Fig 2.1B and 2.3A-B**). Additionally, responses at the distal varicosities were highly direction-selective (DSI = 0.6 ± 0.04, mean ± s.e.m; n = 16 varicosities) and exhibited tuning to the centrifugal direction of the imaged dendritic sector (**Fig 2.3B-E**, Euler et al., 2002). Upon application of 100 nM LY341495, a selective mGluR2 antagonist, centrifugal preference in distal varicosities was significantly reduced (**Fig 2.3E**, DSI = 0.6 ± 0.04 for baseline, n = 16 varicosities versus 0.05 ± 0.03 for LY341495, n = 15 varicosities; $p < 0.0001$ Wilcoxon-Rank Sum Test). Consistent with previous studies, this reduction in directional preference was due to increased visual responses to centripetal motion ($p = 0.002$ Wilcoxon-Rank Sum Test) since the amplitude of centrifugal responses were mostly unaffected

(not significant, p = 0.70 Wilcoxon-Rank Sum Test) (**Fig 2.3C-D**). However, bath application of LY341495 did not result in significant changes to calcium transients at the soma (**Fig. 2.3A-F**, p > 0.05 Wilcoxon-Rank Sum Test).

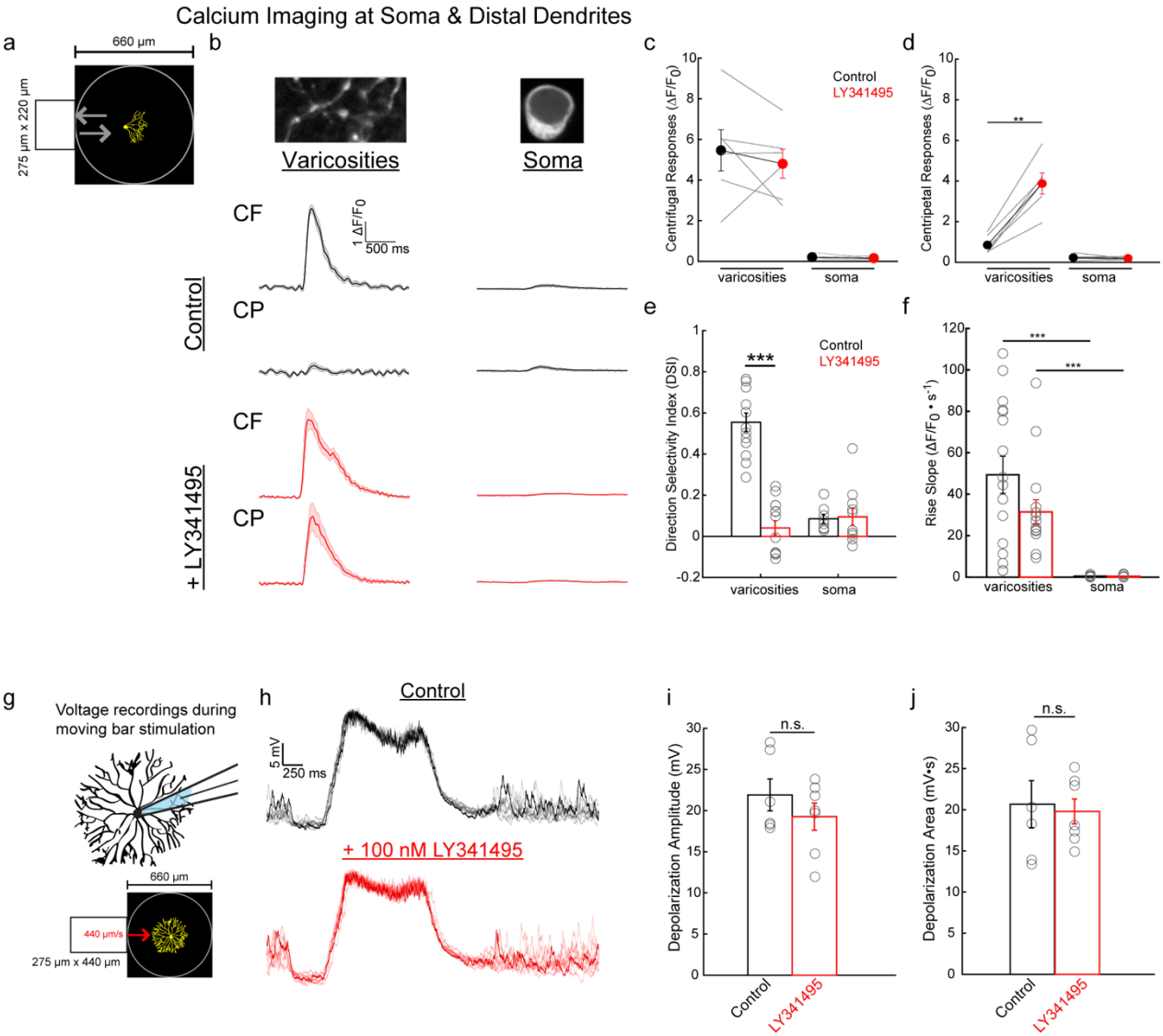

Figure 2.3: mGluR2 blockade results in aberrant activity at the distal dendrites of SACs, but not at the soma. (A) Schematic of experimental setup and visual stimulation for calcium imaging experiments. **(B)** Top: Example images of GCaMP6 fluorescence in distal SAC varicosities (left) and soma (right) from a ChAT-IRES-Cre mouse injected with AAV-7m8.floxed-GCaMP6f. Bottom: Representative fluorescence traces (mean ± s.e.m, $\Delta F/F_0$) recorded at distal varicosities (left) and at the soma (right) during centripetal (CP) and centrifugal (CF) motion before (black) and after application of mGluR2 antagonist (100 nM LY341495, red). **(C)** Pairwise comparison of centrifugal responses before (black, mean ± s.e.m) and after application of 100 nM LY341495 (black, mean ± s.e.m). Gray lines correspond to the average centrifugal response from individual

Figure 2.3 (cont.) cells before and after mGluR2 blockade. Wilcoxon-Rank Sum Test shows no significance: distal varicosities – 5.47 ± 1.02 $\Delta F/F_0$ for baseline conditions versus 4.81 ± 0.71 $\Delta F/F_0$ for LY341495, p = 0.70 n = 6 cells; soma – 0.20 ± 0.04 $\Delta F/F_0$ for baseline conditions versus 0.16 ± 0.03 $\Delta F/F_0$ for LY341495, p = 0.32 n = 7 cells. **(D)** Pairwise comparison of centripetal responses before (black, mean ± s.e.m) and after application of 100 nM LY341495 (black, mean ± s.e.m). Gray lines correspond to the average centripetal response from individual cells before and after mGluR2 blockade. Wilcoxon-Rank Sum Test: distal varicosities – 0.85 ± 0.18 $\Delta F/F_0$ for baseline conditions versus 3.87 ± 0.52 $\Delta F/F_0$ for LY341495, p = 0.002 n = 6 cells; soma – 0.23 ± 0.05 $\Delta F/F_0$ for baseline conditions versus 0.19 ± 0.03 $\Delta F/F_0$ for LY341495, p = 0.54 n = 7 cells. **(E)** Quantification of direction selectivity index (mean ± s.e.m) at distal varicosities (left) and the soma (right) under baseline conditions (black) and during mGluR2 blockade (red). Wilcoxon-Rank Sum Test: distal varicosities – DSI = 0.6 ± 0.04 for WT, n = 16 varicosities versus 0.05 ± 0.03 for LY341495, n = 15 varicosities, p < 0.0001; soma – DSI = 0.09 ± 0.02 for WT, n = 11 cells versus 0.09 ± 0.04 for LY341495, n = 12 cells, p = 0.41. **(F)** Quantification of rise slope (mean ± s.e.m) at distal varicosities (left) and the soma (right) under baseline conditions (black) and during mGluR2 blockade (red). Wilcoxon-Rank Sum Test: distal varicosities – 49.35 ± 8.94 $\Delta F/F_0\ s^{-1}$ for WT, n = 16 varicosities versus 31.42 ± 5.91 $\Delta F/F_0\ s^{-1}$ for LY341495, n = 15 varicosities, p = 0.20; soma – 0.45 ± 0.12 $\Delta F/F_0\ s^{-1}$ for WT, n = 11 cells versus 0.39 ± 0.13 $\Delta F/F_0\ s^{-1}$ for LY341495, n = 12 cells, p = 0.56. **(G)** Schematic of experimental setup for whole-cell current-clamp experiments. **(H)** Representative voltage traces (mean ± s.e.m, $\Delta F/F_0$) recorded the soma (right) during full-field moving bar stimulation before (black) and after application of mGluR2 antagonist (100 nM LY341495, red).Traces correspond to individual trials from the same cell with one trial highlighted in a darker color. **(I)** Quantification of depolarization amplitude (mean ± s.e.m) at the soma under baseline conditions (black) and during mGluR2 blockade (red). Student t-test: 21.91 ± 1.94 mV (n = 6 cells) for baseline versus 19.26 ± 1.65 mV (n = 7 cells), p = 0.32. **(J)** Quantification of depolarization amplitude (mean ± s.e.m) at the soma under baseline conditions (black) and during mGluR2 blockade (red). Student t-test: 20.67 ± 2.87 mV (n = 6 cells) for baseline versus 19.79 ± 1.51 mV (n = 7 cells), p = 0.78.

We then performed whole-cell current-clamp recordings using K^+-based internal to examine changes in subthreshold membrane potential (V_m) and the extent of visual-evoked depolarization before and after mGluR2 blockade (**Fig. 2.3**). Quantification of the peak depolarization amplitude (**Figs. 2.3H-I**, Baseline: 21.91 ± 3.87 mV and LY: 19.26 ± 3.30 mV, mean ± s.e.m) and area (**Fig. 2.3J**, Baseline: 20.67 ± 5.74 mV•s and LY: 19.79 ± 3.02 mV•s, mean ± s.e.m) shows no significant change after bath application of 100 nM LY341495 (p > 0.05 Student t-Test). Together, the lack of evidence of aberrant activity present at the soma through calcium imaging and voltage recording after mGluR2 blockade indicates that the enhanced centripetal responses observed at the distal tips is not a result of trans-somatic propagation. Alternatively, mGluR2 could regulate interactions

between global and local dendritic signals in SACs and the emergence visual responses to centripetal motion could result from these local changes in compartmentalization within individual sectors.

2.3.3 mGluR2 gates the initiation of calcium signals in SAC dendritic sectors

To further look into how mGluR2 can regulate responses along dendritic compartments in SACs, we first investigated the subcellular dendritic distribution of mGluR2. mGluR2 expression patterns were visualized by staining against the intracellular portions of the receptor with a monoclonal primary antibodies (Abcam #ab238432: Rabbit monoclonal anti-mGluR2 antibody) and using fluorescence microscopy (**Figure 2.4A**). Strong mGluR2 immunofluorescence was found in the soma, proximal, and plexus layers (**Figure 2.4A**) suggesting a uniform distribution of mGluR2 from soma to tip. Results from this mGluR2 staining contrasts with the Kv3.1 distribution shown in **Figure 2.2**, which exhibits a proximal-to-distal gradient expression pattern. Therefore, Kv3 and mGluR2 likely regulate partially overlapping dendritic segments but mGluR2 activation can inhibit distally located VGCCs (**Figure 2.4B**).

Activation of mGluR2 is initiated by glutamate release from bipolar cells. Unlike DSGCs, SAC receive tonic glutamatergic inputs at rest which could set a tonic activation of mGluR2 prior to any visual stimulation (**Figure 2.10**). Under baseline conditions, inward currents through N- and P/Q-types of VGCCs can be observed at voltage steps above -20 mV (**Figure 2.4C**). However, upon mGluR2 blockade with 100 nM LY341495 these inward calcium currents become detectable at voltage steps to -40 mV or above (**Figure 2.4C**). This indicates that mGluR2 is at least partially active at rest and that mGluR2-mediated inhibition of VGCCs modulates the threshold for calcium

spike initiation in the distal dendrites. Therefore, mGluR2 could regulate integration of global and local signals by gating the initiation of calcium events.

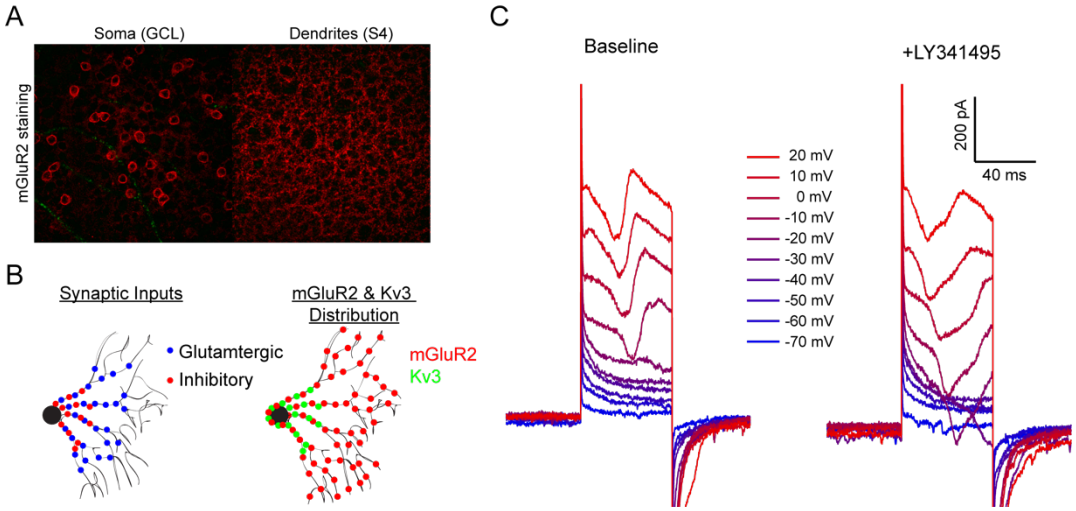

Figure 2.4: Tonic mGluR2 activation regulates threshold for VGCC opening. A) Example fluorescence images of mGluR2 immunostaining in the GCL (left) and S4 (right) plexus layers. B) Schematic illustrating distribution of synaptic inputs (left, red-inhibitory and blue-excitatory) and voltage-dependent mechanisms (right, red-mGluR2 and green-Kv3). C) Currents during applied voltage steps with Cs internal before (left) and after mGluR2 blockade (right).

To compare visual responses to linear motion across dendritic compartments, we induced sparse expression of GCaMP6f using a low-titer viral AAV injection to facilitate tracing of individual dendrites within the dense SAC-network (**Fig. 2.5A**). For these experiments, we also co-expressed tdTomato in SACs to ease focusing of small dendritic segments in which baseline GCaMP6f fluorescence is low. Dendritic sectors were stimulated with a bright bar (275 µm × 220 µm) moving across the entire SAC receptive field at 440 µm/s in the centripetal and centrifugal directions of the imaged sectors. We observed monotonically increasing centrifugal responses with increasing distance from the soma (**Fig. 2.5B,D**). On the other hand, centripetal responses did not increase as dramatically with dendritic distance (**Fig. 2.5B,D**). Similar to previous studies (Euler et al., 2002; Vlasits et al., 2016), we found that centrifugal responses were significantly larger (2:1

CF-to-CP ratio) than centripetal responses at approximately 50% dendritic distance (CF: 2.77 ± 0.86 $\Delta F/F_0$ versus CP: 1.52 ± 0.64 $\Delta F/F_0$; mean ± s.e.m $p = 0.0120$ Wilcoxon-Rank Sum Test, **Fig. 2.5B,D**) and this difference continued to increase (4:1 CF-to-CP ratio) at more distal sites (CF: 6.31 ± 0.96 $\Delta F/F_0$ versus CP: 1.83 ± 0.56 $\Delta F/F_0$ mean ± s.e.m at 90% dendritic distance; $p = 0.002$ Wilcoxon-Rank Sum Test). These differences in motion evoked responses resulted in high direction selectivity indexes in distal dendrites (DSI: 0.32 ± 0.07 at 50% dendritic distance and DSI: 0.62 ± 0.06 at 90% dendritic distance) compared to the soma and proximal regions (DSI: 0.02 ± 0.04, mean ± s.e.m at the soma and DSI: 0.14 ± 0.03, mean ± s.e.m at 10% dendritic distance) (**Fig. 2.5C**). These results show that direction selective signals can be found in the outer half of SAC dendrites and that these differences in directional responses emerge as visual responses to centrifugal motion increase from soma to tip in a graded-like fashion.

To investigate how blocking endogenous mGluR2 signaling impacts light responses across dendritic compartments in SACs, we mapped motion evoked GCaMP6 responses along SAC dendrites before and after application of a selective mGluR2 antagonist (100 nM LY341495). As previously described, bath application of 100 nM of LY341495 lead to enhanced centripetal responses (1.83 ± 0.56 $\Delta F/F_0$ for baseline and 7.50 ± 1.39 $\Delta F/F_0$ for +LY341495; mean ± s.e.m $p = 0.0007$ Wilcoxon-Rank Sum Test) and a loss of direction selectivity (DSI = 0.62 ± 0.06 for baseline and DSI = 0.12 ± 0.03 for +LY341495; mean ± s.e.m $p = 10^{-6}$ Wilcoxon-Rank Sum Test) in the distal dendrites (90% dendritic length) (**Fig. 2.5B-C,E-G**). Interestingly, enhanced peak amplitudes during centripetal motion were only observed at sites located 50% dendritic distances or greater from the soma; whereas sites more proximal and the soma did not exhibit detectable changes after wash-in of 100 nM LY341495 ($p > 0.05$ Wilcoxon-Rank Sum Test, **Fig. 2.5E**). On the other hand, peak amplitudes to centrifugal motion were unaffected by mGluR2 blockade across

all dendritic compartments ($p > 0.05$ Wilcoxon-Rank Sum Test, **Fig. 2.5F**). These results suggest that mGluR2 controls the local initiation of calcium transients and mGluR2-mediated inhibition of VGCCs is critical in suppressing the centripetal response during linear motion. Furthermore, mGluR2 blockade had little influence over perisomatic indicating that other mechanisms, such as passive properties and Kv3-mediated outward currents, prevent the initiation of events in these dendritic compartments and attenuate propagation of signals from tip to soma.

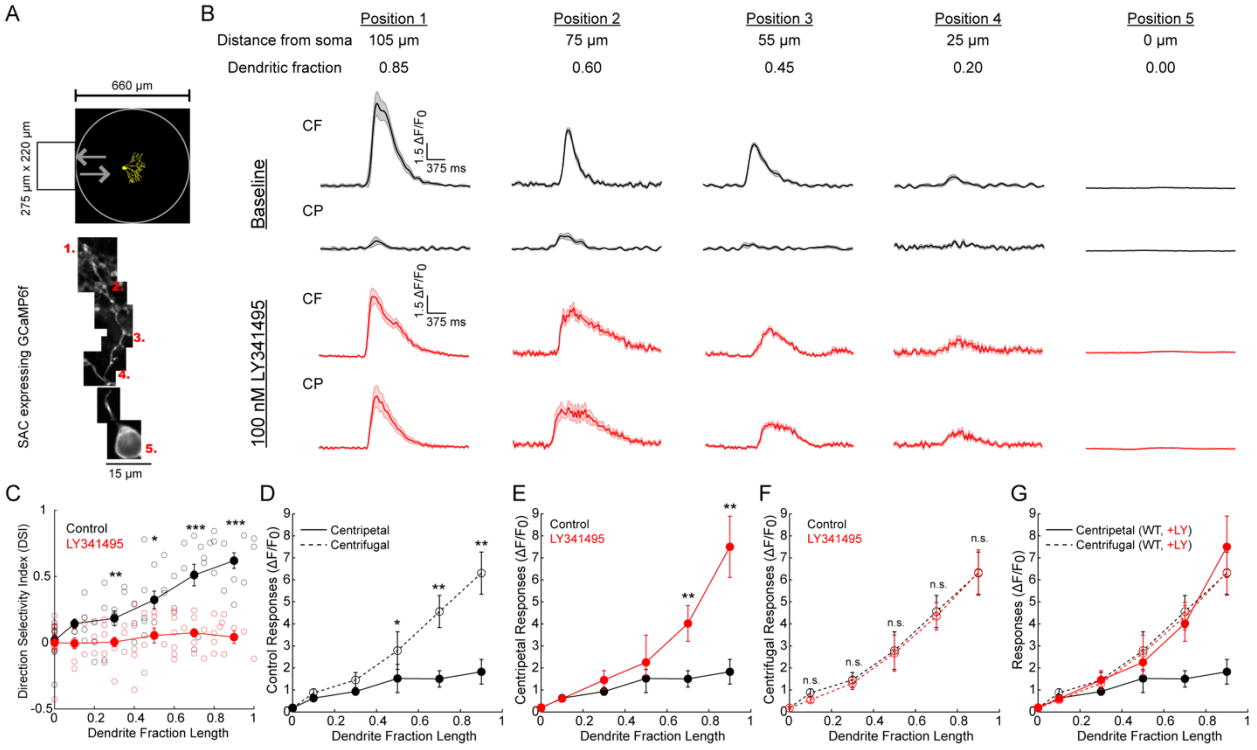

Figure 2.5: mGluR2 regulates local initiation of calcium events in the dendrites of SACs. (A) Top: Schematic of experimental setup and visual stimulation for dendritic calcium imaging. Bottom: Example reconstruction of SAC dendrite expressing GCaMP6. **(B)** Representative fluorescence calcium traces (mean ± s.e.m) during centrifugal (CF) and centripetal (CP) motion before (black) and after application of 100 nM LY341495 (red) at different distances from the soma. **(C)** Quantification of direction selectivity index across dendritic compartments under baseline conditions (black) and mGluR2 blockade (red). Filled circles correspond to binned averages ± s.e.m (bin size of 0.2 fraction length). Open circles represent individual measurements. Wilcoxon-Rank Sum Test; Bin 1 (soma): DSI = 0.02 ± 0.04 for baseline versus 0.00 ± 0.05 for LY341495 $p = 0.74$, Bin 2 (fraction length < 0.2): DSI = 0.14 ± 0.03 for baseline versus -0.01 ± **Figure 2.5 (cont.)** 0.04 for LY341495 $p = 0.04$, Bin 3 (0.2 ≤ fraction length < 0.4): DSI = 0.18 ± 0.06 for baseline versus 0.01 ± 0.04 for LY341495 $p = 0.01$, Bin 4 (0.4 ≤ fraction length < 0.6):

DSI = 0.32 ± 0.07 for baseline versus 0.05 ± 0.06 for LY341495 p = 0.01, Bin 5 (0.6 ≤ fraction length < 0.8): DSI = 0.51 ± 0.08 for baseline versus 0.07 ± 0.03 for LY341495 p = 5.25×10^{-4}, Bin 6 (0.8 ≤ fraction length ≤ 1.0): DSI = 0.62 ± 0.06 for baseline versus 0.04 ± 0.05 for LY341495 p = 2.65×10^{-5}. **(D)** Quantification of fluorescence calcium responses across dendritic compartments during centripetal (CP, filled circles and solid line) versus centrifugal motion (CF, open circles and dashed line). Circles correspond to binned averages ± s.e.m (bin size of 0.2 fraction length). Wilcoxon-Rank Sum Test; Bin 1 (soma): CP = 0.18 ± 0.04 $\Delta F/F_0$ versus CF = 0.18 ± 0.04 $\Delta F/F_0$ p = 0.95, Bin 2 (fraction length < 0.2): CP = 0.63 ± 0.13 $\Delta F/F_0$ versus CF = 0.87 ± 0.19 $\Delta F/F_0$ p = 0.33, Bin 3 (0.2 ≤ fraction length < 0.4): CP = 0.93 ± 0.17 $\Delta F/F_0$ versus CF = 1.45 ± 0.34 $\Delta F/F_0$ p = 0.18, Bin 4 (0.4 ≤ fraction length < 0.6): CP = 1.52 ± 0.64 $\Delta F/F_0$ versus CF = 2.77 ± 0.86 $\Delta F/F_0$ p = 0.01, Bin 5 (0.6 ≤ fraction length < 0.8): CP = 1.50 ± 0.37 $\Delta F/F_0$ versus CF = 4.56 ± 0.73 $\Delta F/F_0$ p = 0.002, Bin 6 (0.8 ≤ fraction length ≤ 1.0): CP = 1.83 ± 0.56 $\Delta F/F_0$ versus CF = 6.31± 0.96 $\Delta F/F_0$ p = 0.002. **(E)** Quantification of calcium responses during centripetal motion across dendritic compartments under baseline conditions (black) and mGluR2 blockade (red). Filled circles correspond to binned averages ± s.e.m (bin size of 0.2 fraction length). Wilcoxon-Rank Sum Test; Bin 1 (soma): CP = 0.18 ± 0.04 for baseline versus 0.21 ± 0.05 for LY341495 p = 0.79, Bin 2 (fraction length < 0.2): CP = 0.63 ± 0.13 $\Delta F/F_0$ for baseline versus 0.61 ± 0.15 for LY341495 p = 0.91, Bin 3 (0.2 ≤ fraction length < 0.4): CP = 0.93 ± 0.17 $\Delta F/F_0$ for baseline versus 1.45 ± 0.42 for LY341495 p = 0.52, Bin 4 (0.4 ≤ fraction length < 0.6): CP = 1.52 ± 0.64 $\Delta F/F_0$ for baseline versus 2.26 ± 0.58 for LY341495 p = 0.20, Bin 5 (0.6 ≤ fraction length < 0.8): CP = 1.50 ± 0.37 $\Delta F/F_0$ for baseline versus 4.02 ± 0.81 for LY341495 p = 0.002, Bin 6 (0.8 ≤ fraction length ≤ 1.0): CP = 1.83 ± 0.56 $\Delta F/F_0$ for baseline versus 7.50 ± 1.39 for LY341495 p = 7.41×10^{-4}. **(F)** Quantification of calcium responses during centrifugal motion across dendritic compartments under baseline conditions (black) and mGluR2 blockade (red). Circles correspond to binned averages ± s.e.m (bin size of 0.2 fraction length). Wilcoxon-Rank Sum Test; Bin 1 (soma): CF = 0.18 ± 0.04 for baseline versus 0.18 ± 0.05 for LY341495 p = 0.99, Bin 2 (fraction length < 0.2): CF = 0.87 ± 0.19 $\Delta F/F_0$ for baseline versus 0.55 ± 0.11 for LY341495 p = 0.18, Bin 3 (0.2 ≤ fraction length < 0.4): CF = 1.45 ± 0.34 $\Delta F/F_0$ for baseline versus 1.30 ± 0.28 for LY341495 p = 0.73, Bin 4 (0.4 ≤ fraction length < 0.6): CF = 2.77 ± 0.86 $\Delta F/F_0$ for baseline versus 2.67 ± 0.82 for LY341495 p = 0.68, Bin 5 (0.6 ≤ fraction length < 0.8): CF = 4.56 ± 0.73 $\Delta F/F_0$ for baseline versus 4.35 ± 0.62 for LY341495 p = 0.56, Bin 6 (0.8 ≤ fraction length ≤ 1.0): CF = 6.31± 0.96 $\Delta F/F_0$ for baseline versus 6.34 ± 1.03 for LY341495 p = 0.95. **(G)** Summary plot using data from **E-F**.

2.3.4 mGluR2 and Kv3 synergistically control dendritic excitability in SACs

mGluR2 and Kv3 represent fundamental voltage-dependent mechanisms for dendritic compartmentalization in SACs. Given their subcellular distribution, mGluR2 and Kv3 likely regulate interactions between dendritic subdomains and the perisomatic region. We therefore tested the synergistic action of mGluR2 and Kv3 in regulating activity in the perisomatic region of SACs by recording voltage at the soma during moving bar visual stimulation before and after

simultaneous blockade of mGluR2 and Kv3 (**Figure 2.6**). We used 1 mM TEA in the extracellular solution to block Kv3 channels (Rudy et al., 1999; Ozaita et al., 2004) and 100 nM LY341495 to block mGluR2. Upon bath application of 1 mM TEA, we occasionally observed fast voltage deflections riding on top of the typical slow depolarization (**Figure 2.7B**, green). These high-frequency voltage deflections became more prominent during concurrent blockade of mGluR2 and Kv3 and resemble spikelet activity (**Figure 2.6B**, blue). Power spectrum analysis of these voltage traces identified increases in voltage signals in the 20 – 50 Hz range for LY341495, 3 – 50 Hz range for TEA, and 3-50 HZ with a pronounced peak at 30 Hz for the combination of LY341495 and TEA (**Fig. 2.7B**).

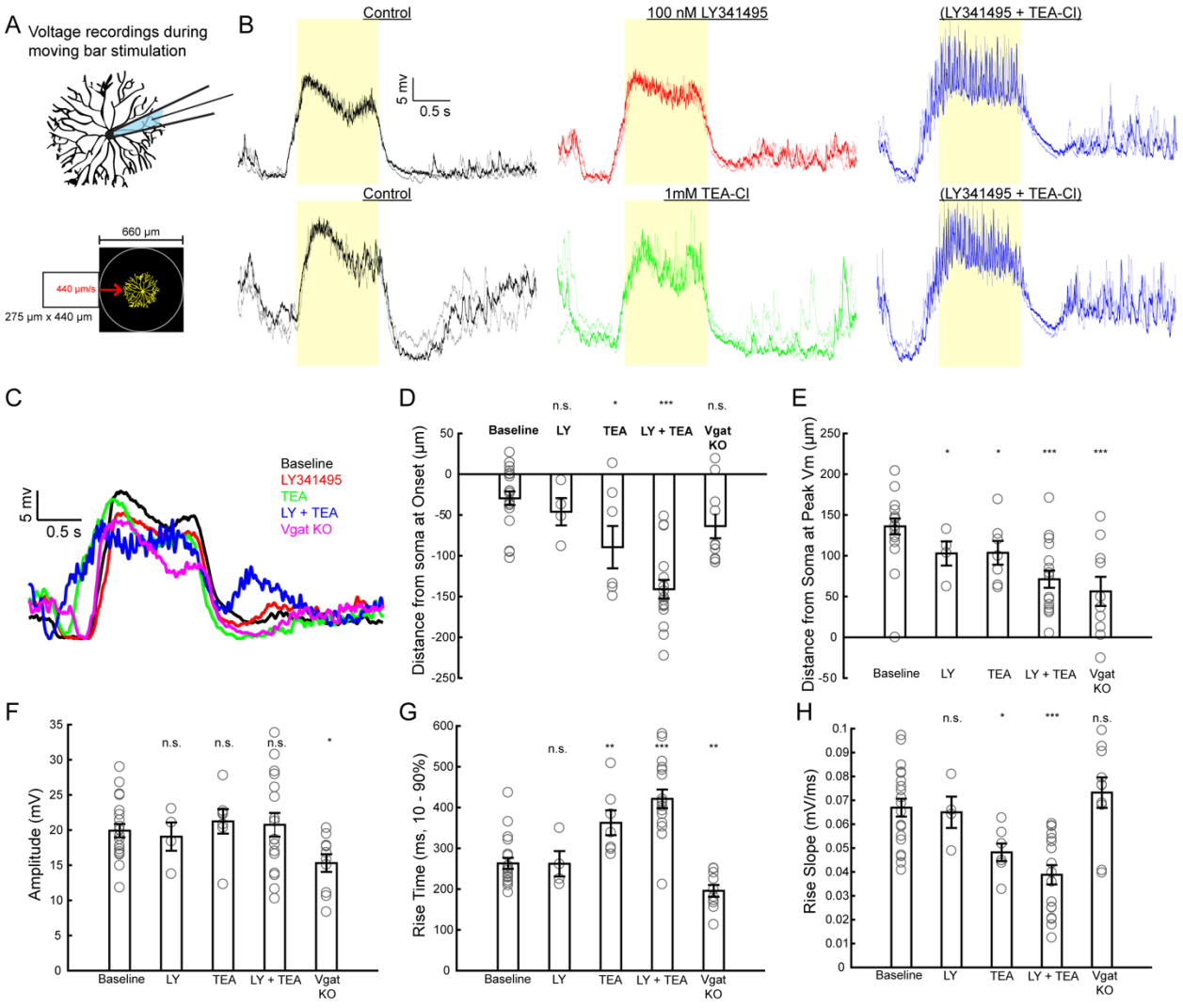

Figure 2.6: mGluR2 and Kv3 synergistically control dendritic integration. (A) Schematics highlighting subcellular distribution of synaptic inputs (left, excitatory – blue and inhibitory – red), mGluR2 (right, red), and Kv3 (right, green). **(B)** Example fluorescence images showing expression of mGluR2 (left, red) and Kv3.1b (right, green) at different optical depths corresponding to GCL and S4. **(C)** Schematic of experimental setup for whole-cell current-clamp experiments. **(D)** Representative voltage traces recorded under baseline (black), 100 nM LY341495 (red), 1 mM TEA-Cl (green), and combination of TEA-Cl and LY341495 (blue). Top: drug wash-in in the follow order - baseline → LY341495 → LY341495 + TEA-Cl. Bottom: drug wash-in in the follow order - baseline → TEA-Cl → LY341495 + TEA-Cl. Traces correspond to individual trials from the same cell with one trial highlighted in a darker color. Yellow shaded region corresponds to the timing that the leading edge of the moving bar is passing through the center excitatory receptive fields of SACs. **(E)** Representative filtered average traces from baseline (black), LY341495 (red), TEA (green), LY + TEA (blue), and Vgat KO (pink) conditions. Quantification of distance from soma at Vm onset **(F)**, distance from soma at maximum Vm **(G)**, depolarization amplitude **(H)**, 10 – 90% rise time **(I)**, and rise slope **(J)** across all conditions described in **E**.

To examine the low-frequency component (typical slow-wave depolarization) across all testing conditions, we computed an averaged filtered voltage trace for each cell by averaging across 5 individual trials and passing the resulting averaged trace through a low-pass filter with a cutoff frequency of 20 Hz (**Fig. 2.6C**). Quantification of the depolarization amplitude (**Fig. 2.6F**) and resting potential (data not shown) shows no significant difference under any of the drug conditions compared to baseline. However, upon mGluR2 or Kv3 blockade the peak of depolarization occurred earlier (LY341495: 102.79 ± 21.75 μm, mean ± s.e.m past the soma, Student's t-test p = 0.0262 and TEA: 103.51 ± 25.43 μm, mean ± s.e.m past the soma, Student's t-test p = 0.0398) (**Fig. 2.6B-C,E**). Furthermore, following application of 1 mM TEA the onset of depolarization occurred earlier (89.70 ± 56.63 μm, mean ± s.e.m prior to the soma, Student's t-test p = 0.0313), an effect that was exacerbated by simultaneous blockade of mGluR2 and Kv3 (146.27 ± 43.76 μm, mean ± s.e.m prior to the soma, Student's t-test $p = 1\times10^{-6}$) (**Figure 2.6D**). SACs form inhibitory connection with other neighboring SACS (Qiang Chen et al., 2016; Ding et al., 2016b); therefore, we would expect these pharmacological manipulations to affect SAC-SAC mutual inhibition

complicating our results. To determine how much of this phenomenon could be explained by disrupted mutual inhibition, we repeated these experiments in transgenic mice in which SAC GABA release is eliminated (Vgat KO mouse) (Qiang Chen et al., 2016; Huang et al., 2019; Pei et al., 2015) (**Fig. 2.6C**). In the Vgat KO mouse, relative timing of depolarization peak occurred significantly earlier than wildtype, similar to the LY + TEA condition (**Fig. 2.6E**). However, the onset of depolarization was not significantly different than wildtype (**Fig. 2.6D**), indicating that the effects seen in TEA and LY + TEA are independent of SAC-SAC mutual inhibition. Together, this data indicates that mGluR2-mediated inhibition of VGCCs and Kv3-mediated currents regulate how inputs are integrated as propagate towards the soma and in their absence the spatiotemporal dynamics of voltage activation in SACs are severely altered.

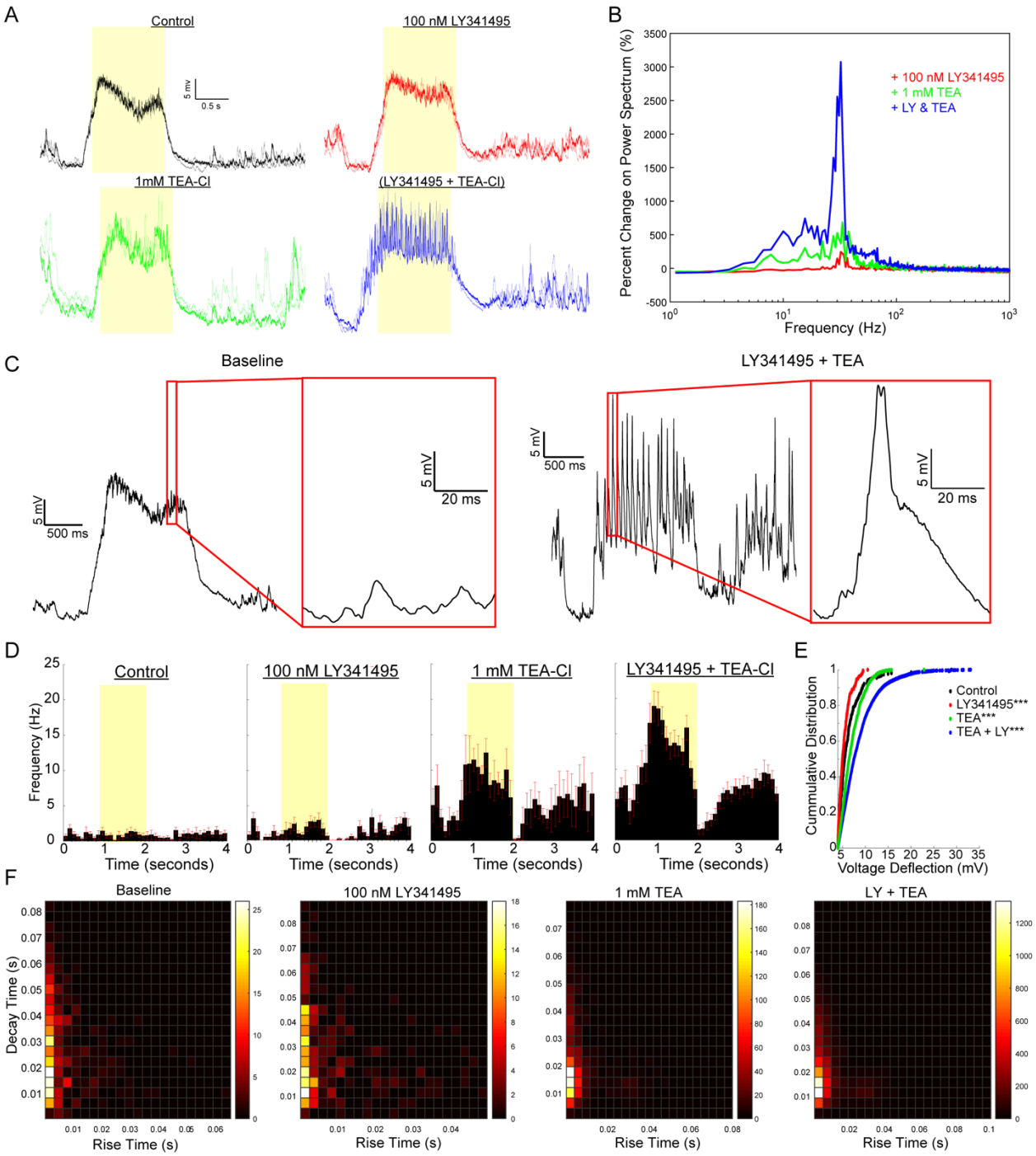

Figure 2.7: mGluR2 and Kv3 synergistically control dendritic excitability. (A) Representative voltage traces recorded under baseline (black), 100 nM LY341495 (red), 1 mM TEA-Cl (green), and combination of TEA-Cl and LY341495 (blue). Traces correspond to individual trials from the same cell with one trial highlighted in a darker color. Yellow shaded region corresponds to the **Figure 2.7 (cont.)** timing that the leading edge of the moving bar is passing through the center excitatory receptive fields of SACs. **(B)** Power spectrum analysis as percent change from baseline. LY341495 (red): n = 8 cells, TEA-Cl (green): n = 7 cells, TEA + LY (blue): n = 19 cells. **(C)** Example trace under baseline condition (left) and after application of both LY341495 and TEA-Cl (right). Inset shows single voltage deflection event. **(D)** Peristimulus histograms (mean ± s.e.m,

100 ms bins) of voltage deflections detected under i.) baseline, ii.) LY341495, iii.) TEA-Cl, and iv.) LY341495 and TEA-Cl conditions. Yellow shaded region corresponds to the timing that the leading edge of the moving bar is passing through the center excitatory receptive fields of SACs. **(E)** Cumulative distribution plot of voltage deflection amplitudes detected under baseline conditions (black), 100 nM LY341495 (red), 1 mM TEA-Cl (green), and combination of TEA-Cl and LY341495 (blue). Kolmogorov-Smirnov test: baseline versus LY341495 $p = 4.50\times10^{-4}$, : baseline versus TEA-Cl $p = 2.00\times10^{-22}$, : baseline versus LY341495 + TEA-Cl $p = 8.06\times10^{-62}$. (F) Rise (10 – 90%) versus decay (90 – 10%) time heatmaps of high-frequency voltage deflections detected under i.) baseline, ii.) LY341495, iii.) TEA-Cl, and iv.) LY341495 and TEA-Cl conditions.

Given the emergence of high-frequency activity at the soma during concurrent blockade of mGluR2 and Kv3, we isolated and analyzed voltage events in the 20 – 50 Hz range across the conditions described above. High-frequency events were isolated by creating a rolling adjusting baseline and using a peak detection algorithm to identify peaks > 4 mV with widths corresponding to 20 – 50 ms. As previously described, these high-frequency events were rarely detected under baseline or upon application of 100 nM LY341495. After application of 1 mM TEA, the frequency of detectable events increased particularly during the time window that the leading (or On) edge of the moving bar traveled across the cell's excitatory receptive field center (**Figure 2.7D**). Despite the higher frequency, blockade of Kv3 alone did not yield larger spikelet amplitudes compared to baseline conditions (**Figure 2.7E**). On the other hand, concurrent blockade of mGluR2 and Kv3 (+ 100 nM LY341495 and 1 mM TEA) resulted in both a higher frequency and larger amplitude of these voltage events (**Figure 2.7D-E**). Results from these experiments reveal a synergistic relationship between mGluR2 and Kv3 in dampening membrane excitability in the perisomatic region of SACs.

To rule out the possibility that bath application of TEA destabilizes the retinal network, we repeated the current-clamp recordings described above using Cs-based internal (110 mM

$CsMeSO_4$ and 5 mM TEA). Although Cs-based internal non-selectively blocks all Kv channels, it enables Kv blockade in a single cell eliminating potential network effects. Therefore, baseline recordings in Cs-internal are analogous to recording in TEA using K-internal. These experiments yielded similar results to K-internal recordings including emergence of spike-like events after bath application of LY341495 (corresponding to Kv and mGluR2 blockade in K^+ internal experiments) with the exception that the resting voltage was more depolarized (**Figure 2.8**), probably due to inability to repolarize the cell because of total Kv blockade.

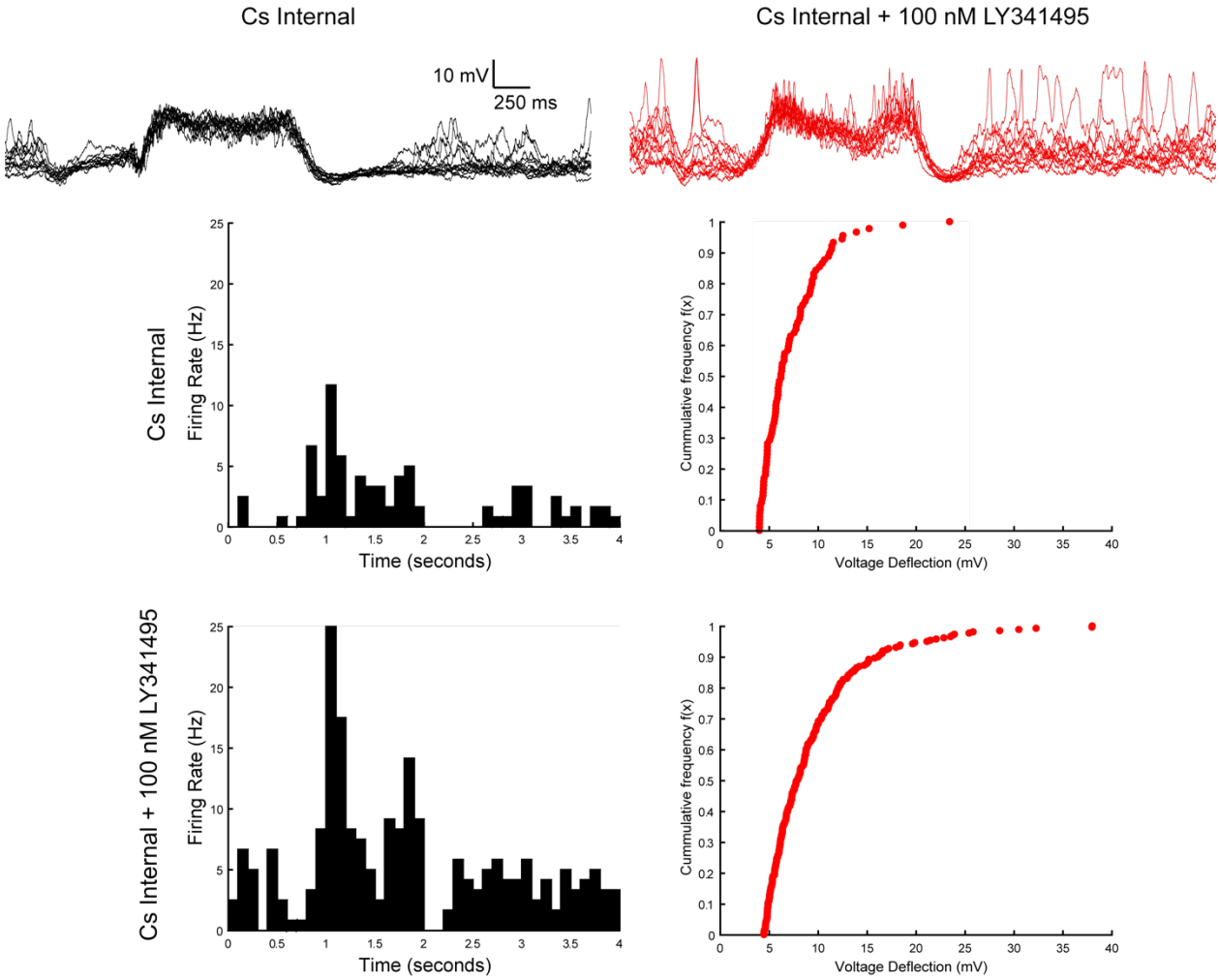

Figure 2.8: Example current-clamp recording using Cesium based internal. Representative traces of current-clamp recordings during moving bar visual stimulation before (black, left) and after application of 100 nM LY341495 (red, right). Representative peristimulus histograms (100 ms bins) of detected high-frequency voltage deflections from recordings shown above). Representative cumulative frequency distribution of voltage deflection amplitude.

2.3.5 Concurrent blockade of mGluR2 and Kv3 in SACs disrupts visual evoked GABAergic inhibition onto DSGCs

Given the profound effects of concurrent mGluR2 and Kv3 blockade in SACs, we investigated the effect of blocking mGluR2 and Kv3 on asymmetric inhibition onto DSGCs. We targeted posterior-preferring On-Off DSGCs using a Drd4-GFP transgenic mouse line and recorded inhibitory postsynaptic currents (IPSCs) during moving bar visual stimulation before and during mGluR2/Kv3 blockade (**Fig. 2.9**). As expected, prior to application of 100 nM LY341495 and 1 mM TEA we observed directionally tuned inhibition onto On-Off DSGCs that was time-locked to the leading and trailing edge of the moving bar passing across the DSGC inhibitory receptive field (**Fig. 2.9A-B**, left). Upon mGluR2/Kv3 blockade, there was drastic reduction in direction selectivity of IPSCs (On: DSI = 0.40 ± 0.07 and Off: DSI = 0.42 ± 0.04 fore baseline versus On: DSI = 0.10 ± 0.03 and Off: DSI = 0.10 ± 0.04 for LY/TEA, mean ± s.e.m) accompanied by a decrease in signal-to-noise ratio (**Fig. 2.9A-C**). Surprisingly, we also noticed a significant increase in the holding current required to maintain the membrane voltage at 0 mV (I_{hold} = 271.81 ± 9.04 pA for baseline compared to I_{hold} = 517.14 ± 41.79 pA upon application of LY341495/TEA, mean ± s.e.m **Fig. 2.9D**). Previous studies on mGluR2 regulation of retinal direction selectivity have reported enhanced inhibition during preferred direction motion; however, application of mGluR2 antagonists alone have not led to changes in null direction inhibition, holding current at 0 mV, or signal-to-noise of SAC-mediated inhibition (Koren et al., 2017). Bath application of 100 nM LY341495 and 1 mM TEA is unlikely to cause changes in membrane resistance in DSGCs because LY341495 is highly selective for mGluR2, which is primarily found in SACs, and external TEA should have negligible effects on the cell of interest since Cs-based internal (110 mM $CsMeSO_4$

and 5 mM TEA) already blocks most potassium channels. Therefore, we tested whether the elevated holding current could represent a biologically relevant inhibitory current by bath applying a GABA-A receptor antagonist SR95531 (gabazine). After wash-in of 25 µM SR95531, the holding current at 0 mV returned to baseline conditions (I_{hold} = 271.81 ± 9.04 pA for baseline compared to I_{hold} = 244.09 ± 6.58 pA for LY341495/TEA/SR95531, mean ± s.e.m) suggesting that the uncontrolled V_m in SACs during mGluR2/Kv3 blockade results in tonic GABA release from SACs to DSGCs. These experiments highlight the downstream effects of disrupted electrotonic isolation in SACs and illustrate how dendritic compartmentalization supports high signal-to-noise synaptic transmission.

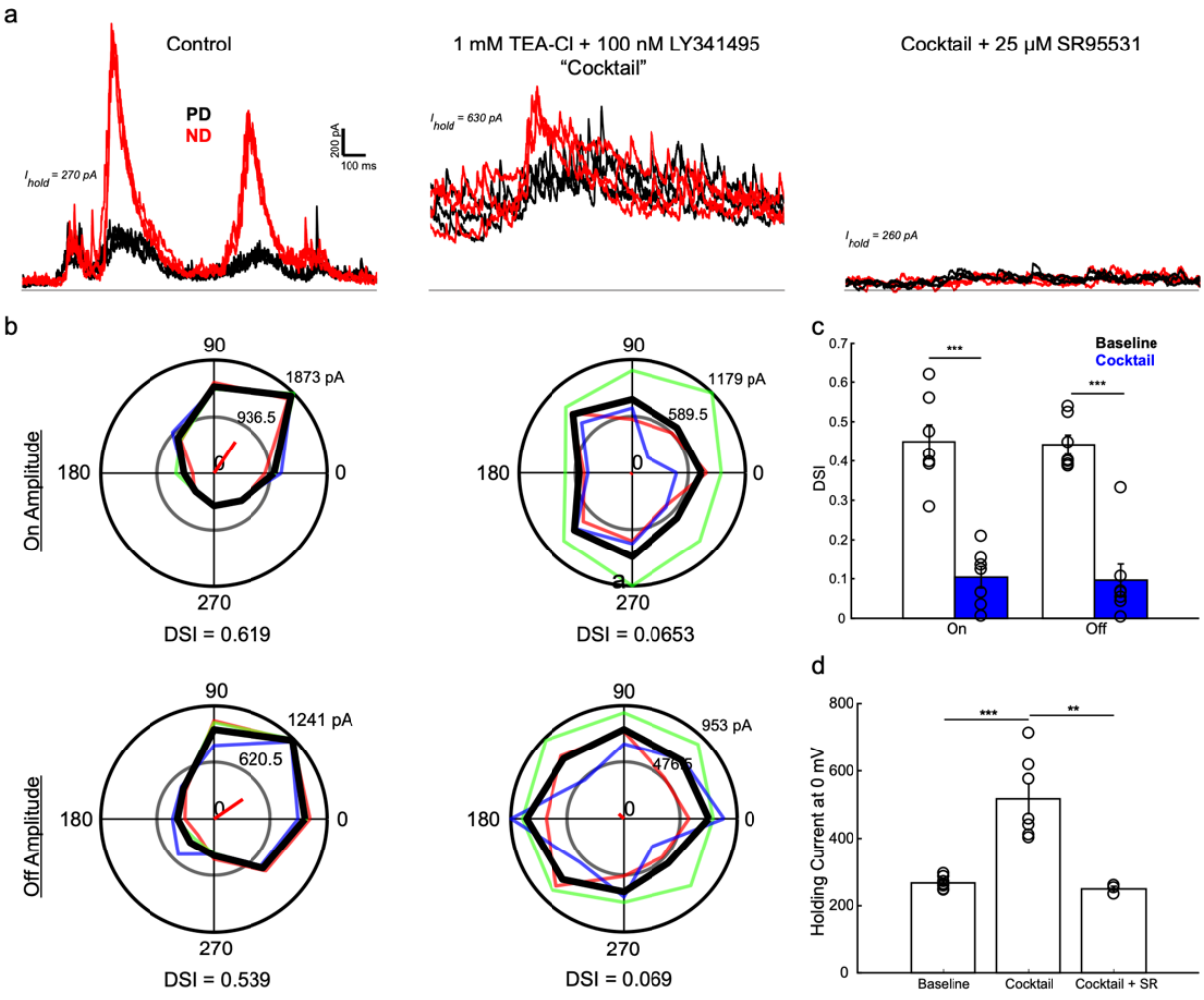

Figure 2.9: mGluR2 and Kv3 blockade disrupt visual-evoked GABAergic transmission from SACs to DSGCs. (A) Representative traces of IPSCs recorded from Drd4+ On-Off DSGCs in voltage-clamp mode (V_{hold} = 0 mV). Preferred direction (black) and null direction (red) under baseline conditions (left), in 1mM TEA-Cl and 100 nM LY341495 (middle), and upon application of TEA-Cl + LY341495 and 25 μM SR95531 (right). Holding currents at 0 mV displayed on the left, gray line indicates 250 pA as a reference. **(B)** Example On and Off component tuning plots from recordings shown in **A** (baseline: left and mGluR2/Kv3 block: right). Colored lines correspond to individual trials and thick black line represents the average across 3 trials. **(C)** Quantification of DSI (mean ± s.e.m) of On and Off IPSC components (n = 7 cells) under baseline conditions (black, On: DSI = 0.40 ± 0.07 and Off: DSI = 0.42 ± 0.04) and after application of TEA-Cl and LY341495 (Cocktail, blue - On: DSI = 0.10 ± 0.03 and Off: DSI = 0.10 ± 0.04). **(D)** Quantification of holding current at 0 mV under baseline conditions (I_{hold} = 271.81 ± 9.04 pA), in Cocktail (I_{hold} = 517.14 ± 41.79 pA), and after application of SR95531 (Cocktail + SR, I_{hold} = 244.09 ± 6.58 pA). n = 7 cells.

2.4 Discussion

Isolated dendrites grant neurons the capability of performing local computations in dendritic subunits; however, the mechanisms that establish electrotonic isolation in SACs are not fully understood. We studied how compartmentalized signaling along SAC dendrites implement centrifugal direction selectivity using a combination of whole-cell patch-clamp electrophysiology and subcellular two-photon imaging of voltage and calcium. Our study highlights how robust detection of motion direction in SAC dendrites relies on tightly regulated interactions across dendritic subdomains and how this fine-balance between electrotonic coupling and isolation can be orchestrated in concert by synaptic and cellular mechanisms. In particular, our experiments indicate that mGluR2 regulates dendritic excitability in SACs and gates interactions between global and local dendritic signals such that non-linear calcium spikes are initiated by motion in the centrifugal direction, but not in the centripetal direction. Furthermore, our findings reveal complementary and synergistic roles of mGluR2 and Kv3 in coordinating dendritic computations in SACs illustrating how voltage-dependent mechanisms modulate excitability to prevent proximal centripetal summation. Lastly, the data presented here challenge the view of the SAC dendrite as

an independent computational unit and rather presents it as an individual subunit with global integration properties (Koren et al., 2017; Tukker et al., 2004).

2.4.1 Signal integration across dendritic subdomains in SACs

Linear motion across the SAC receptive field first activates the inhibitory surround which results in a brief leading hyperpolarization prior to the onset of depolarization (**Figure 2.1**) (Qiang Chen et al., 2016; S. Lee & Zhou, 2006). Then, the visual stimulus activates the excitatory center by first stimulating bipolar cell inputs in the centripetal direction (from tip to soma) of one dendritic sector and then stimulating the opposing sector in the centrifugal direction (soma to tip). The concerted action of passive cable properties, synaptic mechanisms, and Kv3-mediated voltage shunt lead to a low-frequency, low-noise sustained depolarization at the soma. Voltage imaging with ASAP family GEVIs demonstrate that propagation of this subthreshold depolarization establishes a global signal throughout SAC dendritic (**Figure 2.1**). The segregation of synaptic inputs versus outputs and partial electrotonic isolation result in efficient summation at the distal sites of the centrifugally stimulated dendrite (Euler et al., 2002; Koren et al., 2017; Tukker et al., 2004; Vlasits et al., 2016). In contrast, motion in the centripetally stimulated dendrite leads to little summation (Ding et al., 2016a; J. S. Kim et al., 2014; Vlasits et al., 2016) at the distal dendrites.

The thin diameter of SAC proximal dendrites (< 0.3 μm) and outward currents mediated by Kv channels attenuate distally located inputs as they spread towards the soma and produce slow-rising and –decaying low-noise postsynaptic potentials (PSPs) that coincide with locally generated dendritic signals as inputs are sequentially activated from soma to tip (Hagai Agmon-Snir et al., 1998; Poznanski, 1992; Vlasits et al., 2016). Dendritic nonlinearities (N- and P/Q-types VGCCs

and TTX-insensitive voltage-gated sodium channels) likely amplify this cell-intrinsic direction selectivity at distal sites (S. Lee et al., 2010; N. W. Oesch & Taylor, 2010; Tukker et al., 2004) and help maintain robust centrifugal preference over a wide range of visual conditions (Lipin et al., 2015).

2.4.2 mGluR2 gates local interactions in SAC dendrites

While passive models can explain certain aspects of direction selectivity at SAC varicosities, they predict that centripetal summation occurs at proximal sites (Poznanski, 1992; Vlasits et al., 2016). The lack of evidence for proximal centripetal summation (Euler et al., 2002) suggests that additional modulatory mechanisms (Koren et al., 2017; S. Lee & Zhou, 2006) and outward conductances (Ozaita et al., 2004) are likely involved in shunting signal transformations in the proximal dendrites. Neuromodulation by mGluR2 is a potential candidate for this phenomenon since centripetal responses in SAC dendrites are significantly enhanced following mGluR2 blockade (**Figure 2.3 & 2.5**) (Koren et al., 2017). Disrupted mGluR2 signaling in SACs results in the emergence of large calcium transients during centripetal motion at intermediate and distal dendritic locations; however, centripetal calcium responses in the proximal dendrites and soma were not altered by mGluR2 blockade (**Figure 2.4**). Additionally, proper mGluR2 signaling does not regulate the extent of depolarization of the perisomatic region (**Figure 2.3 & 2.6**). Our findings propose that mGluR2 is responsible for gating interactions between the perisomatic region and the intermediate-distal dendrites by modulating VGCC threshold for activation (**Figure 2.4 & 2.5**).

Bipolar cell glutamate release along the SAC proximal-intermediate dendrites activates mGluR2 and elevates the threshold for VGCCs activation (**Figure 2.4 & 2.10**). During centripetal motion

locally generated PSPs do not coincide at the distal dendrites; however, centripetal motion results in a dendritic depolarization close to or above the threshold for VGCC activation in the absence of proper mGluR2 signaling. In contrast, during centrifugal motion locally generated PSPs efficiently sum with the global signal at the distal dendrites depolarizing the membrane above such mGluR2 modulated threshold, rendering centrifugal responses insensitive to mGluR2 blockade. Thus, mGluR2-mediated inhibition of VGCCs dictates the location and the membrane potential at which non-linear transformations can initiate along SAC dendrites, which is imperative to suppressing activity during centripetal motion.

2.4.3 Endogenous activation of mGluR2 by bipolar cell glutamate release

Our understanding of mGluR2-mediated electrotonic isolation implies that endogenous mGluR2 activation is stronger in the proximal dendrites resulting in higher probability of VGCC inhibition in the proximal half of SAC dendrites compared to the distal half. Segregation of bipolar cell inputs along the proximal two-thirds of the dendrites should result in elevated glutamate levels proximally supporting this claim (Ding et al., 2016; Vlasits et al., 2016). Although, anatomical studies in other cell types have reported random distribution of mGluR2 across postsynaptic microdomains (Hayashi et al., 1993; Luján et al., 1997). Further studies will be necessary to determine subcellular localization of mGluR2 in relation to the synaptic cleft in SACs. But, even if mGluR2 is positioned extrasynaptically and is sensitive to glutamate spillover and diffusion, endogenous mGluR2 signaling at distal locations should be relatively weak since VGCCs involved in transmission are operational and we observed large, fast-rising centrifal GCaMP6 transients under baseline conditions. Application of pharmacological mGluR2 agonists blocks inward calcium currents in SACs (Koren et al., 2017) and suppresses synaptic transmission between SACs and DSGCs

(Sethuramanujam et al., 2018). This suggests that distally located is mGluR2 (**Figure 2.4**) is functional but not optimally activated under physiological conditions.

As shown in **Figure 2.10**, SACs experience spontaneous EPSC events at a higher rate than Drd4+ On-Off DSGCs. Tonic excitatory inputs from bipolar cells (Berntson & Taylor, 2000; Hausselt et al., 2007; S. Lee & Zhou, 2006) establish at least partial mGluR2-mediated isolation prior to visual-evoked activity. However, whether mGluR2-mediated electrotonic isolation can be further modulated by visual evoked activity remains an open question. We recorded inward calcium currents while varying luminance conditions to test whether mGluR2-mediated inhibition of VGCCs is sensitive to visual-evoked glutamate release. We observed only minor changes in the voltage threshold and amplitude for inward calcium currents under visual illumination (**Figure 2.11**); however, this does not discard the possibility that visual-evoked glutamate release can enhance mGluR2 activation.

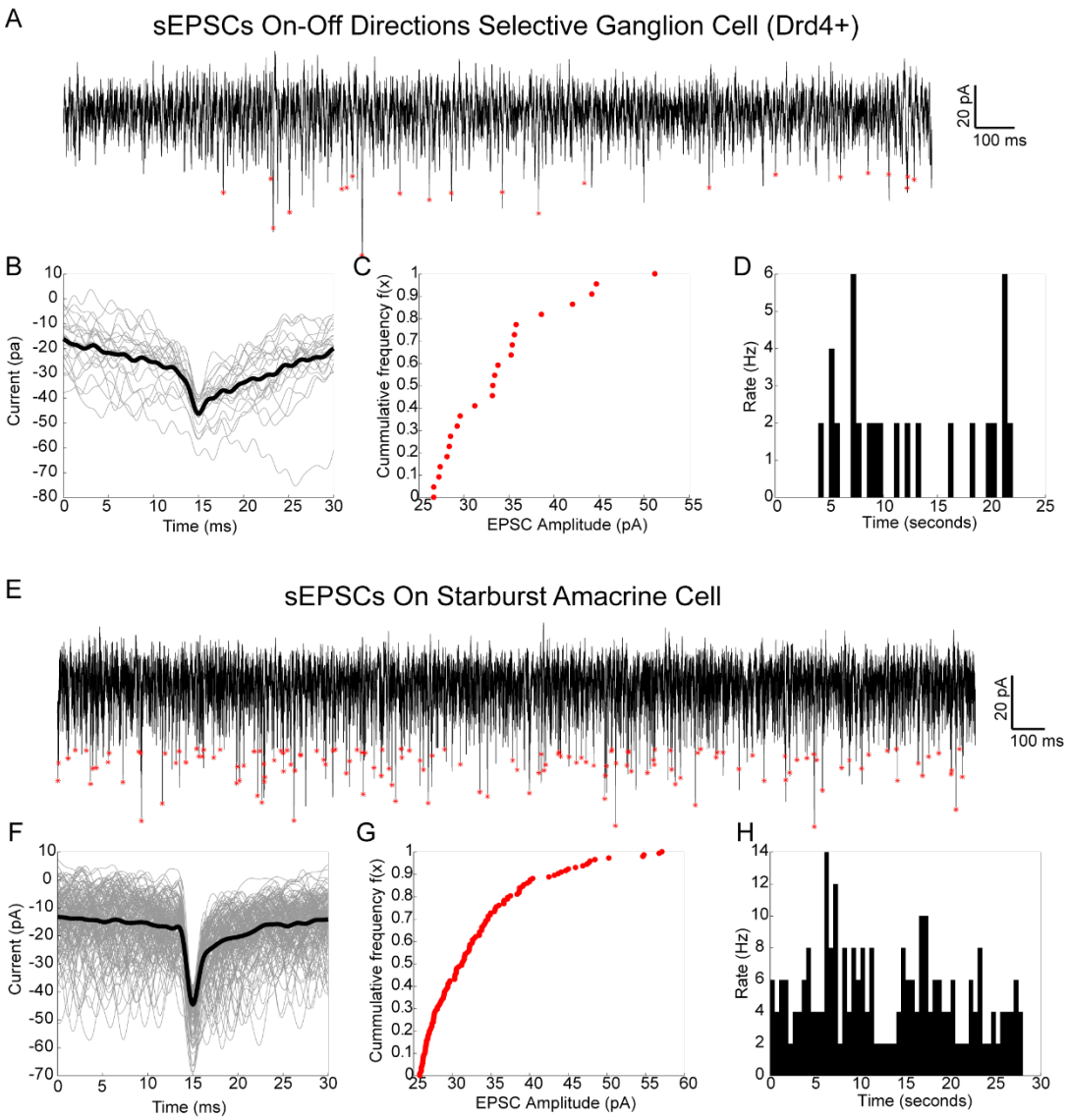

Figure 2.10: SACs receive tonic bipolar cell inputs compared to DSGCs. (A) Representative spontaneous EPSCs (sEPSCs) from posterior-preferring On-Off DSGCs. (B) Overlay of sEPSC events detected in A (gray) and average sEPSC trace (black). (C) Cummulative frequency distribution of EPSC amplitude from events in A-B. Peri-stimulus histogram of sEPSC events using a bin size of 500 ms. (E) Representative spontaneous EPSCs (sEPSCs) from On SACs. (B) Overlay of sEPSC events detected in E (gray) and average sEPSC trace (black). (C) Cummulative frequency distribution of EPSC amplitude from events in E-F. Peri-stimulus histogram of sEPSC events using a bin size of 500 ms.

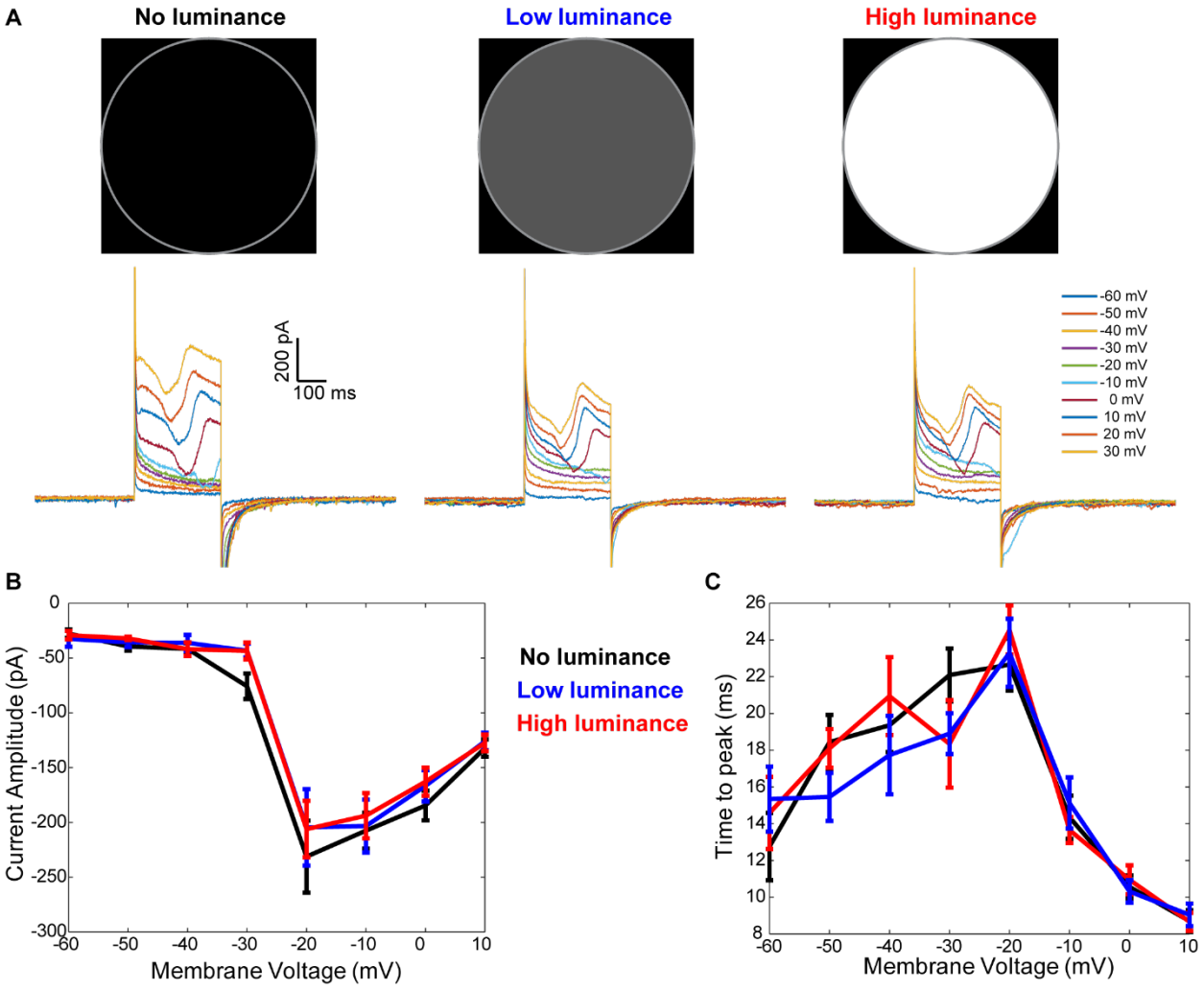

Figure 2.11: Inward calcium currents in SAC show are weakly suppressed by visual illumination. (A) Representative current traces from On SAC after applying a voltage step protocol at different luminance conditions: no illumination (left), 33.33% illumination intensity (middle), and 100% illumination intensity (right). (B) Average I-V curves (n = 9 SACs) at illumination intensities described in A. (C) Time interval to reach peak of inward current at applied voltages.

2.4.4 Sensitivity of GCaMP6 sensors to subthreshold events

A major concern throughout our study involved the sigmoidal response curve of GCaMP6f which predicts lower sensor sensitivity during subthreshold events when calcium levels are low. SACs are non-spiking interneurons and depolarization at the soma is restricted to ~20 mV. The fast-rising GCaMP6f signals observed in the distal dendrites are indicative of N- and P/Q-VGGCC activation. Other sources of calcium fluctuations in SACs potentially include non-selective cation

channels, R-type VGCCs (although these are yet to be reported in mice), and calcium-dependent calcium release. Despite the limited extent of depolarization at the soma, we robustly detected slow-rising calcium transients in the range of 0.2 – 0.8 $\Delta F/F_0$ that correlate well with the peak and duration of somatic depolarization (**Figure 2.1B**), indicating GCaMP6f is able to detect somatic calcium influx during this slow subthreshold depolarization. For our imaging experiments, we only included data from cells exhibiting detectable and consistent somatic transients. Additionally, it is important to note that baseline GCaMP6f fluorescence at the soma was higher than the dendrites; therefore, these transients represent small $\Delta F/F_0$ values but correspond to significant raw ΔF changes. This shows that in this cell type GCaMP6 can accurately report subthreshold events (at -48.98 ± 6.14 mV, mean ± s.e.m).

2.4.5 Dendritic compartmentalization through Kv3-mediated shunting

In addition to mGluR2, SACs express Kv3.1 channels in their proximal dendrites which are believed to contribute to centrifugal preference by further isolating dendritic sectors and help create a steady reliable subthreshold depolarization across the cell (Ozaita et al., 2004; Kaneda et al., 2007). Kv3 channels in SACs begin to open at potentials > -45 mV and prevent depolarization above -40 mV (**Figure 2.2**) suggesting that Kv3-mediated currents generate a proximal voltage-dependent shunt limiting effective depolarization of the perisomatic region. This shunt could provide an additional mechanism by which proximal above threshold summation could be prevented. Current-clamp recordings at the SAC soma during linear motion demonstrated that upon Kv3 blockade the onset and peak timing of depolarization occurred earlier corresponding to the distal tips of the centripetal sector and the proximal region of the centrifugal sector, respectively, rather than the perisomatic region and the distal tips of the centrifugal sector observed

under baseline conditions. These changes in kinetics were accompanied by the occasional presence of high-frequency voltage events, particularly at more depolarized potentials (**Figure 2.2 & 2.6**). Our findings indicate that Kv3 acts on subthreshold membrane potentials and restrains the influence of distal PSPs on perisomatic depolarization. Unlike its function in high-frequency spiking neurons, this represents a new role for Kv3 in which it maintains low-noise levels during subthreshold depolarization and restricts depolarization to potentials close to VGCC opening.

2.4.6 Synergistic regulation of SAC dendritic excitability

As outlined above, Kv3 and mGluR2 have unique contributions to electrotonic isolation by restricting subthreshold depolarization in the perisomatic compartment and suppressing the initiation of nonlinear calcium events in the dendritic sectors, respectively. In the absence of mGluR2 signaling, distal responses lose directional preference but these signals are attenuated by passive filtering and Kv3 as they spread towards the soma and fail to directly propagate to other dendritic sectors. Additionally, Kv3 prevents proximal excitatory inputs from depolarizing the perisomatic region above -45 mV. On the other hand, during Kv3 blockade passive filtering and mGluR2-mediated inhibition of VGCCs prevent the spread of above threshold events towards the soma. Interestingly, concurrent blockade of Kv3 and mGluR2 resulted in a significant increase in the number and amplitude of high-frequency voltage events in the perisomatic region unmasking the synergistic roles of these mechanisms in regulating neuronal excitability and dendritic compartmentalization. In this scenario, subthreshold events propagate across SAC dendritic domains and nonlinear high-frequency events can be initiated and spread throughout the perisomatic region. As a consequence of this increased excitability, SACs tonically release GABA onto DSGCs, and lose the directional tuning of visual evoked activity in this circuit.

2.5 Experimental Procedures

Mice

Chat-IRES-Cre mice (129S6-*Chat*$^{tm2(cre)Lowl}$/J) and floxed *tdTomato* mice (129S6-*Gt(ROSA)26Sor*$^{tm9(CAG-tdTomato)Hze}$/J) were acquired from the Jackson Laboratory. *mGluR2–GFP* mouse line was a generous gift from Dr. Marla Feller at University of California, Berkeley. *Drd4–GFP* mice, in which posterior-preferring DSGCs are selectively labelled, were originally developed by MMRRC in the Swiss Webster background, and were subsequently backcrossed to C57BL/6 background. All strains were backcrossed to the *C57BL/6* background in our laboratory and crossed to each other to create the lines used in this study.

All experiments were performed on healthy mice of normal immune status which had not been previously used for tests or procedures. Mice were housed in 12 hr-12 hr light-dark cycles in groups of 2-5 per cage and were provided with food and water *ad libitum*. For electrophysiology experiments, mice of ages P21-P40 of either sex were used. For imaging experiments, the protocols described in the GCaMP6 imaging section were followed. All procedures to maintain and use mice were in accordance with the University of Chicago Institutional Animal Care and Use Committee (Protocol number ACUP 72247) and in conformance with the NIH Guide for the Care and Use of Laboratory Animals and the Public Health Service Policy.

Whole-mount retina preparation

Mice were anaesthetized with isoflurane and decapitated after dark adaptation. Under infrared illumination, retinas were isolated from the pigment epithelium at room temperature in oxygenated

Ames' medium (Sigma-Aldrich, St. Louis, MO). Isolated retinas were then cut into dorsal or ventral halves (Wei et al., 2010) and mounted ganglion-cell-layer-up on top of a 1 mm^2 hole in a small piece of filter paper (Millipore, Billerica, MA). Retinas were kept in darkness at room temperature in Ames' medium bubbled with 95% O2/5% CO^2 until use (0–7 hr).

Immunostaining

Isolated retinas were fixed in 4% EM Grade PFA (Fisher Scientific # 50980487) in Protectant Buffer Solution (200 mM sucrose, 33.5 mM sodium phosphate monobasic, 33.5 mM sodium phosphate dibasic) (Stradleigh et al., 2015) for 20 minutes and then washed three times with conventional PBS solution (20 minutes). Fixed retinas were then washed in block solution consisting of 10% donkey serum, 1% bovine serum albumin, and 0.5% TritonX in PBS and incubated with primary antibodies (1:500 rabbit anit-mGluR2 and 1:1000 mouse anti-Kv3.1) for 72 hours. Following primary antibody incubation, retinas were washed in block solution and incubated with secondary antibodies (1:1000 Alexa-488 conjugated goat anti-mouse and 1:1000 Alexa-594 conjugated donkey anti-rabbit, Invitrogen) for 7-10 hours. Lastly, retinas were washed in PBS solution and mounted onto microscope glass slides using VectaShield medium (Vector Labs # H-1900) prior to imaging.

Visual stimulation

A white organic light-emitting display (OLEDXL, eMagin, Bellevue, WA; 800 × 600 pixel resolution, 60 Hz refresh rate) was controlled by an Intel Core Duo computer with a Windows seven operating system and was presented to the retina at a resolution of 1.1 μm/pixel. Moving bar stimuli were generated by MATLAB and the Psychophysics Toolbox (Brainard, 1997), and

projected through the condenser lens of the two-photon microscope onto the photoreceptor layer. In the plane of the retina, the OLED image was centered on the soma of SAC of interest. For electrophysiology experiments, a positive-contrast bar (275 μm wide, 440 μm long) moved along the long axis at a speed of 440 μm/sec over a 660μm-diameter field on the retina; and three to five trials were recorded. For calcium imaging experiments, the bars were presented in 10 trials of two pseudorandomized directions (centripetal and centrifugal), which were determined by dendrite orientation. These bars had dimensions of 275 μm x 220 μm. The speed of the bar was 440 μm/s unless otherwise indicated.

Intravitreal AAV injections

Genetically encoded calcium indicator GCaMP6f was expressed in sparse populations of On SACs by intravitreal injection of an 7m8 modified AAV vectors carrying floxed GCaMP6f and floxed tdTomato (gift from the Dr. Sui Wang at Stanford University) into *Chat-IRES-Cre* mice aged P14-25. Viral titers were maintained at 10^{14} for GCaMP6f and 10^{13} for tdTomato. Just prior to injections aliquots from each stock were mixed at equal volumes. Mice were anesthetized using 4μL/g intraperitoneal injection of 10% ketamine/ 5% xylazine in PBS. Animals were placed on their side and the periorbital region was locally anesthetized using one drop of 0.5% proparacaine HCl (Henry Schein, Melville, NY). Using a Femtojet 4i microinjector (Eppendorf, Hamburg, Germany) equipped with sharp pulled glass-pipettes, 1 – 1.5 μL of AAV vector solution was injected into the vitreal space of both eyes. Retinas were isolated, screened, and imaged at 4-8 weeks following injection.

Two-photon calcium imaging of GCaMP6 fluorescence in SACs

GCaMP6 fluorescence of isolated retinas in oxygenated Ames at 32–33°C was imaged in a customized two-photon laser scanning fluorescence microscope (Bruker Nano Surfaces Division). GCaMP6 was excited by a Ti:sapphire laser (Coherent, Chameleon Ultra II, Santa Clara, CA) tuned to 920 nm, and the laser power was adjusted to avoid saturation of the fluorescent signal. Onset of laser scanning induces a transient On response in On SACs that adapts to the baseline in ~3 s. Therefore, to ensure the complete adaptation of this laser-induced response and a stable baseline, visual stimuli were given after 5 s of continuous laser scanning. To separate the visual stimulus from GCaMP6 fluorescence, a band-pass filter (Semrock, Rochester, MA) was placed on the OLED to pass blue light peaked at 470 nm, while two notched filters (Bruker Nano Surfaces Division) were placed before the photomultiplier tubes to block light of the same wavelength. Imaging was performed in the regions of the retina that contain sparsely labeled SACs so that individual dendrites and varicosities could be resolved and the orientation of the dendrites relative to the soma could be determined. The objective was a water immersion objective (60x, Olympus LUMPlanFl/IR). Time series of fluorescence were collected at 20–50 Hz.

Voltage imaging with ASAP family GEVIs

ASAP3b (gift from Dr. Michael Z. Lin) was expressed the same way as GCaMP6f (AAV intravitreal injection into ChAT-Cre mice). Retinas from AAV-CAG.flox.ASAP3b injected mice were isolated after 5 weeks post injection. Two-photon imaging was performed similarly as GCaMP6 with the exception that imaging was performed at 250-300 Hz.

Imaging analysis

Analysis was performed using ImageJ and MATLAB. Regions of interest (ROIs) corresponding to individual varicosities, dendritic shafts, soma, and background were manually selected in ImageJ. The fluorescent time course of each ROI was determined by averaging all pixels within the ROI for each frame. The fluorescence of the background region was subtracted from the raw fluorescent signals of the ROIs in the same imaging window at each time frame. The moving bar visual stimulus used for calcium imaging included 500 ms interval between the end of one sweep and the start of another. Fluorescence intensities during this inter-sweep intervals were used to create a baseline (F0) trace for each ROI by fitting a two-term exponential decay function. Fluorescence measurements were then converted to ΔF/F0 values by calculating $\Delta F=(F-F0)/F0$ for every data point. Trials for given ROIs were discarded if baseline fluorescence values (F0) dropped below 0.1 for calcium imaging or 20 for voltage imaging. Remaining samples were then resampled to 75 Hz for calcium imaging or 1000 Hz for voltage imaging through boxcar method and smoothed using an average sliding window of 4 data points (calcium imaging) or 12 datapoints (voltage imaging). ΔF/F0 traces were then clipped, sorted by visual stimulus direction (centripetal or centrifugal), and averaged over 5-10 trials. Prior to further analysis, traces were subjected to a response quality test $QI = Var[Avg.\ Resp]/Avg(Var[R(t)]) \geq 0.45$ (calcium imaging) or 0.15 (voltage imaging) to ensure consistency across trials. Peak and area ΔF/F0 values, along with time to peak and rise slope for centripetal versus centrifugal responses were calculated using custom MATLAB scripts. Direction selectivity index (DSI), defined as (ΔF/F0_cf - ΔF/F0_cp)/(ΔF/F0_cf + ΔF/F0_cp), was calculated for all ROIs. Lastly, the dendritic fraction for each ROI was calculated by (distance soma to ROI)/(distance soma to dendritic tip).

Cell-targeted patch-clamp electrophysiology

Recordings in this study were performed from ON SACs and posterior-preferring DSGCs. Cells were visualized with infrared light (920 nm) and an IR-sensitive video camera (Watec). For current-clamp recordings, SACs were targeted using either *Chat-IRES-Cre*/floxed *tdTomato* mice or *mGluR2-GFP* mice. Cell identity was confirmed physiologically by the lack action potentials from the voltage traces. Recording electrodes of 3.5–4.5 MΩ were backfilled with a potassium-based internal solution containing (from Sigma): 120 mM $KMeSO_4$, 10 mM KCl, 0.07 mM $CaCl{\bullet}2H_2O$, 10 mM HEPES, 0.1 mM EGTA, 2 mM adenosine 5′-triphosphate (magnesium salt), 0.4 mM guanosine 5′-triphosphate (trisodium salt), 10 mM phosphocreatine (disodium salt),and pH was balanced to 7.25 with KOH. Electrophysiological recordings were acquired at 10 kHz with a Multiclamp 700A amplifier (Molecular Devices) using pCLAMP 10.4 recording software and a Digidata 1440 digitizer. Membrane potential was monitored in current-clamp mode (holding current = 0 pA) during moving bar visual stimulation. For a subset of experiments, SACs currents were monitored using K+ internal in voltage-clamp mode while providing 500 ms voltage steps ranging from -95 mV to +45 mV. In voltage-clamp mode, whole-cell and series resistance (70% at 5 kHz) compensation were performed after break-in prior to recording.

For recordings of synaptic currents, posterior-preferring DSGCs were targeted using Drd4-GFP mice. Recording electrodes were filled with an internal solution containing (in mM): 110 mM $CsMeSO_3$, 2.8 mM NaCl, 4 mM EGTA, 5 mM TEA-Cl, 4 mM adenosine 5'- triphosphate (magnesium salt), 0.3 mM guanosine 5'-triphosphate (trisodium salt), 20 mM HEPES, 10 mM phosphocreatine (disodium salt), and balance pH to 7.2 with CsOH. Currents were recorded at a holding potential of 0 mV while presenting moving bar visual stimulation.

Data analysis for electrophysiological recordings

Current-clamp and voltage-clamp data were analyzed using a combination of Molecular Devices Clampfit software and custom protocols in MATLAB. Depolarization amplitudes and area were computed from the low-frequency component of the voltage recording in MATLAB. First, we isolated the low-frequency component from the recorded voltage traces by taking the average across 5 trials and passing this average trace through a low-pass filter with a cutoff frequency of 20 Hz. Then local minima were identified between 0s and 0.5 s time window to calculate a baseline Vm value. Finally, the depolarization amplitude was defined as the difference between maximum Vm (between 0.5s and 2s) and baseline Vm and depolarization area was defined as the area between the Vm trace (0.5s to 2s) and the baseline Vm. Onset times, rise time (10% to 90%), and decay times (90% to 10%) were quantified in Clampfit.

Power spectra were computed in MATLAB for individual trials across all voltage recordings for frequencies ranging from 0 to 2,500 $\left(\frac{sampling\ frequency}{number\ of\ datapoints}\right)$. We then calculated the average power spectrum for each testing condition (baseline, +LY341495, +TEA, +LY & TEA) and the percent change from base across all frequencies for each of the drug conditions. For analysis of the high-frequency data, local minima were identified every 50 ms along each individual trial to create a rolling adjusting baseline representative of the low-frequency depolarization component. We then fragmented the individual traces into these 50 ms segments and searched for voltage peaks that were 4 mV or more above the baseline for that segment, had peak prominence of 3 mV or more, had widths at half-prominence between 4 – 50 ms, and were at least 15 ms apart. For each peak detected, amplitude (peak – baseline), prominence, time of peak, rise time (10% to 90%), decay time (90% to 10%), and width at half prominence were recorded. From these, we calculated and plotted peri-stimulus time histograms and cumulative distributions.

Inhibitory postsynaptic currents (IPSCs) were recorded from DSGCs in response to a moving bar stimulus. IPSC amplitude, charge transfer, and baseline holding currents were measured in Clampfit software for both On (leading edge) and Off (trailing edge) components across 3 trials of 8 directions of the moving bar stimulus. The average amplitude and charge transfer for all directions were calculated across the 3 trials. Direction selectivity index was calculated using the average responses in the null (maximal IPSC response) and preferred (opposite to null) directions as follows: $DSI = \frac{R_{null} - R_{pref}}{R_{null} + R_{pref}}$.

Chapter 3

Conditional Knock-Out of Vesicular GABA Transporter Gene from Starburst Amacrine Cells Reveals the Contributions of Multiple Synaptic Mechanisms Underlying Direction Selectivity in the Retina

This chapter is a full reprint of Pei et al., *Journal of Neuroscience* (2015), in which I was a secondary author. This work is included with permission from all authors.

Relevant Publication:
Pei, Z., Chen, Q., Koren, D., Giammarinaro, B., Acaron Ledesma, H., & Wei, W. (2015). Conditional knock-out of vesicular GABA transporter gene from starburst amacrine cells reveals the contributions of multiple synaptic mechanisms underlying direction selectivity in the retina. *Journal of Neuroscience*, 35(38), 13219-13232.

3.1 Abstract

Direction selectivity of direction-selective ganglion cells (DSGCs) in the retina results from patterned excitatory and inhibitory inputs onto DSGCs during motion stimuli. The inhibitory inputs onto DSGCs are directionally tuned to the anti-preferred (null) direction and therefore potently suppress spiking during motion in the null direction. However, whether direction-selective inhibition is indispensable for direction selectivity is unclear. Here, we selectively eliminated the directional tuning of inhibitory inputs onto DSGCs by disrupting GABA release from the presynaptic interneuron starburst amacrine cell in the mouse retina. We found that, even without directionally tuned inhibition, direction selectivity can still be implemented in a subset of

On-Off DSGCs by direction-selective excitation and a temporal offset between excitation and isotropic inhibition. Our results therefore demonstrate the concerted action of multiple synaptic mechanisms for robust direction selectivity in the retina.

3.2 Introduction

In mammalian retina, the On-Off type of direction-selective ganglion cell (DSGC) encodes image motion in four cardinal directions (Barlow & Hill, 1963; Clyde W. Oyster & Barlow, 1967). Direction-selective spiking of these cells is generated by distinct patterns of synaptic inputs during preferred and null direction motion. DSGCs receive synaptic inputs from glutamatergic bipolar cells and starburst amacrine cells (SACs), a class of retinal interneuron that corelease GABA and acetylcholine (Brecha et al., 1988; Euler et al., 2002; Kosaka et al., 1988; S. Lee et al., 2010; O'Malley & Masland, 1989; Vaney & Young, 1988). In whole- cell voltage-clamp recordings, the excitatory inputs onto DSGCs are stronger during motion in the preferred direction, whereas the inhibitory inputs are stronger during motion in the null direction (Fried et al., 2005; S. Lee et al., 2010; Park et al., 2014; Taylor & Vaney, 2002). Furthermore, during preferred-direction motion, the inhibitory inputs lag behind the excitatory inputs due to the spatially offset inhibition relative to excitation (Fried et al., 2002; Taylor & Vaney, 2002).

Stronger inhibition elicited by null-direction motion is the central component of all existing models of direction selectivity in the retina. Directional inhibitory inputs onto DSGCs arise from the synergistic action of two mechanisms. The first mechanism is the asymmetric wiring between SACs and DSGCs: SAC processes that are oriented toward the null direction provide the majority of inhibition to a given DSGC (Briggman et al., 2011; Fried et al., 2002; S. Lee et al., 2010; Wei

et al., 2011a; Yonehara et al., 2011). The second mechanism is direction-selective output of SAC processes: presynaptic varicosities in SAC processes are preferentially activated by motion in the centrifugal direction (Euler et al., 2002; Hausselt et al., 2007; S. Lee & Zhou, 2006; N. W. Oesch & Taylor, 2010). Inhibitory inputs onto DSGCs are stronger in the null direction because motion in that direction is centrifugal for null-direction-oriented SAC processes and thereby causes maximal GABA release onto DSGC dendrites. In contrast, motion in the preferred direction is centripetal for null-direction-oriented SAC processes and thereby evokes less GABA release and consequently weaker inhibition onto DSGCs. Although direction- selective inhibitory inputs onto DSGCs are well established in in both rabbit and mouse retinas, whether it is indispensable for direction selectivity has not been tested directly by loss-of-function studies.

Unlike the well-established role of inhibition, the role of the direction-selective excitation that impinges onto DSGCs during image motion remains poorly understood and controversial. Although stronger excitation onto DSGCs when motion is in the preferred direction has been observed consistently in voltage- clamp experiments (Fried et al., 2005; S. Lee et al., 2010; Park et al., 2014; Taylor & Vaney, 2002), the neuronal substrate that implements this direction-selective excitation has not been found. This has raised concern about the limitations of the voltage-clamp technique: the apparent reduction in excitatory conductances during null-direction motion might be caused by electrotonic interactions between the large inhibitory conductance and the excitatory conductance under the condition of imperfect space clamp (Park et al., 2014; Poleg-Polsky & Diamond, 2011; Vaney et al., 2012)**.** How can the pattern of excitatory inputs onto DSGCs be isolated from the influence of inhibitory conductances during motion stimuli? Do other synaptic mechanisms such as direction-selective excitation and temporally offset inhibition contribute to

DSGC's directional spiking or is asymmetric inhibition indispensable for direction selectivity? We addressed these questions by performing a loss-of-function study. Using transgenic mice, we eliminated the direction tuning of inhibitory inputs onto DSGCs by reducing the strength of inhibition in the null direction. We then examined direction selectivity in DSGCs when their inhibitory inputs became isotropic.

3.3 Results

3.3.1 Asymmetric inhibition between SACs and DSGCs is impaired when the Vgat gene is deleted from SACs

We generated a conditional knock-out mouse line in which the vesicular GABA transporter (*Vgat*) gene is selectively deleted in SACs in the retina. This line contains the following transgenes: homozygous floxed Vgat allele (*Vgat* $^{flox/flox}$) to replace the endogenous *Vgat* gene, a choline acetyltransferase *(ChAT)-IRES- Cre* knock-in allele for SAC-specific Cre expression (acronym: C), a *floxed tdTomato* transgene to report functional Cre protein expression (acronym: T), and a *Drd4-GFP* transgene to label On-Off DSGCs that prefer motion in the posterior direction (pDSGCs; acronym: D; Huberman et al., 2009); **Fig. 3.1A**). In these *Vgat* $^{flox/flox}$*CTD* mice, tdTomato expression was turned on and the *Vgat* gene was deleted in SACs, whereas GFP was expressed in pDSGCs (**Fig. 3.1B**). We first confirmed that the VGAT protein is knocked down in SAC processes by double immunostaining for *Vgat* and *VAChT* in *Vgat* $^{flox/flox}$*C* mice. SAC processes in *Vgat* $^{flox/flox}$*C* mice stratify precisely in S2 and S4, where VGAT immunofluorescence signal is absent (**Fig. 3.1C**). We did not detect changes in SAC and pDSGC dendritic morphology (**Fig. 3.1 D, E**) or in gross anatomical organization of the retina in *Vgat* $^{flox/flox}$*C* mice.

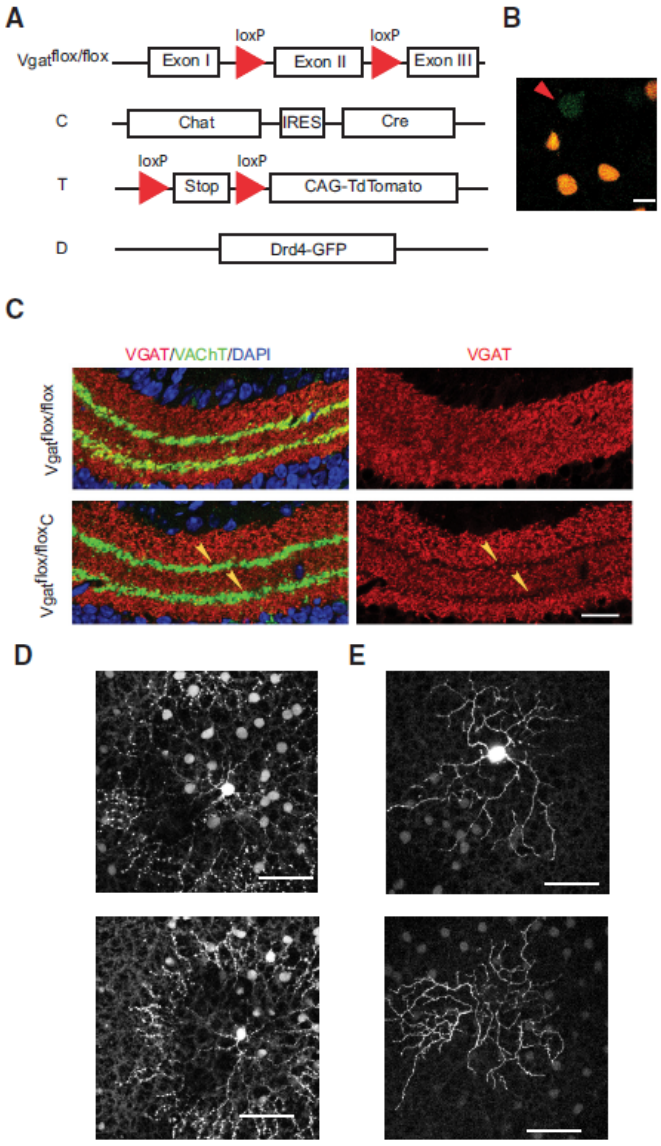

Figure 3.1: VGAT protein is knocked down in SACs from Vgat conditional knock-out mice. **(A)** Schematic diagram showing the transgenes in *Vgat* conditional knock-out mice. **(B)** Two-photon image of the ganglion cell layer from a *Vgat* $^{flox/flox}$*CTD* retina showing a Drd4-GFP labeled pDSGC (red arrowhead) and *tdTomato*-labeled SACs (red somas). Scale bar, 10 µm. **(C)** Left, *Vgat* $^{flox/flox}$ retina (as a control) and *Vgat* $^{flox/flox}$*C* retina immunostained for VGAT, VAChT and DAPI. Right: same images showing the VGAT signal only. Scale bar, 20 µm. Arrows indicate the S2 and S4 sublaminae that contain SAC dendrites. **(D)** Two On SACs from a *Vgat flox/floxCTD* retina filled with Alexa Fluor 594 to show their radial symmetric processes. The dimmer somas in the background are some unfilled SACs expressing *tdTomato* in the same focal planes. Scale bars, 50 µm. **(F)** On and Off dendritic arbors from a pDSGC in a *Vgat* $^{flox/flox}$*CTD* retina filled with Alexa Fluor 488. Scale bars, 50 µm.

We then examined GABA release from SACs by performing paired whole-cell voltage-clamp recordings between SACs and pDSGCs in control (*CTD*) and *Vgat* $^{flox/flox}$*CTD* mice. We included

all SAC-pDSGC pairs with an intersoma distance of 60– 80 m that had overlapping dendritic arbors and clear cholinergic EPSCs. In control mice, SACs from the null side of pDSGCs provide strong GABAergic inputs to pDSGCs, whereas SACs from the preferred side are weakly connected (**Fig. 3.2A–D**). However, in *Vgat* $^{flox/flox}$*CTD* mice, both null and preferred side SAC-pDSGC pairs exhibit severe loss of GABAergic transmission (**Fig. 3.2A–D**). Fifty percent of the preferred side pairs and 32% of the null side pairs show no detectable GABAergic connections (**Fig. 3A**). The rest of the pairs show residual GABAergic responses (**Fig. 3.2B–C**), probably due to GABA release from SACs through residual VGAT protein and/or compensatory mechanisms (Tritsch et al., 2012; Wojcik et al., 2006). However, the strength of GABAergic connections in null side pairs is significantly reduced compared with that of null side pairs in the control group (**Fig. 3.2D**, control null vs KO null). In *Vgat* $^{flox/flox}$*CTD* mice, the IPSCs in null side pairs are still slightly stronger on average than those in preferred side pairs, but this difference is not statistically significant (**Fig. 3.2D**, KO pref vs KO null). We also noted that the amplitude of IPSCs in null side pairs in *Vgat* $^{flox/flox}$*CTD* mice is similar to that of preferred side pairs in the control group (**Fig. 3.2D**). Therefore, the asymmetric GABAergic transmission between SAC and pDSGCs is significantly disrupted in these mice. In contrast, the amplitude of cholinergic EPSCs in pDSGCs is similar in control and *Vgat* $^{flox/flox}$*C*TD mice (**Fig. 3.2E**), indicating that GABA, but not acetylcholine, release from SACs has been selectively affected in *Vgat* $^{flox/flox}$*CTD* mice.

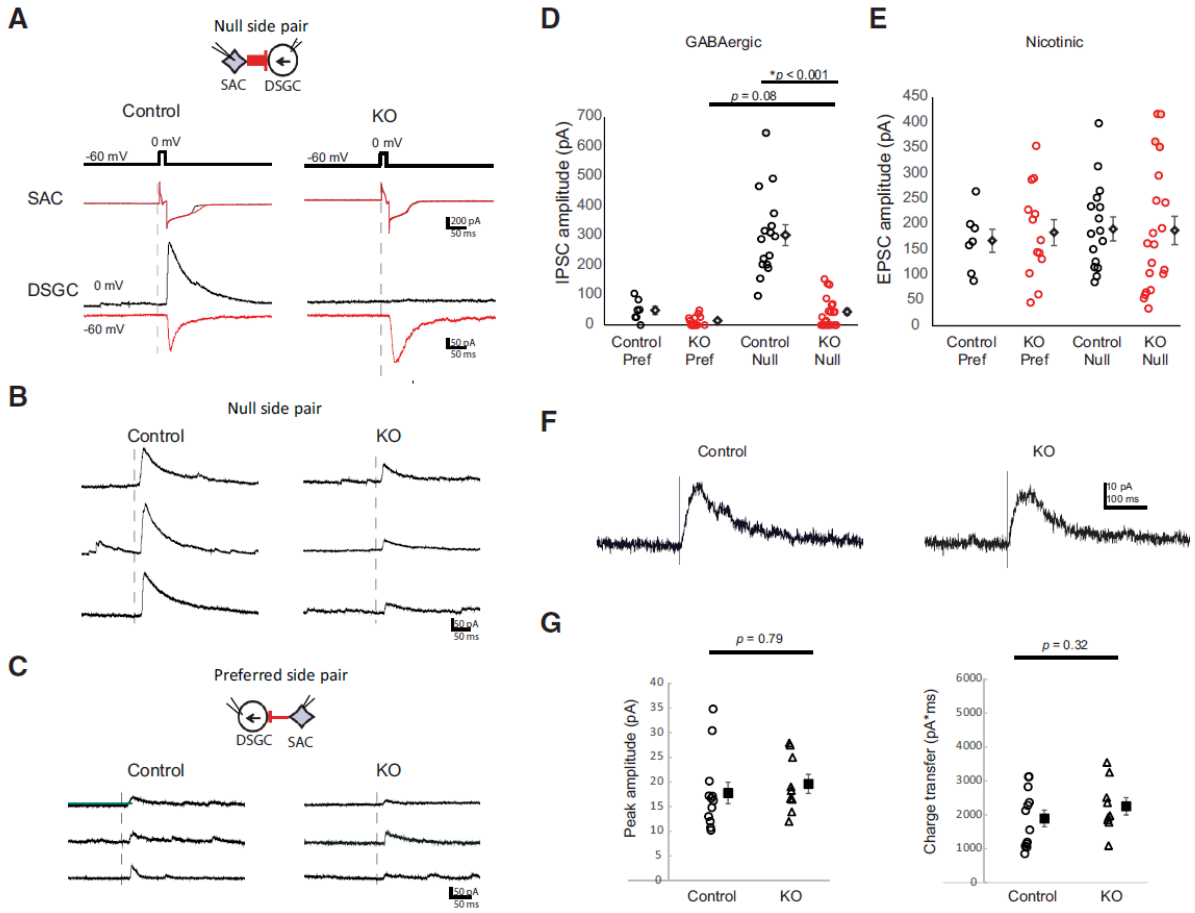

Figure 3.2: Asymmetric inhibition between SACs and pDSGCs is impaired in *Vgat*$^{flox/flox}$*CTD* mice. (A) Voltage-clamp traces from null-side SAC-DSGC pairs in *CTD* (Control) and *Vgat*$^{flox/flox}$*CTD* (KO) mice showing cholinergic EPSCs (red) and GABAergic IPSCs (black) evoked in DSGCs by depolarizing SACs. Dashed lines indicate the onset of voltage step in SACs. Top: schematic diagram shows the relative soma locations in null-side pairs. Black arrow indicates the DSGC's preferred direction. Thicker red arrow indicates stronger GABAergic inputs from null-side SAC. **(B)** Examples of null-side SAC-evoked IPSCs of pDSGCs in Control and KO groups exhibiting residual inhibition. **(C)** Examples of preferred-side SAC-evoked IPSCs in Control and KO groups exhibiting residual inhibition. Top schematic diagram shows the relative soma locations in preferred-side pairs. **(D)** Summary plot of IPSC peak amplitudes in pDSGCs evoked by preferred and null side SACs. Individual data points and statistical summary (mean ± SEM) are shown. Control–Pref: 49.5 ± 13.7 pA, n = 7 cells, 5 mice; Control–Null: 299.7 ± 35.0 pA, n = 16 cells, 8 mice; KO–Pref: 14.8 ± 5.1 pA, n = 13 cells, 8 mice; KO–Null: 44.3 ± 11.3 pA, n = 20 cells, 11 mice. **(E)** As in D summary plot of cholinergic EPSC peak amplitudes. Control–Pref: 167.3 ± 22.4 pA, n = 7 cells, 5 mice; Control–Null: 204.0 ± 23.4 pA, n = 16 cells, 8 mice; KO–Pref: 183.3 ± 25.0 pA, n = 13 cells, 8 mice; KO–Null: 187.2 ± 27.4 pA, n = 20 cells, 11 mice. **(F)** Examples of IPSCs in pDSGCs evoked by uncaging of Rubi-GABA. Synaptic transmission was blocked by 300 M $CdCl_2$. Vertical lines indicate the start of illumination by a 470 nm LED of a 400mspot centered on the DSGC. **(G)** Summary plot of IPSC peak amplitudes (left) and charge transfer (right) in pDSGCs during uncaging of Rubi-GABA. Individual data points and statistical summary (mean ± SEM) are shown. Control: peak amplitude 17.8 ± 2.2 pA, charge transfer 1892.7 ± 245.6

Figure 3.2 (cont.) pA/ms, n = 12 cells, 4 mice; KO: peak amplitude 19.6 ± 1.9 pA, charge transfer 2253.5 ± 254.8 pA/ms, n = 9 cells, 3 mice.

To determine whether the expression of GABA receptors on pDSGCs is altered by knocking out *Vgat* in SACs, we performed uncaging of Rubi-GABA onto a 400-µm-diameter area of the retina centered on pDSGC somas and recorded the GABAergic responses in pDSGCs from control and *Vgat* $^{flox/flox}$*CTD* mice. The cells from both groups show uncaging-induced GABAergic currents with similar peak amplitude and charge transfer (**Fig. 3.2F,G**). This suggests that disrupting GABA release from SACs in *Vgat* $^{flox/flox}$*CTD* mice does not lead to a drastic change in the amount of GABA receptor expression on pDSGCs.

3.3.2 Light response of pDSGCs in the absence of direction-selective inhibition

How do the pDSGCs of *Vgat* $^{flox/flox}$*CTD* mice respond to moving stimuli in the absence of asymmetric inhibition between SACs and pDSGCs? We addressed this question by performing loose-patch and whole-cell voltage-clamp recordings of Drd4-GFP-positive pDSGCs in control mice (*Vgat* $^{flox/flox}$*TD*, *Vgat* $^{flox/flox}$*D*, and *CTD*) and in *Vgat* $^{flox/flox}$*CTD* mice to monitor responses during moving bar stimuli. We also filled the cells with Alexa Fluor 594 after recordings to acquire two- photon image stacks of the recorded pDSGCs. This allowed us to collect data from Drd4-GFP-positive cells that exhibit the characteristic morphology of On-Off DSGCs, namely, looping dendritic arbors that costratify with tdTomato-labeled SAC processes in the S2 and S4 sublaminae (Berson, 2008).

First, we examined the pattern of inhibitory inputs onto pDSGCs in *Vgat*$^{flox/flox}$*CTD* mice. In control mice, the leading and trailing edges of a moving bright bar in the null direction evoked stronger

IPSCs than in the preferred direction in all pDSGCs (**Fig. 3.3A–C**). In *Vgat* $^{flox/flox}$*CTD* mice, a small number of DSGCs exhibited no detectable light-evoked IPSC (15%, 3 of 20 cells) and the rest of the DSGCs showed residual IPSCs (Fig. 3.3A). However, the residual IPSC amplitude and charge transfer in the null and preferred directions were not significantly different (**Fig. 3.3B–C**). The amplitude of the residual IPSCs in *Vgat* $^{flox/flox}$*CTD* mice is comparable to that of preferred-direction evoked IPSCs in the control group (**Fig. 3.3C**). This is consistent with the loss of asymmetric GABAergic transmission between SACs and pDSGCs observed in paired recordings (**Fig. 3.2D**).

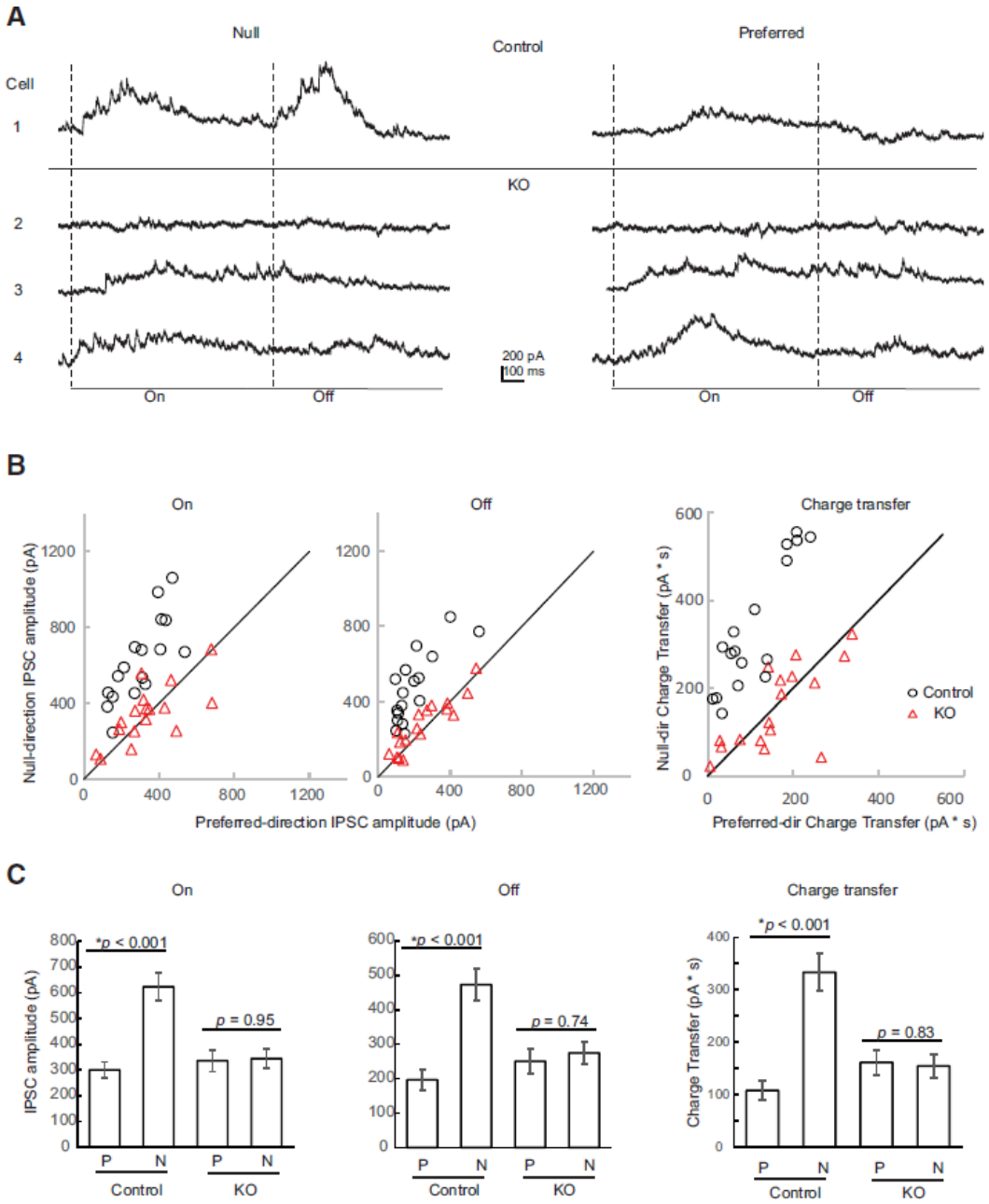

Figure 3.3: Inhibitory inputs onto pDSGCs in *Vgat* $^{flox/flox}$*CTD* mice lose direction selectivity. **(A)** Voltage-clamp recordings of a pDSGC in *Vgat* $^{flox/flox}$*TD* (Control, Cell 1) and of 3 cells in *Vgat* $^{flox/flox}$*CTD* mice (KO, Cell 2– 4) showing inhibitory currents evoked by the leading (On) and trailing (Off) edges of a bright bar moving in the preferred and null directions. Dashed lines separate the leading and trailing edge responses. **(B)** For the On (left) and Off (right) components indicated in (A), summary plots of IPSC peak amplitudes and total charge transfer evoked by null-direction motion against those evoked by preferred-direction motion. Control mice include *Vgat* $^{flox/flox}$*TD*, *Vgat* $^{flox/flox}$*D*, and *CTD* for this figure and subsequent figures. Diagonal lines are unity lines. **(C)** Summary plots showing IPSC amplitudes and total charge transfer in the preferred and null directions for control (n = 17 cells, 10 mice) and KO (n =17 cells, 10 mice) groups. On: control preferred 300.3 ± 31.1 pA, control null 624.1 ± 52.8 pA, KO preferred 336.2 ± 42.0 pA, KO null 344.5 ± 36.9 pA; Off: control preferred 196.3 ± 30.2 pA, control null 472.7 ± 45.0 pA, KO

Figure 3.3 (cont.) preferred 250.4 ± 36.0 pA, KO null 274.3 ± 33.2 pA; total charge transfer: control preferred 108.3 ± 18.0 pA/s, control null 333.5 ± 34.9 pA/s, KO preferred 161.7 ± 23.3 pA/s, KO null 154.6 ± 23.3 pA/s.

Next, we investigated whether the spiking activity of pDSGCs is still direction selective in *Vgat flox/floxCTD* mice using loose-patch recording during moving bar stimuli. We used the normalized vector sum of spiking activity and DSI, defined as $(N_{pref} - N_{null})/(N_{pref} + N_{null})$, where N is the total number of spikes evoked by the leading and trailing edges of the moving bar. The cells were filled with Alexa Fluor 594 after loose- patch recordings for two-photon imaging of their dendritic morphology. To prevent sampling bias, we included all Drd4- GFP-positive pDSGCs with bistratified dendrites at S2 and S4 in our analysis without preselection of cells based on their DSI values. In the control group, the most weakly tuned pDSGC has a DSI value of 0.23 (**Fig. 3.4 A, B**, cell #1). To determine whether a cell shows statistically significant direction selectivity, we performed a bootstrapping analysis with the null hypothesis that spiking activity are uniform in all motion directions. All cells in the control group, including the one with DSI of 0.23, showed significant direction selectivity in the boot- strapping analysis. In *Vgat $^{flox/flox}$CTD* mice, many pDSGCs have DSI values < 0.2 and tuning curves that are not apparently direction selective (**Fig. 3.4 A, B**, cell #3). Therefore, we use the following two criteria to classify pDSGCs in *Vgat $^{flox/flox}$CTD* mice as direction selective: (1) a DSI cutoff of 0.2 and (2) the bootstrapping analysis ($p < 0.05$). According to this method, pDSGCs in *Vgat $^{flox/flox}$CTD* mice are divided into non-direction-selective (non-DS) and direction-selective (DS) groups. We found that 49% (16 of 33 cells) of these pDSGCs belong to the non-DS group and lose direction selectivity in their spiking activity (**Fig. 3.4A**). This indicates that asymmetric inhibition between SACs and DSGCs is indispensable for direction selectivity in some cells. However, the remaining 51% of pDSGCs (17 of 33 cells) in *Vgat $^{flox/flox}$CTD* mice belong to the DS group and show direction-selective spiking

(**Fig. 3.4 A, B**), although their spike DSI and vector sum values are significantly reduced compared with those in the control group (**Fig. 3.4C**). Impaired direction selectivity of all pDSGCs in *Vgat* $^{flox/flox}$*CTD* mice demonstrates that direction-selective inhibition is required for optimal tuning, but it is notable that residual direction selectivity is implemented in half of the pDSGCs in the absence of asymmetric inhibition. After performing loose-patch recordings, we then performed whole-cell patch-clamp recordings from a subset of the pDSGCs from the control, non-DS, and DS groups to measure their excitatory and inhibitory inputs (**Fig. 3.5**).

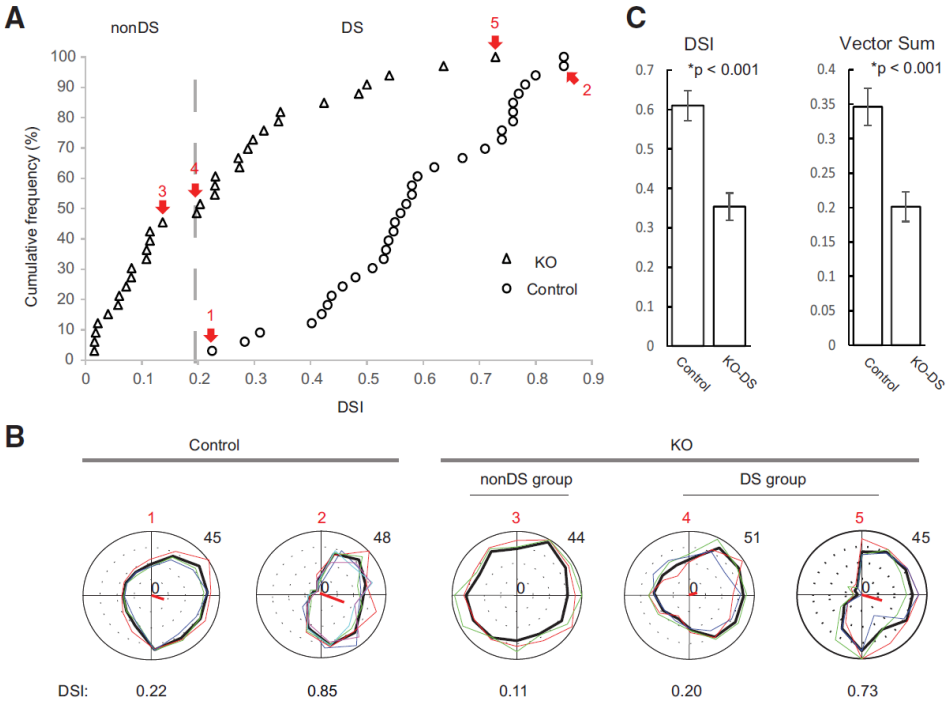

Figure 3.4: Spiking activity remains direction selective in a subpopulation of pDSGCs in Vgat flox/floxCTD mice. (A) Cumulative frequencies of spike DSI from control and *Vgat* $^{flox/flox}$*CTD* (KO) mice. Dashed line indicates cutoff between non-DS and DS groups of pDSGCs in KO mice. Numbers 1–5 indicate individual cells belonging to control, non-DS, and DS groups. **(B)** Polar plots and DSI values of spiking activity for cells labeled 1–5 in (A) illustrate a non-DS cell from a KO mouse (#3), weakly tuned cells in control (#1) and KO (#4) mice, and strongly tuned cells in control (#2) and KO (#5) mice. Colored lines represent individual repetitions and black lines represent the mean number of spikes evoked by bars moving in 12 directions. Red lines in the center represent the vector sum of spiking activity. The maximum number of spikes is shown in the upper right of each plot. **(C)** Summary plot showing DSI and vector sum values in control (n = 33 cells, 20 mice) and KO-DS (n =18 cells, 15 mice) groups. DSI control: 0.59 ± 0.03; KO-DS: 0.37 ± 0.04; vector sum control: 0.35 ± 0.03; KO-DS: 0.20 ± 0.02.

We first investigated whether residual inhibition in *Vgat*$^{flox/flox}$*CTD* mice could account for the difference in spiking activity between the non-DS and DS groups. We quantified the directionality of inhibition using the ratio of IPSC amplitudes in response to bars moving in the null and preferred directions (N/P), where the preferred direction was defined by the angle of the vector sum of the spike-tuning curve. As expected, cells in control mice show high N/P ratios for both On and Off components (**Figs. 3.6A, 2.5A**). However, residual IPSCs in the non-DS and DS groups exhibit similar N/P ratios that are significantly lower than those in control cells (**Figs. 3.6A, 2.5 B, C**). In addition, there is no positive correlation between the IPSC N/P ratios and the spiking DSI values in the DS group of Vgat $^{flox/flox}$CTD mice (**Fig. 3.6B**). This indicates that the directional spiking of pDSGCs in the DS group cannot be explained by the strength of residual inhibitory inputs.

Next, we investigated whether the excitatory inputs onto pDSGCs remain direction selective in *Vgat* $^{flox/flox}$*CTD* mice. The EPSCs in the control and *Vgat* $^{flox/flox}$*CTD* mice are of similar amplitude, suggesting that the excitatory inputs onto pDSGCs in *Vgat* $^{flox/flox}$*CTD* mice are not perturbed by *Vgat* deletion (**Fig. 3.6E**). We used the ratio of EPSC amplitude in the preferred and null directions (P/N) to quantify the directionality of excitatory inputs. Moving bars evoked non-directional excitation onto pDSGCs in the non-DS group (**Figs. 3.6C, 2.5B**). In contrast, motion-evoked excitatory inputs onto pDSGCs in the DS group were still direction selective and tuned to the preferred direction of spiking, similarly to control cells (**Figs. 3.6C, 2.5C**). A positive correlation was found between the DSI and EPSC P/N ratio in the DS group (**Fig. 3.6D**). Furthermore, both the spiking activity and the EPSCs of Drd4-GFP-positive neurons remain tuned to the posterior direction in *Vgat* $^{flox/flox}$*CTD* mice, similar to those in wild-type retinas (**Fig. 3.6F**). Bath application of the $GABA_A$ receptor antagonist gabazine significantly reduced the EPSC P/N ratio in both the

control and DS groups in *Vgat*$^{flox/flox}$*CTD* mice (**Fig. 3.6G**), which is consistent with the hypothesis that DS excitation may involve upstream inhibitory mechanisms other than GABA release from SACs (Fried et al., 2005; S. Lee et al., 2010). Together, these results indicate that directionally tuned excitation contributes to direction-selective spiking activity.

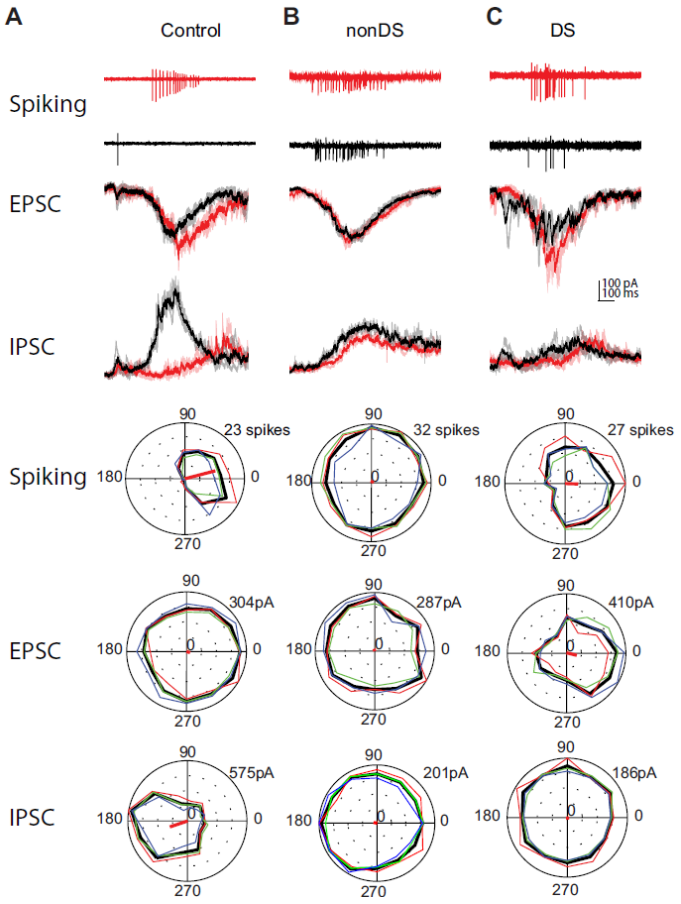

Figure 3.5: Different patterns of excitatory and inhibitory inputs underlie direction-selective spiking of pDSGCs. (A) Example cell from a control mouse showing its spiking activity and excitatory and inhibitory currents evoked by preferred (red) and null (black) direction motion. The preferred direction is determined from spiking activity. Top four rows: traces from electrophysiological recordings of spikes and excitatory (inward) and inhibitory (outward) currents. Lighter traces are three individual repetitions and dark traces are the mean traces of the three repetitions. Lower three rows: polar plots of spiking responses and peak amplitudes of EPSCs and IPSCs. The On responses evoked by the leading edge of the moving bar are shown in this and subsequent examples in this figure. **(B)** Example cell from the non-DS group in a *Vgat*$^{flox/flox}$*CTD* mouse. Excitatory inputs onto this cell are not direction selective. The relative timing between excitation and inhibition is similar for the preferred and null direction motion. **(C)** Example cell from the DS group that received direction-selective excitatory inputs and slightly delayed inhibitory inputs in the preferred direction motion.

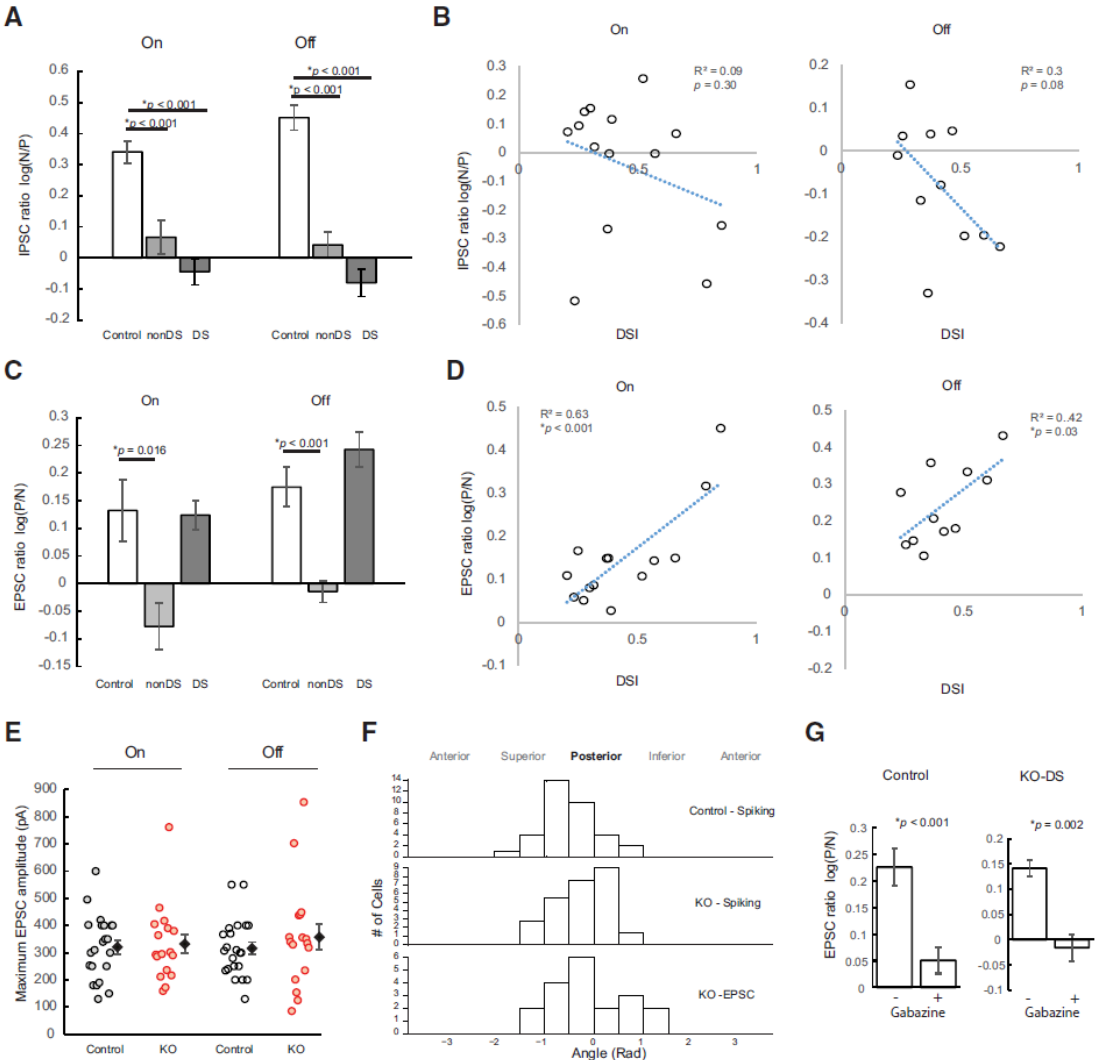

Figure 3.6: The excitatory but not inhibitory inputs onto the pDSGCs from the DS group in Vgat flox/floxCTD mice are directionally tuned to the posterior direction. (A) Summary plot showing the log ratio of IPSC amplitudes in the null and preferred directions (log(N/P)) for On and Off components for control (n =17 cells, 11 mice), non-DS (On: n = 6 cells, Off: n = 11 cells), and DS (On: n = 14 cells, Off: n = 11 cells, On and Off data from 18 mice) groups. Data are represented as mean ± SEM. On: Control 0.34 ± 0.04, non-DS 0.07 ± 0.05, DS -0.04 ± 0.04; Off: Control 0.45 ± 0.04, non-DS 0.05 ± 0.04, DS -0.08 ± 0.04. **(B)** Scatter plots of IPSC log(N/P) ratio versus spike DSI for On (left) and Off (right) components in the DS group. DSI values for On and Off spiking activity are calculated separately. Dashed lines indicate linear regression fit for this and subsequent plots. **(C)** Summary plot showing the log ratio of EPSC amplitudes in the preferred and null directions [log(P/N)] for On and Off components for control (n = 17 cells, 11 mice), non-DS (On: n = 6 cells, Off: n = 11 cells), and DS (On: n = 14 cells, Off: n = 11 cells, On and Off data from 18 mice) groups. On: Control 0.13 ± 0.06, non-DS -0.08 ± 0.04, DS 0.12 ± 0.03; Off: Control 0.17 ± 0.04, non-DS -0.01 ± 0.02, DS 0.24 ± 0.03. **(D)** Scatter plots of EPSC P/N ratio versus spike DSI for On (left) and Off (right) components in the DS group. **(E)** Summary plot showing maximum EPSC amplitudes in pDSGCs from control and KO groups. Filled diamonds represent mean ± SEM. On: Control 320.5 ± 25.0 pA, KO 332.1 ± 34.4 pA; Off: Control 315.8 ± 22.7 pA, KO 357.0 ± 46.9 pA. **(F)** Histograms of preferred directions calculated from spiking activity in

Figure 3.6 (cont.) control mice (top) and spiking activity (middle) and EPSC amplitude (bottom) in KO mice. The preferred directions of EPSCs are determined from the vector sums of peak amplitudes from 12 directions. The visual coordinates are labeled on the top of the histograms. **(G)** Summary plot showing the log of EPSC P/N ratio before (+) and after (-) gabazine application in control and the DS group in Vgat flox/floxCTD mice (KO-DS). Control mice: before gabazine, 0.23 ± 0.04; after gabazine, 0.05 ± 0.02, n = 20 cells, 8 mice; KO-DS: before gabazine, 0.14 ± 0.02; after gabazine, - 0.02 ± 0.02, n = 8 cells, 5 mice. On and Off components are pooled together.

Because direction-selective EPSCs in wild-type mice may result from the presence of stronger inhibitory inputs during motion in the null direction under imperfect voltage-clamp conditions, we further assessed whether residual inhibition could account for the directionality of EPSCs in *Vgat $^{flox/flox}$CTD* mice. If inhibitory currents largely account for direction-selective excitation, then both the IPSC peak amplitude in the null direction and the IPSC N/P ratio would be expected to correlate positively with the EPSC P/N ratio. In control mice, no positive correlation is found between the IPSC N/P ratio and EPSC P/N ratio (On: $R^2 = 0.02$, $p = 0.40$; Off: $R^2 = 0.03$, $p = 0.40$, n =17 cells; linear regression with an F test) or between null-direction IPSC peak amplitude and EPSC P/N ratio for the On component ($R^2 = 0.15$, $p = 0.12$). A weak positive correlation is seen between IPSC amplitude and EPSC P/N ratio for the Off component in control mice ($R^2 = 0.33$, *$p = 0.02$), which might be explained by the difficulty in controlling membrane potential in the more distal Off dendritic arbors of pDSGCs and therefore more pronounced space-clamp errors. However, in *Vgat $^{flox/flox}$CTD* mice, there is no positive correlation between the EPSC P/N ratio and either the IPSC amplitude (On: R^2 =0.34, * $p = 0.01$, negative correlation; Off: $R^2 = 0.001$, $p = 0.90$; n =19 cells) or the IPSC N/P ratio (On: $R^2 = 0.21$, $p = 0.08$; Off: $R^2 = 0.03$, $p = 0.44$). To further rule out the effect of residual inhibition on the directional tuning of pDSGC's spiking activity and EPSCs, we separately analyzed the cells in the DS group with IPSC N/P ratio ≤ 1. All of cells in this group exhibit direction-selective excitation [EPSC log(P/N) = 0.20 ± 0.04, n = 14, On and Off data are pooled together]. In addition, of the DS group, ~8% of the pDSGCs showed directionally tuned

EPSCs but no detectable stimulus-evoked IPSCs, indicating that direction-selective excitation can be the sole mechanism generating direction selectivity in some pDSGCs in *Vgat$^{flox/flox}$CTD* mice. In summary, it is unlikely that imperfect voltage-clamp recording accounts solely for the observed direction selectivity of excitatory inputs. When the inhibitory inputs onto pDSGCs in *Vgat$^{flox/flox}$CTD* mice are abolished or reduced to equal strength during motion in the preferred and null directions, direction selectivity of the spiking activity and of excitatory inputs persists in about half of the pDSGC population.

Because the majority of Drd4-GFP-positive neurons receive residual inhibition in *Vgat$^{flox/flox}$CTD* mice, we examined the relative timing of excitatory inputs and residual inhibitory inputs onto DSGCs during motion stimuli. We measured two parameters: (1) the time of peak current amplitude (t_{peak}) and (2) the time at the center of mass of the total charge transfer (t_{cm}). We then calculated the timing difference between EPSCs and IPSCs (Δt) evoked by the leading edge of the moving bar in the preferred and null directions. The temporal offset is defined as $\Delta t_{pref} - \Delta t_{null}$, with a positive value indicating delayed inhibition in the preferred direction. We did not quantify the temporal delay for the trailing edge response because, in many pDSGCs in *Vgat$^{flox/flox}$CTD* mice, it is difficult to identify precisely the peak time for the Off response due to reduced IPSC amplitude and a sustained component of IPSC between the leading and trailing edge of the moving bar (**Fig. 3.3A**). Analysis using t_{peak} or t_{cm} yields qualitatively the same results. In the control group, the inhibitory inputs onto pDSGCs were significantly delayed compared with the excitatory inputs during motion in the preferred direction (**Figs. 3.7A, 2.5A**). The temporal offset of inhibitory inputs is absent in the non-DS group (**Figs. 3.7A, 2.5B**). For pDSGCs in the DS group,

the residual inhibition is still delayed in the preferred direction motion, but this temporal delay is significantly reduced compared with the control group (**Figs. 3.7A, 2.5C**).

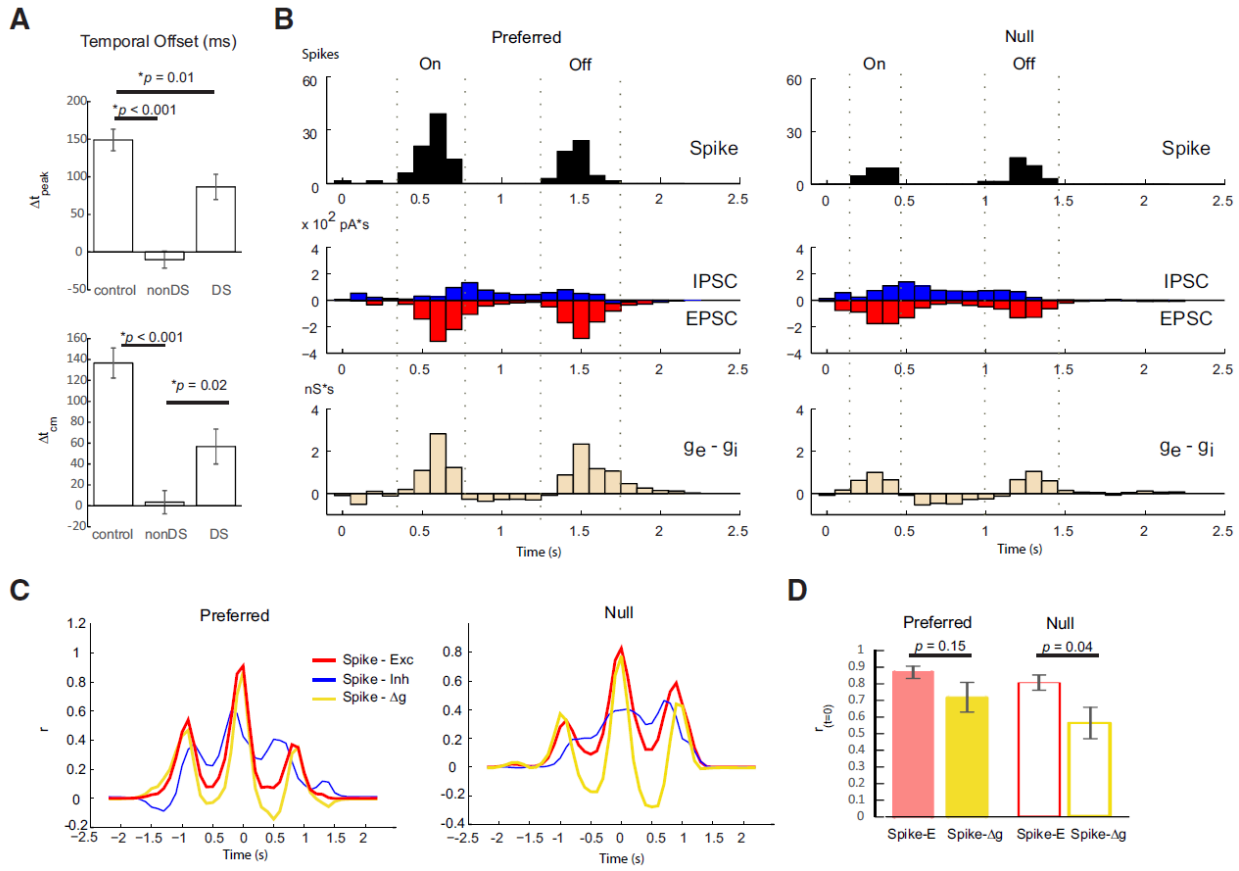

Figure 3.7: Relation between spiking activity and the time course of excitation and inhibition onto pDSGCs in *Vgat$^{flox/flox}$CTD* mice. (A) Summary plots showing the temporal offset of t_{peak} or t_{cm} between EPSCs and IPSCs in pDSGCs evoked by the leading edge of a bright moving bar from the control, non-DS, and DS groups (Δt_{peak}: control, 149.0 ± 14.35 ms, n = 20 cells; non-DS, −10.0 ± 11.2 ms, n = 6 cells; DS, 86.7 ± 16.7 ms, n = 14 cells; Δt_{cm}, control: 136.7 ± 22.7 ms; non-DS, 3.5 ± 9.6 ms; DS, 56.8 ± 23.4 ms. **(B)** Temporally aligned spike-density histograms (top), current-density histograms (middle) for EPSCs (red, inward) and IPSCs (blue, outward), and the relative difference between excitatory and inhibitory conductances (Δg, bottom) of a pDSGC in preferred and null directions of a moving bar stimulus. For B and C, 100 ms bins are used. Time windows of On and Off spikes are indicated by dashed lines. **(C)** Cross-correlograms for the neuron in B. The spiking activity, EPSC, and Δg covary synchronously, as indicated by the correlation coefficient peaking at the t = 0 bin. The two smaller peaks at both sides result from the cross-correlation between On and Off responses during the moving bar stimulus. **(D)** Summary plots showing the cross-correlation coefficient at t = 0 between spiking and EPSC and between spiking and Δg in the preferred and null directions (preferred direction: spike vs EPSC, 0.87 ± 0.04; spike vs Δg, 0.72 ± 0.09; null direction: spike vs EPSC, 0.80 ± 0.04; spike vs Δg, 0.56 ± 0.09, n = 8 cells).

How do directional excitation and temporal delay between excitation and inhibition contribute to the spiking activity in *Vgat*$^{flox/flox}$*CTD* mice? We attempted to address this question by comparing the time course of action potential generation, excitatory and inhibition currents, and the relative difference between excitatory and inhibitory conductances ($\Delta g = g_e - g_i$). The recorded traces were divided into 100 ms bins. The number of action potentials, excitatory and inhibitory currents, and Δg are integrated in each bin for preferred and null directions (**Fig. 3.7B**). Cross-correlograms show that spiking activity is strongly correlated with the excitatory currents (**Fig. 3.7C, D**). We did not observe an improved correlation between spiking activity and Δg (**Fig. 3.7C, D**). This result lends further support to an important role of direction-selective excitation in direction-selective spiking in *Vgat*$^{flox/flox}$*CTD* mice.

3.3.3 Cholinergic component is directional in the DS group of Vgat$^{flox/flox}$*CTD mice*

Because DSGCs receive glutamatergic and cholinergic inputs from bipolar cells and SACs, respectively, we investigated which component of the EPSCs is direction selective in *Vgat*$^{flox/flox}$*CTD* mice. We recorded moving bar-evoked EPSCs from cells in the DS group before and after applying the nicotinic receptor antagonist DHβE (**Fig. 3.8A**). DHβE has been shown to completely block the cholinergic inputs from SACs to DSGCs (Wei et al., 2011a). DHβE-sensitive currents are obtained by subtracting the residual EPSC trace from the one before addition of DHβE. We found that DHβE significantly reduced the peak P/N ratios of EPSCs. However, the DHβE-sensitive currents are direction selective and tuned to the posterior direction in both the On (**Fig. 3.8B–D**) and Off (**Fig. 3.8E, F**) components. Therefore, directionally tuned excitation in *Vgat*$^{flox/flox}$*CTD* mice is mostly attributed to cholinergic inputs from SACs.

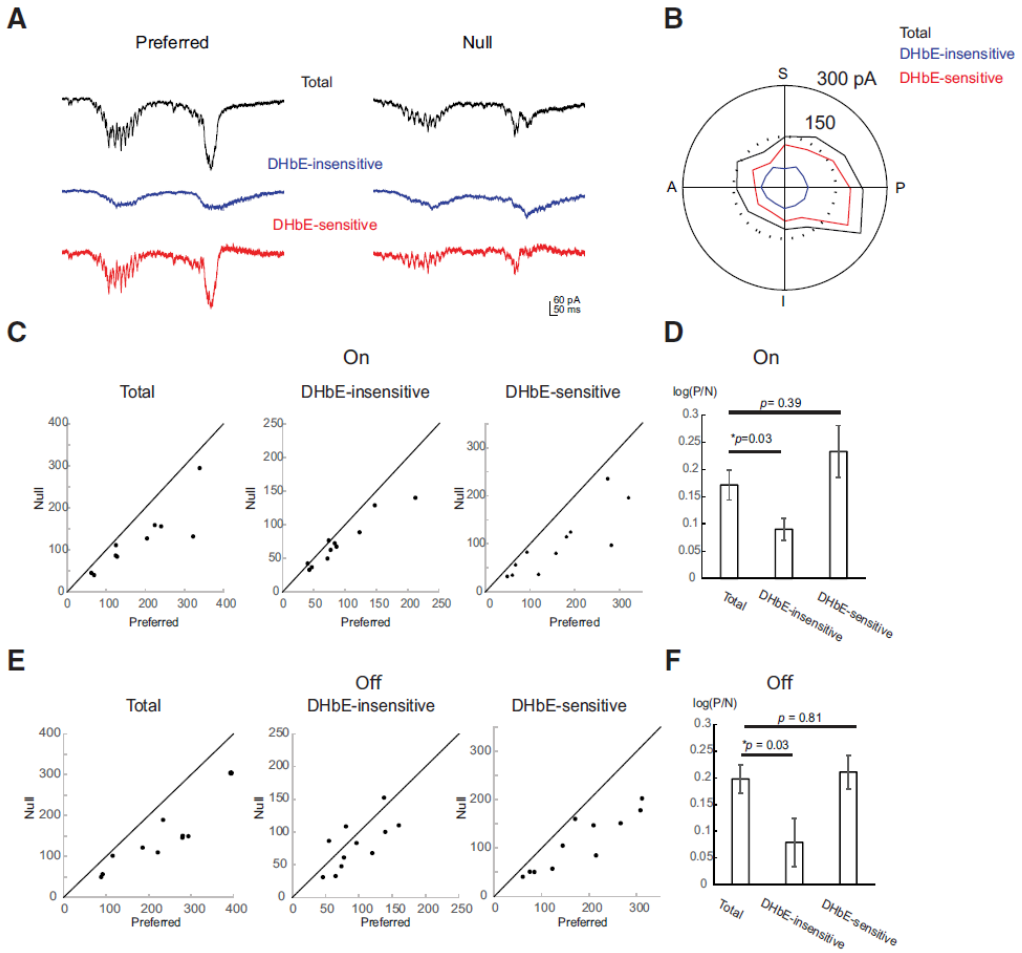

Figure 3.8: Cholinergic component of the EPSCs in the DS group from the *Vgat$^{flox/flox}$CTD* mice is direction selective. (A) Mean EPSC traces (average over three trials) of a pDSGC in the DS group evoked by a moving bar in the preferred and null directions. EPSCs were recorded before (top) and after (middle) 0.08 µm DHβE was applied through perfusion. The subtracted trace (bottom) represents the DHβE-sensitive cholinergic component of the EPSCs. (B) Polar plot of the peak amplitude of the On responses for the total (black), DHβE-insensitive glutamatergic (blue), and DHβE-sensitive cholinergic (red) components from the cell in A. P, Posterior; A, anterior; S, superior; I, inferior. **(C)** For On responses, scatter plots of EPSC peak amplitudes evoked by null-direction motion against those evoked by preferred-direction motion for the total (left), DHβE-insensitive (middle), and DHβE-sensitive (right) components. Diagonal lines are unity lines. **(D)** Summary plot showing the log ratio of EPSC amplitudes in the preferred and null directions [log(P/N)] for the On response for the total (left), DHβE-insensitive (middle), and DHβE-sensitive (right) components. Total: 0.17 ± 0.03; DHβE-insensitive: 0.09 ± 0.02; DHβE-sensitive: 0.23 ± 0.05; n = 11 cells, 8 mice. **(E)** As in C, scatter plots for Off responses. **(F)** As in D, summary plot showing the log ratio of EPSC amplitudes in the preferred and null directions [log(P/N)] for the Off response. Total: 0.20 ± 0.03; DHβE-insensitive: 0.08 ± 0.05; DHβE-sensitive: 0.21 ± 0.03.

3.3.4 Direction selectivity of pDSGCs in Vgat$^{flox/flox}$CTD mice is not due to asymmetric distribution of their dendritic arbors

Asymmetric distribution of dendritic arbors has been proposed as another mechanism underlying direction selectivity in a subtype of On-Off DSGCs that prefer motion in the superior direction (Kay, de la Huerta, et al., 2011; Trenholm et al., 2011) and in a class of Off DSGCs (Kim et al., 2008). To determine whether the direction selectivity observed in pDSGCs from *Vgat*$^{flox/flox}$*CTD* mice results from asymmetric dendritic morphology, we compared the area (**Fig. 3.9A**) and the total length (**Fig. 3.9C**) of dendritic arbors occupying the preferred side versus those occupying the null side and calculated the P/N ratios for each pDSGC. We found random distribution of dendrites along the preferred-null axis and a lack of correlation between the P/N ratio for dendritic arbor area or length and spike DSI (**Fig. 3.9B, D**). Therefore, dendritic morphology does not dictate the directional preference in the pDSGCs in *Vgat*$^{flox/flox}$*CTD* mice.

3.4 Discussion

This study shows that, in the absence of direction-selective inhibition, direction selectivity is not completely abolished in a subset of DSGCs, but is implemented by direction-selective excitatory inputs and temporally offset inhibition. Therefore, multiple synaptic mechanisms act synergistically to ensure robust direction selectivity of mouse DSGCs.

An indispensable role of SACs in direction selectivity has been supported by multiple studies that selectively ablated SACs by toxin treatment (Amthor et al., 2002; Yoshida et al., 2001) or chemogenetic silencing (Vlasits et al., 2014). Because these manipulations abolish both GABA and acetylcholine release from SACs, loss of direction selectivity observed in these studies can result from lack of both excitatory and inhibitory mechanisms. In this study, GABA, but not acetycholine release, was selectively blocked from SACs.

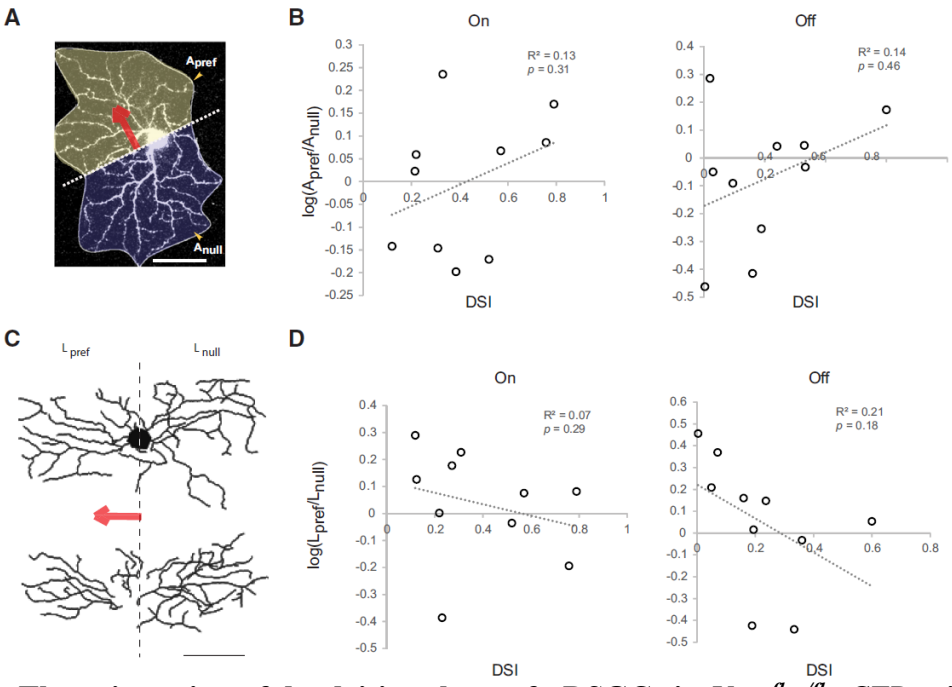

Figure 3.9: The orientation of dendritic arbors of pDSGCs in *Vgat*$^{flox/flox}$*CTD* mice does not predict the cells' preferred directions. (A) Schematic showing the method of measuring dendritic arbor area occupying the preferred (A_{pref}) and null (A_{null}) sides of a pDSGC in a *Vgat*$^{flox/flox}$*CTD* mouse. The image is the Z projection of the On layer of a pDSGC's dendrites acquired by two-photon imaging. Red arrow indicates preferred direction of the cell's spiking activity. Scale bar, 50 µm. **(B)** Scatter plots of the log of the area ratio A_{pref}/A_{null} versus spike DSI in *Vgat*$^{flox/flox}$*CTD* mice for the On and Off components. **(C)** Example of reconstructed On and Off dendritic arbors of a pDSGC for calculating dendritic length. Scale bars, 50 µm. **(D)** Same as B, scatter plots of log dendritic length ratio L_{pref}/L_{null} versus spike DSI in *Vgat*$^{flox/flox}$*CTD* mice.

Pharmacological blockade of GABA receptors by antagonists has been shown to cause loss of direction-selective spiking activity in DSGCs (Ariel & Daw, 1982; Caldwell et al., 1978; Chiao & Masland, 2003; Cohen & Miller, 1995; Kittila & Massey, 1995; Weng et al., 2005)**.** In addition to blocking GABAergic inhibition, GABA receptor antagonists also abolished direction-selective excitatory inputs onto DSGCs in wild-type (Fried et al., 2005; S. Lee et al., 2010) and *Vgat*$^{flox/flox}$*CTD* (**Fig. 3.6G**) mice. Results from these pharmacological experiments can be interpreted in the following two ways. First, direction-selective excitation is generated by presynaptic inhibition onto excitatory presynaptic terminals. Because the residual GABAergic inputs from SACs to DSGCs in *Vgat*$^{flox/flox}$*CTD* mice are nondirectional, this directional

presynaptic inhibition likely comes from additional GABAergic amacrine cell types other than SACs (Hoggarth et al., 2015; Park et al., 2015). The second interpretation is that the relatively small differences in EPSCs in the preferred and null directions may be masked by hyperactivity of retinal network when GABAergic inhibition is nonspecifically blocked by antagonists. We cannot distinguish between the above two possibilities. Furthermore, VGluT3-expressing amacrine cells (S. Lee et al., 2014) have been shown recently to provide excitatory inputs onto DSGCs. How this and other recently identified amacrine cell types are involved in the direction-selective excitatory inputs described in this study is not clear and awaits future studies.

Deletion of *Vgat* from SACs by *ChAT-IRES-Cre* expression appears to cause no detectable change in the rest of the direction-selective circuit during development. Both the SAC-DSGC cholinergic synapses and GABA receptor expression on pDSGCs appear to be unaffected. The strength of light-evoked EPSCs in $Vgat^{flox/flox}CTD$ mice is comparable to that in the wild-type animals. Furthermore, we did not detect enhanced direction selectivity of excitatory inputs in the conditional knock-out mice, suggesting that there is little developmental compensation or reorganization of other synapse types when GABA release from SACs is impaired. Lack of heterosynaptic competition and lack of co-regulation of excitation and inhibition have also been demonstrated in other retinal circuits in mice (Okawa et al., 2014; Schubert et al., 2013). Therefore, the results from $Vgat^{flox/flox}CTD$ mice likely reflect the contributions of excitatory mechanisms to direction selectivity in normal healthy mice, but we cannot completely exclude the possibility of compensatory changes in the circuit.

A major concern about direction-selective excitation observed in voltage-clamp experiments is the underestimation of EPSCs during motion in the null direction due to the presence of strong inhibitory inputs (Poleg-Polsky & Diamond, 2011; Vaney et al., 2012). In *Vgat*$^{flox/flox}$*CTD* mice, null-direction inhibition is severely reduced to a level similar to preferred-direction inhibition or, in some cases, is completely eliminated. This should substantially alleviate the distortion of EPSCs by IPSCs during null-direction motion. Direction-selective excitation is still present in the DS group under these conditions, indicating that there is a genuine difference in the strength of excitatory inputs onto those DSGCs during motion in the preferred and null directions. Furthermore, blocking the cholinergic component of excitation in the DS group reduced direction tuning of excitation, which cannot be explained by voltage-clamp artifacts. The existence of direction-selective excitation in *Vgat*$^{flox/flox}$*CTD* mice also implies that direction-selective EPSCs of DSGCs measured in wild-type mice reflect a genuine excitatory input pattern, although this direction-selective excitation might be quantitatively overestimated because of space-clamp issues, especially at the Off dendritic arbors (Poleg-Polsky & Diamond, 2011). In contrast, pDSGCs in the non-DS group lack directional tuning of their excitation. It is possible that GABA release from SACs is critical for generating direction-selective excitation in the non-DS group. Alternatively, direction-selective excitation may not be a universal mechanism for all DSGCs. Either possibility highlights the heterogeneity of excitatory mechanisms in the direction-selective circuit.

We found that directional excitation in *Vgat*$^{flox/flox}$*CTD* mice is unlikely to be attributed to glutamatergic inputs onto DSGCs. This is consistent with results from functional imaging studies in wild-type mice, which used an extracellular glutamate sensor (iGluSnFR) expressed in On

DSGCs and a subtype of On-Off DSGCs and a calcium sensor (GCaMP3) expressed in On bipolar cell terminals. These studies reported nondirectional glutamatergic responses from these sensors during motion stimuli (Park et al., 2014; Yonehara et al., 2013)**,** indicating that the glutamatergic component of the excitatory conductances is not direction selective in wild-type mice.

The role of acetylcholine in direction selectivity has been less clear. During blockade of GABAergic inhibition, cholinergic excitation has been implicated in motion facilitation in all directions (Chiao & Masland, 2002; He & Masland, 1997)**.** However, whether the contribution of cholinergic excitation is directional in the absence of GABA antagonists has been controversial. Several extracellular recording studies using moving bars showed that nicotinic antagonists do not abolish direction selectivity (Ariel & Daw, 1982; Cohen & Miller, 1995; Kittila & Massey, 1995). In contrast, other studies using drifting gratings showed that a nicotinic antagonist largely eliminated direction selectivity (Grzywacz, Amthor, et al., 1998; Grzywacz, Merwine, et al., 1998). Furthermore, in whole-cell recordings, direction-selective modulation of cholinergic inputs onto DSGCs has been reported (Fried et al., 2005; S. Lee et al., 2010; Park et al., 2014). In this study, we also observe direction-selective cholinergic excitation, suggesting that this mechanism may be used by both wild-type and *Vgat*$^{flox/flox}$*CTD* mice. The conflicting results from past studies may be explained by variability in experimental conditions. Indeed, light responses of retinal ganglion cells have been shown to change with background luminance and contrast (Pearson & Kerschensteiner, 2015; Tikidji-Hamburyan et al., 2015) and the mechanisms of direction selectivity may be modulated by visual stimulus conditions (Lipin et al., 2015; Vlasits et al., 2014).

It is noteworthy that SAC-mediated GABA release in *Vgat*$^{flox/flox}$*CTD* mice is not completely abolished, consistent with previous studies on VGAT knock-out mouse lines (Tritsch et al., 2012; Wojcik et al., 2006). The residual light-evoked IPSCs may come from the residual GABAergic transmission from SACs shown in paired recordings or from inhibitory inputs from other amacrine cell types (Hoggarth et al., 2015; Park et al., 2015). For the pDSGCs in the DS group, although the inhibitory inputs are non-directional, the temporal offset is present albeit reduced compared with the wild-type. This residual temporal offset might result from the weak, statistically nonsignificant bias of residual inhibitory inputs coming from the null-side SACs (**Fig. 3.1D**, KO pref vs KO null). Because SAC processes prefer motion in the centrifugal direction in the wild-type animal, it is unclear why slightly more inputs from null-side SACs did not produce slightly stronger residual inhibition during null-direction motion. One possibility is that reducing GABA release from SACs impairs the centrifugal preference in SACs due to disrupted reciprocal inhibition among SACs (Euler et al., 2002; Hausselt et al., 2007; S. Lee & Zhou, 2006; Münch & Werblin, 2006; N. W. Oesch & Taylor, 2010). Another possibility is that SAC processes are still depolarized more strongly by centrifugal motion, but depletion of vesicular GABA in *Vgat* knock-out mice has a more severe impact on GABA release during the more strongly depolarizing centrifugal stimuli, resulting in overall nondirectional GABA release from SAC processes.

The spiking pattern of DSGCs depends on the interaction between the intrinsic properties of dendrites and patterned excitatory and inhibitory inputs (Cafaro & Rieke, 2010; N. Oesch et al., 2005; Schachter et al., 2010; Sivyer & Williams, 2013; Trenholm et al., 2014). In wild-type mice, motion in the null direction evokes powerful inhibitory inputs onto DSGCs that occur simultaneously with excitatory inputs, whereas motion in the preferred direction evokes weak

inhibitory inputs that are significantly delayed compared with the excitatory inputs. These factors contribute synergistically to the selective suppression of null-direction spiking. In *Vgat*$^{flox/flox}$*CTD* mice, the inhibition in the null direction is severely weakened (similar to the level of that in the preferred direction) and therefore is less effective in vetoing the spiking activity driven by excitatory inputs. As a result, spike generation is strongly correlated with EPSCs in *Vgat*$^{flox/flox}$*CTD* mice. In addition, both spiking activity and EPSCs are tuned to the posterior direction. Together, these findings highlight the importance of an excitation–inhibition interaction in sensory processing and strongly support a role of directional excitation in direction selectivity in a subpopulation of DSGCs.

3.5 Experimental Procedures

Animal Handling and Husbandry

Vgat$^{flox/flox}$ mice (*Slc32a1 tm1Lowl /J*), *ChAT-IRES-Cre* mice (129S6-*Chat* $^{tm2(cre)Lowl}$/J), and floxed *tdTomato* mice (129S6-*Gt(ROSA) 26Sor* $^{tm9(CAG\ -\ tdTomato)Hze}$*/J*) were acquired from The Jackson Laboratory. Drd4-GFP mice were originally developed by MMRRC (http:// www.mmrrc.org/strains/231/0231.html) in the Swiss Webster back- ground, subsequently backcrossed to C57BL/6 background, and were obtained from Dr. Marla Feller at the University of California–Berkeley. All strains were backcrossed to the C57BL/6 background in our laboratory and crossed to each other to create the lines used in this study. Mice of both sexes between postnatal days 18 and 35 were used for paired recording experiments and those at postnatal days 24 –35 were used for light response experiments. All procedures to maintain and use mice were in accordance with the University of Chicago Institutional Animal Care and Use Committee, the

National Institutes of Health's Guide for the Care and Use of Laboratory Animals, and the Public Health Service Policy.

Immunocytochemistry

Mice were anesthetized with isoflurane and decapitated. The eyes were removed and fixed in 4% PFA in PBS overnight at 4°C. Serial coronal sections with a thickness of 12 m were obtained using a cryostat (Leica) and mounted on Superfrost slides (Fisher Scientific). Nonspecific immunoreactivity was suppressed by incubating samples in 10% bovine serum albumin (BSA, Sigma-Aldrich). Primary antibodies included guinea pig anti-Vgat (SY/SY, 1:500) and goat anti-Vesicular Acetylcholine Transporter (VAChT; Millipore, 1:1000). Primary antibodies were diluted in PBS with 5% BSA and 0.2% Triton X-100, applied to the sections and incubated overnight at 4°C. Sections were then washed four times for 20 min each with PBS containing 5% BSA, 0.2% Triton X-100. Secondary antibodies Alexa 594- or Alexa 647- conjugated goat anti-guinea pig (Invitrogen, 1:300) and Alexa 488- conjugated donkey anti-goat (Invitrogen, 1:300) were applied to the sections and incubated for 2 h at room temperature. The samples were then washed four times for 20 min each with PBS. All sections were counter stained with Hoechst 33258 (Sigma-Aldrich). Image data were collected with a Leica TCS SP5 confocal microsystem.

Dual whole-cell patch-clamp recording.

Mice were anesthetized with isoflurane and decapitated. The retinas were isolated in oxygenated artificial CSF (ACSF) at room temperature containing the following (in mM): 119.0 NaCl, 26.2 $NaHCO_3$, 11 D-glucose, 2.5 KCl, 1.0 K_2HPO_4, 2.5 $CaCl_2$, and 1.3 $MgCl_2$. The isolated retinas were then cut into dorsal or ventral halves and mounted ganglion-cell-layer-up on top of a 1 mm^2

hole in a small piece of filter paper (Millipore). The orientation of the preferred direction (posterior) of Drd4-GFP-positive neurons was noted for each piece. Dual whole-cell voltage-clamp recordings from SACs and posterior DSGCs (pDSGCs) were performed in oxygenated ACSF in the presence of 0.05 mM D-AP5 and 0.02 mM DNQX disodium salt. Recording electrodes of 3–5 M were filled with a cesium-based internal solution containing the following (in mM): 110 $CsMeSO_4$, 2.8 NaCl, 4 EGTA, 5 TEA-Cl, 4 adenosine 5-triphosphate (magnesium salt), 0.3 guanosine 5-triphosphate (trisodium salt), 20 HEPES, 10 phosphocreatine (disodium salt), 5 N-ethyllidocaine chloride (QX314), 0.025 Alexa Fluor 488 (for SACs), and 0.025 Alexa Fluor 594 (for pDSGCs), pH 7.25. Neurons were visualized with transmitted visible light from a halogen bulb, a video camera, and a monitor. tdTomato-labeled SACs and GFP-labeled pDSGCs were identified with epifluorescence imaging (X-Cite) or two- photon microscope (Bruker) under a water-immersion objective (60x , LUMPlanFl/IR; Olympus). Data were acquired using PCLAMP 10 recording software and a Multiclamp 700B amplifier (Molecular Devices), low-pass filtered at 4 kHz, and digitized at a sampling rate of 10 kHz. The evoked IPSCs and EPSCs in pDSGCs were isolated by holding the cells at reversal potentials for these conductances (0 mV for GABAergic, -60 mV for cholinergic). The reversal potentials were calculated and then experimentally confirmed by obtaining current–voltage relationships of pharmacologically isolated GABAergic and cholinergic currents in pDSGCs. Only recordings with series resistances < 20 MΩ were used. Liquid junction potential was corrected.

Uncaging of Rubi-GABA.

10 M Rubi-GABA (Tocris Bioscience) was bath applied to the retinas and protected from visible light. A collimated blue LED (470 nm; Thor Laboratories) was flashed for 100 ms through a 60

objective onto a 400- m-diameter area of the retina centered in the soma of the DSGC. Uncaging response was measure by whole-cell voltage-clamp recordings from DSGCs at 0 mV in the presence of 300 M cadmium chloride (Sigma-Aldrich).

Two-photon targeted recording and imaging of GFP-positive neurons for light response.

A white, monochromatic organic light-emitting display (OLEDXL, eMagin; 800 x 600 pixel resolution, 60 Hz refresh rate) was controlled by an Intel Core Duo computer with a Windows 7 operating system. The moving bar stimulus was generated by MATLAB and the Psychophysics Toolbox and projected through the condenser lens of the two-photon microscope onto the photoreceptor layer, centering on the pDSGC soma. White bars in a dark background moved in 12 pseudo- randomly chosen directions spaced at 30 degree intervals at a speed of 500 μm/s on the retina and were presented in three to five repetitions. The percent stimulus contrast $(L_{stimulus} - L_{background})/(L_{stimulus} + L_{background})$ was 80 –100%. A detailed protocol of the two-photon targeted recording of light response can be found in (Wei et al., 2010)**.**

Mice were anesthetized with isoflurane and decapitated after dark ad- aptation. Under infrared illumination, retinas were isolated from the pigment epithelium in oxygenated Ames' medium (Sigma-Aldrich), cut into dorsal and ventral halves, and mounted onto filter papers as de- scribed above. Retinas were kept in darkness at room temperature in Ames' medium bubbled with 95% O_2/5% CO_2 until use (0 –7 h). During recordings, the retinas were perfused with oxygenated Ames at 32–33°C. Cells were visualized with infrared light (900 nm) and an IR-sensitive video camera (Watec). GFP-positive cells were identified by a two- photon microscope (Bruker) and a Ti:sapphire laser (Chameleon Ultra II; Coherent Technologies) tuned to 920 nm. First, an electrode

of 3–5 MΩ was filled with Ames' medium for loose patch recordings of spikes; then, the electrode was carefully removed and a new electrode filled with the cesium-based internal solution was used to obtain whole-cell voltage-clamp recordings from the same cell using the same method and criteria as those used in dual patch-clamp experiments. Light-evoked IPSCs and EPSCs in pDSGCs were isolated by holding the cells at 0 mV and -60 mV, respectively. For Figure 3.6G, 0.0125 mM gabazine (SR-95531, Tocris Bioscience) was applied. At the end of recording, an image stack of the Alexa Fluor 488-filled pDSGCs was acquired with the two-photon microscope at z-intervals of 1.5 m and resampled three times for each z-plane using a 60x objective (Olympus LUMPlanFl/IR 60 /0.90W). Images were acquired to cover the entire dendritic field of the cell. To isolate cholinergic component of the light responses, EPSCs were recorded before and after bath application of 0.008 mM DHβE (Tocris Bioscience) for each cell.

Analysis of electrophysiological data

Data were analyzed using custom protocols in MATLAB. Three to five raw response traces were recorded and averaged to obtain the mean response at each stimulus direction. The peak amplitude of the currents evoked by the leading (On) and treading (Off) edges of the bright bar were used for calculating P/N or N/P ratios. To analyze the relative timing between excitation and inhibition, we first determined the time window of the On response. Light-evoked EPSCs return to baseline after the leading edge of the bar leaves the receptive field. Therefore, the start (t_{start}) and end (t_{end}) times can be determined reliably. Light-evoked IPSCs usually contain a sustained component that does not return to the baseline after the leading edge leaves the receptive field. Therefore, the end time of IPSCs is set to equal the end time of EPSCs. The time of peak (t_{peak}), as well as the time at center of mass of the charge transfer (t_{cm}), during this time window were determined for

synaptic currents recorded at the null and preferred directions. $t_{cm} = \frac{\int_{t_{start}}^{t_{end}} I(t) \cdot t \, dt}{\int_{t_{start}}^{t_{end}} I(t) \, dt}$, adapted from (H. Agmon-Snir & Segev, 1993). For each direction, the relative difference in the timing between EPSC peak and IPSC peak (Δt) was calculated by subtraction. The temporal offset was then determined by ($\Delta t_{preferred} - \Delta t_{null}$), with a positive value indicating delayed inhibition in the preferred direction. Similar calculations were done to determine the temporal offset using t_{cm} for EPSCs and IPSCs. For Figure 3.8, the cholinergic component of the light responses was isolated by subtracting the averaged EPSCs (three trials per direction) after DHβE application from the averaged traces before addition of DHβE.

Analysis of dendritic morphology.

On and Off dendritic arbors of pDSGCs were traced from two-photon image stacks using ImageJ. Each dendritic layer was divided into halves based on the preferred direction of the cell's spiking activity. A line perpendicular to the preferred direction was drawn at the position of the cell body to separate the dendritic arbors into the preferred side and null side regions. The total dendritic length in each region was measured from the traced skeleton. The area of the dendritic arbors was determined by first connecting the tips of the dendrites to a polygon and then fitting it to a cubic spline curve.

Statistical analysis.

Grouped data are presented as mean SEM. Statistical analysis was performed using MATLAB. Linear regression with an F test (two-sided) was used for Figures 2.6 and 2.9. A two-sample Kolmogorov– Smirnov test was used for Figure 3.4C. Cross-correlation was performed for Figure 3.7. For the rest of the figures, data were tested for normality and statistical differences were

examined using one-way ANOVA and post hoc comparisons using Student's t test with Bonferroni corrections. The statistical significance of spike-tuning curves during motion stimuli was determined by the bootstrapping analysis (Efron & Tibshirani, 1986; Stark & Abeles, 2005). For each cell, the spike counts during moving bar stimuli (12 directions, three to five repetitions) were randomly sampled and replaced using a bootstrapping algorithm 10,000 times. The null hypothesis is that spiking activity is isotropic during moving bar stimuli. direction selective index (DSI) and vector sum values were computed for each resampled dataset. The nonparametric 95% confidence limits were determined from the distribution of DSI and vector sum values of the bootstrapped datasets. To be classified as direction selective, a cell needs to have significant DSI and vector sum values and a DSI ≥ 0.2.

Chapter 4

Retinal origin of direction selectivity in the superior colliculus

This chapter is a full reprint of Shi et al., *Nature Neuroscience* (2017), in which I was a secondary author. This work is included with permission from all authors.

Relevant Publication:
Shi, X., Barchini, J., Acaron Ledesma, H., Koren, D., Jin, Y., Liu, X., & Cang, J. (2017). Retinal origin of direction selectivity in the superior colliculus. *Nature neuroscience*, 20(4), 550-558.

4.1 Abstract

Detecting visual features in the environment such as motion direction is crucial for survival. The circuit mechanisms that give rise to direction selectivity in a major visual center, the superior colliculus (SC), are entirely unknown. Here, we optogenetically isolate the retinal inputs that individual direction-selective SC neurons receive and find that they are already selective as a result of precisely converging inputs from similarly-tuned retinal ganglion cells. The direction selective retinal input is linearly amplified by the intracollicular circuits without changing its preferred direction or level of selectivity. Finally, using 2-photon calcium imaging, we show that SC direction selectivity is dramatically reduced in transgenic mice that have decreased retinal selectivity. Together, our studies demonstrate a retinal origin of direction selectivity in the SC, and reveal a central visual deficit as a consequence of altered feature selectivity in the retina.

4.2 Introduction

Neurons in the brain are specialized in detecting unique features in the environment. In the visual system, many neurons at various stages of processing respond selectively to stimuli moving along specific directions or having particular orientations (Priebe & Ferster, 2012; Vaney et al., 2012; Wei & Feller, 2011). Such direction and orientation selectivity are critical for motion sensing and image processing, leading to visually guided behaviors that are important for survival. Not surprisingly, the circuit mechanisms of direction and orientation selectivity have been extensively studied. However, these studies have mostly focused on the retina and primary visual cortex (V1) (Priebe & Ferster, 2012; Vaney et al., 2012) while neglecting the SC, a major retinal target and vision center.

The SC, or optic tectum, is an evolutionarily conserved structure that receives direct retinal input in all vertebrates (Cang & Feldheim, 2013; Gandhi & Katnani, 2011; May, 2006). It was the most sophisticated visual center until the neocortex recently evolved in mammals. Even in mice, a mammalian species that has become a useful model in vision research (Huberman & Niell, 2011), 85–90% of retinal ganglion cells (RGCs) project to the SC (Ellis et al., 2016), making it the most prominent visual structure in this species. Although the SC is mostly known for its functions in initiating rapid gaze shift toward salient stimuli, neurons in its superficial layers (i.e., the visual layers), including the stratum griseum superficiale (SGS) and stratum opticum (SO), display diverse visual response properties. In particular, selectivity for motion direction has been observed in the superficial SC of all mammalian species that have been studied, including tree shrews (Albano et al., 1978), cats (McIlwain & Buser, 1968), hamsters (Rhoades & Chalupa, 1976), squirrels (C. R. Michael, 1972), rabbits (R. H. Masland et al., 1971), rats (Fortin et al., 1999) and

mice (Drager & Hubel, 1975). Direction selectivity has also been observed in the primate SC, although it is much less prominent (Cynader & Berman, 1972; Marrocco & Li, 1977). Surprisingly, despite the fact that it has been almost half a century since direction selectivity was first described in the mammalian SC, its underlying circuit and synaptic mechanisms remain entirely unknown.

Several mechanisms could give rise to the direction selectivity seen in superficial SC neurons. First, they could inherit it directly from direction-selective (DS) retinal inputs. Indeed, direction-selective ganglion cells (DSGCs) have been discovered in the retina of a number of species, and most of the DSGCs project to the superficial SC (Dhande & Huberman, 2014). In mice, several subtypes of DSGCs preferentially terminate their axons in the upper half of the SGS, while most of the non-DSGCs tend to project to the lower half (Huberman et al., 2008, 2009; Kay, de la Huerta, et al., 2011; I. J. Kim et al., 2010). Notably, DS collicular neurons are also organized in a depth-specific manner, where they are most concentrated in the topmost lamina of the SGS and become less prevalent with depth (Inayat et al., 2015). This correspondence between the anatomical and functional organization supports the idea that similarly tuned DSGCs could project to common targets, thereby providing SC neurons with a synaptic drive that is biased toward certain directions.

Second, direction selectivity in the SC could arise from a specific arrangement of retinal inputs that are not individually tuned. In his motion-detector model, Reichardt proposed that direction selectivity could be generated by nonselective inputs that have different temporal delays. In such a model, these inputs are arranged such that stimuli moving in the preferred direction would result in the synchronous arrival of synaptic inputs and consequently a large depolarization in the

postsynaptic cell onto which they converge. On the other hand, stimuli moving in the opposite direction would cause only a small depolarization because the inputs would arrive asynchronously. This scenario was indeed shown to underlie direction selectivity in cat V1, as revealed by both extracellular and intracellular recordings (Priebe & Ferster, 2005; Saul & Humphrey, 1992). Whether a similar mechanism exists for direction selectivity in the SC is not known.

Finally, direction selectivity in the SC could be computed de novo. In this scenario, the combined retinal input that a DS SC neuron receives would be nonselective for motion direction. Direction selectivity could then arise via dynamic interactions within the local circuits, such as tuned or spatially offset inhibition, as originally proposed by Barlow and Levick for retinal direction selectivity (Barlow & Levick, 1965).

In this study, we set out to determine which of the above mechanisms could give rise to direction selectivity in the mouse SGS. In one set of experiments, we isolated the retinal inputs that individual SGS neurons receive by combining in vivo whole-cell voltage-clamp recording and optogenetic silencing. In another, we reduced the selectivity of DSGCs by genetically manipulating retinal circuits and then studied the impact on SGS direction selectivity using two-photon calcium imaging. Together, these experiments demonstrate for the first time that direction selectivity in the SGS is inherited from DSGCs in the retina; consequently, disrupting DSGCs' tuning leads to altered feature selectivity in the SC.

4.3 Results

4.3.1 Vm–spike transformation in SGS neurons

To study the synaptic mechanisms of direction selectivity in the superficial SC, we carried out *in vivo* whole-cell recording of SGS neurons in urethane-anesthetized mice with the entire V1 removed. First, we recorded SGS neurons under current-clamp mode to reveal their spiking and the underlying membrane potential (V_m) changes in response to sweeping bars in different directions (**Fig. 4.1A-C**). Various degrees of direction selectivity were observed in the recorded cells, including a substantial population that was highly selective in its spiking responses (for example, **Fig. 4.1B-E**). Using the normalized vector sum as an index, which we refer to as the global direction selectivity index (gDSI), we found that 27% of the SGS neurons were highly DS in their spiking (gDSI of spikes $\geq$ 0.25; n = 14 of 52 cells), consistent with our previous extracellular studies across the entire depth of the SGS (Wang et al., 2010). The gDSIs of spikes (gDSI-spike) and of V_m (gDSI-V_m) were overall correlated for individual cells, but gDSI-spike was greater in most cases (**Fig. 4.1F**), as expected from the nonlinear effect of the spike threshold (Priebe & Ferster, 2012). As the vast majority of selective SGS neurons (gDSI-spike $\geq$ 0.25) had gDSI-$V_m \geq$ 0.1 (n = 11 of 14 cells), we subsequently used 0.1 as a cutoff for classifying Vm and excitatory postsynaptic current (EPSC) responses as highly DS. Notably, the V_m-to-spike transformation in the SGS neurons was not as steep as seen in the DS cells in cat or mouse visual cortex. The ratio between DSI-spike and DSI-V_m was ~3 in cat V1 (Priebe & Ferster, 2005) and ~6 in mouse V1 (Li et al., 2015), but only ~1.2 in mouse SGS. In fact, a number of the recorded cells showed nearly identical tuning curves and gDSI values between their spiking and V_m responses (**Fig. 4.1F** and **Fig. 4.2**). Consistently, some SGS cells showed very weak, barely detectable depolarization to bars moving along their nonpreferred directions (for example, **Fig. 4.2**), a phenomenon rarely seen in cortical DS cells (Li et al., 2015; Priebe & Ferster, 2005). Furthermore, the preferred directions of SGS cells were similar for spike and V_m responses,

especially for highly DS cells (**Fig. 4.1G**). These observations thus suggest that synaptic inputs likely play a more important role in determining direction selectivity in the mouse SGS.

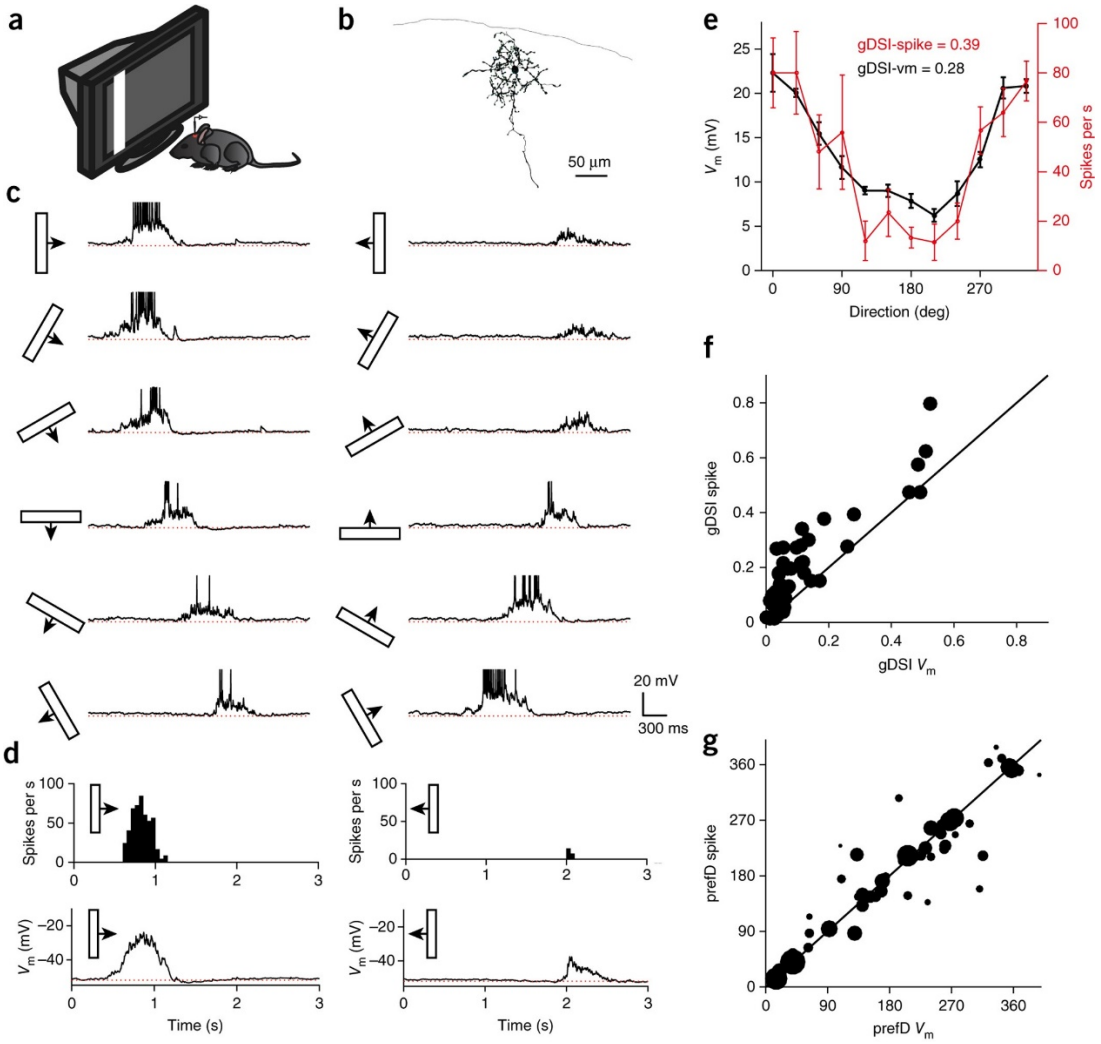

Figure 4.1: Membrane potential responses of SGS neurons to sweeping bars. (A) A schematic of the experimental setup. **(B)** Morphology of an example SGS neuron. **(C)** Membrane potential (V_m) traces from the neuron in b in response to sweeping bars. The movement direction is diagramed by the bar and arrow to the left of each trace. Action potentials are truncated at −10 mV to better reveal visually evoked V_m responses. The red dotted lines indicate the resting membrane potential of −53 mV. **(D)** Mean spike and V_m responses of the neuron in b to bars moving along its preferred (left column) and opposite (right) directions. Peristimulus spike time histograms (top) and trial-averaged V_m traces (bottom) are shown. The red dotted lines indicate the resting V_m. **(E)** Direction tuning curves of the neuron in b for peak V_m (black, left axis) and spike rate (red, right axis). Note that the V_m tuning curve is slightly above the spike tuning curve around the nonpreferred directions. Data are presented as mean ± s.e.m.; n = 5, 5, 5, 5, 5, 6, 6, 7, 6, 6, 5 and 6 trials for the 12 directions, respectively. **(F)** Scatter plot of gDSI-spike versus gDSI-V_m (n = 52 cells). Most cells have gDSI-spike values greater than their gDSI-V_m, but some have nearly identical values (i.e., on the marked identity line). **(G)** Scatter plot of the preferred direction

Figure 4.1 (cont.) (prefD) for spike versus that for V_m responses. The diameter of each dot is scaled to the gDSI-spike of that cell. The solid line is the line of identity. Note that the preferred directions are similar for spike and V_m responses, especially for highly selective cells.

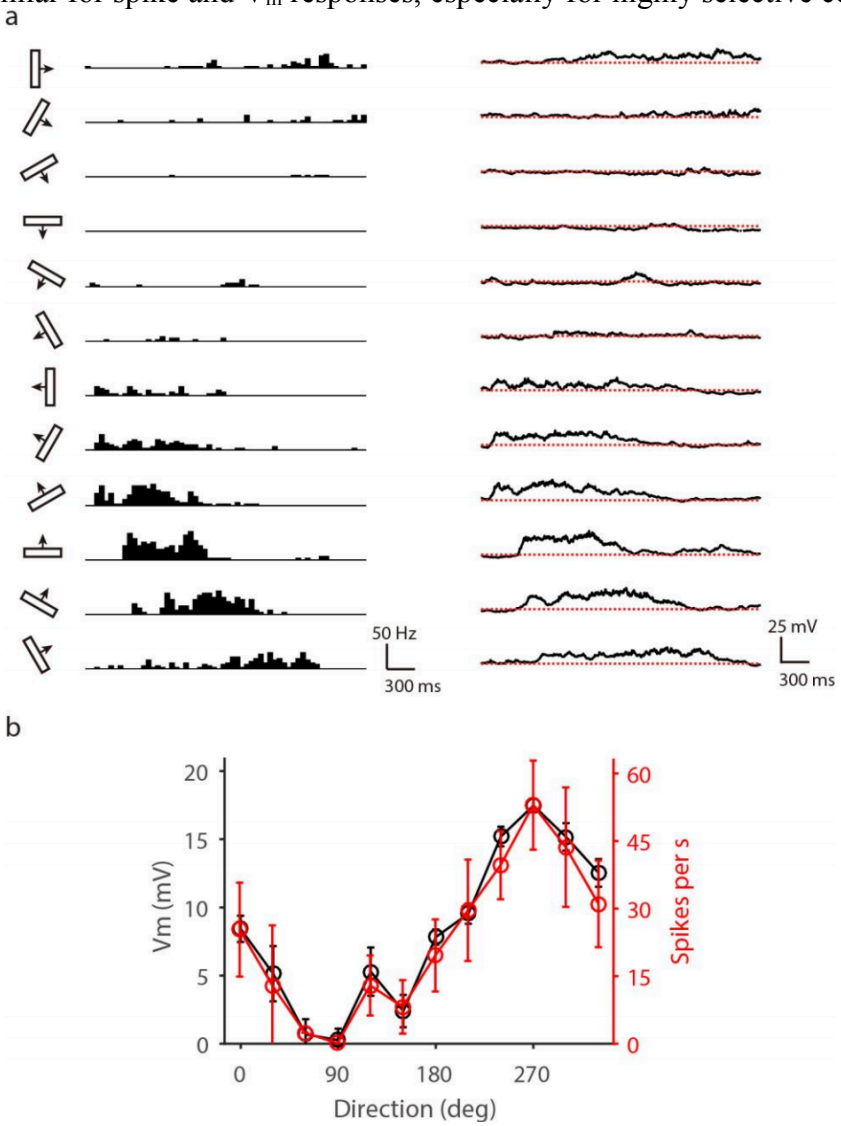

Figure 4.2: Spike and Vm responses of an example SGS neuron to sweeping bars of different directions. (A) Peri-stimulus spike time histograms (left) and trial-averaged Vm (right) of an example SGS neuron in response to sweeping bars of 12 directions. The red dotted lines indicate the resting membrane potential of -55 mV. **(B)** The direction tuning curves for peak Vm (black, left axis) and spike rate (red, right axis) of the same neuron. Note that the two tuning curves are nearly identical. Data are presented as mean ± s.e.m., and n = 7, 6, 7, 6, 6, 7, 5, 6, 7, 6, 5, 7 trials for the 12 directions, respectively.

4.3.2 SGS direction selectivity originates from individually tuned retinal input

SGS neurons receive several sources of synaptic inputs, including both excitation and inhibition. To isolate the excitatory inputs, we next performed whole-cell voltage-clamp recording. These experiments were done in transgenic mice that expressed channelrhodopsin-2 (ChR2) in GABAergic inhibitory neurons. By illuminating the exposed SC with a blue LED (light-emitting diode), we were able to photoactivate local inhibitory neurons and suppress excitatory neurons in the SGS (**Fig. 4.3**). This allowed us to achieve three goals. First, we could identify whether the recorded cells were excitatory or inhibitory by their responses to LED photoactivation (**Fig. 4.4**). Second, we were able to determine the reversal potential of inhibitory currents in the recorded excitatory neurons individually (**Fig. 4.4**). As expected from the fact that the same internal solution was used in all recordings, the inhibitory reversal potential was very consistent across cells (−64.92 ± 0.21 mV, n = 43 cells; **Fig. 4.4**). We thus used the same holding potential (−65 mV) for voltage clamp of inhibitory neurons, even though the reversal potential could not be determined directly in these cells because of ChR2 activation. Finally, optogenetic activation of local inhibitory neurons in these mice could silence excitatory neurons in the SGS and remove local excitatory interactions, thereby exposing the retinal input to the recorded cells (**Fig. 4.3**). This allowed us to analyze and compare the selectivity of retinal and total excitatory inputs to each SGS neuron individually.

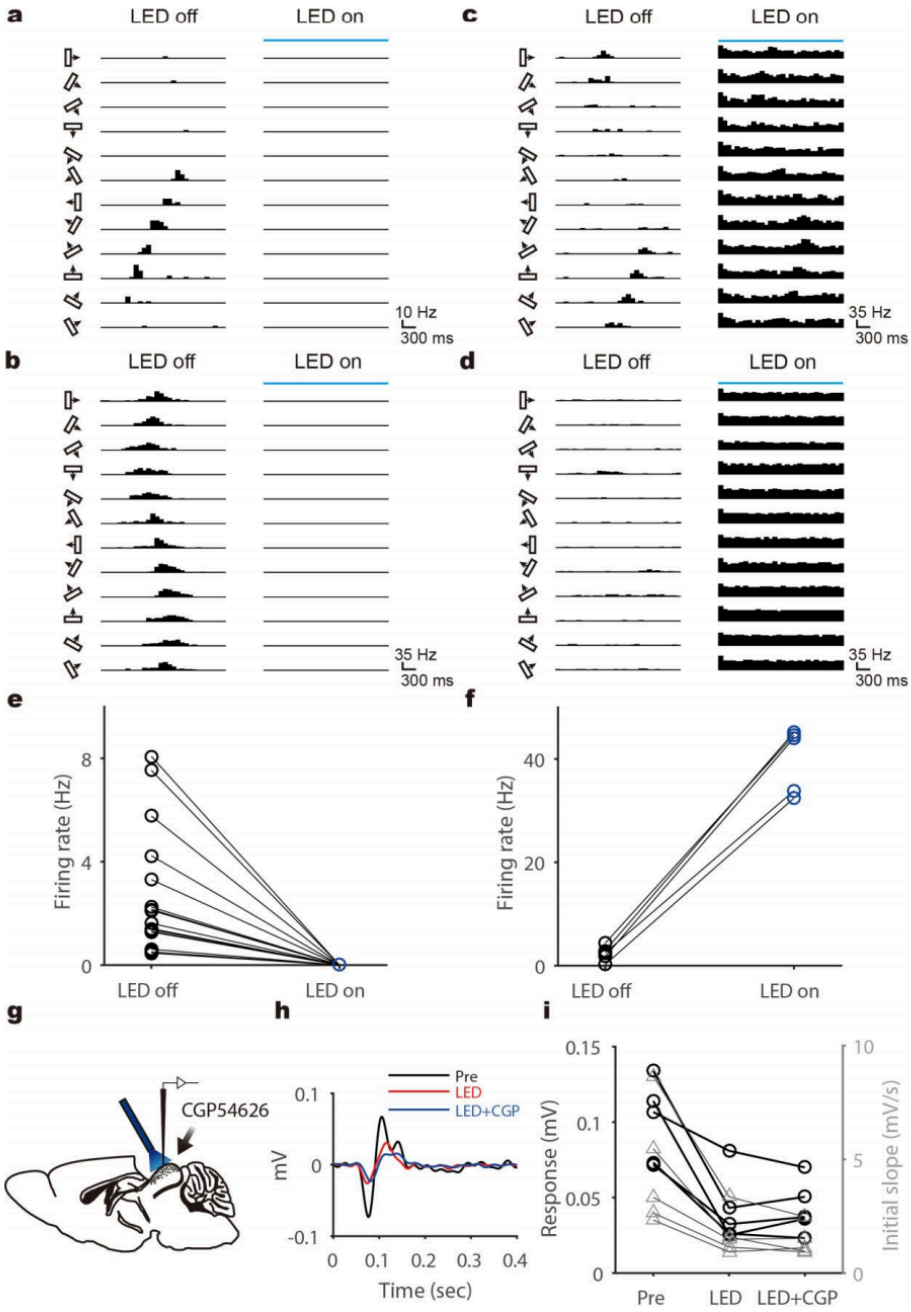

Figure 4.3: Blue LED light effectively silenced excitatory SGS neurons.
(A-B) Peri-stimulus spike time histograms (PSTHs) of two example excitatory SGS neurons in response to sweeping bars of different directions in the absence (left) or presence (right) of LED illumination. There was no spike response to bars of any moving directions under LED. **(C-D)** PSTHs of two example inhibitory neurons in response to sweeping bars of different directions in the absence (left) or presence (right) of LED. Note that LED illumination evoked sustained firing in these cells. **(E-F)** Mean firing rates without and with LED illumination for excitatory (n = 16) and inhibitory (n = 5) SGS neurons. The mean firing rates were calculated for the 3-sec stimulation period for each of the 12 conditions, and the maximum value under LED-off was used to compare with the value of the same stimulus condition under LED-on for each cell. **(G)** A schematic of experimental setup to examine whether optogenetic activation of GABAergic neurons could affect

Figure 4.3 (cont.) retinal transmission by potentially acting presynaptically through GABAB receptors. Visually-evoked local field potentials (LFP) were recorded in the SGS before and 15-45 minutes after administration of the GABAB receptor antagonist CGP54626 (10 μM) to the SC surface. **(H)** An example of LFP responses to a 20° diameter circle flashing on and off. Responses are the average across 40–60 trials. Time zero represents the onset of each flashing on or off. **(I)** Average LFP N1 response (the first large negative waveform) amplitudes (black) and initial slopes (gray) during no LED illumination (Pre), LED illumination (LED) and LED with CGP54626 administration (LED+CGP). The initial slope is the average slope of all points from the response onset to the 30% of the N1 peak amplitude. CGP54626 did not affect the average response (LED: 0.04 ± 0.01; LED+CGP: 0.04 ± 0.01; p = 0.81, W = 3, Wilcoxon test, 5 mice) nor the initial slope (1.70 ± 0.43; LED+CGP: 1.40 ±0.29; p = 0.31, W = 9, Wilcoxon test, 5 mice) when the SC was silenced by LED photoactivation of GABAergic neurons.

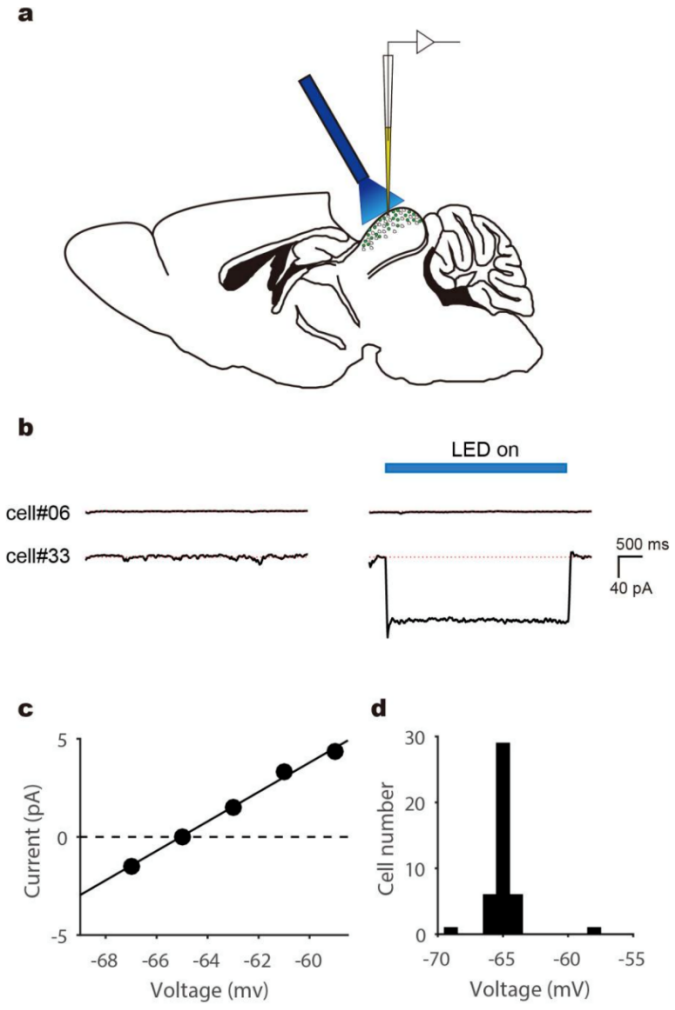

Figure 4.4: In vivo whole-cell voltage-clamp recording and optogenetic photostimulation. **(A)** A schematic of experimental setup. **(B)** Trial-averaged current (I_m) traces of example excitatory (cell #06) and inhibitory (cell #33) cells in response to blue LED illumination. Recordings were done in Gad2-Cre X floxed ChR2 transgenic mice, and the holding potential was -65 mV. Note that LED illumination induced a large sustained ChR2 current in the inhibitory cell, and no change in the excitatory cell. The red dotted lines indicate the mean I_m in the absence of

Figure 4.4 (cont.) LED illumination. **(C)** Mean I_m caused by LED activation versus holding potential of an example excitatory SGS neuron. The reversal potential of inhibition was determined by adjusting the holding potential to minimize the amplitude of the inhibitory postsynaptic current evoked by photostimulation of Gad2+ neurons. The solid line indicates the linear regression (R^2 = 0.99, $F_{1,3}$ = 410.6, $p < 0.001$, linear regression; $r = 0.996$, $p < 0.001$, Pearson correlation).which crosses the zero-current line at the voltage of -65.08 mV, i.e., the reversal potential of inhibitory currents for this cell. **(D)** Distribution of the reversal potential determined in excitatory cells (n = 43).

We first analyzed the total EPSCs in the absence of LED photoactivation. Consistent with the above observation of highly tuned V_m responses, the visually evoked total EPSCs in many SGS neurons, including both excitatory and inhibitory neurons, were DS (for example, **Fig. 4.5A-B** and **Fig. 4.6**). In fact, the gDSI distributions of visually evoked peak excitation (gDSI of EPSC (gDSI-EPSC) = 0.13 ± 0.01, n = 87) and V_m responses (gDSI-V_m = 0.12 ± 0.02, n = 52) were very similar (**Fig. 4.5D**). Furthermore, we recorded both V_m and EPSC responses in a small number of cells (n = 23) and found that their gDSI values were nearly identical (**Fig. 4.5E**). Specifically, for cells that were highly selective in their V_m (gDSI-$V_m \geq 0.1$; **Fig. 4.5E**), all of them (n = 7 of 7) received selective EPSCs (gDSI-EPSC ≥ 0.1). Conversely, all of the cells whose gDSI-$V_m < 0.1$ had gDSI-EPSC < 0.1 (n = 16 of 16). In other words, the excitatory input that individual SGS neurons received was a deciding factor in their degree of direction selectivity. Similarly, the preferred direction of the V_m was also determined by the EPSC (**Fig. 4.5F**). These results thus suggest that local inhibition in the SGS did not generate direction selectivity *de novo* from nonselective excitatory input.

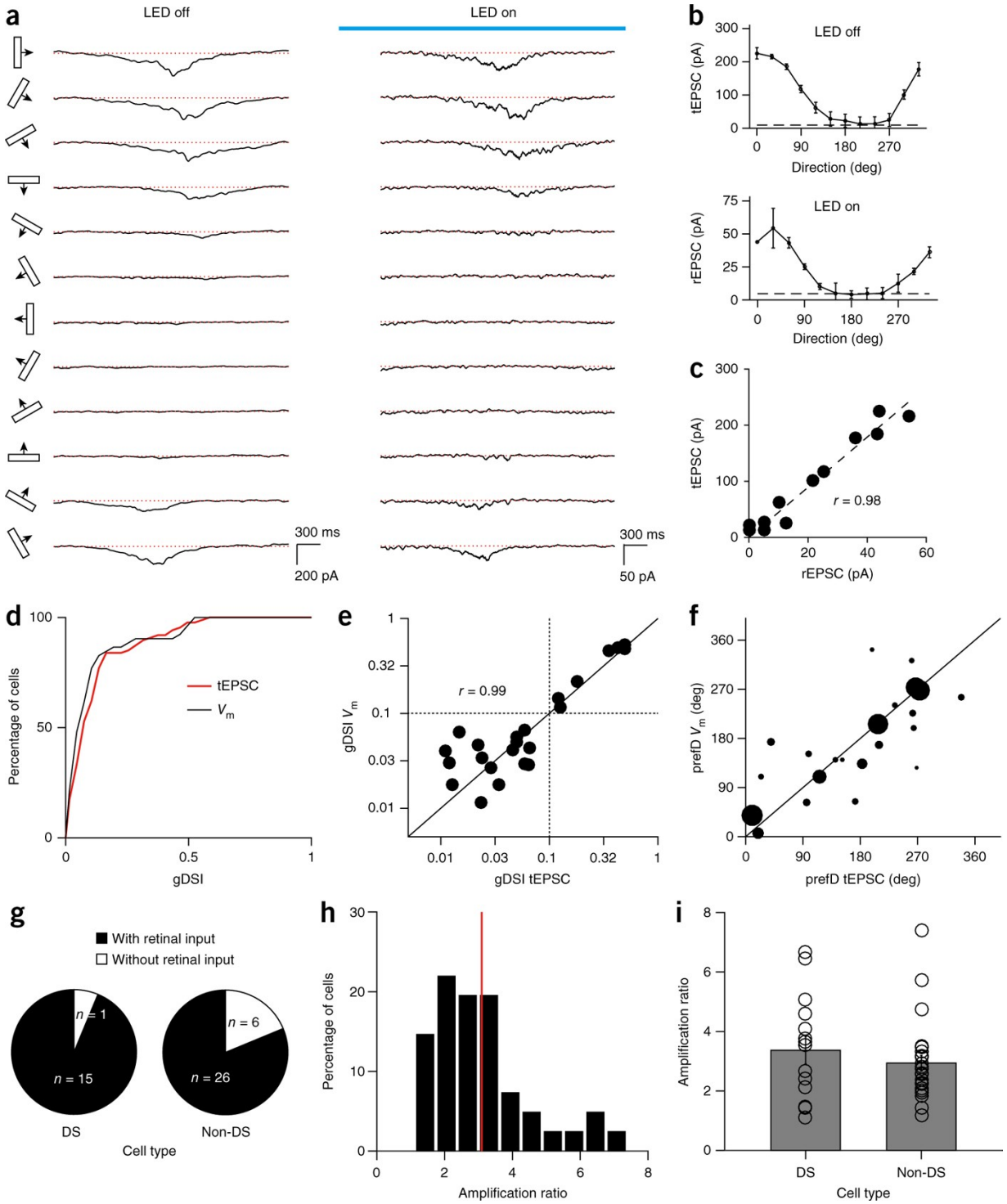

Figure 4.5: Voltage-clamp recording and optogenetic silencing to isolate retinal excitation to SGS neurons. (A) Trial-averaged EPSC traces of an example SGS neuron to bars moving along 12 directions in the absence (left panel) or presence (right) of LED illumination (as indicated by the blue bar). The red dotted lines indicate the mean current level in the absence of visual stimulus. **(B)** Direction tuning curves of total EPSC (tEPSC, top) and retinal input (rEPSC, bottom) for the cell in a. The dashed lines indicate 3 standard deviations (s.d.) above the mean current level as determined in the absence of visual stimulus. Data are presented as mean ± s.e.m.; n = 8, 7, 7, 7,

Figure 4.5 (cont.) 6, 7, 7, 7, 7, 7, 6 and 6 trials in the top panel and n = 3 for all directions in the bottom panel. **(C)** Scatter plot of tEPSC versus rEPSC for the cell in a. Peak rEPSC and tEPSC amplitudes are plotted for the responses to 12 directions of bars. The dashed line is the linear regression of the data points ($R^2 = 0.95$, $F_{1,10} = 192.7$, $P < 0.001$, linear regression; $r = 0.98$, $P < 0.001$, Pearson correlation). **(D)** Cumulative distributions of gDSI for tEPSC (n = 87 cells from 58 mice, red) and for V_m (n = 52 cells from 41 mice, black), indicating that tEPSC and V_m have nearly identical gDSI distributions (P = 0.30, K-S statistic = 0.17, Kolmogorov-Smirnov test). **(E)** Scatter plot of gDSI values for tEPSC and V_m in the same cells (n = 23 cells from 21 mice). They are well correlated ($r = 0.99$, $P < 0.001$, Pearson correlation) and similar in values (P = 0.18, W = 90, Wilcoxon signed-rank test). Note that the plot is shown in log–log axis to better illustrate the cells with low gDSI. The dotted lines indicate gDSI levels of 0.1. **(F)** Scatter plot of the preferred direction (prefD) for V_m versus tEPSC. The diameter of each dot is scaled to the gDSI-V_m of that cell. Note that the preferred directions are similar for tEPSC and V_m responses, especially for highly selective cells. The solid lines in both e and f are the lines of identity. **(G)** Percentage of cells that receive direct retinal input in DS (n = 15 of 16) and non-DS (n = 26 of 32) SGS neurons. **(H)** Distribution of amplification ratios of all cells that receive direct retinal inputs (n = 41). The red line indicates the mean of the distribution. **(I)** Similar amplification ratio between DS (3.37 ± 0.46, n = 15 cells from 13 mice) and non-DS (2.94 ± 0.26, n = 26 cells from 20 mice) SGS neurons (P = 0.41, U = 164, Mann-Whitney U-test). Data are presented as mean ± s.e.m.

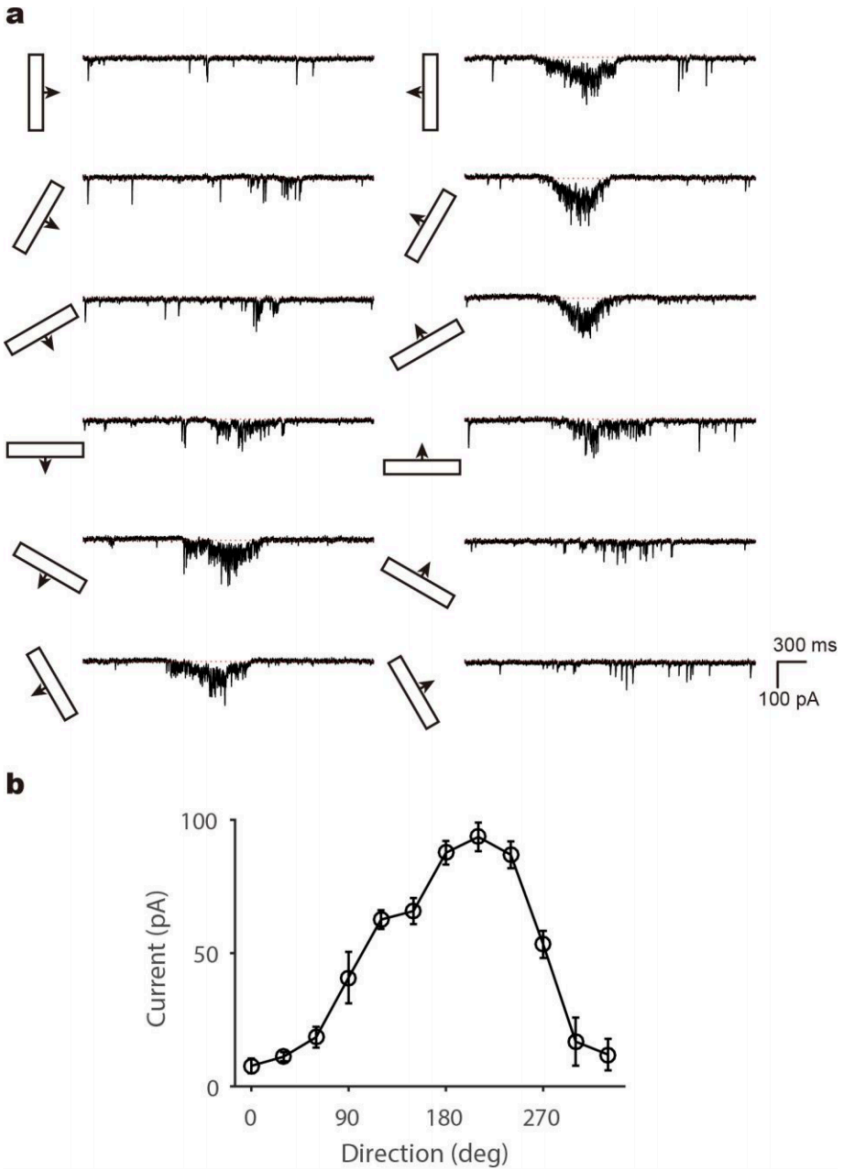

Figure 4.6: Excitatory postsynaptic currents in response to sweeping bars.
(A) Raw traces of excitatory postsynaptic currents (EPSCs) of an example SGS neuron in response to sweeping bars of different directions. Red dotted lines indicate the mean current level in the absence of visual stimulus. **(B)** Direction tuning curve for the peak amplitude of the filtered and trial-averaged EPSCs. Note that the peak EPSC at the non-preferred direction is nearly zero in this cell, indicating a lack of excitatory inputs. Data are presented as mean ± s.e.m., and n = 7, 7, 6, 6, 8, 6, 7, 6, 6, 6, 6, 7 trials for the 12 directions, respectively.

Most SGS neurons still showed visually evoked excitation upon optogenetic silencing of local excitatory neurons (n = 41 of 48, 85.4%), including both excitatory and inhibitory neurons (**Fig. 4.11**), indicating that they received direct retinal inputs. In particular, a slightly larger portion of

the DS cells (n = 15 of 16, 93.8%) were directly innervated by the retina than non-DS cells (n = 26 of 32, 81.3%; **Fig. 4.5G**). When comparing the peak amplitudes of total and retinal EPSCs in the same cells (tEPSCs and rEPSCs, respectively), we found that the retinal inputs were amplified by intracollicular circuits in a largely linear fashion (for example, **Fig. 4.5C**), similarly to the transformation of inputs from thalamus to visual cortex (Li et al., 2013; Lien & Scanziani, 2013). The amplification ratio ranged from 1.11 to 7.39, with a mean of 3.09 ± 0.24 (n = 41; **Fig. 4.5H-I**). Consistent with the largely linear amplification (**Fig. 4.9**), rEPSCs and tEPSCs of the same cells were similarly tuned in their peak response amplitudes (for example, **Fig. 4.5A-B**). Indeed, the gDSI values and preferred directions were well correlated between rEPSCs and tEPSCs, and this was the case for both excitatory and inhibitory neurons (**Fig. 4.8A-C**). In other words, the DS SGS cells, i.e., cells that have high gDSI values for their tEPSC and resulting V_m, receive similarly tuned retinal excitation. Furthermore, the intracollicular excitatory inputs, determined as the difference between tEPSC and rEPSC (**Fig. 4.12**), displayed selectivities largely similar to those of the retinal inputs (**Fig. 4.8D-F**). These analyses thus indicate that the direction selectivity of SGS neurons was determined by their retinal inputs, which were further amplified by similarly tuned intracollicular inputs to maintain the directional preference and level of selectivity.

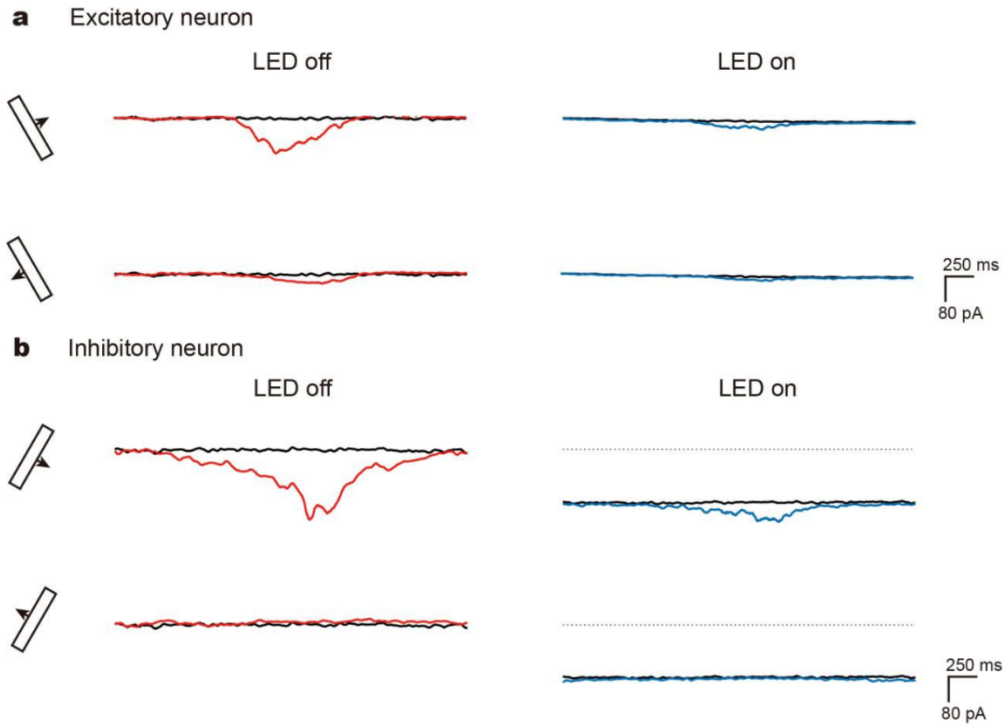

Figure 4.7: Isolating SGS neurons' retinal inputs. (A) Trial-averaged current (I_m) traces of an example excitatory cell to sweeping bars at its preferred (top) and opposite (bottom) directions, in the absence (left, red traces) or presence of LED illumination (right, blue traces). Black lines are the I_m traces in the absence of visual stimulation. **(B)** Trial-averaged I_m traces of an example inhibitory cell of the same conditions. The black dotted line indicates the baseline I_m level in the absence of LED photoactivation. For both excitatory and inhibitory cells, the I_m under the condition without visual stimulus as indicated by the corresponding black lines was used as the baseline for calculating total and retinal EPSCs.

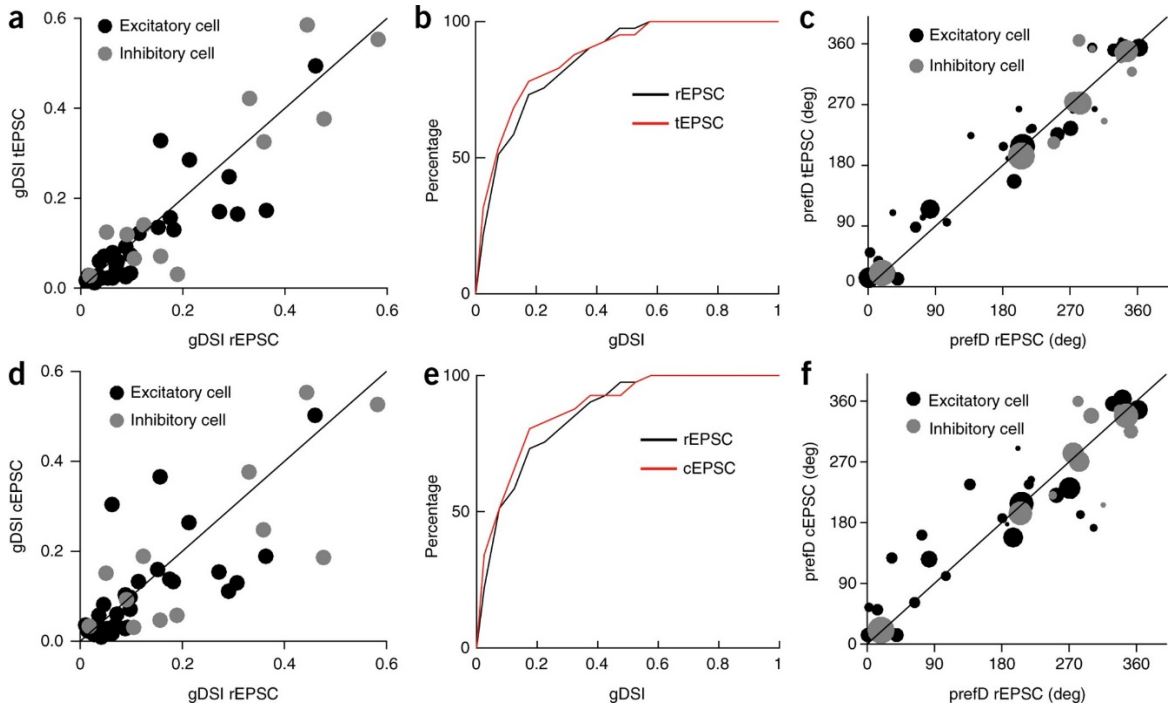

Figure 4.8: Retinal excitation and total excitation are similarly tuned in SGS neurons. (A) Scatter plot of gDSI of peak tEPSC versus that of peak rEPSC, indicating their gDSI values were well correlated (n = 41 cells from 28 mice, r = 0.89, P < 0.001, Pearson correlation). The gDSI values for tEPSCs and rEPSC were similar in cells that receive DS excitation (i.e., cells whose gDSI-tEPSC or gDSI-rEPSC ≥ 0.1, n = 22 of 41 cells, P = 0.34, W = 61, Wilcoxon signed-rank test). **(B)** Cumulative distribution of data shown in A. **(C)** The preferred direction (prefD) of the peak tEPSC versus that of peak rEPSC. The diameter of each dot is scaled to the gDSI of that cell's tEPSC. **(D-F)** As in A-C, but comparing collicular EPSC (cEPSC) versus rEPSC. In D, n = 41 cells from 28 mice, r = 0.77, P < 0.001, Pearson correlation; n = 23 cells whose gDSI-cEPSC or gDSI-rEPSC ≥ 0.1, P = 0.30, W = 70, Wilcoxon signed-rank test. In F, the diameter of each dot is scaled to the gDSI of that cell's peak rEPSC. The solid lines in A, C, D and F are the lines of identity.

The selective retinal inputs could result from summing inputs that are individually tuned, such as from DSGCs (**Fig. 4.10A-B**). Alternatively, individual retinal inputs may not be DS, but their integration in the postsynaptic neuron could take place in a precise spatiotemporal manner to generate larger EPSC peaks at the preferred direction than at the opposite direction. For example, a difference in response latency between the non-DS retinal inputs could cause them to arrive at the postsynaptic cell synchronously in response to the preferred direction but asynchronously to the opposite direction, thus resulting in different peak amplitudes (**Fig. 4.10C**), as proposed

originally by Reichardt for motion detection. In this latter scenario, the total charge of the retinal EPSCs would be much less selective than their peaks or even entirely non-tuned, which would be analogous to the emergence of orientation selectivity in the visual cortex (Lien & Scanziani, 2013). To determine which of the two scenarios is true for the retinocollicular transformation of direction selectivity, we calculated the integral of rEPSCs during responses evoked by the moving bars and compared its direction selectivity to that of the peak rEPSC. The integral of retinal input was in fact similarly selective or even more selective in a few cells, compared to the peak rEPSC (**Fig. 4.10D-E** and **Fig. 4.13**), ruling out the aforementioned second scenario. The averaged tuning curves of peak rEPSC and integral rEPSC were very similar, nearly identical to that of total EPSC (**Fig. 4.10F**), confirming that SC direction selectivity originates from individually tuned retinal inputs. Finally, the same integral-versus-peak analysis showed that the intracollicular excitatory inputs also followed the first scenario (**Fig. 4.12**), indicating that DS SGS neurons were preferentially connected with other collicular neurons that prefer similar directions.

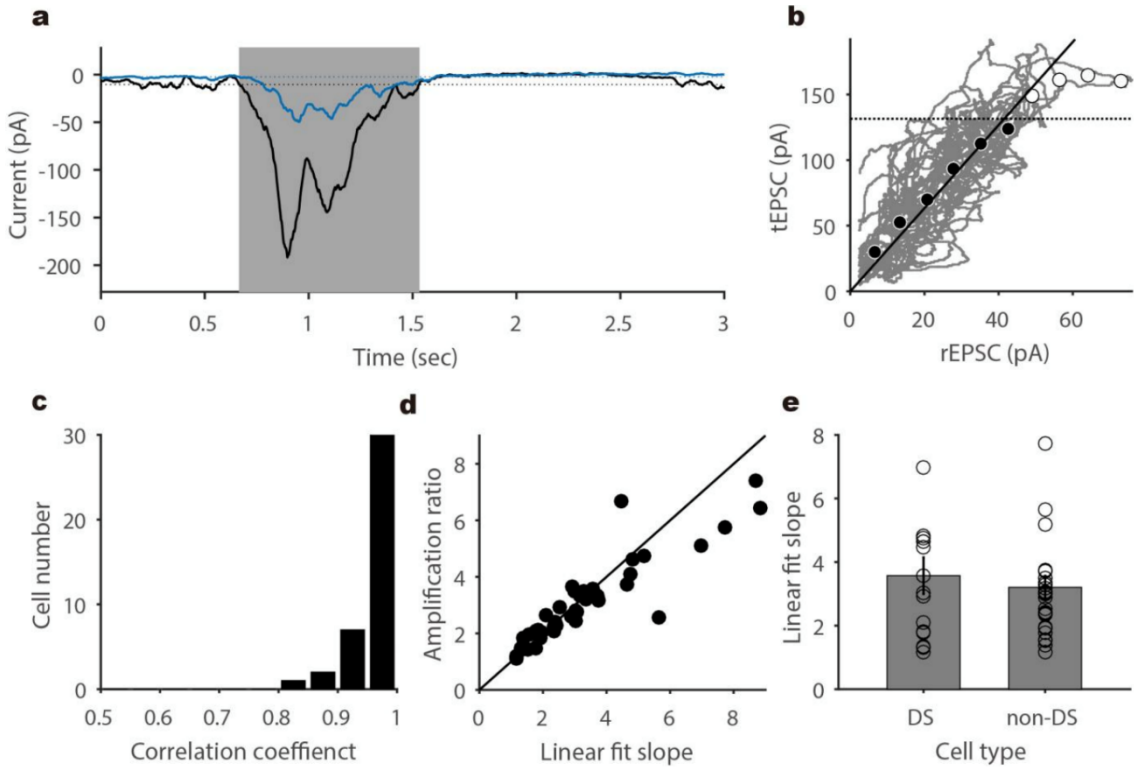

Figure 4.9: Amplification of retinal excitation by intracollicular circuits. (A) Trial-averaged traces of total EPSC (black line, tEPSC) and retinal EPSC (blue line, rEPSC) of an example SGS neuron in response to a moving bar. Gray shade indicates the time window for calculation, which is defined as the duration in which both rEPSC and tEPSC were below their respective "cutoff" (blue dotted line for rEPSC and black for tEPSC). The cutoff was determined as two standard deviations below the baseline, which was the condition when a blank visual stimulus (gray screen) was shown instead of bars. **(B)** Retinal-total EPSC transformation for this cell. Plotted are the corresponding rEPSC and tEPSC at each time point in the response
window for all 12 stimulus directions. The black and white dots are the mean values in 10 evenly-divided bins from 0 to the maximum rEPSC. Black dotted line indicates 80% of the maximum bin-averaged tEPSC. The black solid line is the linear regression of the bin averaged points that are below the 80% line (R^2 = 0.99, F1,4 = 369.4, $p < 0.001$, linear regression; r = 0.99, $p < 0.001$, Pearson correlation). The bin-averaged points above the 80% line were not included in the linear regression analysis due to possible saturation of tEPSC responses. **(C)** Distribution of correlation coefficient of linear regression between rEPSC and tEPSC (n = 41 cells). **(D)** Amplification ratio (the one shown in **Fig. 4.3**), calculated as the ratio of peak tEPSC over peak rEPSC, each averaged over 12 stimulus directions, versus the linear regression slope as calculated in b (n = 41). The two methods gave similar results for the recorded cells. Note that some points are below the identity line possibly due to saturation of tEPSC responses in those cells. e, Similar slopes between DS (3.57 ± 0.58, n = 15 cells from 13 mice) and non-DS (3.21 ± 0.36, n = 26 cells from 20 mice) SGS neurons (p = 0.84, U =187, Mann-Whitney U test).

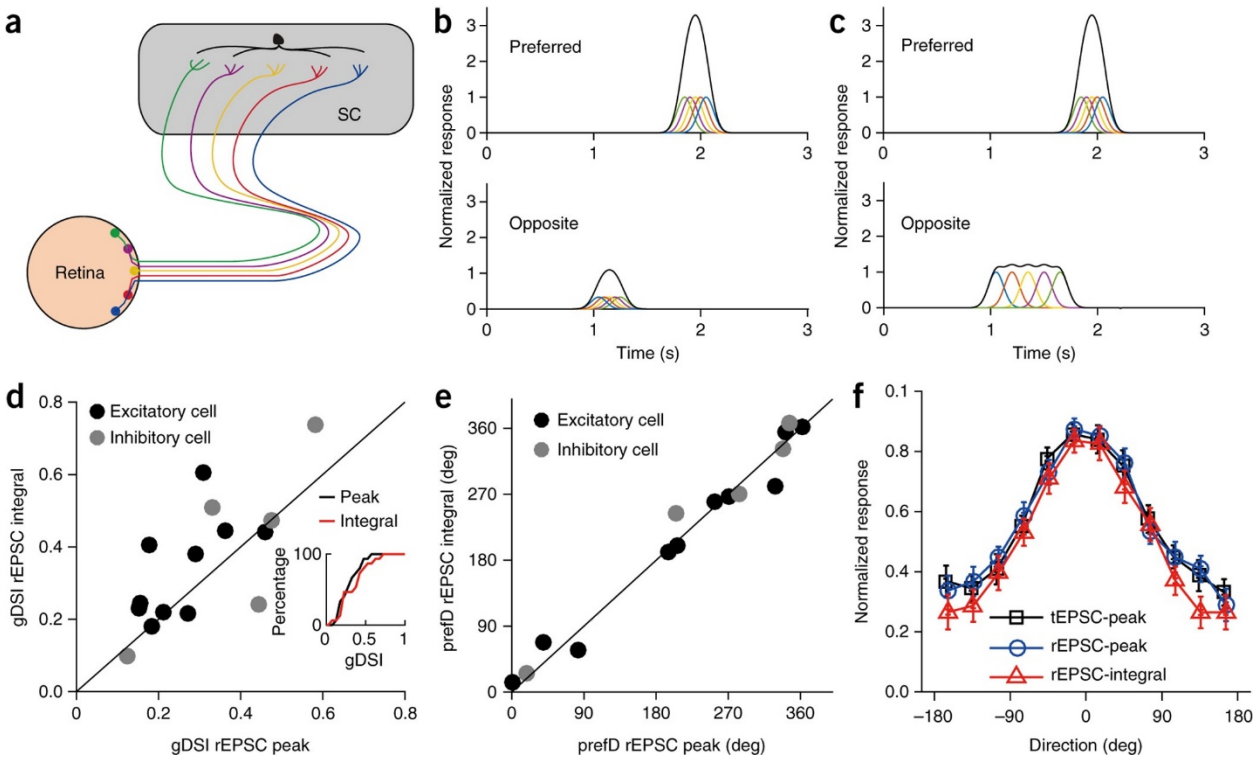

Figure 4.10: SGS direction selectivity originates from individually tuned retinal inputs. (A–C) Two different scenarios in which retinal inputs could give rise to direction selectivity in the SGS. **(B)** In one scenario, individual retinal inputs, as indicated by traces of different colors, are selective for similar directions, thus resulting in larger excitation to the preferred (top) than to the opposite direction (bottom). **(C)** In the other scenario, individual retinal inputs respond with similar amplitudes to all directions. These non-DS retinal inputs arrive at the postsynaptic cell synchronously in response to the preferred direction (top) and asynchronously to the opposite direction (bottom), thus resulting in different peak amplitudes. In this scenario, the total charge of rEPSC would be much less selective than their peaks. **(D)** gDSI of rEPSC integral and peak were correlated ($r = 0.71$, $P = 0.003$, Pearson correlation) and similar for individual DS neurons ($P = 0.11$, $W = 58$, Wilcoxon signed-rank test, $n = 15$ cells from 13 mice), supporting the scenario shown in b. Inset shows the cumulative distribution of the two. **(E)** The integral and peak of retinal EPSCs prefer similar directions in DS SGS neurons. The solid lines in d and e are the lines of identity. **(F)** Averaged tuning curves for tEPSC peaks (black), rEPSC peaks (blue) and rEPSC integrals (red) in DS SGS neurons ($n = 15$ cells from 13 mice). Individual curves were normalized by their maximum responses and aligned to their preferred directions. They were then averaged for plotting. Error bars represent s.e.m.

4.3.3 Genetic disruption of retinal direction selectivity reduces selectivity in the SGS

Our *in vivo* whole-cell experiments support the conclusion that the direction selectivity of SGS neurons originates from converging inputs of similarly tuned DSGCs. If this is indeed the case, a reduction of retinal direction selectivity would compromise the selectivity in the SGS. We next

tested this prediction using genetic manipulation. GABAergic inhibition provided by starburst amacrine cells is a critical factor in generating direction selectivity in the retina (Vaney et al., 2012; Wei & Feller, 2011), and it can be eliminated by knocking out (KO) the vesicular GABA transporter (*Vgat*) gene *Slc32a1* from these cells by crossing *loxP*-flanked *Slc32a1* (*Slc32a1*$^{flox/flox}$ or *Vgat*$^{flox/flox}$) with choline acetyltransferase *(ChAT)-IRES-Cre* mice (Pei et al., 2015). We then performed two-photon calcium imaging in the ganglion cell layer of these KO mice using the genetically encoded calcium indicator GCaMP6s (T. W. Chen et al., 2013). In particular, we focused on the On-Off DSGCs because they are the ones that primarily project to the SGS (Dhande & Huberman, 2014). In wild-type (WT) littermate controls, 9.3% of cells in the ganglion cell layer were On-Off DSGCs (**Fig. 4.11A-C**; n = 60 of 648 cells from 9 mice), consistent with previous studies (Baden et al., 2016; Sanes & Masland, 2015). In contrast, in KO mice, the percentage of cells that displayed On-Off DS responses was significantly reduced (**Fig. 4.11C**; n = 19 of 566 cells, 3.4%, from 14 mice; $P < 0.001$, χ^2 test). Because cholinergic inputs to the SC terminate in the intermediate and deep layers and do not co-release GABA, these ChAT-Vgat KO mice provided us with a unique opportunity to study the effect of altered retinal direction selectivity on the visual response properties of superficial SC neurons.

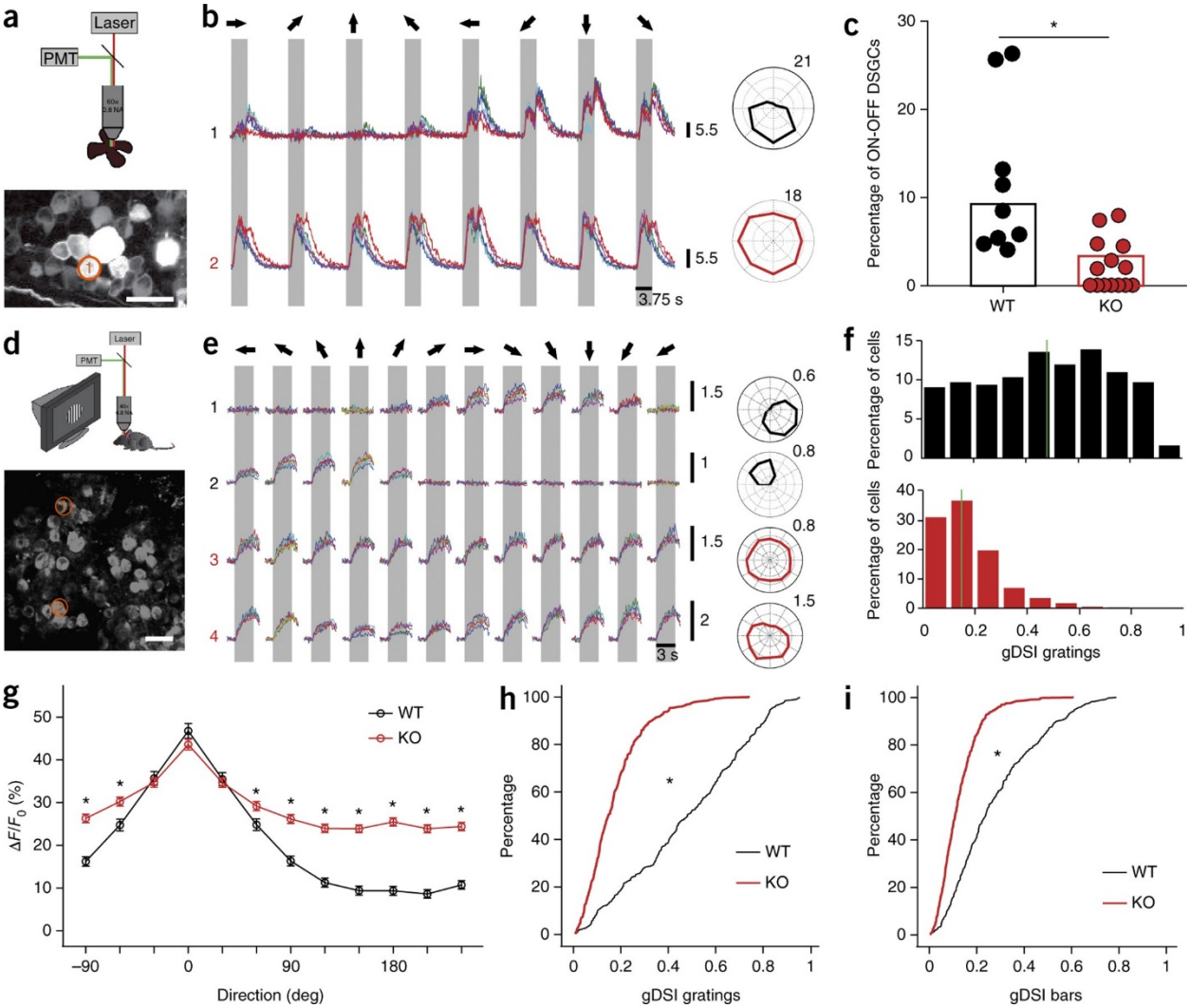

Figure 4.11: Genetic disruption of retinal direction selectivity reduces selectivity in the SGS. **(A)** A schematic of two-photon calcium imaging of retina (top). The bottom panel shows a max-intensity projection of GCaMP6 fluorescence in an example field of view. Scale bar, 25 μm. **(B)** Top (trace 1): Ca2+ signals of the RGC circled in a to the presentation of moving bars in eight directions (different colors represent separate trials). The gray shade corresponds to the time interval in which the bar stimulus sweeps across the field of view and the arrows represent the directions of movement in relation to the polar plots on the right. This cell showed DS responses to both leading and trailing edges of the moving bars, indicating that it was an On-Off DSGC. Bottom (trace 2): an On-Off cell from a *Vgat* conditional KO mouse. Corresponding polar plots are shown to the right. **(C)** Summary plot showing the percentages of On-Off DSGCs in WT (black, n = 60 of 648 cells from 9 mice) and KO (red, n = 19 of 566 cells from 14 mice) retinas ($P < 0.001$, $\chi^2 = 17.3$, χ^2 test). Data points represent percentages of On-Off DSGCs in individual mice. **(D)** A schematic of two-photon imaging of the SGS (top) and an example field of view from a WT (bottom). Scale bar, 20 μm. **(E)** Ca^{2+} signals of the two neurons (1 and 2) circled in d and of two neurons from a Vgat KO (3 and 4), in response to drifting gratings. The gray boxes mark the duration of stimulation. The movement directions of the bar are represented by arrows on top. Corresponding polar plots are shown to the right. **(F)** gDSI distribution of WT (top, black) and KO (bottom, red) cells to drifting gratings. The solid green lines indicate the medians of distributions.

Figure 4.11 (cont.) (G) Average WT (black, n = 310 cells from 5 mice) and KO (red, n = 407 from 8 mice) tuning curves to gratings after aligning each cell's preferred direction at 0. Data are presented as mean ± s.e.m. *P < 0.001, Mann-Whitney U-test. **(H)** Cumulative distribution of the data shown in f (P < 0.001, K-S statistic = 0.61, Kolmogorov-Smirnov test). **(I)** Cumulative distribution of gDSI to sweeping bars (P < 0.001, K-S statistic = 0.43, Kolmogorov-Smirnov test). Scale bars for the Ca^{2+} signals and polar plots in b and e represent the change in fluorescence from baseline ($\Delta F/F_0$).

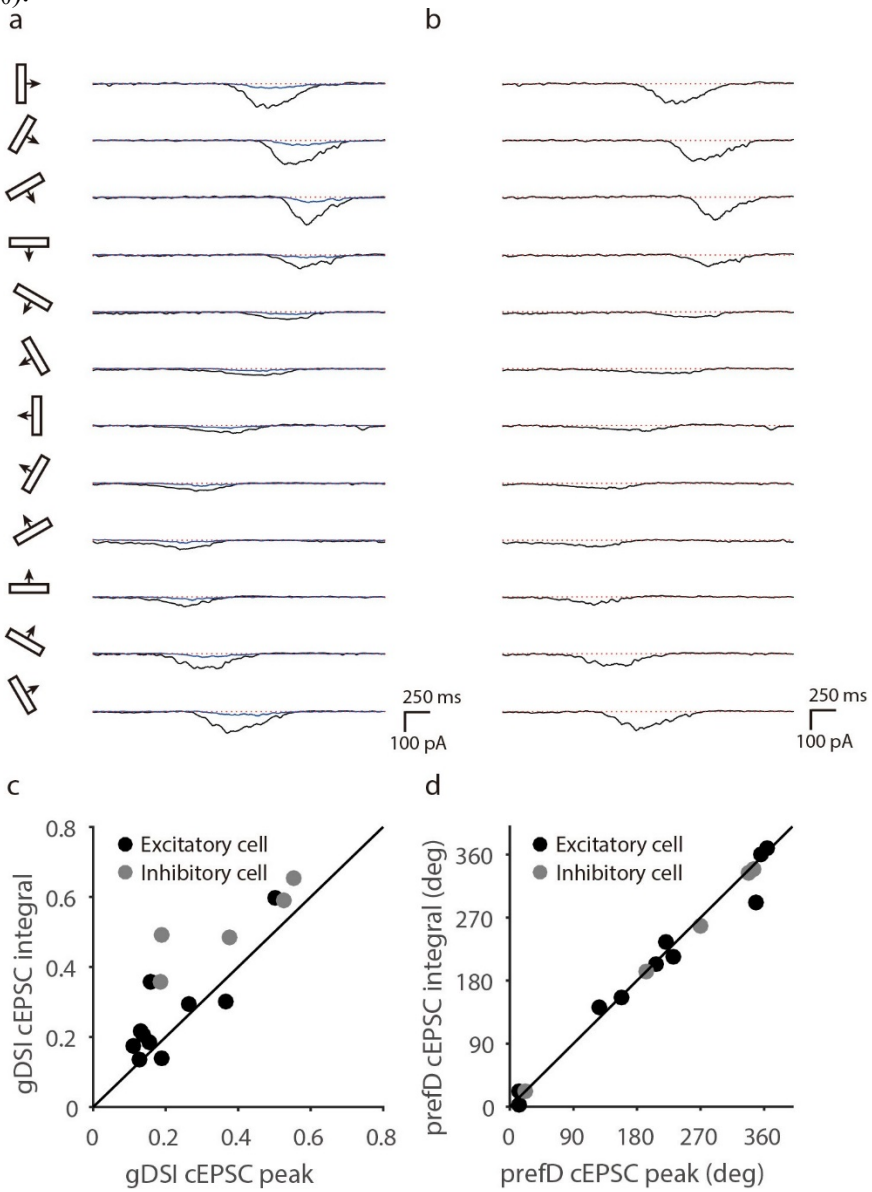

Figure 4.12: Analysis of intracollicular excitation of SGS neurons. (A) Trial-averaged total (left, black traces) and retinal (left, blue traces) EPSCs of an example SGS neuron to sweeping bars of different directions. **(B)** Current traces of intracollicular excitation, calculated by point-by-point subtraction of the two traces in (A). Red dotted lines in (A) and (B) indicate the baseline EPSC level in the absence of visual stimulation. **(C)** gDSI of intracollicular EPSC (cEPSC) integral and peak are correlated for direction selective SGS neurons (r = 0.85, p < 0.001, Pearson correlation; n = 15 cells from 13 mice). The gDSI of cEPSC peak were smaller than that of its

Figure 4.12 (cont.) integral in many cells ($p = 0.003$, $W = 100$, Wilcoxon test), possibly due to its saturation at preferred directions. Importantly, the fact that cEPSC integral is even more selective means it follows the scenario in Figure 4.10b, indicating that the selective intracollicular excitatory input is from individually tuned SGS neurons. (D) The integral and peak of cEPSCs prefer similar directions in DS SGS neurons. The solid lines in both panel c and d are the lines of identity.

We first performed intrinsic imaging and found normal SC retinotopic maps in the KO mice (**Fig. 4.14**). Next, we performed two-photon calcium imaging of the top-most SGS lamina, which we previously showed is enriched with DS neurons that have overlapping On-Off receptive fields (Inayat et al., 2015). The receptive field structures of the imaged cells were largely normal in the KO mice, with subtle increases in subfield size and completely normal On-Off overlaps (**Fig. 4.15**). The small increase in subfield size was consistent with the reduced inhibition in their retina of the KO mice. Also consistent with this was the finding that slightly more cells were responsive in the KO mice. When stimulated with drifting gratings or sweeping bars, 46.5% (310 of 667 cells to gratings) or 47.2% (315 of 667 cells to bars) were responsive in WT littermate controls, compared to 50.0% (407 of 821 cells, to gratings) or 61.5% (505 of 821, to bars) in the KO mice. As expected, the vast majority of the responsive cells in this lamina were DS in WT (**Fig. 4.11D-F**; gDSI ≥ 0.25; n = 235 of 310 cells to gratings, 76%; and 146 of 315 cells to bars, 46%). Preferred motion directions were more widely represented than the four cardinal directions in the retina (**Fig. 4.16**), presumably due to specifically combining inputs of DSGCs that prefer neighboring cardinal directions. Notably, in the KO mice, many fewer cells were DS in this lamina (n = 84 of 407 to gratings, 21%; and 35 of 505 to bars, 7%; **Fig. 4.11F**). The mean and median gDSI values in the KO mice (0.17 ± 0.01 and 0.15 to gratings; 0.13 ± 0.00 and 0.11 to bars) were significantly lower than in the controls (0.48 ± 0.01 and 0.48 to gratings, 0.28 ± 0.01 and 0.24 to bars; **Fig. 4.11H-I**; $P < 0.001$ for both gratings and bars, Kolmogorov–Smirnov test). Notably, this reduction in direction selectivity was caused by increased responses to the nonpreferred directions (**Fig.**

4.11G), consistent with decreased inhibitory inputs onto On-Off DSGCs in the retina. Together, these data demonstrate that disrupting DSGCs' tuning led to reduced selectivity in SGS neurons, thereby confirming the retinal origin of SGS direction selectivity.

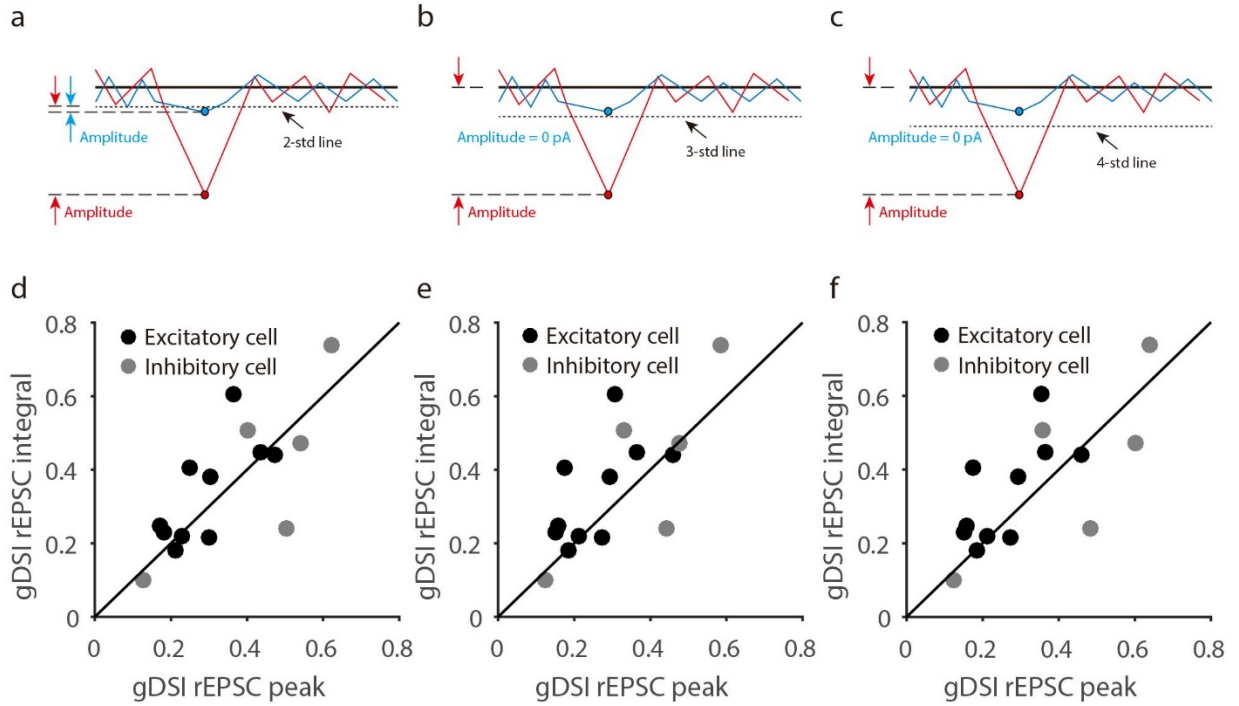

Figure 4.13: Retinal EPSC peak and integral have similar gDSI values, independent of analysis methods. (A-C) Diagrams of the 3 methods used for calculating retinal EPSC peak amplitudes. In each panel, the red trace represents a strong response, e.g., to the preferred direction, and the blue trace represents a weak response. The solid black line is the "baseline", calculated as the mean of the EPSCs to the "blank stimulus" (gray screen). The dotted line is the "cutoff", calculated as 2 (A), 3 (B) or 4 (C) standard deviations away from the baseline. In (A), the EPSC peak is calculated as the amplitude from the cutoff line, i.e., the dotted line. In (B) and (C), the EPSC peak is calculated as the amplitude from the baseline, i.e., the solid black line, but for conditions where the peak EPSC was weaker than the cutoff, the corresponding response magnitude were set as 0. Note that different ways of calculation may result in slight under- or over-estimation of weak responses due to spontaneous synaptic events. (D-F) gDSI of retinal EPSC integral and peak are similar for direction selective SGS neurons (n = 15) with the three calculation methods directly above. The EPSC integral in all panels was calculated for the response window determined as described in Methods. Panel (E) is the same one shown in Figure 4.10. The solid lines in panel d, e and f are the lines of identity.

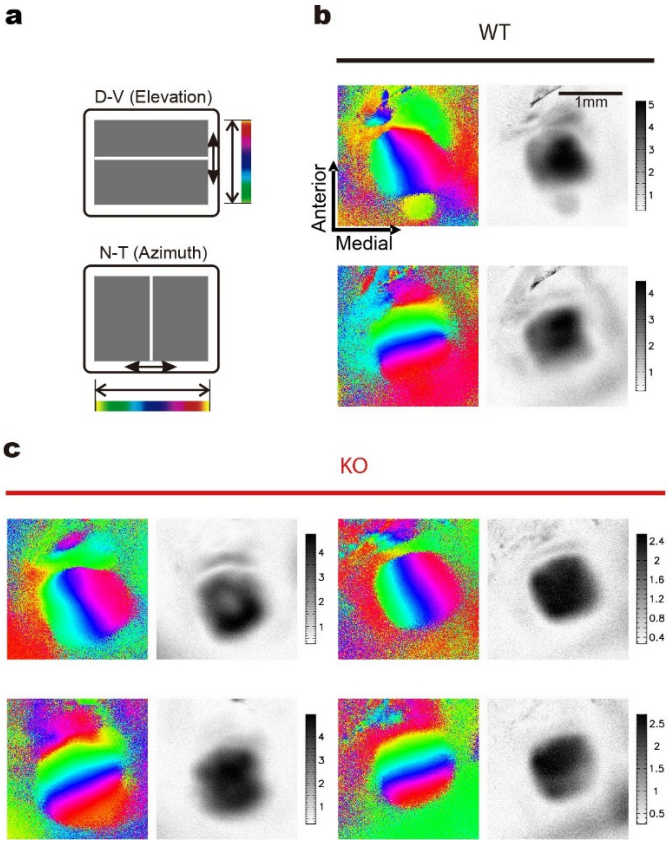

Figure 4.14: Normal retinotopic maps in ChAT-Vgat KO mice. (A) Visual stimulus protocol for generating the elevation (top) and azimuth (bottom) maps in the SC. The color scales represent the position of the moving bar on the stimulus monitor and the corresponding retinotopic locations in the SC. **(B)** (top) Elevation map in a WT mouse. Both retinotopy (left) and response magnitude (right) are shown. The gray scale represents the response amplitude as a fractional change in reflection x 104. (bottom) Azimuth map for the same animal. **(C)** Elevation and azimuth maps from two Vgat KO mice. The panel layout is the same as in (B). D, dorsal; V, ventral; N, nasal; T, temporal. See Cang et al (Journal of Neuroscience, 2008, 28(43):11015-23), for details of intrinsic imaging of retinotopic maps in the SC.

4.4 Discussion

In this study, we both isolated and manipulated the retinal input in order to study its role in generating SGS direction selectivity. The whole-cell recording and optogenetic silencing experiments demonstrate that DS SGS neurons received retinal input that was already selective, generated by precisely converging inputs from similarly tuned DSGCs. The selective retinal input was amplified by intracollicular circuits without changing its preferred direction or level of selectivity. The resulting membrane potential depolarization in the SGS neuron then led to a

slightly more selective spiking response due to the nonlinear effect of thresholding. Consistent with these results, we also found that SGS direction selectivity was reduced in mice with altered retinal selectivity. Our studies thus demonstrate that SGS neurons inherited their direction selectivity from DSGCs in the retina, a finding that has important implications for understanding signal processing in the early visual system.

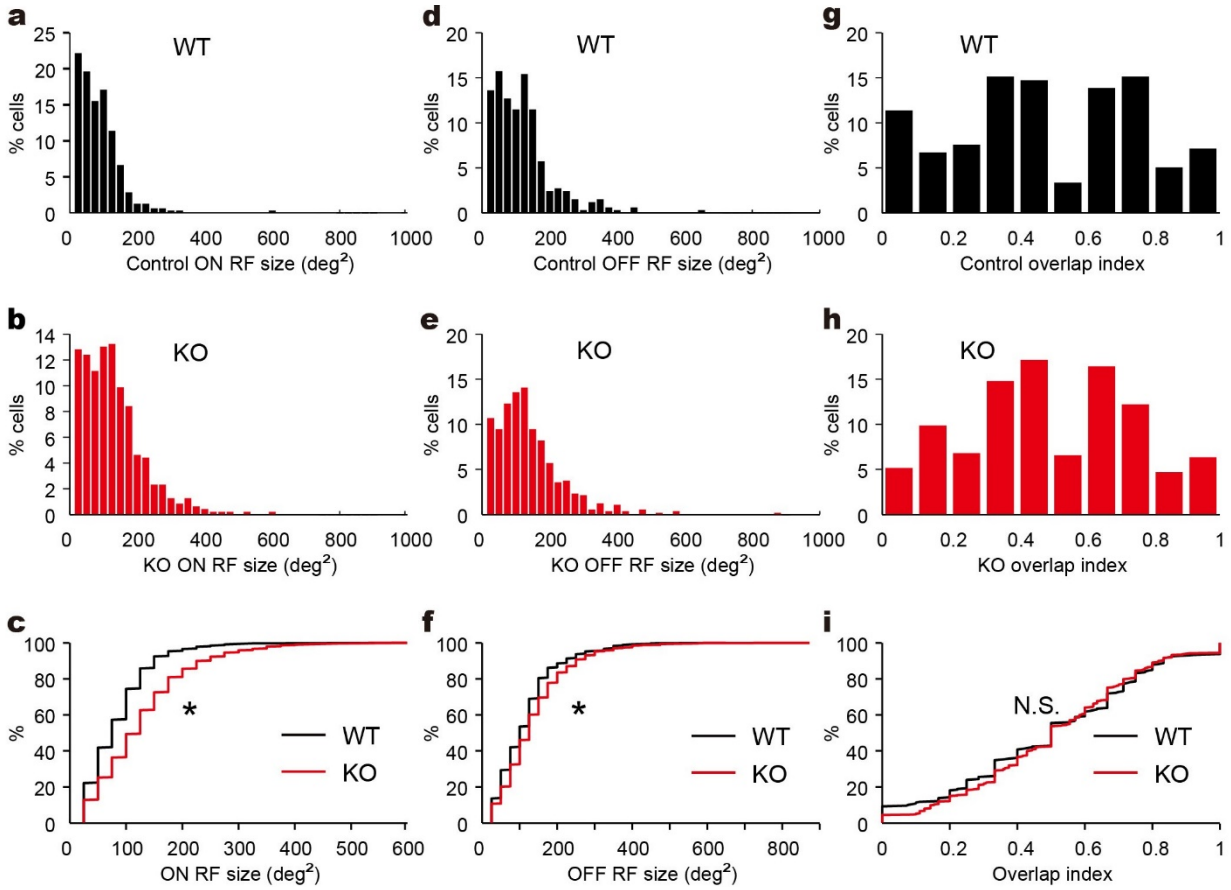

Figure 4.15: Receptive field structure of superficial SGS neurons. (A) Distribution of On receptive field (RF) sizes (in deg^2) in WT (n = 316, 5 mice, mean ± s.e.m. = 85.84 ± 3.46, median = 75). **(B)** Distribution of On RF sizes in KO (n = 476, 8 mice, 128.31 ± 4.04, 125). **(C)** Cumulative distributions of the data shown in (A) and (B) (asterisk (*) indicates $p < 0.001$, K-S statistic = 0.2500, Kolmogorov-Smirnov test). **(D)** Distribution of Off RF sizes in WT (n = 331, 5 mice, 118.20 ± 4.72, 100). **(E)** Distribution of Off RF sizes in KO (n=561, 8 mice, 138.19 ± 4.10, 125). **(F)** Cumulative distributions of the data shown in (D) and (E) (asterisk (*) indicates $p = 0.0137$, K-S statistic = 0.1084, Kolmogorov-Smirnov test). **(G)** On-Off overlap index in WT (n = 238, 5 mice, 0.50 ± 0.02, 0.50). **(H)** On-Off overlap index in KO (n = 426, 8 mice, 0.51 ± 0.01, 0.50). **(I)** Cumulative distribution of the data shown in (G) and **(H)** ($p = 0.5909$, K-S statistic = 0.0618, Kolmogorov-Smirnov test). See (Inayat et al., 2015), for details of 2-photon imaging of SGS neurons' RFs and quantification.

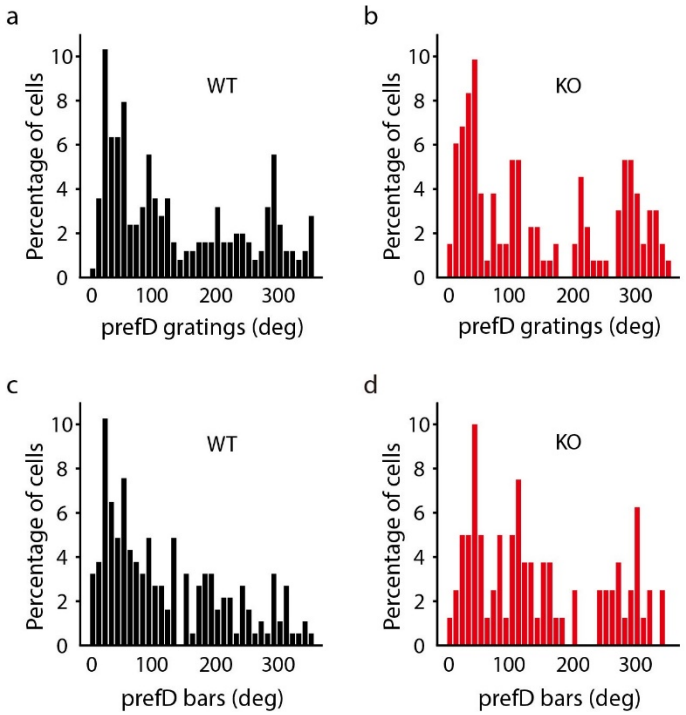

Figure 4.16: Preferred directions of superficial SGS neurons as determined by two-photon calcium imaging. (A) Histogram of the preferred direction (prefD) distribution of superficial SGS neurons in WT mice, in response to drifting gratings. Only cells that had gDSI ≥ 0.2 were included (n = 252 out of 310 total responsive cells). This cutoff was applied to all panels. **(B)** Histogram of the preferred direction distribution in Vgat KO mice, in response to drifting gratings (n = 132/407 total responsive cells). **(C-D)** Histogram of the preferred direction distribution in WT (C) and Vgat KO (D) mice, in response to sweeping bars (n = 185/315 in WT and 80/505 in KOs).

It is known that individual SGS neurons are innervated by several RGCs (Chandrasekaran et al., 2007). Consequently, in order to provide DS excitation to the postsynaptic neuron, the converging DSGCs must prefer similar directions. In addition, a new directional preference would emerge when the DSGCs that prefer neighboring cardinal directions precisely converge. Our findings therefore indicate that well-controlled developmental mechanisms must exist to ensure the precise and selective targeting of DSGCs in the SGS. Consistent with this idea, several subtypes of DSGCs have been found to project primarily to the upper SGS (Dhande & Huberman, 2014), which contains more DS cells than the lower SGS (Inayat et al., 2015). How such depth-specific targeting

is established during development and how even more precise patterns of connectivity are generated at the level of individual cells have not been studied.

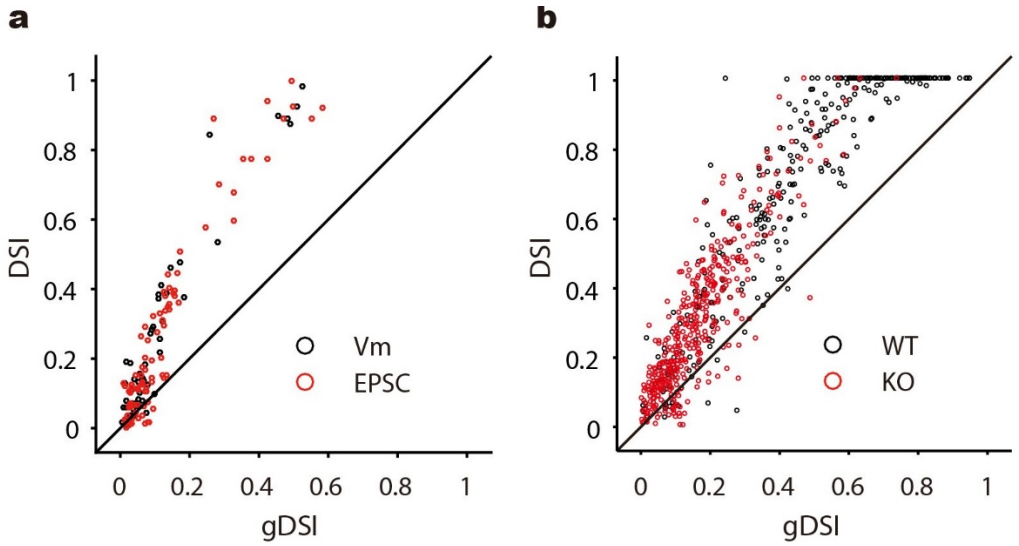

Figure 4.17: Relationship between DSI and gDSI. (A) Relationship between DSI and gDSI for whole-cell recording data (n = 52 for V_m from 41 mice, black; and n = 87 for EPSC from 58 mice, red). (B) Relationship between DSI and gDSI for two-photon imaging data of the SC, in response to drifting gratings (n = 310, 5 WT mice, black; n = 407, 8 KO mice, red). The solid lines in both panels are the lines of identity.

Our data further show that the intracollicular excitation that DS SGS neurons received was also tuned to similar directions, thereby amplifying the retinal inputs without changing their preferred direction or levels of selectivity. This result thus indicates that, within the SGS, excitatory neurons that prefer similar directions are preferentially connected. A similar nonrandom connectivity has been revealed for orientation-selective cells in the mouse visual cortex (Cossell et al., 2015; Ko et al., 2011; W. C. A. Lee et al., 2016), and its emergence requires visual experience (Ko et al., 2013). The exact wiring diagram of the SGS circuits and their development have not yet been studied. Given that the mouse retinocollicular pathway is already a productive model for studying cell types and neural development (Cang & Feldheim, 2013), future studies of this pathway will likely reveal the molecular and cellular mechanisms that establish the precise connections from the retina to the

SGS and within the SGS, both of which are necessary to generate and maintain feature selectivity in the superior colliculus.

Direction-selectivity is an evolutionarily conserved property seen in many visual structures and in various species. In zebrafish, for example, RGC subtypes that prefer different directions project to segregated layers in the optic tectum, and the tectal neurons with matching preferred directions arborize their dendrites in the corresponding layers (Gabriel et al., 2012; Lowe et al., 2013; Nikolaou & Meyer, 2012; Robles et al., 2013). This suggests that the DS retinal inputs could determine the direction preference of tectal neurons, consistent with our findings here in the mouse SC. In monkeys, a very small population of DS neurons was found in the SC (Cynader & Berman, 1972; Marrocco & Li, 1977), largely consistent with the fact that DSGCs have so far remained elusive in primates. It is certainly possible that DSGCs may be discovered with new genetic and imaging techniques in the future and that they may give rise to the observed SC direction selectivity. Alternatively, the weak DS responses in the primate SC could result from the excitatory input from visual cortex, which includes DS cells. This possibility has in fact been addressed in cats by lesioning or cooling the cortex, but unfortunately these studies yielded conflicting results (Hoffmann & Straschill, 1971; Ogasawara et al., 1984). On the other hand, cortical input does not appear to affect SC selectivity in rodents. For example, in ground squirrels, SC direction selectivity remain unchanged when visual cortex is removed, leading to the proposal that the DS cells receive their inputs from the retina (Ch R. Michael, 1970). We have recently shown that in mice cortical inputs do not affect the magnitude or looming speed tuning of SC responses under anesthesia and only increase the response magnitude in the awake condition (Zhao et al., 2014). Our current study, in which the animals were anesthetized and their V1 removed, demonstrates that retinal input was

the origin of the direction selectivity in the mouse SC. Future studies will be needed to determine whether cortical input could modulate SC direction-selective responses under certain behaviors in mice or even give rise to SC direction selectivity in primates.

In addition to direction selectivity, SGS neurons also display a number of other response properties, such as size preference, motion selectivity and speed tuning (Gale & Murphy, 2014; Wang et al., 2010; Zhao et al., 2014). These properties could be generated by integrating inputs from DSGCs, other RGC subtypes, local intracollicular circuits and afferent inputs from visual cortex. In terms of local circuits, the SGS contains a large population of inhibitory neurons. Inhibition could sharpen direction selectivity if it is tuned to the opposite direction or offset spatiotemporally, as shown for DS neurons in zebrafish tectum (Gabriel et al., 2012) and mouse visual cortex (Li et al., 2015). Although we did not directly address the role of synaptic inhibition in this study, our data indicate that it is not required to generate direction selectivity in SGS neurons or to sharpen its tuning. This is because the excitatory inputs that individual DS neurons receive are already selective and tuned to the same level as V_m. On the other hand, inhibitory neurons in the topmost SGS lamina are known to be DS (Inayat et al., 2015). It is thus conceivable that these inhibitory neurons may provide direction-specific interactions between stimulus center and stimulus surroundings in response to complicated visual scenes. Future studies will be needed to determine the spatial and direction tuning of inhibition in SGS neurons in order to reveal the functions of the SGS in visual processing.

In conclusion, the diverse response properties in the SC are generated by selective and precise connections in the retinocollicular and intracollicular circuits. Using the genetic and optogenetic

tools available in mice, we discovered the neuronal mechanism underlying direction selectivity, one of the most important properties. Given the fundamental importance of the SC in visually guided behaviors, we are confident that our findings will motivate exciting future studies of visual system organization, function and development.

4.5 Experimental Procedures

Animal Preparation

C57BL/6 wild-type (WT) and transgenic mice of both sexes were used in this study. Gad2-IRES-cre mice (Stock no. 010802) and Ai32 (RCL-ChR2(H134R)/EYFP, Stock no. 012569) were acquired from Jackson Laboratory and crossed to generate heterozygous offspring that express ChR2 in Gad2+ cells for *in vivo* optogenetic experiments (n = 85). Additional WT mice were also used for *in vivo* whole cell recording (n = 25). For 2-photon calcium imaging in the retina and SC, $Vgat^{flox/flox}$ mice (Stock no. 012897*)* and ChAT-IRES-Cre mice (Stock no. 006410) were originally acquired from Jackson Laboratory and crossed to knock out vesicular GABA transmitter (*Vgat*) gene from *choline acetyltransferase* (*ChAT*)+ cells. These strains were backcrossed to the C57BL/6 background (Huberman et al., 2009). Both KOs (n = 21) and littermate controls (n = 14) were used. All experimental procedures were approved by the Northwestern University and the University of Chicago Institutional Animal Care and Use Committee.

For *in vivo* experiments, mice between postnatal day 45 and 90 were anesthetized with urethane (1.2 g/kg in 10% saline solution, i.p.) and then sedated by chlorprothixene (10 mg/kg in water, i.m.) as described before (Li et al., 2013; Saul & Humphrey, 1992). Atropine (0.3 mg/kg in 10% saline) and dexamethasone (2 mg/kg in 10% saline) were administrated subcutaneously. The

animal was then transferred onto a heating pad for recording or imaging. The animal's body temperature was monitored through a rectal thermoprobe and maintained at 37 ℃ through a feedback heater control module (Frederick Haer Company, Bowdoinham, ME). Toe-pinch reflex was monitored during experiments to test for depth of anesthesia. Additional Urethane (0.2–0.3 g/kg) was administered when necessary. After the mice were anesthetized, the scalp was shaved and skin removed to expose the skull. For whole cell and single unit recording, a metal plate was mounted on top of the skull with Metabond (Parkell, Edgewood, NY) mixed with black ink. The plate was then mounted to a steel stand on the vibration isolation table. A thin layer of silicon oil was applied on both eyes to prevent drying. A craniotomy (~3.5 ×1.5 mm^2) was performed on the left hemisphere, and the tissues including V1 overlaying the SC was removed by aspiration to expose the SC. The procedures for imaging are described below.

In vivo whole-cell recording

Blind whole cell patch clamp was performed to record SGS neurons intracellularly. Glass pipettes had tip openings of 1.5-2μm (5-7MΩ). For current-clamp recordings, the K^+-based internal solution contained 135 mM K-gluconate, 7 mM KCl, 0.5 mM EGTA, 10 mM HEPES, 10 mM Na-phosphocreatine, 4 mM Mg-ATP, 0.4 mM Na-GTP and 0.5% biocytin. The pH was adjusted to 7.25 with KOH. For voltage-clamp recordings, both K^+-based (n = 54) and Cs^+-based (n = 21) internal solution were used. The Cs^+-based internal solution contained 125mM Cs-gluconate, 2mM CsCl, 0.5mM EGTA, 10mM HEPES, 1mM QX-314, 5mM TEA-Cl, 10mM Na-phosphocreatine, 4mM Mg-ATP, 0.4mM Na-GTP and 0.5% biocytin. The pH was adjusted to 7.25 with CsOH. K^+-based internal solution was used to try to record EPSCs and V_m from the same cells, and Cs^+-based internal solution was used only for recording EPSCs. No difference was found between using K^+-

based and Cs^+-based internal solutions for recording EPSCs. Glass pipettes were advanced perpendicularly to the horizontal plane of the mouse head until just touching the SC surface. 2% agarose in artificial cerebrospinal fluid solution (ACSF, containing 140mM NaCl, 2.5mM KCl, 11mM Glucose, 20mM HEPES, 2.5mM $CaCl_2$, 3mM $MgSO_4$, 1mM NaH_2PO_4) was then added onto the exposed SC to stabilize the brain. A small piece of wet gauze was covered onto the agarose to prevent drying. Pipettes were then inserted into the SC.

Electrical signals were amplified using MultiClamp 700B (Axon Instruments, CA), and acquired with System 3 workstation (Tucker Davis Technologies, FL) at 10 kHz. Pipette capacitance and the electrode resistance were compensated initially. For current-clamp recordings, only the cells with stable resting membrane potentials and series resistance lower than 80 MΩ across the duration of the recordings were included in our analysis. No current injection was applied during recordings except for measurement of series resistance (Pei et al., 2015). For voltage-clamp recordings, neurons were clamped at the reversal potential of inhibition, which was determined by adjusting the holding potential to minimize the amplitude of the inhibitory postsynaptic current evoked by photostimulation of Gad2+ neurons (**Fig. 4.4**). The mean reversal potential for inhibitory currents in excitatory cells was -64.82 ± 0.25 mV (n = 36). For recordings of inhibitory cells, -65 mV was used as the holding potential to isolate excitatory currents. Only cells with stable current baselines and series resistance lower than 50 MΩ across the duration of the recordings were included in our analysis. Note that the reported values were not corrected for the junction potential. The depths of recorded cells were between 0 and 300 μm (reading from the micromanipulator) from the point where the pipette broke into the thin membrane of SC surface as indicated by a large sudden and

quickly recovered electrical signal change. The morphology of 9 biocytin-stained cells further confirmed the accuracy of the manipulator readings and that all cells were in the SGS.

Histology

After *in vivo* whole-cell recordings, mice were overdosed with euthanasia solution (150 mg/kg pentobarbital) and perfused with PBS and then 4% paraformaldehyde (PFA). The brain was immersed in 4% PFA overnight. Coronal slices of 150μm were cut from the fixed brain using a vibrating blade microtome (VT1000S, Leica Microsystems). The labeled cells were revealed by visualizing biocytin with streptavidin-Alex Fluor 488 conjugate (Invitrogen). Images were captured using a Zeiss LSM5 Pascal confocal microscope (Carl Zeiss, Jena, Germany) in z-series scanning and reconstructed in Filament Tracer of Imaris (Bitplane, Zurich, Switzerland).

In vivo extracellular recording

Tungsten electrodes (5-10 MΩ, FHC) were inserted perpendicularly into the SC. The SC surface was estimated visually under the microscope. 2% agarose in ACSF was then applied onto the exposed SC. SGS neurons were recorded between 0 and 300μm below the surface. The electrical signals were filtered between 0.3 and 5 kHz for spikes and sampled at 25 kHz using a System 3 workstation (Tucker Davis Technologies, FL). The spike waveforms were further sorted offline in OpenSorter (Tucker Davis Technologies, FL) to isolate single units as described before (Drager & Hubel, 1975; Li et al., 2013).

Two-photon calcium imaging of SGS neurons

We followed our recently published procedures of 2-photon imaging of the superficial SGS neurons (Saul & Humphrey, 1992). Briefly, a craniotomy was performed on the left hemisphere, starting at the lambda point and extending ~3 mm both laterally and rostrally. Tissues overlaying the SC were removed by aspiration. Once the SC was exposed, a glass pipette (inner diameter of 10-20 μm) filled with freshly-made solution containing Cal-520AM (1.13 mM) and SR101 was lowered into the tissue. Twenty pulses of 2.3 nl each (46 nl total volume), at 20 s interval, were delivered to inject the Cal-520 solution at a depth of 500 μm below the surface. The same procedure was repeated after retracting the pipette to a depth of 250 μm. The pipette was left in the tissue for 1-2 min before being slowly retracted. The SC was then covered by ACSF. Imaging was performed 1-2h after loading.

Once the injection procedure was complete, a small metal plate was mounted on the mouse's head with MetaBond (Parkell), which, when clamped under the microscope, resulted in the imaged SC surface being largely flat and perpendicular to the objective. A shield was placed around the craniotomy to block light from the visual stimulus during imaging. The SC was covered by 3% agarose in ACSF for stability. Imaging was performed with a 2-photon microscope (2P-SGS, Bruker Nano Surface Division) at an excitation wavelength of 800 nm, and with a 40X/0.8NA objective (Leica). Data were acquired using PrairieView software with a spiral scan at 2X optical zoom, resulting in a circular field of view with a diameter of 135 μm. Image resolution was 256x256 pixels and the acquisition rate 8.079 Hz.

Optogenetic silencing of SGS excitatory neurons

To photostimulate ChR2-expressing cells, we used an optic fiber (0.2 mm core diameter) driven by a blue LED (470 nm, Doric Lenses) placed ~0.5 mm above the exposed SC. The tip of the LED

fiber was placed at a similar position in all mice. During recordings, it was buried in the agarose that was applied to reduce the pulsation of the brain and protect the tissue. To prevent direct photostimulation of the eyes by the LED light, the Metabond used for mounting the head plate was prepared with black ink. The agarose surface was painted with black ink, and a piece of thick black paper was carefully placed around the fiber to ensure that light could not be seen from the front and sides, as described before (31). The LED was driven by a square wave starting from 500 ms before the onset of each visual stimulus and ending at 100 ms after the offset of each visual stimulus (3600 ms for sweeping bars, as described below). The intensity of LED light was ~160 mW/mm^2 at the tip of the optic fiber in all recordings, which was confirmed to be reliably effective in silencing SGS excitatory neurons.

Visual stimulation

For *in vivo* experiments, visual stimuli were generated with Matlab Psychophysics toolbox (33,34) on a LCD (37.5 cm × 30 cm, 60 Hz refresh rate, ~50 cd/m^2 mean luminance) or a CRT monitor (40 cm × 30 cm, 60 Hz, ~35 cd/m^2 luminance). The monitor was placed 25 cm away from the eye contralateral to the recording/imaging site (the right eye). For 2-photon imaging, the screen was also tilted at an angle matching that of the mouse's head, given that the mouse's nose was slightly elevated to correct for the curvature of SC and allow imaging from a relatively flat surface. The ipsilateral eye was covered throughout the experiments.

Two types of visual stimuli were used to determine direction selectivity of SGS neurons. First, sweeping bars of 5° wide drifting at a speed of 30°/s were used in both physiology and imaging experiments. The drifting directions were varied between 0° and 330° (12 steps, 30° spacing),

which were presented in a pseudorandom sequence together with a "blank stimulus" (gray screen at the mean luminance). In whole cell recording, the inter-stimulus interval was 0.5 or 1 sec when there was no LED illumination, and 10 sec where LED was used in order to allow the stimulated inhibitory cells to recover. In 2-photon imaging, the inter-stimulus interval was 3 sec. Second, drifting sinusoidal gratings were also used in the imaging experiments, at 0.08 cpd, 2Hz, 100% contrast (Saul & Humphrey, 1992). They were presented at 12 movement directions (0°-330°, with 30° increments) in a pseudorandom order within a circular window (32° in diameter and surrounded by a grey background) near the center of the imaged cells' receptive fields (which was determined by flashing white or black squares as described in reference (Saul & Humphrey, 1992). The stimulus duration was 3 sec and inter-stimulus interval 5 sec. Each stimulus was repeated 4-6 times for imaging and 3-8 times for recording.

Data analysis

Whole cell recording data were first analyzed using a custom MATLAB program (originally written by a former lab member Dr. Xinyu Zhao). For current-clamp data, spikes were detected by calculating the first derivative of raw voltage traces (dV/dt), and the start of a spike was the time point when dV/dt reached a manually set positive threshold. Individual traces were carefully inspected to ensure proper spike detection. Peri-stimulus spike time histograms (PSTHs) were calculated by trial-averaging the spike counts in each 50 ms time bin. Subthreshold V_m were extracted by removing spikes from the raw voltage traces by a 6 ms median filter. The subthreshold V_m traces were trial-averaged for each stimulus condition. The trial-averaged V_m trace for the blank stimulus (i.e., gray screen) was used to calculate the mean (V_m baseline) and standard deviation of spontaneous V_m fluctuations. The V_m baseline was then subtracted from the trial-

averaged V_m trace for each visual stimulus condition, i.e., bars of certain direction.

For voltage-clamp data, the current traces (I_m) were firstly smoothed by a 40 ms mean filter and then trial-averaged for each stimulus condition. For visual stimulus conditions in the absence of LED photoactivation (i.e., LED-off), the EPSC baseline was calculated as the mean of the trial-averaged I_m trace to the blank stimulus, and subtracted from the trial-averaged trace of each condition. For LED-on conditions, I_m traces were similarly trial-averaged for each stimulus condition. For inhibitory cells, all traces showed LED-activated ChR2 currents in addition to visually-evoked EPSCs (Extended Data **Fig. 4.11**). For excitatory cells, the trace of the blank condition was flat in most cells (Extended Data **Fig. 4.11**); but in some cells, a slowly increasing inward current was seen during LED stimulation, possibly the "bystander currents" mediated by acid-sensing ion channels (Baden et al., 2016). The dynamic of this slow current, when existed, was always the same for all stimulus conditions of the same cell, including the blank stimulus. We therefore did a point-by-point subtraction of a further-smoothed trace of the blank condition from the trace of each condition. This was done for both excitatory and inhibitory cells to remove the LED-evoked currents, while keeping the fluctuations in each trace (including the blank condition, which was used to determine baseline fluctuation). Finally, the intracollicular EPSC traces were generated by a point-by-point subtraction of retinal EPSC (LED-on) from the total EPSC (LED-off) traces (Extended Data **Fig. 4.12).**

For analyzing V_m and EPSCs, we determined time windows of responses to the sweeping bars. This was necessary for finding "response" magnitude for directions that evoked weak or no responses. To do this, we first calculated a cutoff threshold, which was the V_m or EPSC level 2 standard deviations away from the baseline fluctuation (determined from the blank condition as

described above). The widest segment of the traces that were above (for V_m) or below (for EPSC) the threshold was determined as the response time window for each stimulus condition. This time window was expanded if there were any short above-threshold segments within 150ms of the 2 sides. Next, the conditions that evoked wider time windows were used to guide the analysis of other conditions, to ensure that the estimation of response window was not too conservative or inaccurate for non-preferred directions. Specifically, for conditions where the window was narrower than 1/3 of the widest window of this cell (or 333 ms if the widest window is bigger than 1s), the response time window determined from the opposite direction, reversed in timing, was used. All traces were checked visually to confirm that the time windows were determined properly. Peak V_m and spike rate were calculated for the response time window of each stimulus condition, subtracting the mean values of blank condition. For EPSCs, they could spontaneously fluctuate across the threshold, thus leading to an overestimation of the weak responses. Therefore, for data shown in the main text, if the peak EPSCs were within 3 standard deviations of the baseline, they were manually set to 0. We compared this with other methods of calculation (**Fig. 4.13**) and found no difference in our conclusions. Finally, the EPSC charge integral for each stimulus condition was quantified as the time integral of the data points in the response time window as determined above.

For SC 2-photon imaging data, we followed our published procedures of analysis (Saul & Humphrey, 1992). Briefly, regions of interest (ROIs) were drawn manually on the average images, and the intensity values for all pixels in each ROI were averaged for each frame to obtain the raw Ca^{2+} signal of each cell. From the raw signal, for each stimulus presentation, $\Delta F/F_0 = (F - F_0)/F_0$, was calculated, where F_0 was the mean of the baseline signal over a fixed interval of 1.25 sec (for

gratings) or 0.75sec (for bars) before stimulus onset; and F was the fluorescence signal from 250 ms after stimulus onset to 500 ms after stimulus offset. A cell was considered responsive if its mean F (for gratings) or peak F (for bars) was more than two standard deviations above F_0 for at least one of the stimulus conditions. The mean (for gratings) or peak (for bars) value of $\Delta F/F_0$ for each of the stimulus conditions was then used to determine the direction tuning curves for every responsive cell.

To quantify the degree of direction selectivity, we calculated a global direction selectivity index (gDSI), which is the vector sum of responses normalized by the scalar sum of responses (Chandrasekaran et al., 2007; Saul & Humphrey, 1992): $gDSI = \frac{\sum R_\theta e^{i\theta}}{\sum R_\theta}$, where R_θ is the response magnitude of spikes, V_m, EPSC, or $\Delta F/F_0$, at θ direction of bars or gratings. The preferred direction is quantified as the angle of the vector sum of responses.

To classify whether a cell was direction selective in **Figure 4.8**, we used a criterion of gDSI-EPSC ≥ 0.1. In the 17 cells that met this criterion and received direct retinal inputs, 3 cells showed in their tuning curves a small but obvious second peak at the direction opposite to the preferred direction, thus leading to their global orientation selectivity index ($gOSI = \frac{\sum R_\theta e^{i2\theta}}{\sum R_\theta}$) greater than *gDSI*. For all of the other 14 cells, their *gDSI* was greater than *gOSI.* We therefore did not include these 3 cells in DS cells, but none of our conclusions would change if these 3 cells were included.

All pooled data were presented as mean ± SEM. Statistical significant was calculated using two independent sample *t* tests or paired *t* tests, or K-S test as mentioned in the text. All analyses and graph plotting were performed in MATLAB (MathWorks) or Prism (GraphPad Software Inc).

Retinal calcium imaging and data analysis

WT littermate controls and Vgat KO mice were injected intravitreally after eye opening at P18 with an AAV2 viral vector carrying GCaMP6s (University of Pennsylvania Vector Core). After 21 days, the injected mice were dark adapted for 1 hour and their retinas were dissected in the dark under infrared (IR) light. During dissection, the retina was cut into dorsal and ventral pieces following the procedure described by (Wei et al., 2010) and the nasal direction for each piece was annotated. The dissected retinas were kept in darkness at room temperature in Ames' medium bubbled with 95% O2/5% CO^2 until use (0–7 h). Cells were visualized with IR light (>900 nm) and an IR-sensitive video camera (Watec). Light responsive, GCaMP6s-positive cells were identified by a two-photon microscope (Bruker Nano Surface Division) and a Ti:sapphire laser (Coherent Chameleon Ultra II) tuned to 920 nm while presenting a flashing spot (660 um diameter) from a monochromatic organic light-emitting display (OLEDXL, eMagin; 800×600 pixel resolution, 60-Hz refresh rate). Imaging was performed at an excitation wavelength of 920 nm with a 60X objective while the field of view was presented with a positive contrast 990 μm x 220 μm moving bar stimulus in a dark background moving in 8 pseudorandomly chosen directions spaced at 45 degree intervals at a speed of 440 μm/sec on the retina (~15 °/sec in visual space). Data were acquired using PrairieView software in a 100 μm x 100 μm field of view. Image resolution was 256 x 256 pixels and the acquisition rate ~13 Hz.

Raw frames were uploaded onto ImageJ software in which regions of interest (ROIs) were manually drawn to enclose the soma of each GCaMP6s expressing cell and for a background region where there was no detectable GCaMP6s expression. Using the TimeSeries Analyzer plugin for ImageJ, we calculated the average intensity over time for all ROIs. In MATLAB, the

background trace was subtracted from the light responsive somatic traces to remove noise. The background subtracted traces were then truncated and sorted by direction of the moving bar stimulus and the peak of each calcium transient was used to calculate $\Delta F/F_0$ as described above. For each responsive cell, we calculated gDSI and gOSI as described above and $DSI = \frac{R_{pref} - R_{opp}}{R_{pref} + R_{opp}}$, where R_{pref} is the cell's response at the preferred direction (i.e., maximal response), and R_{opp} is the cell's response to the direction opposite to the preferred one. Cells showing responses to both the leading and trailing edge of the positive contrast moving bar and whose DSI > 0.2 and gDSI > gOSI were classified as On-Off DSGCs.

Chapter 5

Transgenic Approaches for Functional Imaging in Retinal Ganglion Cells

The immunostaining data presented in this chapter was collected by Qi Geng (now graduate student at University of Michigan).

5.1 Abstract

Calcium imaging has become a powerful tool in neuroscience research allowing the visualization and monitoring activity of neuronal populations. In particular, recent studies have utilized calcium imaging to classify populations of retinal neurons into retinal ganglion cell subtypes based on their light response characteristics (Baden et al., 2016; Sabbah et al., 2017) and to record activity across subcellular compartments (Chapot et al., 2017; Qiang Chen et al., 2016; Euler et al., 2002). Over the last several years, genetically encodable calcium indicators (GECIs) have become the gold standard for functional imaging since they can be expressed in molecularly-defined subpopulations and exhibit high sensitivity (T. W. Chen et al., 2013; Dana et al., 2018). Despite the numerous advances in viral vector technologies, homogeneous expression of GECIs in retinal tissue still remains challenging. Here, we characterize two transgenic mouse lines that target retinal ganglion cells (RGCs) and a subset of horizontal cells for functional imaging. These transgenic lines eliminate the need of performing intravitreal injections and reduce the variability between mice.

In addition, genetic manipulations can be introduced into these mouse lines to dissect the contributions of interneurons to various retina computations. For example, we show how disrupting GABA signaling from starburst amacrine cells (SACs) reduces direction selective responses in the RGC population.

5.2 Introduction

The ability to monitor neural activity during behavior has been instrumental in providing links between neural activity and function. Over the last several decades, neuroscience research has taken advantage of various optical methods, including calcium imaging, to track the activity of neurons over extended periods of time since these allow for recordings of neuronal populations and subcellular compartments and are minimally invasive compared to multi-electrode arrays. Additionally, the development of genetically encodable calcium indicators (GECIs), such as GCaMP6, have made it possible to isolate the activity of genetically defined populations with single action potential sensitivity (T. W. Chen et al., 2013; Pnevmatikakis et al., 2016). GECIs have been traditionally targeted to specific cell types through viral vector techniques (Bedbrook et al., 2018; Khabou et al., 2016). While viral techniques are efficient in introducing foreign genes into neurons, they often require challenging surgeries and result in non-homogenous expression patterns.

In the particular case of the retina, intravitreal injections can cause retinal damage and lead to expression restricted the area around the injection site biasing the sample population (Sabbah et al., 2017). All of these factors contribute to experimental variability between mice and retinal tissues. Additionally, the possibility of using GECIs for early developmental studies have been

limited due to the time window needed for expression, which is in the order of several weeks (Chang et al., 2017). Several transgenic mouse lines have been developed that result in stable, homogenous expression of GCaMP6 and circumvent the challenges associated with viral technologies listed above (Dana et al., 2014; Ivanova et al., 2010; Steinmetz et al., 2017).

In the early visual system, retinal ganglion cells (RGCs) carry visual feature sensitive information (Baden et al., 2016) to the downstream visual processing centers of brain (Ellis et al., 2016; Martersteck et al., 2017), such as the lateral geniculate nucleus (LGN) and the superior colliculus (SC). Transgenic mouse lines that exclusively label RGCs in the ganglion cell layer would allow proper sampling of all the output channels in the retina and provide the means to better understand how the retina encodes visual information. Previous immunostaining and anatomical tracing experiments have suggested that some molecular markers, such as vesicular glutamate transporter 2 (vGluT2) and Thy1, can be used to label most, if not all, RGCs (Qian Chen et al., 2012; Ellis et al., 2016; Martersteck et al., 2017; Wässle et al., 2006). While these markers provide genetic access to RGCs, their use for population level functional imaging in the retina has yet to be reported. Here, we focused in the characterization of the Vglut2-IRES-Cre and Thy1-GCaMP6f 5.17 as Cre-dependent and Cre-independent transgenic mouse lines for retinal calcium imaging. Our findings demonstrate that both of these genetic lines have similar expression patterns and can be used to reliably identify visual feature encoding RGCs.

5.3 Results

5.3.1 Labeling of retinal neurons by Vglut2-Cre and Thy1-GCaMP6f 5.17 transgenic lines

To assess whether the *Vglut2-IRES-Cre* and the *Thy1-GCaMP6f 5.17* (referred as Thy1-GCaMP6f further on) transgenic lines target similar populations of neurons in the retina, we generated a hybrid mouse line containing the *Vglut2-IRES-Cre*, *floxed TdTomato*, and *Thy1-GCaMP6f* transgenes (**Figure 5.1a**). In this mouse, all Vglut2-Cre+ cells will be expressing the red-fluorescent protein, TdTomato, and all Thy1+ cells will be expressing the genetically encoded calcium sensor, GCaMP6f. Isolated retinas from these mice were then fixed (4% paraformaldehyde for 20 mins) and stained using anti-GFP and anti-RFP primary antibodies to enhance the GCaMP6 and TdTomato immunofluorescence, respectively. Using laser-scanning two-photon microscopy we recorded the red- and green-shifted signals across the entire volume of 0.36 mm^2 (or 600 μm × 600 μm) patches of mouse retina. As expected, we observed strong TdTomato and GCaMP6f signals from the ganglion cell layer (GCL) (**Figure 5.1a-b**). In the GCL, Vglut2-cre+ and Thy+ signals co-localize in 97.97 ± 0.44% of the cells, Vglut2-Cre+ only signal were observed in 1.23 ± 0.21% of the cells, and Thy1+ only signals were observed in 0.80 ± 0.28% of the cells (**Figure 5.1c**). Examples of single labeled cells are indicated by white arrowheads. The average cell densities observed at the GCL in these 0.36 mm^2 patches of retina (3621.53 ± 213.17 cells/mm^2 and 3606.59 ± 214.10 cells/mm^2 for the Vglut2-TdTomato and Thy1-GCaMP6f signals, respectively) fall well within the range previously reported for retinal ganglion cells (RGCs) in the mouse retina (Jeon et al., 1998).

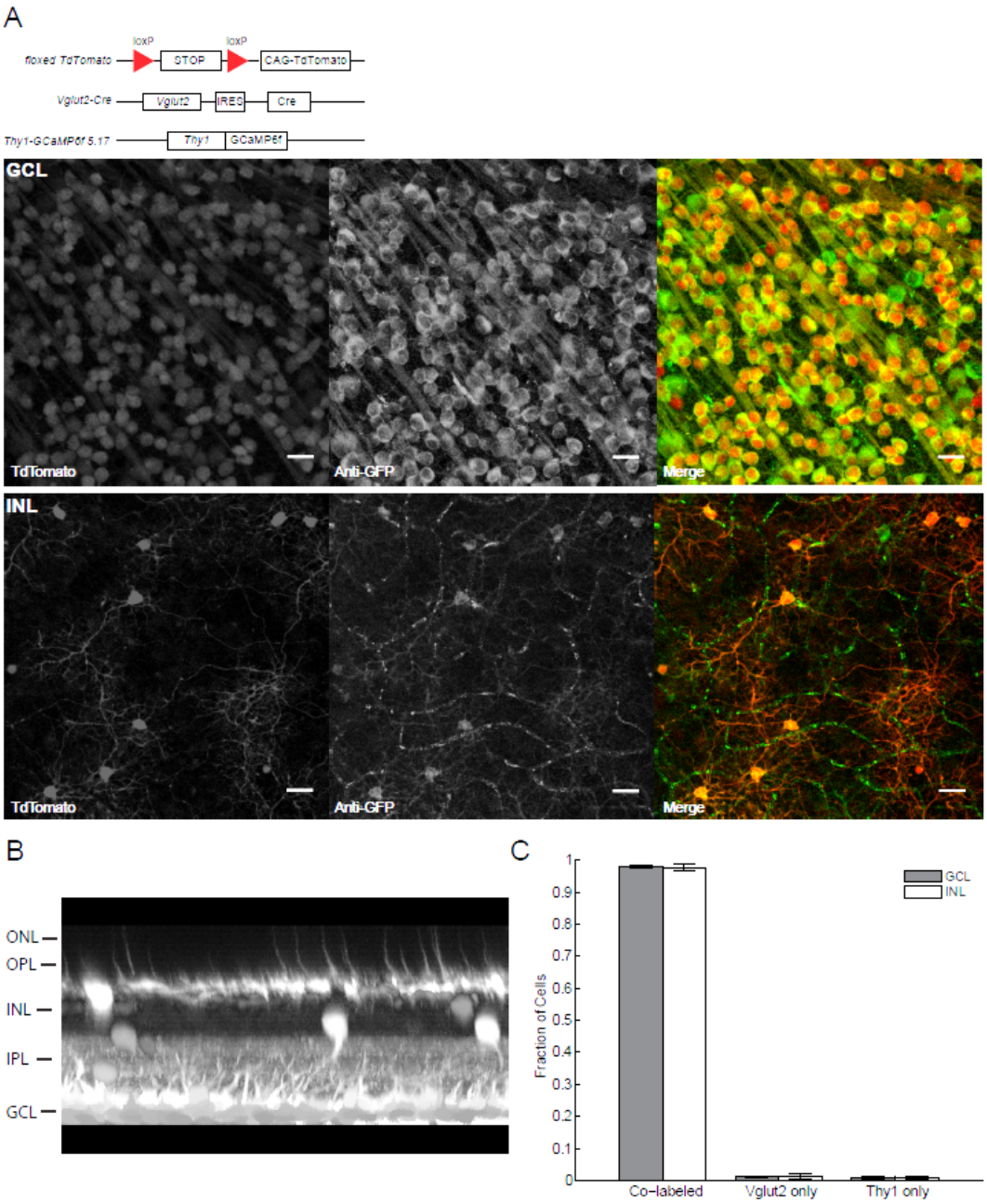

Figure 5.1: Retinal expression patterns of Vglut2-IRES-Cre and Thy1-GCaMP6 5.17 mouse lines. (A) Top: Schematic of transgenes in Vglut2/TdTomato/Thy1-GCaMP6 hybrid mouse. Middle: Two-photon laser scanning microscope images of Expression pattern of Vglut2-Cre and Thy1-GCamp6f 5.17 in the GCL. Bottom: Expression pattern of Vglut2-Cre and Thy1-GCamp6f 5.17 in the INL. **(B)** XY maximum intensity projection of an image stack of a patch of retina taken with a two-photon laser scanning microscope. Fluorescence expression in cell bodies within the ganglion cell layer (GCL) and inner nuclear layer (INL) is apparent. **(C)** Quantification of co-localization of Vglut2-IRES-Cre and Thy1-GCaMP6f 5.17 signals in both the GCL (gray) and INL (white). Plotted at mean ± s.e.m. n = 8 stacks, 3 mice.

To confirm that the expression pattern in these lines is restricted to RGCs and does not include displaced GABAergic amacrine cells (ACs), we stained TdTomato expressing retinas with anti-GAD67 and GCaMP6 expressing retinas with anti-VGLUT2. Our results indicate that these mouse lines do not label GABAergic ACs in the GCL, since we observed clear separation between TdTomato signal and the anti-GAD67 (**Figure 5.2a**). Additionally, we observed strong co-localization between GCaMP6 signals and the Vglut2 protein stain, verifying that the targeted cells are in fact VGLUT2-expressing RGCs (**Figure 5.2b**).

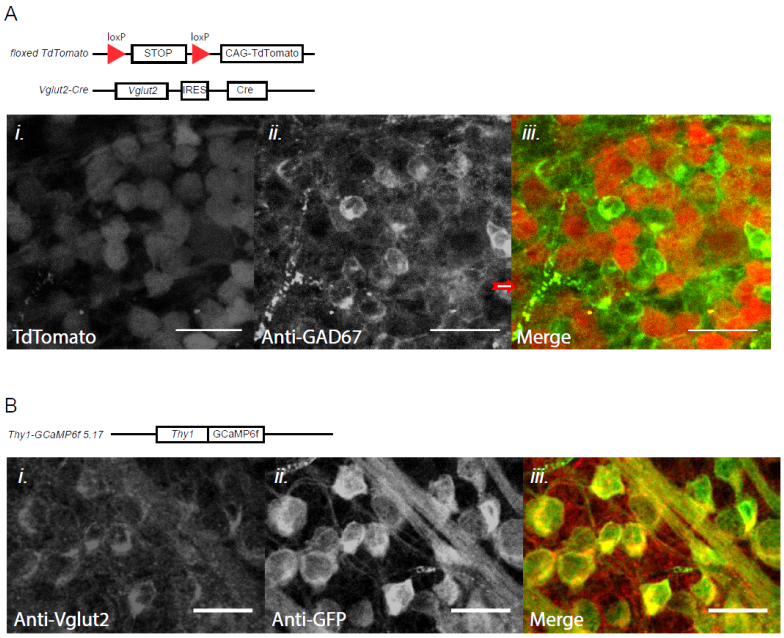

Figure 5.2: Labeling of Vglut2-Cre and Thy1-GCaMP6f in the GCL is restricted to RGCs. **(A)** GAD67 stain in Vglut2-Cre retinas demonstrates clear separation between Vglut2+ and GAD67+ cells. **(B)** Vglut2 stain in Thy1-GCaMP6f retinas shows complete co-localization with Thy1 signal.

Surprisingly, we also observed strong TdTomato and GCaMP6f signals in subsets of cells in the inner nuclear layer (INL) and outer plexiform layer (OPL) (**Figure 5.1b**). In the INL, Vglut2-cre+ and Thy+ signals co-localize in 97.72 ± 1.17% of the cells, while Vglut2-cre+ only signals were observed in 1.47 ± 0.88% of the cells and Thy1+ only signals were observed in 0.81 ± 0.42% of the cells (**Figure 5.1**). It is important to note that the green "swirls" (pointed with red arrowheads)

in our fluorescent images correspond to blood vessels since our green-shifted (Alexa 488 conjugated) secondary antibodies were anti-mouse IgG. These cells in the INL captivated our attention since, to the best of our knowledge, cell types known to express VGLUT2 in the INL have yet to be reported. The identity of these neurons will be further characterized in the latter sections of this report. The labeled cells in the OPL correspond to a subset of S-cone pedicles (656.38 ± 48.24 cells/mm^2) that have been demonstrated to express Vglut2 (Wässle et al., 2006), which account for ~5% of the entire cone population according to previously reported total cone densities. Our data demonstrates that the Thy1-GCaMP6 founder line targets the same population of cones in the OPL.

5.3.2 Classification of RGCs through functional imaging

Anatomical evidence suggests that *Vglut2-IRES-Cre* and *Thy1-GCaMP6* founder lines target all RGC types (**Figures 5.1 & 5.2**) (Martersteck et al., 2017), but the populations labeled by these mouse lines have not been described based on their light response properties. To characterize RGC responses to visual stimulation, we generated mice containing *loxP*-flanked GCaMP6f and Vglut2-IRES-Cre (Vglut2-GCaMP6f mice) transgenes and performed two-photon laser scanning calcium imaging in the GCL of retinas from Vglut2-GCaMP6f and Thy1-GCaMP6f 5.17 mice (**Figure 5.3a**). These lines represent Cre-driven (Vglut2) and Cre-independent (Thy1) forms of transgenic GCaMP6 expression, each having advantages and disadvantages which will be discussed later.

In these experiments, we recorded visual evoked GCaMP6f signals from 1,350 RGCs from 4 mice and 833 RGCs from 4 mice in the *Vglut2-IRES-Cre* and *Thy1-GCaMP6f* mouse lines, respectively, while presenting a bright moving bar stimulus (four trials of a 275 µm x 880 µm in 8 pseudorandom

directions). The 880 μm distance between the leading and trailing edge of the moving bar stimulus provide clear temporal separation between On and Off light response components. We detected RGCs exhibiting On-Off (50.77% ± 0.26 in Vglut2-Cre and 34.62% ± 1.54 in Thy1 mice; data shown as mean ± s.e.m.; p = 0.001), On (25.92% ± 1.16 in the Vglut2-Cre and 36.89% ± 3.91 in the Thy1 mouse; n.s. p = 0.0587), and Off (11.97% ± 0.55 in the Vglut2-Cre and 10.79% ± 1.46 in the Thy1 mouse, n.s. p = 0.5362) responses to the moving bar stimulus (**Figure 5.3b, d**). From the recorded RGCs, 2.99 ± 1.42% in Vglut2-Cre and 2.94 ± 0.911% in Thy1 (n.s.; p = 0.9807, data not shown) exhibited typical light response properties of suppressed by contrast cells, or uniformity detectors as they have been referred to in the past (Jacoby & Schwartz, 2018; Sivyer et al., 2010; Tien et al., 2015), and 8.82 ± 1.40% and 11.39 ± 2.18% (n.s.; p = 0.422) of RGCs were unresponsive cells in the Vglut2 and Thy1 transgenic mouse lines, respectively (**Figure 5.3c**). The lack of responses in this small fraction of cells can be attributed to our chosen stimulus, which might not maximally activate some RGC types, and minor damage during dissection.

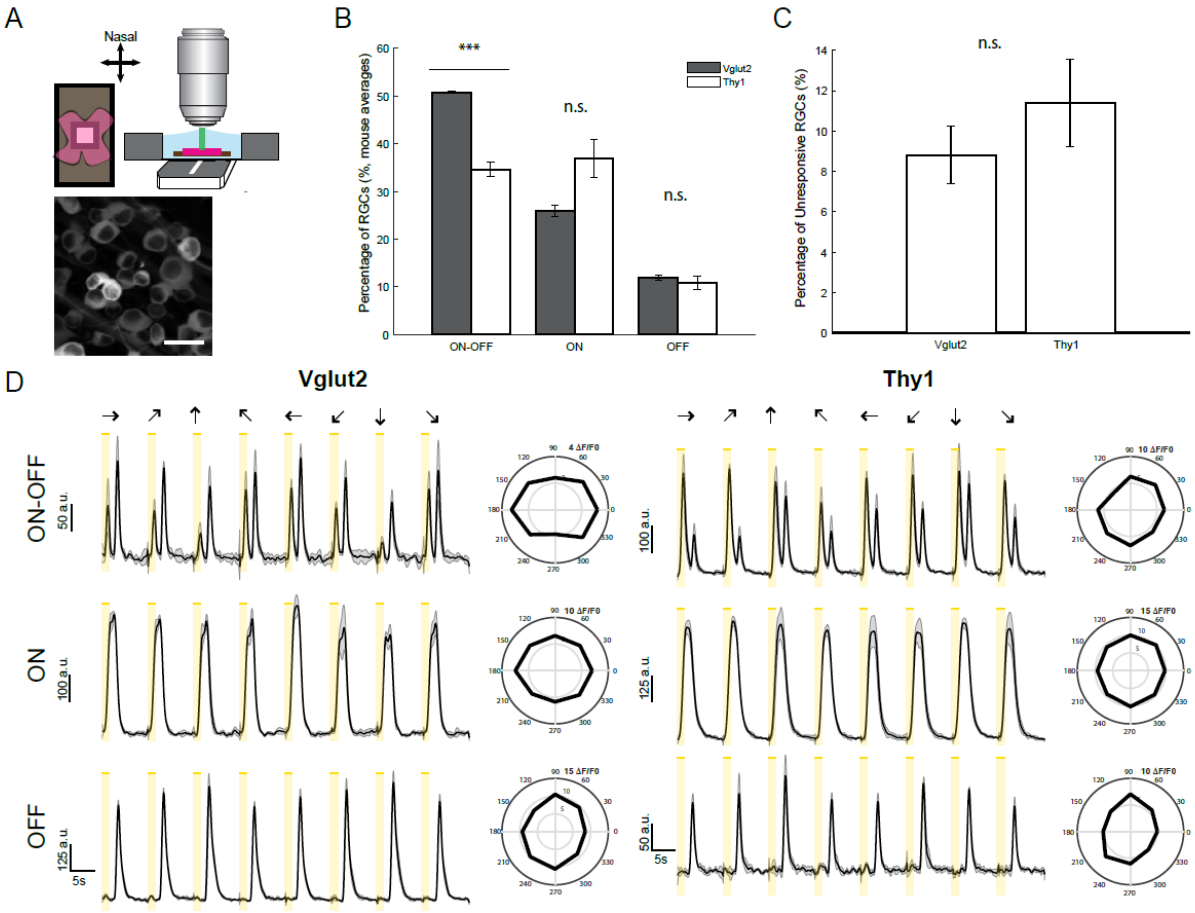

Figure 5.3. Functional imaging using transgenic mouse lines. (A) Schematic showing calcium imaging experimental setup. Dissected retinas are placed onto a recording chamber with the GCL facing upwards and the nasal direction pointing forwards. Retinas are perfused with Ames solution during the entirety of the experiment. Two-photon laser scanning microscopy is used to record GCaMP6 calcium transients while presenting a moving bar stimulus onto the PRL using an OLED. The bottom panel shows a max-intensity projection of GCaMP6 fluorescence in an example field of view. Scale bar, 25 µm. **(B)** Summary plot showing the percentages of On-Off, On, and Off RGCs in Vglut2-IRES-Cre (grey , n = 684 On-Off cells, 360 On cells, and 160 Off cells out of 1,350 RGCs from 4 mice) and Thy1-GCaMP6f 5.17 (white, n = 293 On-Off cells, 322 On cells, and 86 Off cells out of 833 RGCs from 4 mice) retinas ($P = 0.001$ for On-Off, On and Off n.s., $P > 0.05$). **(C)** Quantification of unresponsive RGCs in both Vglut2-IRES-Cre and Thy1-GCaMP6f 5.17 transgenic lines (n.s.; $P > 0.05$). **(D)** Representative traces of On-Off, On, and Off RGCs in the Vglut2-IRES-Cre and Thy1-GCaMP6f 5.17 transgenic lines. The arrows on the top indicate the direction of the 250 µm × 800 µm moving bar stimulus in relation to the tuning plots on the right. Yellow shadow indicates the duration of the leading edge (On edge) passing through a 600 µm in diameter circular mask.

In addition to RGCs of different response polarities, a significant fraction of GCaMP6 positive RGCs in both transgenic lines showed directional responses to the moving bar stimulus,

corresponding to the commonly studied direction selective ganglion cells (DSGCs) (Barlow & Hill, 1963; W. Sun et al., 2006; Weng et al., 2005). Using direction selectivity index ($DSI = R_{pref} - R_{null}/R_{pref} + R_{null}$) as a measure of directional tuning, we found 14.76% ± 1.13 and 16.83% ± 1.35 of cells exhibiting direction selective responses (DSI ≥ 0.35) in the Vglut2-Cre and Thy1 mouse lines, respectively. These can be further classified into On-Off DSGCs (11.33% ± 1.02 in the Vglut2 and 13.00% ± 1.57 in the Thy1 mouse, n.s. p = 0.4694), On DSGCs (3.32% ± 0.42 in the Vglut2 and 3.67% ± 0.89, n.s. p = 0.7725), and Off DSGCs(0.11% ± 0.06 in the Vglut2 and 0.16% ± 0.14 in the Thy1, n.s. p = 0.7872) DSGCs (**Figure 5.4**).

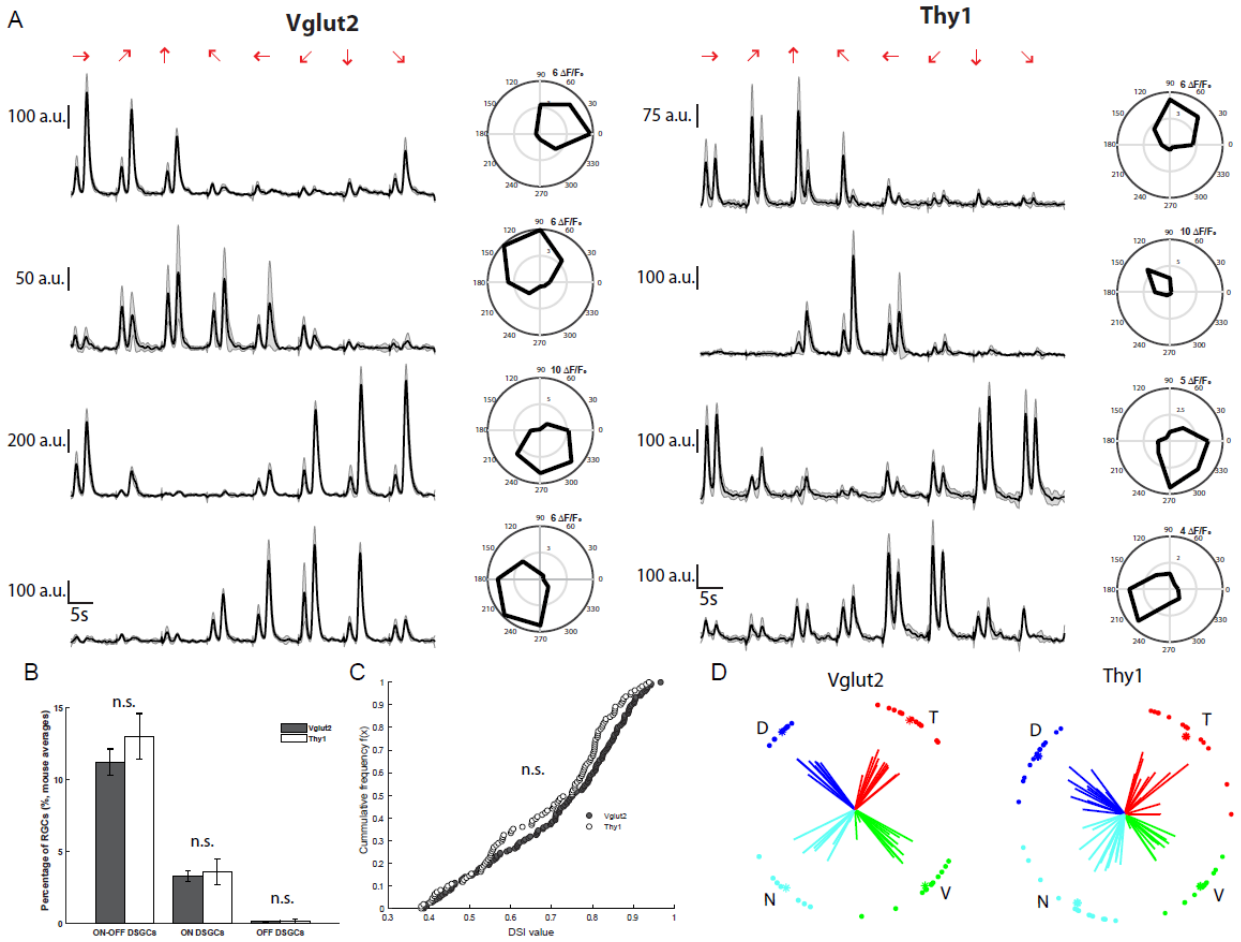

Figure 5.4: Four subclasses of On-Off DSGCs identified using transgenic calcium imaging. **(A)** Representative traces of On-Off DSGCs from the Vglut2-IRES-Cre and Thy1-GCaMP6f 5.17 transgenic lines tuned to the four cardinal preferred directions. **(B)** Average percentages by mouse of DSGCs (DSI ≥ 0.35) in the Vglut2-IRES-Cre (*n* = 157 On-Off DSGCs, 49 On DSGCs, and 2

Figure 5.4 (cont.) Off DSGCs out of 1,350 RGCs from 4 mice, grey) and Thy1-GCaMP6f 5.17 (*n* = 112 On-Off DSGCs, 33 On DSGCs, and 2 Off DSGCs out of 833 RGCs from 4 mice, white) lines. No statistical difference between Vglut2-IRES-Cre and Thy1-GCaMP6f 5.17 were observed (P > 0.05). **(C)** Cumulative distributions of On-Off DSGC DSI values for Vglut2-IRES-Cre (n = 157 cells, grey) and for Thy1-GCaMP6f 5.17 (n = 112 cells, white), indicating that Vglut2-IRES-Cre and Thy1-GCaMP6f 5.17 On-Off DSGCshave nearly identical DSI distributions (*P* = 0.1560, K-S statistic = 0.1385, Kolmogorov-Smirnov test). **(D)** The preferred directions of On-Off DSGCs are plotted as a polar plot of vector sums for the Vglut2-IRES-Cre (left) and Thy1-GCaMP6f 5.17 (right) lines. The preferred directions were grouped into nasal (N), temporal (T), dorsal (D), and ventral (V) preferring by using k-means clustering (k = 4). The asterisks indicate the centroid of each cluster.

Particularly, On-Off DSGCs have been subject of extensive study given their abundancy in the GCL (Baden et al., 2016; Sabbah et al., 2017), link to downstream visual centers (Cruz-Martín et al., 2014; Huberman et al., 2009; Liang et al., 2018; Shi et al., 2017), and the numerous molecular markers available to target them for mechanistic studies (Dhande et al., 2013; Huberman et al., 2009; Trenholm et al., 2011). In both transgenic lines, the preferred directions of On-Off DSGCs cluster along the four cardinal directions (**Figure 5.4D**), suggesting that both the Vglut2 and Thy1 lines can be used to study all four subpopulations of On-Off DSGCs (nasal, temporal, dorsal, and ventral preferring). Analysis of the cumulative distributions of DSIs from On-Off DSGCs (n = 153 cells from 4 Vglut2 mice; n = 111 cells from 4 Thy1 mice) indicate that the DSI distributions from both mouse lines are not statistically different from each other (p = 0.1560, KS statistic = 0.1385, KS test; **Figure 5.4C**). The evidence presented here demonstrates that similar populations of RGC subtypes can identified through functional imaging using both Vglut2 and Thy1 transgenic GCaMP6 lines, including feature selective RGCs.

5.3.3 Dissection of retinal circuits through population functional imaging

Pharmacological and genetic manipulations are used to manipulate synaptic loci in retinal circuits and study the role they play in generating the distinct visual channels that encode information

leaving the retina. While both the Vglut2 and Thy1 transgenic lines are well suited for pharmacology experiments, they each possess advantages and disadvantages regarding genetic manipulations. For example, the Vglut2 line allows GCaMP6 expression to be driven by Cre-recombinase. This mouse line is compatible with other Cre-dependent manipulations of postsynaptic components in RGCs, such as receptors, voltage-gated ion channels, and proteins involved in biochemical cascades. On the other hand, the Thy1 line expresses GCaMP6 in a Cre-independent fashion making this mouse line compatible with both presynaptic and postsynaptic genetic manipulations that use the Cre-lox system. Here, we demonstrate that by introducing the *ChAT-IRES-Cre* and $Vgat^{flox/flox}$ transgenes into the Thy1 mouse line we can selectively knockout the vesicular GABA transporter (VGAT) in starburst amacrine cells (SACs) (Pei et al., 2015) with the intention of studying how the population of On-Off DSGCs is affected when asymmetric inhibition from SACs is disrupted (**Figure 5.5A**).

We recorded calcium transients from 356 RGCs from 3 Vgat KO mice during moving bar visual stimulation and analyzed their light response characteristics. In the Vgat KO mouse, we identified 35.66% ± 5.46 On-Off (versus 34.62% ± 1.54 in Thy1 mouse; n.s. $p = 0.8685$), 30.05 % ± 1.30 On (versus 36.89% ± 3.91 in the Thy1 mouse; n.s. $p = 0.2687$), and 11.44% ± 0.89 Off (versus 10.79% ± 1.46 in the Thy1 mouse, n.s. $p = 0.780$) responses to the moving bar stimulus (**Figure 5.5B**).

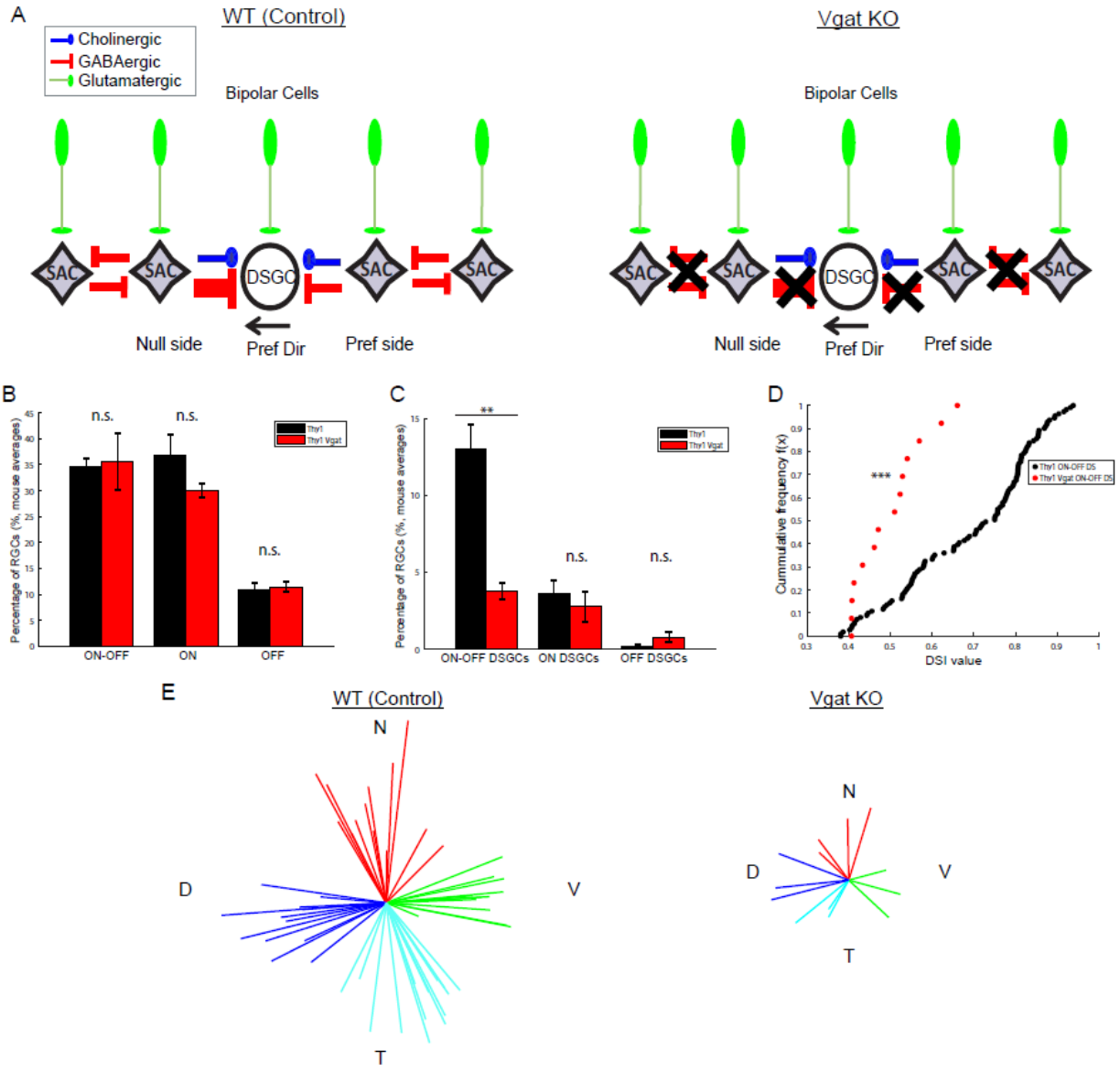

Figure 5.5: Direction selectivity is impaired but not abolished in the *Vgat* KO mouse. (A) Schematic describing genetic manipulation in the Vgat KO mouse. GABA release from SACs is disrupted, eliminating asymmetric inhibition onto DSGCs and mutual inhibition between SACs **(B)** Summary plot showing the percentages of DSGCs in WT Thy1-GCaMP6 (n = 112 On-Off DSGCs, 33 On DSGCs, and 2 Off DSGCs out of 833 RGCs from 4 mice, grey) and Vgat KO Thy1-GCaMP6 (n = 16 On-Off DSGCs, 12 On DSGCs, and 3 Off DSGCs out of 356 RGCs from 3 mice, white) retinas (P = 0.0093 for On-Off DSGCs, n.s. P > 0.05 for On and Off DSGCs). **(C)** Cumulative distributions of On-Off DSGC DSI values for WT Thy1-GCaMP6f (*n* = 112 cells from 4 mice, grey) and Vgat KO Thy1-GCaMP6f (*n* = 16 cells from 3 mice, white), (*P* < 0.001, K-S statistic = 0.6213, Kolmogorov-Smirnov test). **(D)** Quantification of On-Off, On, and Off RGCs in WT Thy1-GCaMP6f (grey, n = 293 On-Off cells, 322 On cells, and 86 Off cells out of 833 RGCs from 4 mice) and Vgat KO Thy1-GCaMP6f (white, n = 123 On-Off cells, 108 On cells, and 40 Off cells out of 356 RGCs from 3 mice) retinas (n.s., P > 0.05).

As expected, we observed a drastic reduction in the fraction of On-Off DSGCs (4.01% ± 0.41 in the Vgat KO versus 13.00% ± 1.57 in the Thy1 mouse, $p = 0.0093$). While direction selectivity is impaired in the Vgat KO, it is not abolished (**Figure 5.5C-D**). Interestingly, there was no statistical difference between the populations of On DSGCs (3.33% ± 1.46 in the Vgat KO versus 3.67% ± 0.89 in the Thy1 mouse, n.s. $p = 0.8687$) and Off DSGCs (0.7645% ± 0.3411 in the Vgat KO versus 0.16% ± 0.14 in the Thy1mouse, n.s. $p = 0.1921$). Additionally, all four subpopulations (nasal, temporal, dorsal, and ventral preferring) of On-Off DSGCs were reduced and no bias towards directional preference was observed.

5.3.4 Neuronal population in the INL

As previously mentioned, both Vglut2-Cre and Thy1-GCaMP6f lines label a population of neurons in the INL (**Figure 5.1**). These neurons have laterally extending dendrites in the OPL and have morphologies that resemble horizontal cells (**Figure 5.6A**). We performed experiments using anti-GAD67 and anti-VGLUT2 primary antibodies to identify the nature of these neurons. The labeled cells in the INL were not immunoreactive to either GAD67 (data not shown) or VGLUT2 stains (**Figure 5.6C**). Further immunohistochemistry experiments staining for Calbindin d28K, a known horizontal cell marker, revealed that these neurons are actually a subset of horizontal cells (**Figure 5.6D**) with an average density of 211.39 ± 34.91 cells/mm2, comprising approximately 16.30% of the entire horizontal cell population according to our Calbindin d28K stain. We therefore analyzed the spatial distribution of the labeled somas and discovered that they form a regular mosaic (regularity index = 2.1359 ; $p < 0.01$ versus a random distribution; n = 455 cells), with ~38 μm distance between somas.

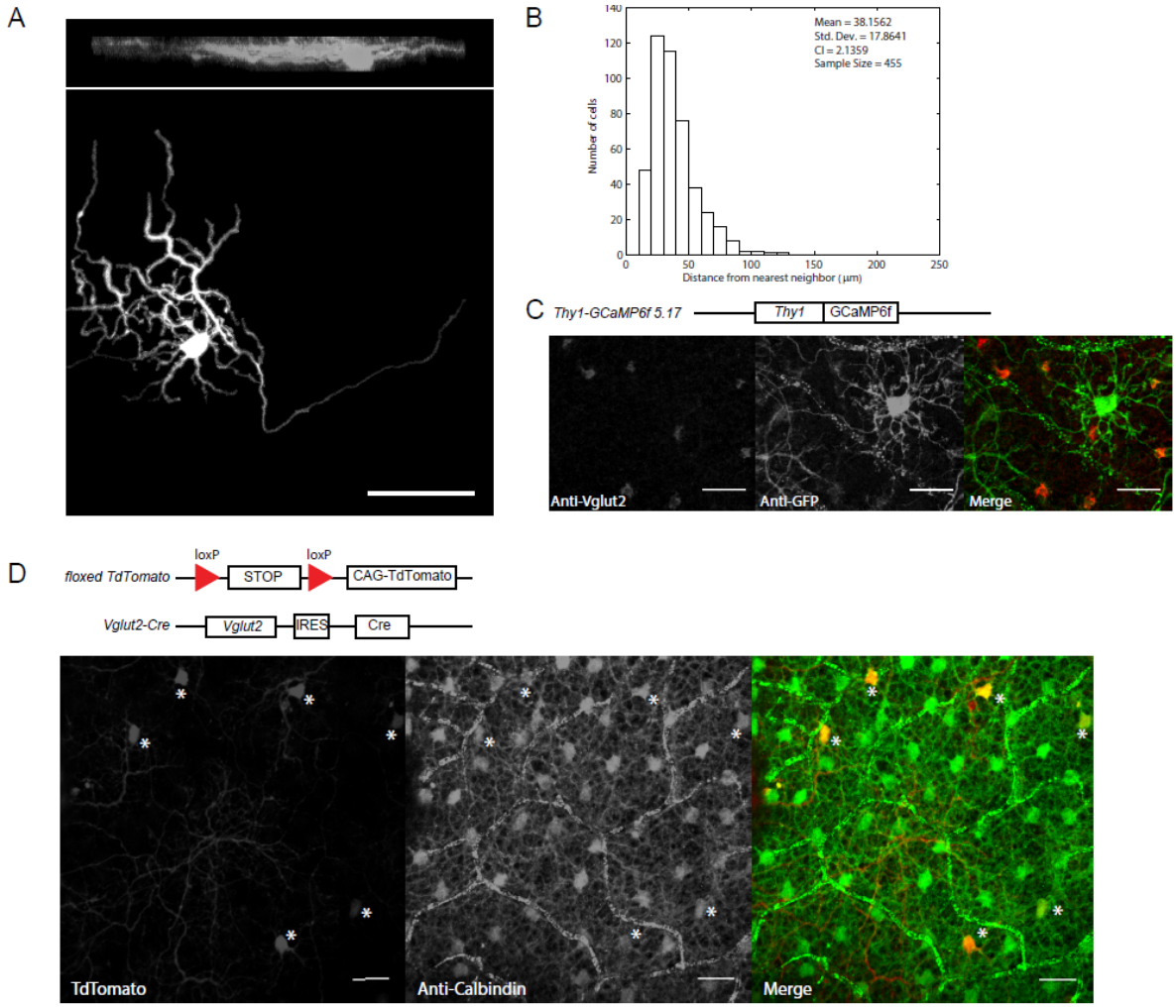

Figure 5..6: Vglut2-IRES-Cre and Thy1-GCaMP6f lines label a subset of mouse horizontal cells. (A) Top: XZ maximum projection of INL labeled cell showing laterally extending dendrites slightly above the soma. Bottom: Reconstruction of a traced and filled INL labeled cell showing horizontal cell-like dendritic morphology. Scale bar, 25 µm. **(B)** Nearest neighbor analysis of INL labeled cells. **(C)** Anti-Vglut2 stain shows clear separation between Vglut2 protein signal and GCaMP6. **(D)** Anti-Calbindin D-28K stain demonstrates co-localization with Vglut2-IRES-Cre signal.

Finally, we tested whether calcium transients could be recorded from the horizontal cell population during light response. For these experiments, we focused on GCaMP6+ cells in the INL from dark-adapted retinas and presented a moving bar visual stimulus as described above. We failed to detect reliable responses using the Thy1-GCaMP6f mouse line because the GCaMP6 signal was weak and it was difficult to detect visual evoked transients from the background noise. On the other

hand, we were able to robustly measure light response from 59/68 horizontal cells using the Vglut2-Cre mouse line (**Figure 5.7**). These neurons showed suppression of GCaMP6 fluorescence upon exposure to bright visual stimulus which rebounded in darkness.

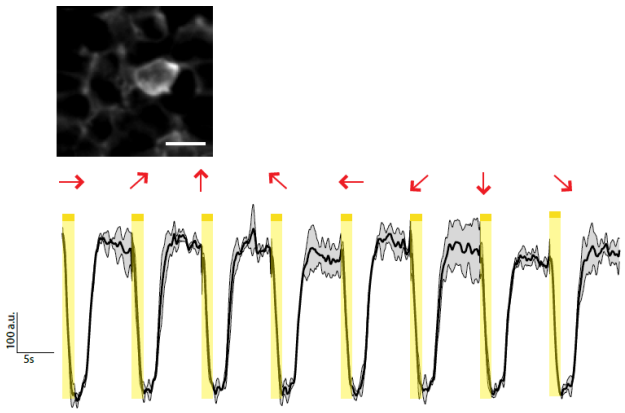

Figure 5.7: Functional imaging in mouse horizontal cells using transgenic expression of GCaMP6. (A) Maximum projection of a representative imaging window for functional imaging of horizontal cells. **(B)** Calcium transients during 275 µm × 880 µm moving bar stimulus.

5.4 Discussion

Transgenic approaches of GECI expression have been advantageous decreasing variability across experiments and diminishing experimental preparation for calcium imaging experiments. The use of transgenic mouse lines expressing GCaMP6 have become more common in systems neuroscience, in which experiments aim to monitor the activity of large populations of neurons in a particular brain area. Despite their advantages, transgenic techniques have not been employed in retina studies in part due to lack of characterization of expression patterns. Here, we characterized two transgenic approaches of expressing GCaMP6 in RGCs: Vglut2-IRES-Cre and Thy1-GCaMP6f 5.17.

Many transgenic mouse lines have focused on expressing GCaMP6 under the Thy1 promoter since it labels most excitatory projecting (axon bearing) neurons (ref). According to this definition, these

mouse lines should target GCaMP6 expression to RGCs. In fact, previous reports using a Thy1-GCaMP3 mouse shows robust expression in the GCL, although a distinction between RGCs and displaced ACs was not made (Chen et al., 2012). Another alternative is to conditionally express GCaMP6 using a combination of Cre-recombinase under a RGC marker and a *floxed GCaMP6f* transgene. The *Vglut2-IRES-Cre* mouse line is an ideal candidate since other major glutamatergic neurons in the inner retina, such as bipolar cells and glutamatergic amacrine cells, use VGLUT1 or VGLUT3, respectively (Della Santina et al., 2016; Haverkamp & Wässle, 2004; S. Lee et al., 2014; Sherry et al., 2003). Our double labeling experiments in **Fig. 5.1** demonstrated that Vglut2-IRES-Cre and Thy1-GCaMP6 5.17 target very similar populations of neurons in the retina. In the GCL, both of these transgenic line exclusively target RGCs (**Figure 5.2**), therefore representing Cre-dependent and independent forms of expressing GCaMP6f in the same neuronal population.

Using two-photon laser scanning microscopy and moving bar visual stimulation, we grouped visual responses into RGC classes according to their light response properties. We chose the moving bar visual stimulus since it allowed us to probe for directional responses and On/Off preference simultaneously. Additionally, many RGC types exhibit enhanced responses to moving stimuli (Grzywacz et al., 1993; C. W. Oyster, 1968). We robustly detected On-Off, On, and Off light responses from both transgenic lines. It is important to note that we observed a dorsal-ventral gradient of GCaMP6f expression in the Thy1-GCaMP6f mouse line, with stronger GCaMP6f signal in the dorsal retina, which could explain subtle differences in On-Off versus On ratios (**Figure 5.3**). Many of light-responsive RGCs exhibit no directional or orientation tuning corresponding to transient/sustained alpha types, suppressed by contrast cells, and local edge detector W3 types (Baden et al., 2016). Our chosen stimulus (250 μm × 800 μm moving bar)

evoked reliable responses from most RGCs (> 90%), but we recognize that this was not optimal for RGCs with large-field excitatory centers or those with small excitatory center and large inhibitory surrounds potentially leading some cells to be categorized as unresponsive.

The percentage of On-Off RGCs (50.77% for Vglut2 and 34.62% for Thy1) we detected greatly surpassed those previously reported in studies utilizing Oregon BAPTA-1 (OGB-1, 20.84%) (Bos et al., 2016) and multi-electrode arrays (21.5%) (Tian & Copenhagen, 2003). This could be due to our choice of moving bar stimulus over stationary light flashes that are commonly used to probe for light-response polarity. Alternatively, it is possible that GCaMP6f's enhanced sensitivity allowed us to detect responses that would otherwise be missed with other techniques.

Among our sampled RGC population, we detected several types of DSGCs (14.76% for Vglut2 and 16.83% for Thy1). According to preliminary data from sequential calcium imaging and single-unit recordings from individual cells, a DSI ≥ 0.35 criterion for calcium imaging correlates to a DSI ≥ 0.20 for spiking. On-Off DSGCs were the most numerous compared to other RGC types consistent with previous studies (Baden et al., 2016; Bos et al., 2016; Sabbah et al., 2017). The speed of the moving bar stimulus (400 μm/s) was within the preferred range for On-Off DSGCs; but, it might fail to reveal certain On directional responses such those associated with slow On DSGCs (W. Sun et al., 2006). Although small in numbers, we also identified RGCs with robust Off directional responses (I. J. Kim et al., 2008).

To demonstrate that these transgenic lines are compatible with genetic manipulations for microcircuit dissection at the population level, we generated a Thy1-GCaMP6f mouse in which the *Vgat* gene was conditionally knocked out in starburst amacrine cells (SACs) (Pei et al., 2015).

This allowed us to study the dependency of retinal direction selectivity to asymmetric inhibition from the entire DSGC population. We detected similar distributions of On-Off, On, and Off RGCs in the *Vgat* KO mouse suggesting RGC laminar targeting and On/Off segregation is unaffected by eliminating SAC GABA release. Orientation sensitive responses were also unaffected by the *Vgat* KO manipulation adding evidence for minimal developmental compensation in this mouse model (data not shown).

As expected, we observed a significant reduction in On-Off directional responses in the *Vgat* KO mouse (Pei et al., 2015; Shi et al., 2017). All four subtypes of On-Off DSGCs were similarly affected by eliminating SAC GABA release. However, preferred directions failed to cluster along the four cardinal directions in the *Vgat* KO mouse and RGCs with On-Off directional responses (DSI $\geq$ 0.35) had lower tuning strength compared to wildtype mice. This suggests that asymmetric inhibition onto DSGCs is required for optimal tuning and clustering of preferred directions. In the absence of asymmetric inhibition, direction selectivity could be achieved by mechanisms that traditionally work in parallel with directional inhibition including direction selective excitation (Pei et al., 2015; Percival et al., 2019), dendritic bias (Trenholm et al., 2011), and dendritic conductances (Sivyer & Williams, 2013). Remaining directional tuning following application of GABA-A receptor antagonists has been attributed to dendritic bias in ventral-preferring Hb9+ On-Off DSGCs (Trenholm et al., 2011); however, morphological asymmetry has not been observed in other subtypes and therefore cannot explain all directional responses in the *Vgat* KO mouse. It is possible that direction-selective cholinergic excitation, such as that observed in a subpopulation of nasal-preferring Drd4+ On-Off DSGCs (Pei et al., 2015), is widespread among DSGC subtypes explaining these directional responses.

Interestingly, we did not observe differences in the abundance of On or Off directional responses in the *Vgat* KO mouse compared to wildtype. Directional tuning in Off DSGC has been attributed to a strong morphological bias along the preferred direction, allowing these cells to compute direction selectivity independently of asymmetric inhibition due to passive cable properties (I. J. Kim et al., 2008). In On DSGCs, directional responses can be mediated through asymmetric spatiotemporal integration of excitatory inputs (Matsumoto et al., 2019) and generation of dendritic spikes (Brombas et al., 2017).

In addition to their targeting in the GCL, we found that *Vglut2-IRES-Cre* and *Thy1-GCaMP6f* mouse line label neurons in the INL, which we then confirmed as a subset of horizontal cells. This was surprising since horizontal cells are considered to be inhibitory neurons and both Vglut2 and Thy1 are traditional excitatory markers. We failed to detect any VGLUT2+ puncta in these neurons leaving the question whether these are in fact glutamatergic horizontal cells still unanswered. One possible scenario is that these neurons release glutamate earlier on in development and downregulate their VGLUT2 expression by the third postnatal week. Regardless of whether these are glutamatergic horizontal cells of not, GCaMP6f can be expressed these neurons using the Vglut2-Cre and Thy1-GCaMP6f mouse lines. Viable calcium responses were recorded from the somas of these neurons; however, they are sparse enough that individual dendrites can be traced and potentially imaged.

5.5 Experimental Procedures

Mice

Vglut2-IRES-Cre (Slc17a6$^{tm2(cre)Lowl}$), Ai95 floxed GCaMP6f (129S-Gt(ROSA)26Sor$^{tm95.1(CAG-GCaMP6f)Hze}$/J), floxed *tdTomato* (129S6-*Gt(ROSA)26Sor$^{tm9(CAG-tdTomato)Hze}$*/J), *Vgat$^{flox/flox}$* (*Slc32a1<tm1Lowl>/J*), and *Chat-IRES-Cre* (129S6-Chat$^{tm2(cre)Lowl}$/J) mice were acquired from the Jackson Laboratory. All strains were backcrossed to the *C57BL/6* background in our laboratory, and crossed to each other to create the lines used in this study. Mice of ages P21-P28 of either sex were used. All procedures to maintain and use mice were in accordance with the University of Chicago Institutional Animal Care and Use Committee (Protocol number ACUP 72247) and in conformance with the NIH Guide for the Care and Use of Laboratory Animals and the Public Health Service Policy.

Whole-mount retina preparation

After dark adaptation for > 30 min, mice were anesthetized with isoflurane and euthanized by decapitation. Retinas were isolated from the pigment epithelium under infrared illumination at room temperature in oxygenated Ames' medium (Sigma-Aldrich, St. Louis, MO). Slits were cut on the whole retinas to mark the cardinal directions and then mounted ganglion-cell-layer-up on top of a 3.5-4 mm^2 hole in a small piece of filter paper (Millipore, Billerica, MA). For immunohistochemistry experiments, retinas were cut into dorsal and ventral halves and mounted on top of a 1-1.5 mm^2 hole in a small piece of filter paper. The mounted retinas were kept in darkness at room temperature in Ames' medium bubbled with 95% O_2/5% CO_2 until use (0–8 hr).

Immunohistochemistry

Retinas were fixed in paraformaldehyde (PFA, 4% wt/vol in PBS) for 20 mins on a 24-well plate. Following fixation, the 24-well plate was plate on a shaker and the retina pieces were washed in

PBS three times for 20 mins. The retina pieces were incubated in block solution (10% donkey serum, 1% BSA and 0.5% TritonX in PBS) 3X for 20 mins. The retina pieces were incubated with one or more of the following primary antibodies for 72 hours at 4°C: mouse anti-GFP (1:500, Millipore #MAB3580) to enhance the fluorescence of the GFP-based GCaMP6f indicator, mouse anti-GAD67 (1:500, #MAB5406) to label GABAergic amacrine cells, rabbit anti-Vglut2 (1:1000, Synaptic Systems #135403) to verify expression of the vesicular glutamate transporter 2 protein, and mouse anti-Calbindin (1:500, Sigma Aldrich C9848), a known horizontal cell marker. After primary antibody incubation, the retina pieces were rinsed with block solution 3X for 20 mins on the shaker at room temperature. The retina tissues were then incubated Alexa-conjugate secondary antibodies at 1:750 or 1:1000 concentrations for 5 hours. Following secondary antibody incubation, the retina tissues were rinsed in PBS 3X for 20 mins. The retina pieces were left in the last PBS wash for 2 hours before mounting. The retina tissues were then mounted onto glass slides using Vectashield and imaged using a laser scanning Ti:sapphire two-photon microscope.

Visual stimulation

A white organic light-emitting display (OLEDXL, eMagin, Bellevue, WA; 800 × 600 pixel resolution, 60 Hz refresh rate) was controlled by an Intel Core Duo computer with a Windows seven operating system and was presented to the retina at a resolution of 1.1 μm/pixel. Moving bar stimuli were generated by MATLAB and the Psychophysics Toolbox (Brainard, 1997), and projected through the condenser lens of the two-photon microscope onto the photoreceptor layer. For the moving bar stimulus, a positive-contrast bar (220 μm wide, 880 μm long) moved along the long axis in 8 pseudo-randomly chosen directions at a speed of 440 μm/sec over a 660μm-diameter field on the retina; and four trials were recorded for each direction. The percent stimulus contrast

was calculated as ($L_{stimulus} - L_{background}$)/ ($L_{stimulus} + L_{background}$). Unless otherwise noted (i.e., **Figure 7D**), the intensity of the moving bar was ~6.3×104 isomerizations (R*)/rod/s, lying in the photopic range, and the background intensity was ~1800 R*/rod/s, lying at the lower end of the photopic range.

Two-photon calcium imaging of GCaMP6 fluorescence

GCaMP6 fluorescence of isolated retinas in oxygenated Ames at 32–33°C was imaged in a customized two-photon laser scanning fluorescence microscope (Bruker Nano Surfaces Division). GCaMP6 was excited by a Ti:sapphire laser (Coherent, Chameleon Ultra II, Santa Clara, CA) tuned to 920 nm, and the laser power was adjusted to avoid saturation of the fluorescent signal. Onset of laser scanning induces a transient two-photon response that adapts to the baseline in ~3 s. Therefore, to ensure the complete adaptation of this laser-induced response and a stable baseline, visual stimuli were given after 10 s of continuous laser scanning. To separate the visual stimulus from GCaMP6 fluorescence, a band-pass filter (Semrock, Rochester, MA) was placed on the OLED to pass blue light peaked at 470 nm, while two notched filters (Bruker Nano Surfaces Division) were placed before the photomultiplier tubes to block light of the same wavelength. The objective was a water immersion objective (20x, Olympus). Time series of each imaging window (~100×100 μm at the GCL and ~25×25 μm in the INL) were collected at 17 Hz or higher.

Data Analysis

Analysis was performed using ImageJ and MATLAB. Raw frames were uploaded onto ImageJ software in which regions of interest (ROIs) were manually drawn to enclose the soma of each GCaMP6 expressing cell and for a background region where there was no detectable GCaMP6s

expression. These manually selected ROIs were then imported into MATLAB, where custom written scripts were used to calculate the average intensity over time for all ROIs. In MATLAB, the background trace was subtracted from the light responsive somatic traces to remove noise. The background subtracted traces were then truncated and sorted by direction of the moving bar stimulus. We calculated a quality index (QI) to measure how well a given cell responded to the visual stimulus (Baden et al., 2016). If all trials are identical such that the mean response is a perfect representative of the response, QI is equal to 1. On the other hand, if all trials are completely random with fixed variance (so that the mean response is not informative about the individual trial responses), QI falls towards 0. We implemented a quality threshold of QI ≥ 0.45 for the response from a given cell to be considered for further analysis.

If the light response from a cell passes the quality test, then for moving bar stimulus presentation, the peak of each calcium transient was used to calculate $\Delta F/F_0$ = (F−F0)/F0, where F0 was the mean of the baseline signal over a fixed interval of 1 sec before any stimulus onset. For each cell, we calculated the DS angle and DSI=$(R_{pref}-R_{opp})/(R_{pref}+R_{opp})$, where R_{pref} is the cell's response at the preferred direction (i.e., maximal response), and R_{opp} is the cell's response to the direction opposite to the preferred one. Tuning curves were plotted using the average $\Delta F/F_0$ for each direction. The 880μm long bar allows for clear separation between responses to the leading and trailing edge of the moving bar. Cells showing responses to the leading edge were classified as On, cells showing responses to the trailing edge were classified as Off, and cells showing responses to both leading and trailing edges were classified as On-Off.

Chapter 6

On-Off retinal axial selective receptive fields and their developmental timeline

6.1 Introduction

The detection of salient features from the environment is fundamental for guiding animal behavior and crucial to survival. In the visual system, certain neurons fire action potentials selectively to a particular orientation of an edge or contour in the visual scene (Hubel & Wiesel, 1959). This property – termed axis or orientation selectivity – is widely observed across multiple structures in the early visual pathways (Niell & Stryker, 2008; Zhao et al., 2013) and is first encoded in the retina by orientation selective ganglion cells (OSGCs) (Antinucci & Hindges, 2018; Levick & Thibos, 1980). OSGCs have been reported across multiple species (Levick, 1967; Levick & Thibos, 1980; Nath & Schwartz, 2016; Venkataramani & Taylor, 2010), making it a highly conserved retinal cell-type. Orientation selective ganglion cells (OSGCs) with a diversity of light response properties have been reported in the mammalian retina (Antinucci et al., 2016; Baden et al., 2016) and their axons have been shown to project to the outer shell of the lateral geniculate nucleus (LGN) (Liang et al., 2018), suggesting a possible influence of retinal orientation selectivity in the retino-geniculo-cortical pathway. Despite encoding a fundamental feature and comprising a

significant fraction (~ 15%) of the RGC population, OSGCs are less understood compared to other RGC types.

Orientation sensitive receptive fields have been extensively studied in the rabbit retina (Levick, 1967; Venkataramani & Taylor, 2010, 2016) and more recently in the mouse retina (Nath & Schwartz, 2016, 2017). On and Off OSGCs with preferred orientation along the cardinal axes (nasal-temporal and dorsal-ventral) have been identified (Baden et al., 2016), suggesting these can be subdivided into horizontal- and vertical- preferring subtypes (Nath & Schwartz, 2016, 2017; Venkataramani & Taylor, 2010, 2016). Horizontal- and vertical-preferring Off OSGCs exhibit asymmetric elongated dendritic fields biased along the preferred orientation (Nath & Schwartz, 2017; Venkataramani & Taylor, 2010), while such dendritic asymmetry was only observed in horizontal-preferring On OSGCs (Nath & Schwartz, 2016). Additionally, GABAergic and glycinergic inhibition have been implicated in both On and Off retinal orientation sensitivity through a variety of circuit mechanisms, including direct inhibition (Nath & Schwartz, 2016), presynaptic inhibition (Venkataramani & Taylor, 2010), and disinhibitory motifs (Venkataramani & Taylor, 2016). Large-scale surveys of visual-evoked activity from GCL using multi-electrode arrays (H. Chen et al., 2014) and calcium imaging (Baden et al., 2016) have reported orientation-tuned RGCs with responses to both light onset and offset suggesting the possibility of an On-Off OS type.

Furthermore, the lack of molecular markers have limited developmental studies focusing on retinal orientation sensitive receptive fields. Orientation tuned receptive fields have been observed in the retina at the time of eye-opening (H. Chen et al., 2014), but whether these retinal circuits continue

to mature upon visual experience has not been explored. After the termination of stage II cholinergic retinal waves (P10), neural activity in the mouse retina is dominated by stage III glutamatergic waves (Kerschensteiner, 2016) and light-evoked activity through closed eyelids (Tiriac et al., 2018). At this stage activity-dependent mechanisms are not believed to play an instructive role in the development of retinal receptive fields (Elstrott & Feller, 2009), but could be important for the refinement of receptive field properties and synaptic connections (Bos et al., 2016). For example, light-evoked DS responses in the retina have been observed as early as P11 (2 days prior to eye-opening) and asymmetric wiring between SACs and DSGCs develop in the absence of retinal waves and visual experience. Although visual experience is not required for generating retinal direction selectivity, visual experience plays a role in clustering the preferred directions of DSGCs along the four cardinal axes potentially through reorganization of dendrite orientation. In comparison, the developmental mechanisms that give rise to OS RFs are completely unknown.

Here, we use two-photon laser-scanning calcium imaging and transgenic expression of GCaMP6f to monitor complex receptive fields in the mouse retina across developmental stages. Our findings demonstrate that On-Off OSGC are a prominent retinal cell type that undergoes significant maturation during the first week after eye-opening. This developmental increase in On-Off orientation tuned receptive fields was unaffected by visual deprivation from P9 – P28. Additionally, On-Off OSGCs exhibit an antagonistic center-surround receptive field structure and their tuning is sensitive to GABA-A receptor antagonists. On-Off OSGCs represent a novel retinal channel encoding for the orientation of object within the visual scene whose developmental timeline extends beyond the onset of visual experience.

6.2 Results

6.2.1 Identification of orientation-sensitive RGCs in the mature mouse retina

We employed two-photon laser scanning calcium imaging during visual stimulation (**Figure 6.1A**) in effort to describe the diversity of orientation sensitive responses in the mouse RGC population. GCaMP6f was expressed exclusively in RGCs by crossing *floxed-GCaMP6f* and *Vglut2-IRES-Cre* transgenic mice in our laboratory (characterized in Chapter 5). This technique resulted in uniform labeling of RGCs (**Figure 6.1A**) without causing retinal damage (Chapot et al., 2017; Dana et al., 2014) and diminished variability between experimental days. We stimulated retinas with a bright 250 μm × 800 μm bar moving at 400 μm/s in 8 pseudorandom directions in order to simultaneously probe for direction- and orientation-sensitive responses. Prior to further classification, RGC responses were subjected to a quality test (QI ≥ 0.45) to ensure consistency across trials (Baden et al., 2016). RGCs with OSI ≥ 0.4 were identified as OSGCs and those with DSI ≥ 0.4 were identified as DSGCs. If the OSI and DSI of a given RGC were both ≥ 0.4, they would be labeled according to their stronger selectivity index. Furthermore, RGCs were classified as On-Off, On, or Off according to their responses to the leading and trailing edges of the moving bar and their respective ON-OFF index (see Experimental Procedures).

We recorded GCaMP6f signals from 108 field of views (99.5 μm × 99.5 μm, at 17.2 Hz) from 12 mice, each containing 35 ± 14 RGCs (mean ± std). In total, we sampled 3,708 RGCs from postnatal day 21 – 30 mice and 93% of the somas exhibited reliable visual-evoked responses. For the experiments below, we utilize On-Off DS responses as controls since these have been extensively described in the mouse retina (Baden et al., 2016; Bos et al., 2016; Huberman et al., 2009; Sabbah et al., 2017). We detected RGCs exhibiting On-Off (50.77% ± 0.26, ON-OFF index = 0.14 ± 0.007,

mean ± s.e.m), On (25.92% ± 1.16, ON-OFF index = 0.47 ± 0.01, mean ± s.e.m), and Off (11.97% ± 0.55, ON-OFF index = -0.25 ± 0.02, mean ± s.e.m) responses to the moving bar stimulus (mean ± s.e.m). Among this population we identified On-Off, On, and Off OSGCs (**Figure 6.1B**). In response to our 250 µm × 800 µm moving bar stimulus, On-Off OSGCs are the most numerous representing 8.67 ± 0.97% of the entire RGC population, compared to 2.75 ± 0.86% and 1.21 ± 0.74% for On and Off OSGCs respectively (**Figure 6.1C**). On-Off DS responses comprised 11.33 ± 1.02% of the RGC population which agrees with previous studies (Baden et al., 2016; Sabbah et al., 2017). This data indicates that On-Off OS receptive fields represent a major output channel of the mouse retina.

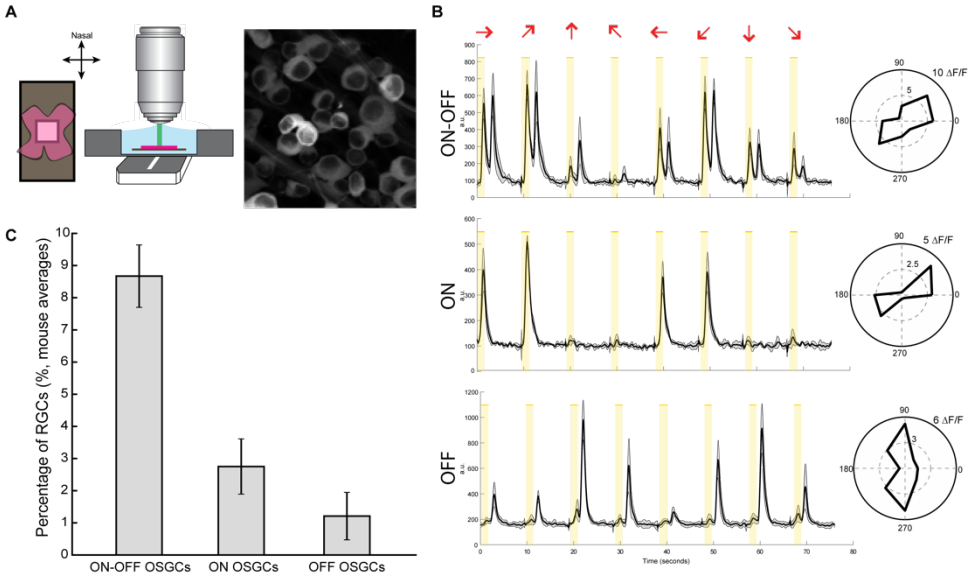

Figure 6.1. Diversity of orientation-sensitive ganglion cells (OSGCs) in the mouse retina. (A) Left: Schematic showing experimental setup for two-photon calcium imaging during visual stimulation. Right: Maximum projection of GCaMP6f-expressing RGCs in the Vglut2-IRES-Cre mouse. **(B)** Representative traces of On-Off (top), On (middle), Off (bottom) OSGCs in response to 250 µm × 800 µm moving bar visual stimulation. **(C)** Quantification of On-Off, On, and Off OSGCs in the mature mouse retina.

6.2.2 Development of On-Off OS responses in the mouse retina extends beyond the onset of visual experience

Although major developmental processes involved in murine retinal circuit formation, such as laminar targeting and synaptogenesis, are considered to finalized by eye-opening, recent work has demonstrated that circuit refinement continues well beyond the onset of visual experience (Bos et al., 2016; H. Chen et al., 2014; Dunn et al., 2013; Tian & Copenhagen, 2003). OSGCs represent a major output channel of the mammalian retina; yet, nothing is known regarding the developmental time course of orientation sensitive receptive fields or whether these are subject to experience-dependent plasticity. To ensure similar sensitivity as the mature retina, optimal GCaMP6 expression in RGCs must be achieved early on development. The onset of GCaMP6 expression through transgenic approaches is tied to the specific activation timeline of chosen promoters. Expression of VGLUT2 in the mouse GCL begins at the end of the first postnatal week (Rauen et al., 1996; Wässle et al., 2006) suggesting that the use of *Vglut2-IRES-Cre* to express GCaMP6 would lead to viable accumulation of in RGCs by the onset of visual evoked activity (P10).

Similar as above, we performed two-photon laser scanning calcium imaging during moving bar visual stimulation just prior to eye-opening (P12-14). Using the same criteria (QI $\geq$ 0.45 and OSI $\geq$ 0.4), we identified all three types of orientation sensitive responses prior to eye-opening (On-Off: 2.03 ± 0.48%, On: 2.36 ± 0.72%, and Off: 0.92 ± 0.30%); however, the abundance of On-Off OS responses were significantly lower compared to one week after eye-opening (P12 – 14: 2.03 ± 0.48% versus >P21: 8.67 ± 0.97%, $p = 2 \times 10^4$ Student t-test). This developmental increase in OS responses was not biased towards a particular preferred orientation (**Figure 6.2C-D**). At both developmental stages, enhanced average silhouette values were observed when a total of two clusters were used to group the preferred axes (**Figure 6.2B**). The centroids of these clusters aligned with the cardinal axes suggesting that both horizontal- and vertical-preferring On-Off OS

responses were found prior to eye-opening and one week after eye-opening. Furthermore, in both populations the distribution of preferred orientations could be accurately described by a von Mises distribution (**Figure 6.2C-D**).

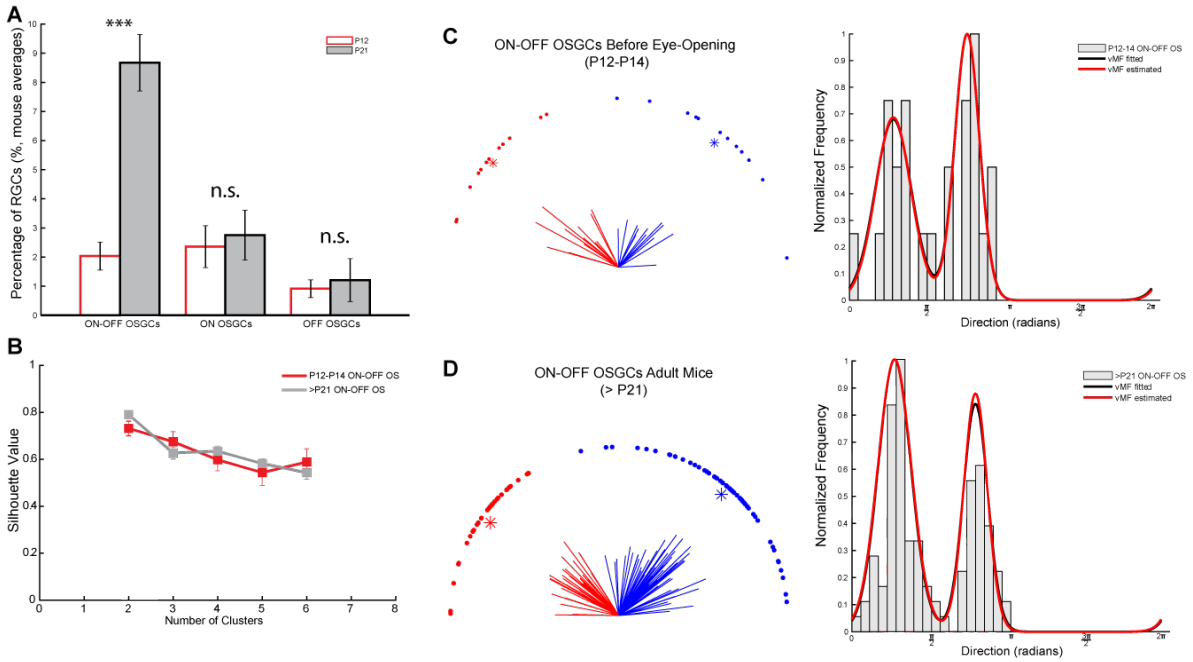

Figure 6.2: Increase in abundance of On-Off OS responses during the first week after eye-opening. (A) Quantification of On-Off, On, and Off OSGCs prior to eye-opening (P12-14) and one week after eye-opening (P21-25). **(B)** Average silhouette values as a function of the different cluster numbers (2-6 clusters) for On-Off OSGC prior to eye-opening (red) and one week after eye-opening (gray). Polar plots of preferred axes from On-Off OSGCs prior to eye-opening **(C, left)** and one week after eye-opening **(D, left)**. Horizontal (blue) versus vertical (red) preferred axes were clustered using k-means clustering using k = 2 clusters. Asterisks represent the centroid of each cluster and the length of each axis corresponds to strength of their vector sum, or gOSI. Normalized histograms of preferred axis distributions from On-Off OSGCs prior to eye-opening **(C, right)** and one week after eye-opening **(D, right)**. von Mises distributions calculated using parameters (centroid and dispersion of each cluster) from experimental data (red) and fitted using a maximum-likelihood estimator (black).

By comparison, the abundance of direction selective responses was relatively unchanged. There was a slight decrease in On-Off DSGCs (P12 – 14: 11.62 ± 0.86% versus >P21: 9.34 ± 0.62%) and increase in On DSGCs (P12 – 14: 1.75 ± 0.25% versus >P21: 2.87 ± 0.51%), but these were not significant (**Figure 6.3A**). Although retinal direction selectivity is established prior to eye-opening (Elstrott et al., 2008), we observed refinement in the clustering of preferred directions

consistent with previous studies (Figure 6.3D-C) (Bos et al., 2016). For instance, the preferred directions from the "mature" On-Off DSGC populations exhibited a sharp increase in average silhouette value when the number of clusters were increased from 3 to 4. Whereas, the silhouette values for the population prior to eye-opening appear to be randomly distributed according to cluster number (Figure 6.3B). One week after eye-opening the preferred directions of On-Off DSGCs cluster along the four cardinal directions (nasal, temporal, dorsal, and ventral). On the other hand, prior to eye-opening silhouette value analysis predicts tighter clustering with 3 groups; but, their distrubutions cannot be recapitulated well by a mixture of three Gaussian distributions (**Figure 6.3**). Lastly, we detected similar percentages of RGCs displaying On-Off, On, and Off responses prior to eye-opening compared to one week after eye opening (P21-24) ($p > 0.05$ Student t-test, data not shown); however, there was a strong bias for stronger Off responses compared to On prior to eye-opening (**Figure 6.4**).

6.2.3 Visual experience does not play a role in the maturation of On-Off OS receptive fields

The timeline of the above described increase in abundance of On-Off OS responses coincides with the onset of visual experience making us wonder if visual-evoked activity plays an instructive role in the formation of these complex receptive fields. To address this question, we raised mouse pups from the *Vglut2-IRES-Cre/floxed-GCaMP6f* line in complete darkness from P9-P28. Two-photon calcium imaging was performed as previously described.

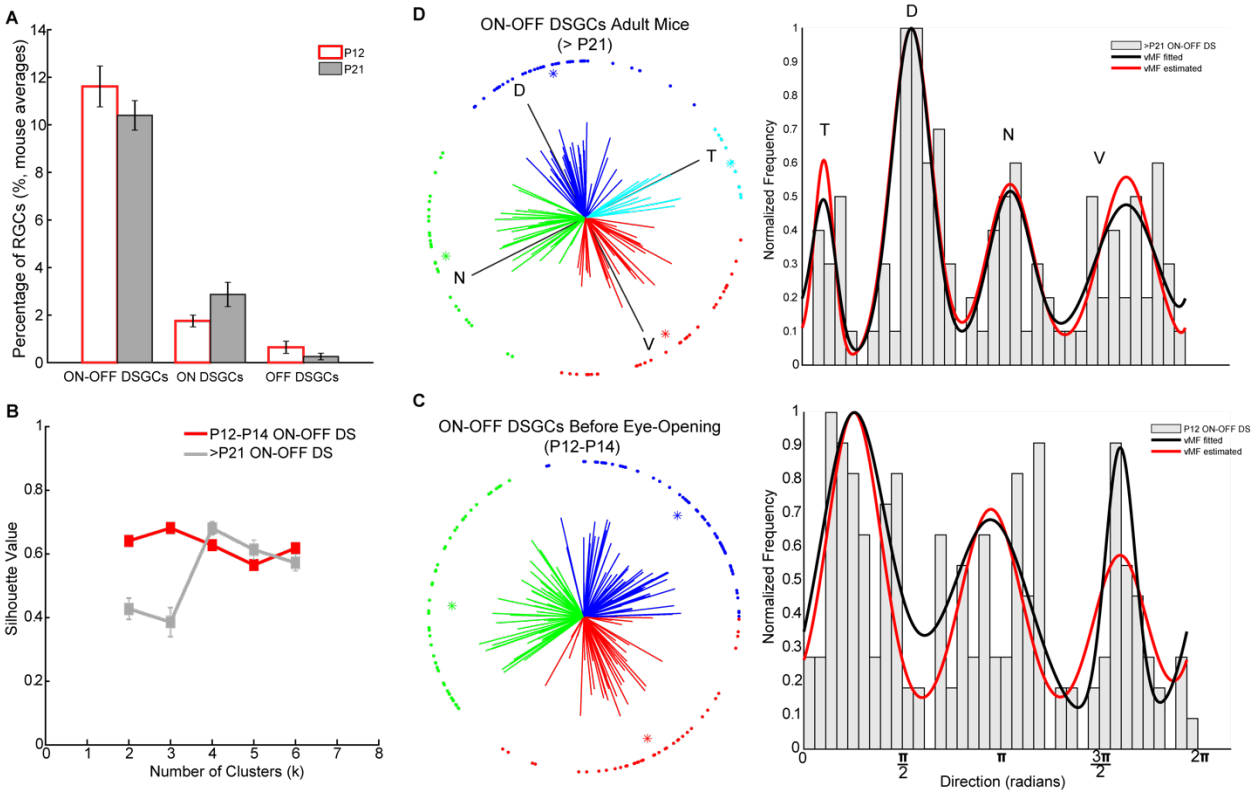

Figure 6.3: On-Off DSGCs do not show similar developmental patterns compared to On-Off OSGCs. (A) Quantification of On-Off, On, and Off DSGCs prior to eye-opening (P12-14) and one week after eye-opening (P21-25). **(B)** Average silhouette values as a function of the different cluster numbers (2-6 clusters) for On-Off DSGC prior to eye-opening (red) and one week after eye-opening (gray). Polar plots of preferred directions from On-Off DSGCs prior to eye-opening **(C, left)** and one week after eye-opening **(D, left)**. "Adult" On-Off DSGC preferred directions were clustered into 4 groups corresponding to nasal (green), temporal (cyan), dorsal (blue), and ventral (red). P12-14 On-Off DSGC preferred directions were clustered into 3 groups. Asterisks represent the centroid of each cluster and the length of each axis corresponds to strength of their vector sum, or gDSI. Normalized histograms of preferred direction distributions from On-Off DSGCs prior to eye-opening **(C, right)** and one week after eye-opening **(D, right)**. von Mises distributions calculated using parameters (centroid and dispersion of each cluster) from experimental data (red) and fitted using a maximum-likelihood estimator (black).

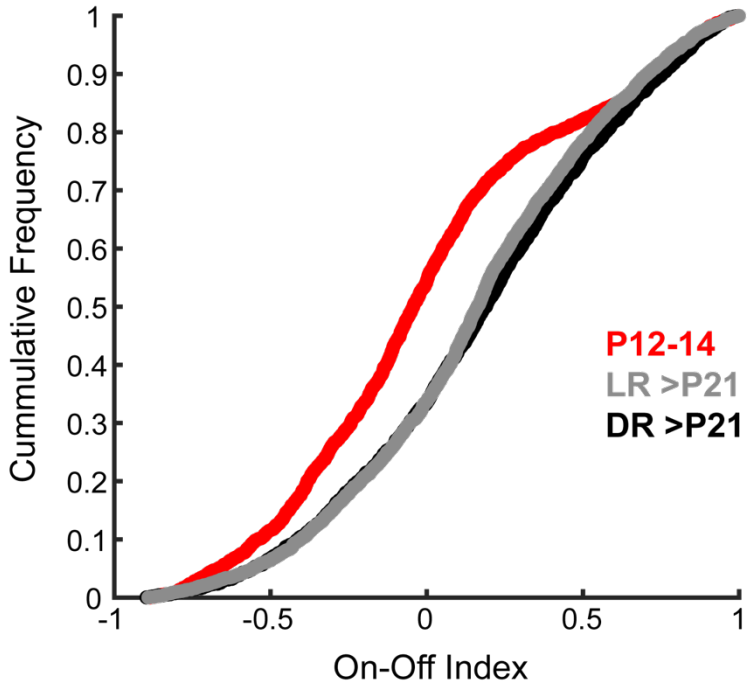

Figure 6.4: Comparison of On-Off index distribution between Vglut2+ RGCs prior to eye-opening (P12-14), light-reared adults, and dark-reared adults.

In summary, neither direction-selective or orientation sensitive responses were affected by dark-rearing. On-Off OS responses were detected at similar levels compared to light-reared animals (**Figure 6.5B**). The abundance of On-Off DSGCs in dark-reared mice were comparable to both P12 – 14 and >P21 light-reared mice (**Figure 6.5A**). Interestingly, despite no difference On-Off DS abundance we found that On-Off DSI distribution in P12 – 14 mice was significantly leftward shifted compared to adult retinas (KS-test, $p = 4.7 \times 10^{-6}$) (**Figure 6.5C**). Similarly, On-Off OSIs from P12 – 14 mice were leftward shifted compared to mature retinas (KS-test, $p = 4.5 \times 10^{-4}$) (**Figure 6.5D**). Visual deprivation from P9 – 28 did not lead to changes in tuning strength in On-Off DSGCs or On-Off OSGCs compared to light-reared adults (KS-test, $p > 0.05$). Although directional tuning was unaffected by dark-rearing, clustering analysis failed to show an increase in average silhouette values at $k = 4$ compared to animals raised in 12-hr light-dark cycles (data not shown). On-Off OS responses in dark-reared and light-reared animals showed similar trends

in silhouette values; however, dark-reared average silhouette values were lower across all cluster numbers compared to light-reared mice (data not shown). These experiments demonstrate that the developmental increase in On-Off OS response we observed in the mouse retina is not dependent on visual experience occurring between P9 – 28.

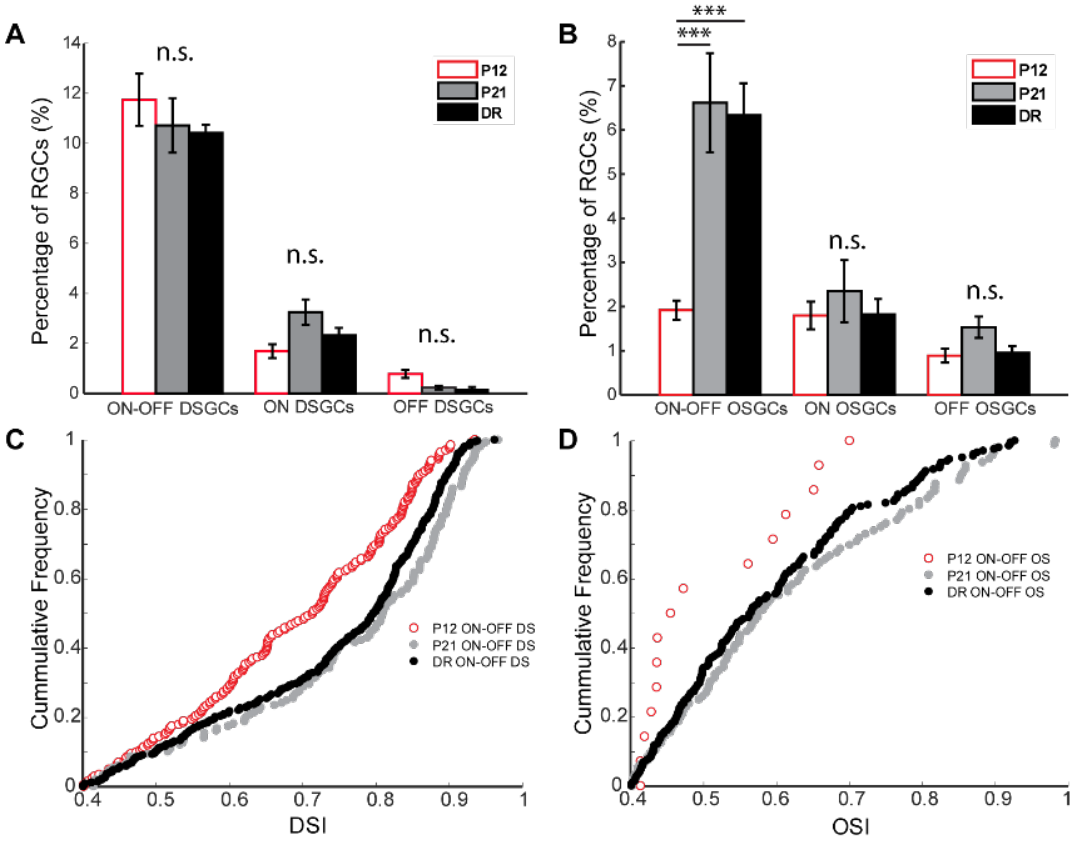

Figure 6.5: Developmental increase in On-Off OSGCs is unaffected by dark-rearing. (A) Quantification of On-Off DSGCs in P12-P14 (red), > P21 light-reared (gray), and > P21 dark-reared (black) mice. **(B)** Quantification of On-Off OSGCs in P12-P14 (red), > P21 light-reared (gray), and > P21 dark-reared (black) mice. **(C)** Cummulative distributions of On-Off DSIs (C) and On-Off OSIs **(D)** from P12-P14 (red), >P21 light-reared (gray), and > P21 dark-reared (black) mice.

6.2.4 Response properties of On-Off orientation sensitive receptive fields

To further characterize On-Off OS receptive fields, we stimulated mature retinas with three moving bar visual stimuli: (1) a wide bar (600 µm × 800 µm), (2) standard "narrow" bar (250 µm

× 800 μm), and (3) vertical bar (600 μm × 90 μm). Calcium responses to the wide and vertical bar will be compared to the narrow bar used above. We will test interactions between the surround and the excitatory center using the wide bar stimulus and determine spatial asymmetry with the vertical bar.

On-Off OS responses comprised 2.03 ± 0.09% of all responses when stimulated a wide moving bar compared to 7.54 ± 0.54% when stimulated with a narrow moving bar. We therefore utilized responses to the narrow bar to identify On-Off OSGCs and compared strength in orientation tuning and amplitude of preferred responses across all three visual stimuli (**Figure 6.6**). Responses to the wide and vertical bars yielded smaller OSI compared to responses to the narrow moving bar ($p < 0.001$, paired Student t-test). OSI differences emerged due to lower preferred-axis responses to both vertical and wide moving bar (**Figure 6.6**, $p < 0.001$, paired Student t-test), rather than enhanced responses along the null axis (data not shown). These results are consistent with the idea of an antagonistic center-surround receptive field structure and On-Off OS sensitivity to local stimuli (Baden et al., 2016).

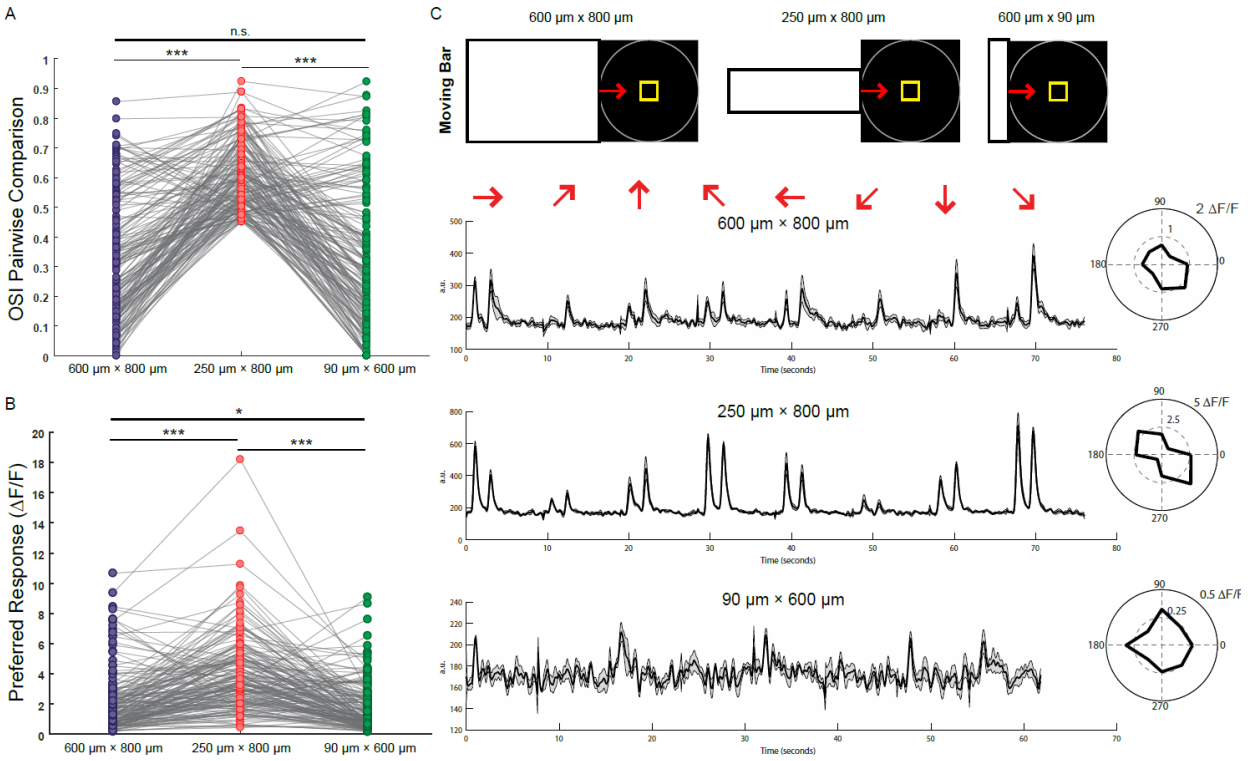

Figure 6.6: On-Off OSGCs are suppressed by surround stimulation. (A) Pairwise orientation selectivity index (OSI) comparison during 600 µm × 800 µm (purple), 250 µm × 800 µm (red), and 90 µm × 600 µm (green) moving bars. **(B)** Pairwise preferred axis response comparison during 600 µm × 800 µm (purple), 250 µm × 800 µm (red), and 90 µm × 600 µm (green) moving bars. **(C)** Representative calcium responses to 600 µm × 800 µm (top), 250 µm × 800 µm (middle), and 90 µm × 600 µm (bottom) moving bars.

We then tested On-Off OS sensitivity to GABA-A receptor antagonists by stimulating the retina with the narrow moving bar (250µm × 800µm) during two-photon calcium imaging before and application of 10 µM SR95531 (gabazine) (**Figure 6.7**). As previously shown, we robustly detected On-Off OS (OSI ≥ 0.4) responses with the narrow moving bar. Following bath application of gabazine, all On-Off OSGCs exhibited a decrease in orientation tuning strength (Student t-test $p < 0.001$) (**Figure 6.7A**). Although a select few remained orientation selective (OSI ≥ 0.4), the vast majority of On-Off OSGCs lost their orientation tuning when GABA-A receptors were blocked. The loss of tuning upon GABA-A receptor blockade can be explained by enhanced null-axis responses ($p < 0.001$, paired Student's t-test) (**Figure 6.7B-C**). In contrast, changes in

preferred-axis responses appear to be random with some cells showing increase, decrease, and no change.

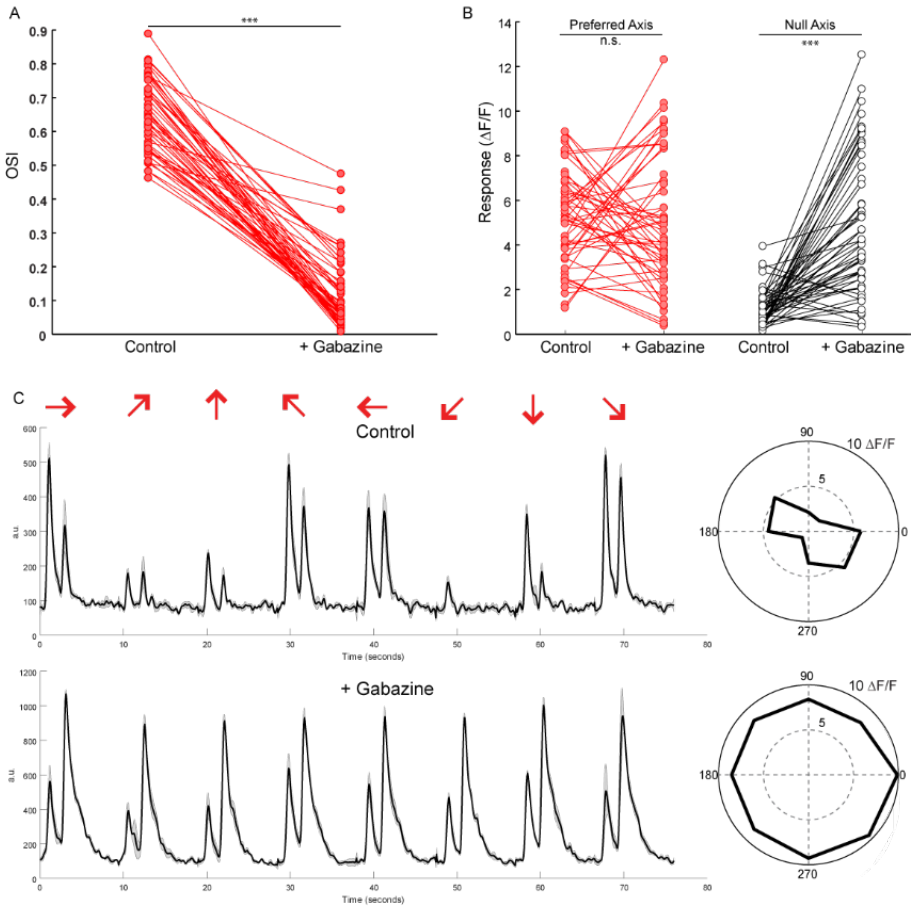

Figure 6.7: On-Off OSGCs are sensitive to GABA-A receptor antagonists. (A) Pairwise OSI comparison before and after bath application of gabazine (SR95531) (paired Student t-test, $p < 0.001$). **(B)** Calcium responses before and after bath application of gabazine (paired Student t-test, Preferres Axis: $p > 0.05$ versus Null Axis: $p < 0.001$). **(C)** Representative calcium reponses from an On-Off OSGC to 250 µm × 800 µm moving bar before and after application of gabazine.

Lastly, we developed a method to target On-Off OSGCs for patch clamp recordings based on the online analysis of multiphoton calcium imaging. This allowed us to correlate the GCaMP6f signals with a spiking output and describe On-Off OS receptive fields based on their spiking properties. In this experiment, RGCs of interest (DSGCs and OSGCs) in a given field of view were identified based on their calcium traces, particularly responses to leading and trailing edges and tuning strength (DSI or OSI). Once identified, On-Off DSGC and On-Off OSGC somas were targeted for

loose-attached patch-clamp recordings (**Figure 6.8**). For OSGCs, spiking data was recorded during the presentation of a variety of visual stimuli, including flashing oriented bars and moving bars.

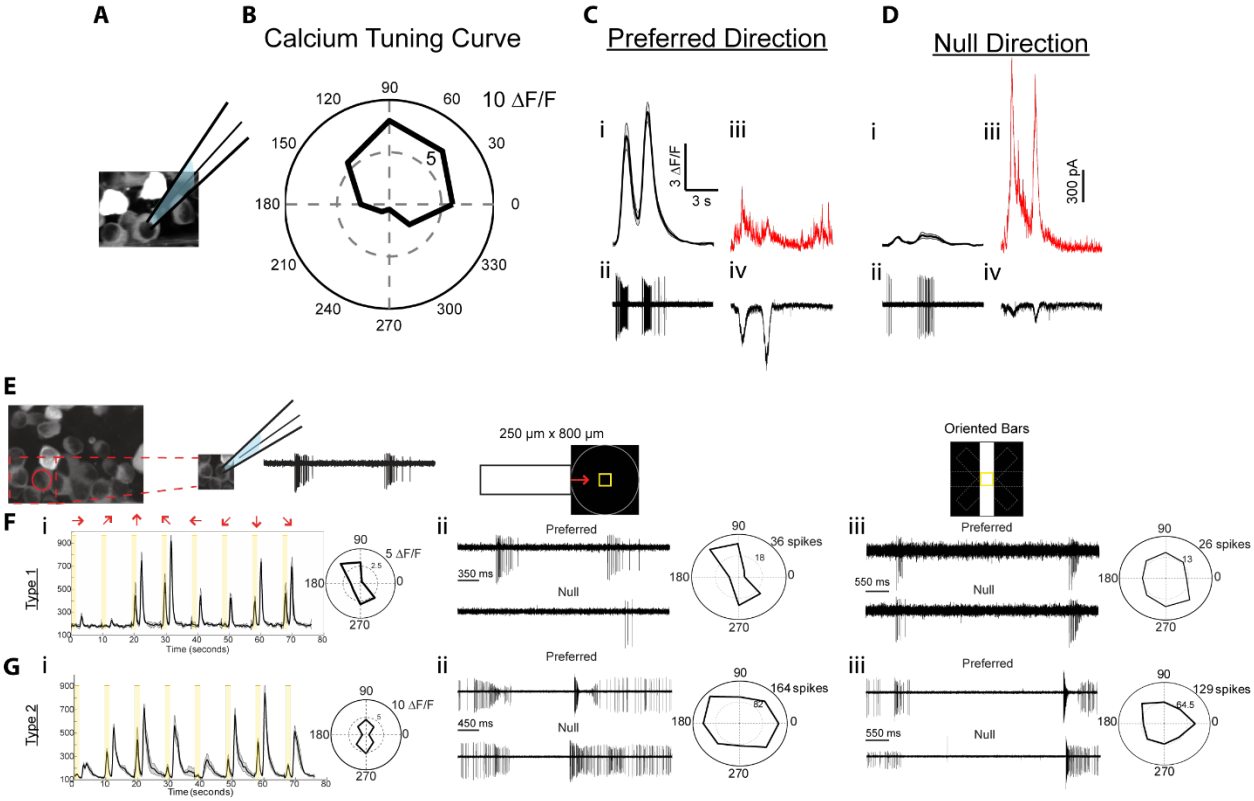

Figure 6.8: Calcium imaging guided-electrophysiology reveals On-Off OSGC subpopulations. (A-D) Example On-Off DSGC identified through calcium imaging targeted for extracellular and whole-cell recordings. Preferred **(C)** and null direction **(D)** calcium responses (i), spiking (ii), IPSCs (red, iii), and EPSCs (black, iv). **(E-G)** Examples of targeted type I **(F)** and type II **(G)** On-Off OSGCs subpopulations. Calcium responses (i, left: mean ± s.e.m. traces, right: tuning curves) to 250 μm × 800 μm moving bar. Loose-attached spiking responses to 250 μm × 800 μm moving bar (ii) and 90 μm × 600 μm flashing oriented bars (iii). Preferred and null axes are determined from calcium tuning curves in (i).

We targeted On-Off DSGCs to validate this procedure (**Figure 6.8A-D**). Calcium traces and electrophysiological recordings from anterior-preferring On-Off DSGCs show highly correlated responses (example cell: DSI (spiking) = 0.63 versus DSI (Ca^{+2}) = 0.88). Furthermore, whole-cell recordings in voltage-clamp mode from the example neuron in **Figure 6.8A** reveal both direction selective inhibition and excitation. On the other hand, loose-attached recordings revealed two distinct firing patterns from On-Off OSGCs. The first subpopulation (Type I) exhibit an axis-

selective spike count to the moving bar visual stimulation, but not to the flashing stationary edges suggesting that these are selective to the axis of image motion (**Fig. 6.8F i-iii**). On the other hand, the second subpopulation (Type II) did not exhibit an orientation- or axis-selective spike count; instead, they experience a sharp increase in firing rate that lead to sodium channel inactivation (sodium-block) when presented with a preferred oriented edge (**Fig 6.4F i-iii**). Further experiments are needed to determine the relative abundance of these cell types within our On-Off OSGC population and whether these can be further categorized by their axial preference (horizontal versus vertical preferring). Additionally, the cell-type specific relationships between calcium dynamics and spiking activity described here highlight the diversity of signal transformations among the RGC population.

6.2.5 Molecular signatures among motion sensitive RGC groups

As previously mentioned, the lack of molecular markers has been a limiting factor in mechanistic studies focusing on retinal orientation selectivity. Recent work has demonstrated that RGCs can be subdivided into three distinct classes based on key, non-overlapping transcription factors: *Isl2*, *Trb2*, and *Satb2* (Sweeney et al., 2019). *Trb2*+ RGCs project to the non-image forming brain areas and include ipRGCs and On DSGCs (Sweeney et al., 2014, 2019). On the other hand, *Isl2*+ and *Satb2*+ RGCs project to both the SC and dLGN; but, *Isl2*+ RGCs comprise mostly of monostratified On and Off Alpha RGCs (Triplett et al., 2014). Since RGC boutons with On-Off OS visual responses have been observed in both dLGN and SC, we verified whether On-Off OSGCs were part of the *Satb2*+ RGC subpopulation.

We obtained an inducible *Satb2-IRES-CreERT* mouse line from Dr. David Feldheim and crossed it with mice containing *floxed-TdTomato* and *mGluR2-GFP* transgenes to asses RGC density and stratification in the IPL (**Figure 6.9** middle). Following induction of Cre expression with CNO, we observed relatively sparse TdTomato expression in RGCs and GFP expression in SACs (**Figure 6.9A**). In the GCL, *Satb2*+ RGCs were found with an average cell density of 1,336.98 ± 61.74 cells/mm^2 (**Figure 6.9** middle) compared to 3621.53 ± 213.17 cells/mm^2 in the *Vglut2-IRES-Cre* line (**Figure 6.9** left), suggesting Satb2+ RGCs represent ~ 36.92% of the total RGC population. In contrast, On SACs in the GCL were found at an average cell density of 1294.96 ± 65.34 cells/mm^2. Some *Satb2*+ dendrites were observed in the S5 sublamina of the IPL, nevertheless the vast majority of dendrites from *Satb2*+ RGCs stratified between S4 and S1 sublaminae. Some RGCs were seen to co-stratify well the On and Off SAC ChAT bands (S4 and S2 sublaminae) suggesting the inclusion of On-Off DSGCs in this mouse line.

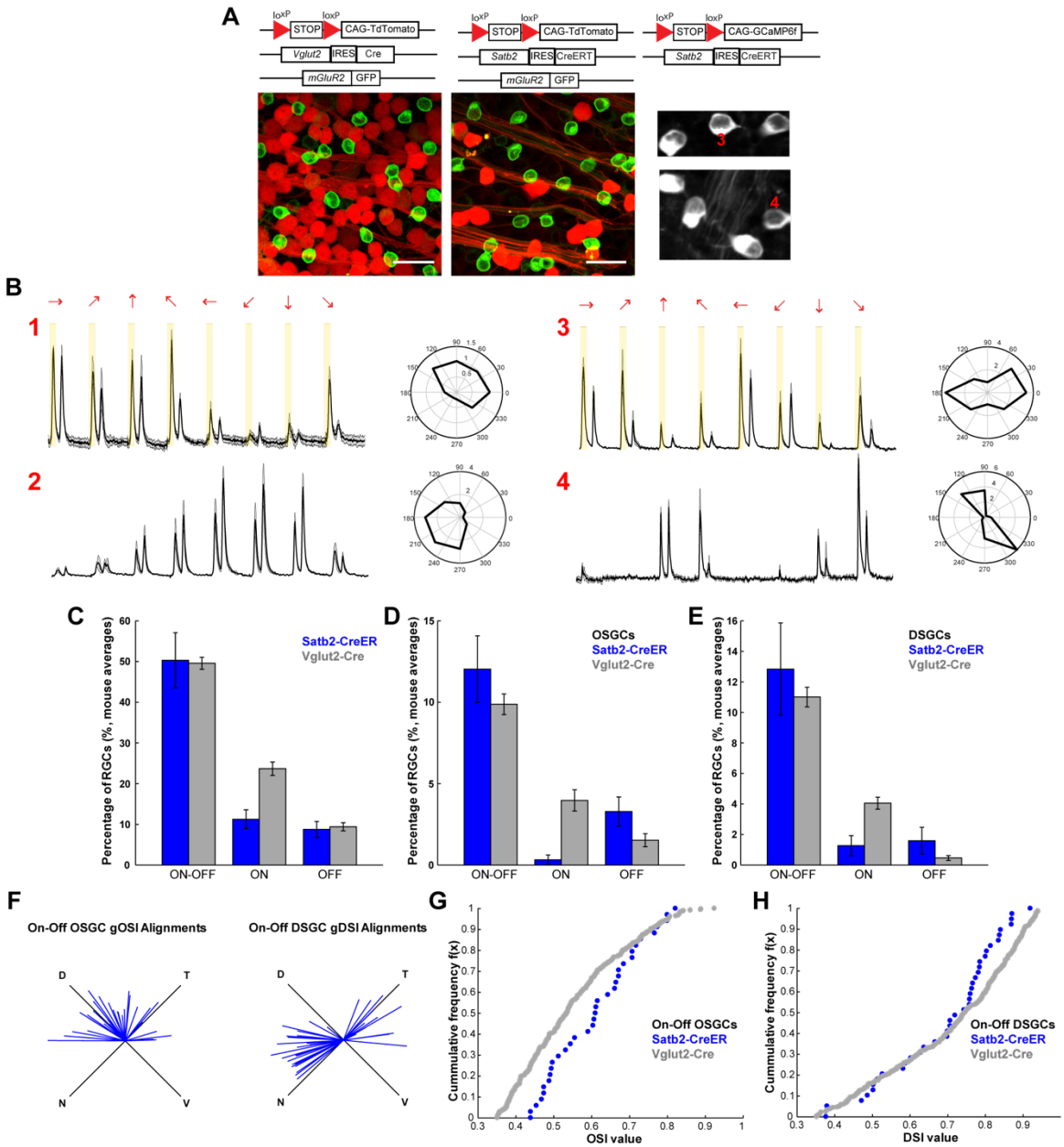

Figure 6.9: Satb2+ RGCs include a fraction of On-Off OSGCs and On-Off DSGCs. (A) Left: Example GCL fluorescence image from *Vglut2-IRES-Cre/floxed-TdTomato/mGluR2-GFP* mice. Middle: Example GCL fluorescence image from *Satb2-IRES-CreERT/floxed-TdTomato/mGluR2-GFP* mice. Right: Example projection images of *Satb2-IRES-CreERT*$^{+}$ RGCs expressing GCaMP6f. **(B)** Representative calcium traces of temporal- (1) and nasal-preferring (2) On-Off DSGCs and horizontal- (3) and vertical-preferring (4) On-Off OSGCs from the Satb2-CreERT/floxed-GCaMP6f mouse. Quantification of On-Off, On, and Off RGCs **(C)**, OSGCs **(D)**, and DSGCs **(E)** in Satb2-CreER (blue) versus Vglut2-Cre (gray) mice. **(F)** Polar plots of On-Off OSGC preferred axes (left) and On-Off DSGC preferred directions (right) from the Satb2-CreER mouse. Cummulative frequency distributions on On-Off OSI **(G)** and On-Off DSI **(H)** values from the Satb2-CreER (blue) versus the Vglut2-Cre (gray) mice.

In order to classify *Satb2*+ RGCs into functional groups according to their visual responses, we bred mice carrying both the *Satb2-IRES-CreERT* and *floxed-GCaMP6f* transgenes (**Figure 6.9** right). After induction of Cre expression, we recorded calcium responses from GCaMP6f-expressing *Satb2*+ RGCs while stimulating the retina with a bright moving bar (250 μm × 800 μm) to probe for direction and orientation selectivity and determine On/Off preference. In the Satb2-IRES-CreERT line, we observed a significant bias towards Off and On-Off responses (**Figure 6.10**, KS-test $p = 10^{-10}$), which led to a decrease in classification of On RGCs in this line (**Figure 6.9C**). Among the On-Off population, we identified both orientation and direction selective groups (**Figure 6.9B, D-E**). Interestingly, only On-Off DSGCs with preferred directions along the nasal-temporal axis (posterior-preferring and anterior-preferring On-Off DSGCs) were found, while both horizontal-preferring and vertical-preferring On-Off OSGCs were identified (**Figure 6.9F**). These results are consistent with previous studies showing that Off sustained RGCs and On-Off DSGCs (anterior- and posterior-preferring) display SATB2+ nuclei after immunostaining (Dhande et al., 2019). Our data adds to these findings by demonstrating that some On-Off OSGCs express the *Satb2* marker, although further experiments are needed to determine whether Satb2+ OSGCs include Type I, Type II, or both.

Orientation selectivity is a prominent feature of the early visual system and had become a model computation to study processing of sensory information. Orientation selectivity if first computed in the retina (Nath & Schwartz, 2016, 2017; Passaglia et al., 2002; Venkataramani & Taylor, 2010); but, the mechanisms underlying retinal orientation selective receptive fields and their development is far less understood compared to higher order visual areas, such as visual striate cortex (V1) (Priebe, 2016). In this study, we report the prevalence of On-Off OS receptive fields in the mouse

retina and describe a delayed maturation timeline compared to other complex retinal receptive fields. Knowledge on the extent of OS receptive fields in the murine retina is becoming increasingly important as the mouse becomes the animal model of choice for studying neural circuits and visual processing.

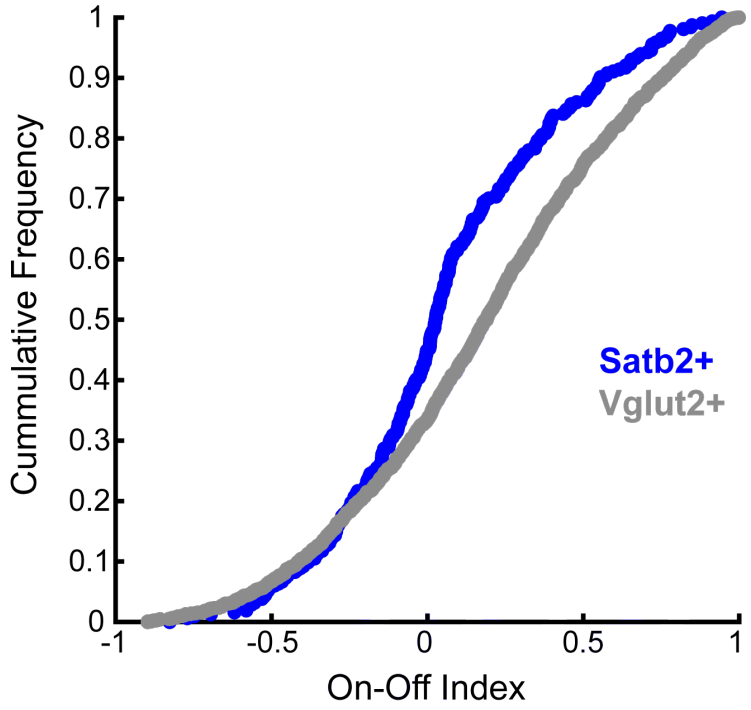

Figure 6.10: Comparison of On-Off index distribution between Satb2+ and Vglut2+ RGCs.

Comparison of visual responses to moving bar stimuli prior to eye-opening to one week after eye-opening revealed a developmental increase in abundance of On-Off OS calcium responses suggesting that the period following the onset of visual experience is important for the maturation of these complex receptive fields. Despite coinciding with the onset of visual experience, dark-rearing these animals during development does not limit the increase in On-Off OS visual responses indicating that visual experience does not play an instructive role in the formation of these complex receptive fields. Similarly, orientation selectivity in mouse V1 continues to mature

following eye-opening (Rochefort et al., 2011) putting into question whether this is influenced by retinal mechanisms.

6.3 Experimental Procedures

Mice

Vglut2-IRES-Cre (Slc17a6$^{tm2(cre)Lowl}$), Ai95 floxed GCaMP6f (129S-Gt(ROSA)26Sor$^{tm95.1(CAG-GCaMP6f)Hze}$/J), floxed *tdTomato* (129S6-*Gt(ROSA)26Sor$^{tm9(CAG-tdTomato)Hze}$*/J) mice were acquired from the Jackson Laboratory. *Satb2-CreERT* mice were obtained from the laboratory of Dr. David Feldheim and mGluR2-GFP mice were a gift from Dr. Marla Feller. All strains were backcrossed to the *C57BL/6* background in our laboratory, and crossed to each other to create the lines used in this study. Mice of ages P21-P28 of either sex were used. All procedures to maintain and use mice were in accordance with the University of Chicago Institutional Animal Care and Use Committee (Protocol number ACUP 72247) and in conformance with the NIH Guide for the Care and Use of Laboratory Animals and the Public Health Service Policy.

Whole-mount retina preparation

After dark adaptation for > 30 min, mice were anesthetized with isoflurane and euthanized by decapitation. Retinas were isolated from the pigment epithelium under infrared illumination at room temperature in oxygenated Ames' medium (Sigma-Aldrich, St. Louis, MO). Slits were cut on the whole retinas to mark the cardinal directions and then mounted ganglion-cell-layer-up on top of a 3.5-4 mm^2 hole in a small piece of filter paper (Millipore, Billerica, MA). For immunohistochemistry experiments, retinas were cut into dorsal and ventral halves and mounted on top of a 1-1.5 mm^2 hole in a small piece of filter paper. The mounted retinas were kept in darkness at room temperature in Ames' medium bubbled with 95% O_2/5% CO_2 until use (0–8 hr).

Visual stimulation

A white organic light-emitting display (OLEDXL, eMagin, Bellevue, WA; 800 × 600 pixel resolution, 60 Hz refresh rate) was controlled by an Intel Core Duo computer with a Windows seven operating system and was presented to the retina at a resolution of 1.1 μm/pixel. Moving bar stimuli were generated by MATLAB and the Psychophysics Toolbox (Brainard, 1997), and projected through the condenser lens of the two-photon microscope onto the photoreceptor layer. For the moving bar stimulus, a positive-contrast bar (220 μm wide, 880 μm long) moved along the long axis in 8 pseudo-randomly chosen directions at a speed of 440 μm/sec over a 660μm-diameter field on the retina; and four trials were recorded for each direction. The percent stimulus contrast was calculated as $(L_{stimulus} - L_{background})/ (L_{stimulus} + L_{background})$. Unless otherwise noted (i.e., **Figure 7D**), the intensity of the moving bar was ~6.3×104 isomerizations (R*)/rod/s, lying in the photopic range, and the background intensity was ~1800 R*/rod/s, lying at the lower end of the photopic range.

Two-photon calcium imaging of GCaMP6 fluorescence

GCaMP6 fluorescence of isolated retinas in oxygenated Ames at 32–33°C was imaged in a customized two-photon laser scanning fluorescence microscope (Bruker Nano Surfaces Division). GCaMP6 was excited by a Ti:sapphire laser (Coherent, Chameleon Ultra II, Santa Clara, CA) tuned to 920 nm, and the laser power was adjusted to avoid saturation of the fluorescent signal. Onset of laser scanning induces a transient two-photon response that adapts to the baseline in ~3 s. Therefore, to ensure the complete adaptation of this laser-induced response and a stable baseline, visual stimuli were given after 10 s of continuous laser scanning. To separate the visual stimulus

from GCaMP6 fluorescence, a band-pass filter (Semrock, Rochester, MA) was placed on the OLED to pass blue light peaked at 470 nm, while two notched filters (Bruker Nano Surfaces Division) were placed before the photomultiplier tubes to block light of the same wavelength. The objective was a water immersion objective (20x, Olympus). Time series of each imaging window (~100×100 µm at the GCL and ~25×25 µm in the INL) were collected at 17 Hz or higher.

Data Analysis

Analysis was performed using ImageJ and MATLAB. Raw frames were uploaded onto ImageJ software in which regions of interest (ROIs) were manually drawn to enclose the soma of each GCaMP6 expressing cell and for a background region where there was no detectable GCaMP6s expression. These manually selected ROIs were then imported into MATLAB, where custom written scripts were used to calculate the average intensity over time for all ROIs. In MATLAB, the background trace was subtracted from the light responsive somatic traces to remove noise. We then fitted the baseline fluorescence over time to single or two-term exponential decay function using datapoints corresponding to the time between each moving bar sweep. Using the fitted F0 traces, raw fluorescence data was transformed to $\Delta F/F_0$ = (F−F0)/F0. The $\Delta F/F_0$ traces were then truncated and sorted by direction of the moving bar stimulus. We calculated a quality index (QI) to measure how well a given cell responded to the visual stimulus (Baden et al., 2016). If all trials are identical such that the mean response is a perfect representative of the response, QI is equal to 1. On the other hand, if all trials are completely random with fixed variance (so that the mean response is not informative about the individual trial responses), QI falls towards 0. We implemented a quality threshold of QI ≥ 0.45 for the response from a given cell to be considered for further analysis.

For each cell, we calculated the DS angle and DSI = $\frac{R_{Pref} - R_{Null}}{R_{Pref} + R_{Null}}$, where R_{pref} is the cell's response at the preferred direction (i.e., maximal response), and R_{Null} is the cell's response to the direction opposite to the preferred one. The orientation selectivity index (OSI) of each cell was calculated using the following equation, OSI = $\frac{\sum R_{Pref} - \sum R_{Null}}{\sum R_{Pref} + \sum R_{Null}}$, where R_{Pref} and R_{Null} correspond to responses along the preferred and null axes. Tuning curves were plotted using the average $\Delta F/F_0$ for each direction. The 880 μm long bar allows for clear separation between responses to the leading and trailing edge of the moving bar. Cells showing responses to the leading edge were classified as On, cells showing responses to the trailing edge were classified as Off, and cells showing responses to both leading and trailing edges were classified as On-Off. On-Off preference was measured as $OOi = \frac{\langle R_{ON} \rangle_t - \langle R_{OFF} \rangle_t}{\langle R_{ON} \rangle_t + \langle R_{OFF} \rangle_t}$ where R_{ON} and R_{OFF} correspond to response amplitudes to the On (leading) and Off (trailing) edges of the moving bar.

References

Ackman, J. B., & Crair, M. C. (2014). Role of emergent neural activity in visual map development. In *Current Opinion in Neurobiology*. https://doi.org/10.1016/j.conb.2013.11.011

Agmon-Snir, H., & Segev, I. (1993). Signal delay and input synchronization in passive dendritic structures. *Journal of Neurophysiology*. https://doi.org/10.1152/jn.1993.70.5.2066

Agmon-Snir, Hagai, Carr, C. E., & Rinzel, J. (1998). The role of dendrites in auditory coincidence detection. *Nature*. https://doi.org/10.1038/30505

Albano, J. E., Humphrey, A. L., & Norton, T. T. (1978). Laminar organization of receptive-field properties in tree shrew superior colliculus. *Journal of Neurophysiology*. https://doi.org/10.1152/jn.1978.41.5.1140

Albright, T. D. (1984). Direction and orientation selectivity of neurons in visual area MT of the macaque. *Journal of Neurophysiology*. https://doi.org/10.1152/jn.1984.52.6.1106

Amthor, F. R., Keyser, K. T., & Dmitrieva, N. A. (2002). Effects of the destruction of starburst-cholinergic amacrine cells by the toxin AF64A on rabbit retinal directional selectivity. *Visual Neuroscience*. https://doi.org/10.1017/S0952523802194119

Amthor, F. R., Takahashi, E. S., & Oyster, C. W. (1989). Morphologies of rabbit retinal ganglion cells with complex receptive fields. *Journal of Comparative Neurology*. https://doi.org/10.1002/cne.902800108

Ankri, L., Ezra-Tsur, E., Maimon, S. R., Kaushansky, N., & Rivlin-Etzion, M. (2020). Antagonistic Center-Surround Mechanisms for Direction Selectivity in the Retina. *Cell Reports*. https://doi.org/10.1016/j.celrep.2020.107608

Antinucci, P., & Hindges, R. (2018). Orientation-selective retinal circuits in vertebrates. In *Frontiers in Neural Circuits*. https://doi.org/10.3389/fncir.2018.00011

Antinucci, P., Suleyman, O., Monfries, C., & Hindges, R. (2016). Neural Mechanisms Generating Orientation Selectivity in the Retina. *Current Biology*. https://doi.org/10.1016/j.cub.2016.05.035

Ariel, M., & Daw, N. W. (1982). Effects of cholinergic drugs on receptive field properties of rabbit retinal ganglion cells. *The Journal of Physiology*. https://doi.org/10.1113/jphysiol.1982.sp014104

Bachman, K. M., & Balkema, G. W. (1993). Developmental expression of a synaptic ribbon antigen (B16) in mouse retina. *Journal of Comparative Neurology*. https://doi.org/10.1002/cne.903330109

Baden, T., Berens, P., Franke, K., Román Rosón, M., Bethge, M., & Euler, T. (2016). The functional diversity of retinal ganglion cells in the mouse. *Nature*. https://doi.org/10.1038/nature16468

Barlow, H. B., & Hill, R. M. (1963). Selective Sensitivity to Direction of Movement in Ganglion Cells of the Rabbit Retina. *Science*. https://doi.org/10.1126/science.139.3553.412

Barlow, H. B., & Levick, W. R. (1965). The mechanism of directionally selective units in rabbit's retina. *The Journal of Physiology*. https://doi.org/10.1113/jphysiol.1965.sp007638

Bedbrook, C. N., Deverman, B. E., & Gradinaru, V. (2018). Viral Strategies for Targeting the Central and Peripheral Nervous Systems. *Annual Review of Neuroscience*. https://doi.org/10.1146/annurev-neuro-080317-062048

Berntson, A., & Taylor, W. R. (2000). Response characteristics and receptive field widths of on-bipolar cells in the mouse retina. *Journal of Physiology*. https://doi.org/10.1111/j.1469-7793.2000.00879.x

Berson, D. M. (2008). Retinal Ganglion Cell Types and Their Central Projections. In *The Senses: A Comprehensive Reference*. https://doi.org/10.1016/B978-012370880-9.00280-2

Blankenship, A. G., & Feller, M. B. (2010). Mechanisms underlying spontaneous patterned activity in developing neural circuits. In *Nature Reviews Neuroscience*. https://doi.org/10.1038/nrn2759

Bodnarenko, S. R., & Chalupa, L. M. (1993). Stratification of on and off ganglion cell dendrites depends on glutamate-mediated afferent activity in the developing retina. *Nature*. https://doi.org/10.1038/364144a0

Bos, R., Gainer, C., & Feller, M. B. (2016). Role for visual experience in the development of direction-selective circuits. *Current Biology*. https://doi.org/10.1016/j.cub.2016.03.073

Brecha, N., Johnson, D., Peichl, L., & Wassle, H. (1988). Cholinergic amacrine cells of the rabbit retina contain glutamate decarboxylase and γ-aminobutyrate immunoreactivity. *Proceedings of the National Academy of Sciences of the United States of America*. https://doi.org/10.1073/pnas.85.16.6187

Briggman, K. L., Helmstaedter, M., & Denk, W. (2011). Wiring specificity in the direction-selectivity circuit of the retina. *Nature*, *471*(7337), 183–188. https://doi.org/10.1038/nature09818

Brombas, A., Kalita-De Croft, S., Cooper-Williams, E. J., & Williams, S. R. (2017). Dendro-dendritic cholinergic excitation controls dendritic spike initiation in retinal ganglion cells. *Nature Communications*. https://doi.org/10.1038/ncomms15683

Cafaro, J., & Rieke, F. (2010). Noise correlations improve response fidelity and stimulus encoding. *Nature*. https://doi.org/10.1038/nature09570

Caldwell, J. H., & Daw, N. W. (1978). New properties of rabbit retinal ganglion cells. *The Journal of Physiology*. https://doi.org/10.1113/jphysiol.1978.sp012232

Caldwell, J. H., Daw, N. W., & Wyatt, H. J. (1978). Effects of picrotoxin and strychnine on rabbit retinal ganglion cells: lateral interactions for cells with more complex receptive fields. *The Journal of Physiology*. https://doi.org/10.1113/jphysiol.1978.sp012233

Cang, J., & Feldheim, D. A. (2013). Developmental Mechanisms of Topographic Map Formation and Alignment. *Annual Review of Neuroscience*. https://doi.org/10.1146/annurev-neuro-062012-170341

Chandrasekaran, A. R., Shah, R. D., & Crair, M. C. (2007). Developmental Homeostasis of Mouse Retinocollicular Synapses. *Journal of Neuroscience*. https://doi.org/10.1523/JNEUROSCI.4383-06.2007

Chang, Y. C., Walston, S. T., Chow, R. H., & Weiland, J. D. (2017). GCaMP expression in retinal ganglion cells characterized using a low-cost fundus imaging system. *Journal of Neural Engineering*. https://doi.org/10.1088/1741-2552/aa7ded

Chapman, B., & Stryker, M. P. (1993). Development of orientation selectivity in ferret visual cortex and effects of deprivation. *Journal of Neuroscience*. https://doi.org/10.1523/jneurosci.13-12-05251.1993

Chapot, C., Behrens, C., Rogerson, L., Baden, T., Pop, S., Berens, P., Euler, T., & Schubert, T. (2017). Local signals in mouse horizontal cell dendrites. *BioRxiv*. https://doi.org/10.1101/143909

Chen, H., Liu, X., & Tian, N. (2014). Subtype-dependent postnatal development of direction-and orientation-selective retinal ganglion cells in mice. *Journal of Neurophysiology*. https://doi.org/10.1152/jn.00320.2014

Chen, Qian, Cichon, J., Wang, W., Qiu, L., Lee, S. J. R., Campbell, N. R., DeStefino, N., Goard, M. J., Fu, Z., Yasuda, R., Looger, L. L., Arenkiel, B. R., Gan, W. B., & Feng, G. (2012). Imaging Neural Activity Using Thy1-GCaMP Transgenic Mice. *Neuron*. https://doi.org/10.1016/j.neuron.2012.07.011

Chen, Qiang, Pei, Z., Koren, D., & Wei, W. (2016). Stimulus-dependent recruitment of lateral inhibition underlies retinal direction selectivity. *ELife*. https://doi.org/10.7554/eLife.21053

Chen, T. W., Wardill, T. J., Sun, Y., Pulver, S. R., Renninger, S. L., Baohan, A., Schreiter, E. R., Kerr, R. A., Orger, M. B., Jayaraman, V., Looger, L. L., Svoboda, K., & Kim, D. S. (2013). Ultrasensitive fluorescent proteins for imaging neuronal activity. *Nature*. https://doi.org/10.1038/nature12354

Chiao, C. C., & Masland, R. H. (2002). Starburst cells nondirectionally facilitate the responses of direction-selective retinal ganglion cells. *Journal of Neuroscience*. https://doi.org/10.1523/jneurosci.22-24-10509.2002

Chiao, C. C., & Masland, R. H. (2003). Contextual tuning of direction-selective retinal ganglion cells. *Nature Neuroscience*. https://doi.org/10.1038/nn1147

Cohen, E. D. (2001). Voltage-gated calcium and sodium currents of starburst amacrine cells in the rabbit retina. *Visual Neuroscience*. https://doi.org/10.1017/S0952523801185135

Cohen, E. D., & Miller, R. F. (1995). Quinoxalines block the mechanism of directional selectivity in ganglion cells of the rabbit retina. *Proceedings of the National Academy of Sciences of the United States of America*. https://doi.org/10.1073/pnas.92.4.1127

Cossell, L., Iacaruso, M. F., Muir, D. R., Houlton, R., Sader, E. N., Ko, H., Hofer, S. B., & Mrsic-Flogel, T. D. (2015). Functional organization of excitatory synaptic strength in primary visual cortex. *Nature*. https://doi.org/10.1038/nature14182

Cruz-Martín, A., El-Danaf, R. N., Osakada, F., Sriram, B., Dhande, O. S., Nguyen, P. L.,

Callaway, E. M., Ghosh, A., & Huberman, A. D. (2014). A dedicated circuit links direction-selective retinal ganglion cells to the primary visual cortex. *Nature*. https://doi.org/10.1038/nature12989

Cynader, M., & Berman, N. (1972). Receptive-field organization of monkey superior colliculus. *Journal of Neurophysiology*. https://doi.org/10.1152/jn.1972.35.2.187

Dana, H., Chen, T. W., Hu, A., Shields, B. C., Guo, C., Looger, L. L., Kim, D. S., & Svoboda, K. (2014). Thy1-GCaMP6 transgenic mice for neuronal population imaging in vivo. *PLoS ONE*. https://doi.org/10.1371/journal.pone.0108697

Dana, H., Sun, Y., Mohar, B., Hulse, B., Hasseman, J. P., Tsegaye, G., Tsang, A., Wong, A., Patel, R., Macklin, J. J., Chen, Y., Konnerth, A., Jayaraman, V., Looger, L. L., Schreiter, E. R., Svoboda, K., & Kim, D. S. (2018). High-performance GFP-based calcium indicators for imaging activity in neuronal populations and microcompartments. *Nature Methods*. https://doi.org/10.1101/434589

Della Santina, L., Kuo, S. P., Yoshimatsu, T., Okawa, H., Suzuki, S. C., Hoon, M., Tsuboyama, K., Rieke, F., & Wong, R. O. L. (2016). Glutamatergic Monopolar Interneurons Provide a Novel Pathway of Excitation in the Mouse Retina. *Current Biology*. https://doi.org/10.1016/j.cub.2016.06.016

Dhande, O. S., Estevez, M. E., Quattrochi, L. E., El-Danaf, R. N., Nguyen, P. L., Berson, D. M., & Huberman, A. D. (2013). Genetic dissection of retinal inputs to brainstem nuclei controlling image stabilization. *Journal of Neuroscience*. https://doi.org/10.1523/JNEUROSCI.2778-13.2013

Dhande, O. S., & Huberman, A. D. (2014). Retinal ganglion cell maps in the brain: Implications for visual processing. In *Current Opinion in Neurobiology*. https://doi.org/10.1016/j.conb.2013.08.006

Dhande, O. S., Stafford, B. K., Franke, K., El-Danaf, R., Percival, K. A., Phan, A. H., Li, P., Hansen, B. J., Nguyen, P. L., Berens, P., Taylor, W. R., Callaway, E., Euler, T., & Huberman, A. D. (2019). Molecular fingerprinting of on–off direction-selective retinal ganglion cells across species and relevance to primate visual circuits. *Journal of Neuroscience*. https://doi.org/10.1523/JNEUROSCI.1784-18.2018

Ding, H., Smith, R. G., Poleg-Polsky, A., Diamond, J. S., & Briggman, K. L. (2016a). Species-specific wiring for direction selectivity in the mammalian retina. *Nature*. https://doi.org/10.1038/nature18609

Ding, H., Smith, R. G., Poleg-Polsky, A., Diamond, J. S., & Briggman, K. L. (2016b). Species-specific wiring for direction selectivity in the mammalian retina. *Nature*, *535*(7610), 105–110. https://doi.org/10.1038/nature18609

Drager, U. C., & Hubel, D. H. (1975). Responses to visual stimulation and relationship between visual, auditory, and somatosensory inputs in mouse superior colliculus. *Journal of Neurophysiology*. https://doi.org/10.1152/jn.1975.38.3.690

Dunn, F. A., DellaSantina, L., Parker, E. D., & Wong, R. O. L. (2013). Sensory experience shapes the development of the visual system's first synapse. *Neuron*.

https://doi.org/10.1016/j.neuron.2013.09.024

Efron, B., & Tibshirani, R. (1986). Bootstrap methods for standard errors, confidence intervals, and other measures of statistical accuracy. *Statistical Science*. https://doi.org/10.1214/ss/1177013815

Ellis, E. M., Gauvain, G., Sivyer, B., & Murphy, G. J. (2016). Shared and distinct retinal input to the mouse superior colliculus and dorsal lateral geniculate nucleus. *Journal of Neurophysiology*. https://doi.org/10.1152/jn.00227.2016

Elstrott, J., Anishchenko, A., Greschner, M., Sher, A., Litke, A. M., Chichilnisky, E. J., & Feller, M. B. (2008). Direction Selectivity in the Retina Is Established Independent of Visual Experience and Cholinergic Retinal Waves. *Neuron*. https://doi.org/10.1016/j.neuron.2008.03.013

Elstrott, J., & Feller, M. B. (2009). Vision and the establishment of direction-selectivity: a tale of two circuits. In *Current Opinion in Neurobiology*. https://doi.org/10.1016/j.conb.2009.03.004

Euler, T., Detwiler, P. B., & Denk, W. (2002). Directionally selective calcium signals in dendrites of starburst amacrine cells. *Nature*. https://doi.org/10.1038/nature00931

Euler, T., & Masland, R. H. (2000). Light-evoked responses of bipolar cells in a mammalian retina. *Journal of Neurophysiology*. https://doi.org/10.1152/jn.2000.83.4.1817

Famiglietti, E. V. (1992). Dendritic Co-stratification of ON and ON-OFF directionally selective ganglion cells with starburst amacrine cells in rabbit retina. *Journal of Comparative Neurology*. https://doi.org/10.1002/cne.903240303

Famiglietti, Edward V. (1983). "Starburst" amacrine cells and cholinergic neurons: mirror-symmetric ON and OFF amacrine cells of rabbit retina. *Brain Research*. https://doi.org/10.1016/0006-8993(83)91293-3

Feller, M. B., Wellis, D. P., Stellwagen, D., Werblin, F. S., & Shatz, C. J. (1996). Requirement for cholinergic synaptic transmission in the propagation of spontaneous retinal waves. *Science*. https://doi.org/10.1126/science.272.5265.1182

Fisher, L. J. (1979). Development of synaptic arrays in the inner plexiform layer of neonatal mouse retina. *Journal of Comparative Neurology*. https://doi.org/10.1002/cne.901870207

Ford, K. J., & Feller, M. B. (2012). Assembly and disassembly of a retinal cholinergic network. In *Visual Neuroscience*. https://doi.org/10.1017/S0952523811000216

Fortin, S., Chabli, A., Dumont, I., Shumikhina, S., Itaya, S. K., & Molotchnikoff, S. (1999). Maturation of visual receptive field properties in the rat superior colliculus. *Developmental Brain Research*. https://doi.org/10.1016/S0165-3806(98)00157-6

Fransen, J. W., & Borghuis, B. G. (2017). Temporally Diverse Excitation Generates Direction-Selective Responses in ON- and OFF-Type Retinal Starburst Amacrine Cells. *Cell Reports*. https://doi.org/10.1016/j.celrep.2017.01.026

Fried, S. I., Münch, T. A., & Werblin, F. S. (2002). Mechanisms and circuitry underlying

directional selectivity in the retina. *Nature*. https://doi.org/10.1038/nature01179

Fried, S. I., Münch, T. A., & Werblin, F. S. (2005). Directional selectivity is formed at multiple levels by laterally offset inhibition in the rabbit retina. *Neuron*. https://doi.org/10.1016/j.neuron.2005.02.007

Gabriel, J. P., Trivedi, C. A., Maurer, C. M., Ryu, S., & Bollmann, J. H. (2012). Layer-Specific Targeting of Direction-Selective Neurons in the Zebrafish Optic Tectum. *Neuron*. https://doi.org/10.1016/j.neuron.2012.12.003

Gale, S. D., & Murphy, G. J. (2014). Distinct representation and distribution of visual information by specific cell types in mouse superficial superior colliculus. *Journal of Neuroscience*. https://doi.org/10.1523/JNEUROSCI.2768-14.2014

Gandhi, N. J., & Katnani, H. A. (2011). Motor Functions of the Superior Colliculus. *Annual Review of Neuroscience*. https://doi.org/10.1146/annurev-neuro-061010-113728

Gauvain, G., & Murphy, G. J. (2015). Projection-specific characteristics of retinal input to the brain. *Journal of Neuroscience*. https://doi.org/10.1523/JNEUROSCI.4298-14.2015

Gavrikov, K. E., Nilson, J. E., Dmitriev, A. V., Zucker, C. L., & Mangel, S. C. (2006). Dendritic compartmentalization of chloride contransporters underlies directional responses of starburst amacrine cells in retina. *Proceedings of the National Academy of Sciences of the United States of America*. https://doi.org/10.1073/pnas.0604551103

Grzywacz, N. M., Amthor, F. R., & Borg-Graham, L. J. (1993). Does Synaptic Facilitation Mediate Motion Facilitation in the Retina? In *Computation and Neural Systems*. https://doi.org/10.1007/978-1-4615-3254-5_24

Grzywacz, N. M., Amthor, F. R., & Merwine, D. K. (1998). Necessity of acetylcholine for retinal directionally selective responses to drifting gratings in rabbit. *Journal of Physiology*. https://doi.org/10.1111/j.1469-7793.1998.575be.x

Grzywacz, N. M., Merwine, D. K., & Amthor, F. R. (1998). Complementary roles of two excitatory pathways in retinal directional selectivity. *Visual Neuroscience*. https://doi.org/10.1017/S0952523898156109

Hanson, L., Sethuramanujam, S., de Rosenroll, G., Jain, V., & Awatramani, G. B. (2019). Retinal direction selectivity in the absence of asymmetric starburst amacrine cell responses. *ELife*. https://doi.org/10.7554/eLife.42392

Hausselt, S. E., Euler, T., Detwiler, P. B., & Denk, W. (2007). A dendrite-autonomous mechanism for direction selectivity in retinal starburst amacrine cells. *PLoS Biology*. https://doi.org/10.1371/journal.pbio.0050185

Haverkamp, S., & Wässle, H. (2004). Characterization of an Amacrine Cell Type of the Mammalian Retina Immunoreactive for Vesicular Glutamate Transporter 3. *Journal of Comparative Neurology*. https://doi.org/10.1002/cne.10962

Hayashi, Y., Momiyama, A., Takahashi, T., Ohishi, H., Ogawa-Meguro, R., Shigemoto, R., Mizuno, N., & Nakanishi, S. (1993). Role of a metabotropic glutamate receptor in synaptic modulation in the accessory olfactory bulb. *Nature*. https://doi.org/10.1038/366687a0

He, S., & Masland, R. H. (1997). Retinal direction selectivity after targeted laser ablation of starburst amacrine cells. *Nature*. https://doi.org/10.1038/38723

Hodgkin, A. L., & Huxley, A. F. (1945). Resting and action potentials in single nerve fibres. *The Journal of Physiology*. https://doi.org/10.1113/jphysiol.1945.sp004114

Hoffmann, K. P., & Straschill, M. (1971). Influences of cortico-tectal and intertectal connections on visual responses in the cat's superior colliculus. *Experimental Brain Research*. https://doi.org/10.1007/BF00234310

Hoggarth, A., McLaughlin, A. J., Ronellenfitch, K., Trenholm, S., Vasandani, R., Sethuramanujam, S., Schwab, D., Briggman, K. L., & Awatramani, G. B. (2015). Specific wiring of distinct amacrine cells in the directionally selective retinal circuit permits independent coding of direction and size. *Neuron*. https://doi.org/10.1016/j.neuron.2015.02.035

Hoon, M., Okawa, H., Della Santina, L., & Wong, R. O. L. (2014). Functional architecture of the retina: Development and disease. In *Progress in Retinal and Eye Research*. https://doi.org/10.1016/j.preteyeres.2014.06.003

Huang, X., Rangel, M., Briggman, K. L., & Wei, W. (2019). Neural mechanisms of contextual modulation in the retinal direction selective circuit. *Nature Communications*. https://doi.org/10.1038/s41467-019-10268-z

Hubel, D. H., & Wiesel, T. N. (1959). Receptive fields of single neurones in the cat's striate cortex. *The Journal of Physiology*. https://doi.org/10.1113/jphysiol.1959.sp006308

Huberman, A. D., Manu, M., Koch, S. M., Susman, M. W., Lutz, A. B., Ullian, E. M., Baccus, S. A., & Barres, B. A. (2008). Architecture and Activity-Mediated Refinement of Axonal Projections from a Mosaic of Genetically Identified Retinal Ganglion Cells. *Neuron*. https://doi.org/10.1016/j.neuron.2008.07.018

Huberman, A. D., & Niell, C. M. (2011). What can mice tell us about how vision works? In *Trends in Neurosciences*. https://doi.org/10.1016/j.tins.2011.07.002

Huberman, A. D., Wei, W., Elstrott, J., Stafford, B. K., Feller, M. B., & Barres, B. A. (2009). Genetic Identification of an On-Off Direction- Selective Retinal Ganglion Cell Subtype Reveals a Layer-Specific Subcortical Map of Posterior Motion. *Neuron*. https://doi.org/10.1016/j.neuron.2009.04.014

Inayat, S., Barchini, J., Chen, H., Feng, L., Liu, X., & Cang, J. (2015). Neurons in the most superficial lamina of the mouse superior colliculus are highly selective for stimulus direction. *Journal of Neuroscience*. https://doi.org/10.1523/JNEUROSCI.0173-15.2015

Ivanova, E., Hwang, G. S., & Pan, Z. H. (2010). Characterization of transgenic mouse lines expressing Cre recombinase in the retina. *Neuroscience*. https://doi.org/10.1016/j.neuroscience.2009.10.021

Jacoby, J., & Schwartz, G. W. (2018). Typology and circuitry of suppressed-by-contrast retinal Ganglion cells. In *Frontiers in Cellular Neuroscience*. https://doi.org/10.3389/fncel.2018.00269

Jeon, C. J., Strettoi, E., & Masland, R. H. (1998). The major cell populations of the mouse retina. *Journal of Neuroscience*. https://doi.org/10.1523/JNEUROSCI.18-21-08936.1998

Johnson, J., Tian, N., Caywood, M. S., Reimer, R. J., Edwards, R. H., & Copenhagen, D. R. (2003). Vesicular neurotransmitter transporter expression in developing postnatal rodent retina: GABA and glycine precede glutamate. *Journal of Neuroscience*. https://doi.org/10.1523/jneurosci.23-02-00518.2003

Kaneda, M., Ito, K., Morishima, Y., Shigematsu, Y., & Shimoda, Y. (2007). Characterization of voltage-gated ionic channels in cholinergic amacrine cells in the mouse retina. *Journal of Neurophysiology*. https://doi.org/10.1152/jn.01022.2006

Karten, H. J., & Brecha, N. (1983). Localization of neuroactive substances in the vertebrate retina: Evidence for lamination in the inner plexiform layer. *Vision Research*. https://doi.org/10.1016/0042-6989(83)90033-0

Kay, J. N., de la Huerta, I., Kim, I. J., Zhang, Y., Yamagata, M., Chu, M. W., Meister, M., & Sanes, J. R. (2011). Retinal ganglion cells with distinct directional preferences differ in molecular identity, structure, and central projections. *Journal of Neuroscience*. https://doi.org/10.1523/JNEUROSCI.0907-11.2011

Kay, J. N., Voinescu, P. E., Chu, M. W., & Sanes, J. R. (2011). Neurod6 expression defines new retinal amacrine cell subtypes and regulates their fate. *Nature Neuroscience*, *14*(8), 965–972. https://doi.org/10.1038/nn.2859

Kerschensteiner, D. (2016). Glutamatergic retinal waves. In *Frontiers in Neural Circuits*. https://doi.org/10.3389/fncir.2016.00038

Khabou, H., Desrosiers, M., Winckler, C., Fouquet, S., Auregan, G., Bemelmans, A. P., Sahel, J. A., & Dalkara, D. (2016). Insight into the mechanisms of enhanced retinal transduction by the engineered AAV2 capsid variant -7m8. *Biotechnology and Bioengineering*. https://doi.org/10.1002/bit.26031

Kim, I. J., Zhang, Y., Meister, M., & Sanes, J. R. (2010). Laminar restriction of retinal ganglion cell dendrites and axons: Subtype-specific developmental patterns revealed with transgenic markers. *Journal of Neuroscience*. https://doi.org/10.1523/JNEUROSCI.4779-09.2010

Kim, I. J., Zhang, Y., Yamagata, M., Meister, M., & Sanes, J. R. (2008). Molecular identification of a retinal cell type that responds to upward motion. *Nature*. https://doi.org/10.1038/nature06739

Kim, J. S., Greene, M. J., Zlateski, A., Lee, K., Richardson, M., Turaga, S. C., Purcaro, M., Balkam, M., Robinson, A., Behabadi, B. F., Campos, M., Denk, W., & Seung, H. S. (2014). Space-time wiring specificity supports direction selectivity in the retina. *Nature*. https://doi.org/10.1038/nature13240

Kittila, C. A., & Massey, S. C. (1995). Effect of ON pathway blockade on directional selectivity in the rabbit retina. *Journal of Neurophysiology*. https://doi.org/10.1152/jn.1995.73.2.703

Ko, H., Cossell, L., Baragli, C., Antolik, J., Clopath, C., Hofer, S. B., & Mrsic-Flogel, T. D. (2013). The emergence of functional microcircuits in visual cortex. *Nature*. https://doi.org/10.1038/nature12015

Ko, H., Hofer, S. B., Pichler, B., Buchanan, K. A., Sjöström, P. J., & Mrsic-Flogel, T. D. (2011). Functional specificity of local synaptic connections in neocortical networks. *Nature*. https://doi.org/10.1038/nature09880

Koike, C., Obara, T., Uriu, Y., Numata, T., Sanuki, R., Miyata, K., Koyasu, T., Ueno, S., Funabiki, K., Tani, A., Ueda, H., Kondo, M., Mori, Y., Tachibana, M., & Furukawa, T. (2010). TRPM1 is a component of the retinal ON bipolar cell transduction channel in the mGluR6 cascade. *Proceedings of the National Academy of Sciences of the United States of America*. https://doi.org/10.1073/pnas.0912730107

Koren, D., Grove, J. C. R., & Wei, W. (2017). Cross-compartmental Modulation of Dendritic Signals for Retinal Direction Selectivity. *Neuron*. https://doi.org/10.1016/j.neuron.2017.07.020

Kosaka, T., Tauchi, M., & Dahl, J. L. (1988). Cholinergic neurons containing GABA-like and/or glutamic acid decarboxylase-like immunoreactivities in various brain regions of the rat. *Experimental Brain Research*. https://doi.org/10.1007/BF00247609

KUFFLER, S. W. (1953). Discharge patterns and functional organization of mammalian retina. *Journal of Neurophysiology*. https://doi.org/10.1152/jn.1953.16.1.37

Lee, S., Chen, L., Chen, M., Ye, M., Seal, R. P., & Zhou, Z. J. (2014). An unconventional glutamatergic circuit in the retina formed by vGluT3 amacrine cells. *Neuron*, *84*(4), 708–715. https://doi.org/10.1016/j.neuron.2014.10.021

Lee, S., Kim, K., & Zhou, Z. J. (2010). Role of ACh-GABA Cotransmission in Detecting Image Motion and Motion Direction. *Neuron*. https://doi.org/10.1016/j.neuron.2010.11.031

Lee, S., & Zhou, Z. J. (2006). The Synaptic Mechanism of Direction Selectivity in Distal Processes of Starburst Amacrine Cells. *Neuron*. https://doi.org/10.1016/j.neuron.2006.08.007

Lee, W. C. A., Bonin, V., Reed, M., Graham, B. J., Hood, G., Glattfelder, K., & Reid, R. C. (2016). Anatomy and function of an excitatory network in the visual cortex. *Nature*. https://doi.org/10.1038/nature17192

Levick, W. R. (1967). Receptive fields and trigger features of ganglion cells in the visual streak of the rabbit's retina. *The Journal of Physiology*. https://doi.org/10.1113/jphysiol.1967.sp008140

Levick, W. R., & Thibos, L. N. (1980). Orientation bias of cat retinal ganglion cells. *Nature*. https://doi.org/10.1038/286389a0

Levick, W. R., & Thibos, L. N. (1982). Analysis of orientation bias in cat retina. *The Journal of Physiology*. https://doi.org/10.1113/jphysiol.1982.sp014301

Li, Y. T., Ibrahim, L. A., Liu, B. H., Zhang, L. I., & Tao, H. W. (2013). Linear transformation of thalamocortical input by intracortical excitation. *Nature Neuroscience*. https://doi.org/10.1038/nn.3494

Li, Y. T., Liu, B. H., Chou, X. L., Zhang, L. I., & Tao, H. W. (2015). Strengthening of direction selectivity by broadly tuned and spatiotemporally slightly offset inhibition in mouse visual

cortex. *Cerebral Cortex*. https://doi.org/10.1093/cercor/bhu049

Liang, L., Fratzl, A., Goldey, G., Ramesh, R. N., Sugden, A. U., Morgan, J. L., Chen, C., & Andermann, M. L. (2018). A Fine-Scale Functional Logic to Convergence from Retina to Thalamus. *Cell*. https://doi.org/10.1016/j.cell.2018.04.041

Lien, A. D., & Scanziani, M. (2013). Tuned thalamic excitation is amplified by visual cortical circuits. *Nature Neuroscience*. https://doi.org/10.1038/nn.3488

Lin, M. Z., & Schnitzer, M. J. (2016). Genetically encoded indicators of neuronal activity. In *Nature Neuroscience*. https://doi.org/10.1038/nn.4359

Lipin, M. Y., Rowl Taylor, W., & Smith, R. G. (2015). Inhibitory input to the direction-selective ganglion cell is saturated at low contrast. *Journal of Neurophysiology*. https://doi.org/10.1152/jn.00413.2015

Livingstone, M. S., & Conway, B. R. (2003). Substructure of direction-selective receptive fields in macaque V1. *Journal of Neurophysiology*. https://doi.org/10.1152/jn.00822.2002

Lowe, A. S., Nikolaou, N., Hunter, P. R., Thompson, I. D., & Meyer, M. P. (2013). A Systems-based dissection of retinal inputs to the zebrafish tectum reveals different rules for different functional classes during development. *Journal of Neuroscience*. https://doi.org/10.1523/JNEUROSCI.1866-13.2013

Luján, R., Roberts, J. D. B., Shigemoto, R., Ohishi, H., & Somogyi, P. (1997). Differential plasma membrane distribution of metabotropic glutamate receptors mGluR1α, mGluR2 and mGluR5, relative to neurotransmitter release sites. *Journal of Chemical Neuroanatomy*. https://doi.org/10.1016/S0891-0618(97)00051-3

Marrocco, R. T., & Li, R. H. (1977). Monkey superior colliculus: properties of single cells and their afferent inputs. *Journal of Neurophysiology*. https://doi.org/10.1152/jn.1977.40.4.844

Martersteck, E. M., Hirokawa, K. E., Evarts, M., Bernard, A., Duan, X., Li, Y., Ng, L., Oh, S. W., Ouellette, B., Royall, J. J., Stoecklin, M., Wang, Q., Zeng, H., Sanes, J. R., & Harris, J. A. (2017). Diverse Central Projection Patterns of Retinal Ganglion Cells. *Cell Reports*. https://doi.org/10.1016/j.celrep.2017.01.075

Masland, R. H., Chow, K. L., & Stewart, D. L. (1971). Receptive-field characteristics of superior colliculus neurons in the rabbit. *Journal of Neurophysiology*. https://doi.org/10.1152/jn.1971.34.1.148

Masland, Richard H. (2012). The neuronal organization of the retina. *Neuron*, *76*(2), 266–280. https://doi.org/10.1016/j.neuron.2012.10.002

Matsumoto, A., Briggman, K. L., & Yonehara, K. (2019). Spatiotemporally Asymmetric Excitation Supports Mammalian Retinal Motion Sensitivity. *Current Biology*. https://doi.org/10.1016/j.cub.2019.08.048

Maturana, H. R., & Frenk, S. (1963). Directional movement and horizontal edge detectors in the pigeon retina. *Science*. https://doi.org/10.1126/science.142.3594.977

May, P. J. (2006). The mammalian superior colliculus: Laminar structure and connections. In

Progress in Brain Research. https://doi.org/10.1016/S0079-6123(05)51011-2

McIlwain, J. T., & Buser, P. (1968). Receptive fields of single cells in the cat's superior colliculus. *Experimental Brain Research*. https://doi.org/10.1007/BF00235906

Meister, M., Wong, R. O., Baylor, D. A., & Shatz, C. J. (1991). Synchronous bursts of action potentials in ganglion cells of the developing mammalian retina. *Science (New York, N.Y.)*, *252*(5008), 939–943. http://www.ncbi.nlm.nih.gov/pubmed/2035024

Michael, C. R. (1972). Visual receptive fields of single neurons in superior colliculus of the ground squirrel. *Journal of Neurophysiology*. https://doi.org/10.1152/jn.1972.35.6.815

Michael, Ch R. (1970). Integration of retinal and cortical information in the superior colliculus of the ground squirrel. In *Brain, Behavior and Evolution*. https://doi.org/10.1159/000125472

Miller, R. F., & Bloomfield, S. A. (1983). Electroanatomy of a unique amacrine cell in the rabbit retina. *Proceedings of the National Academy of Sciences of the United States of America*. https://doi.org/10.1073/pnas.80.10.3069

Morgan, J. L., Dhingra, A., Vardi, N., & Wong, R. O. L. (2006). Axons and dendrites originate from neuroepithelial-like processes of retinal bipolar cells. *Nature Neuroscience*. https://doi.org/10.1038/nn1615

Morgan, J. L., Schubert, T., & Wong, R. O. L. (2008). Developmental patterning of glutamatergic synapses onto retinal ganglion cells. *Neural Development*. https://doi.org/10.1186/1749-8104-3-8

Morgans, C. W., Zhang, J., Jeffrey, B. G., Nelson, S. M., Burke, N. S., Duvoisin, R. M., & Brown, R. L. (2009). TRPM1 is required for the depolarizing light response in retinal ON-bipolar cells. *Proceedings of the National Academy of Sciences of the United States of America*. https://doi.org/10.1073/pnas.0908711106

Morrie, R. D., & Feller, M. B. (2015). An Asymmetric Increase in Inhibitory Synapse Number Underlies the Development of a Direction Selective Circuit in the Retina. *The Journal of Neuroscience : The Official Journal of the Society for Neuroscience*, *35*(25), 9281–9286. https://doi.org/10.1523/JNEUROSCI.0670-15.2015

Münch, T. A., & Werblin, F. S. (2006). Symmetric interactions within a homogeneous starburst cell network can lead to robust asymmetries in dendrites of starburst amacrine cells. *Journal of Neurophysiology*. https://doi.org/10.1152/jn.00628.2005

Nath, A., & Schwartz, G. W. (2016). Cardinal orientation selectivity is represented by two distinct ganglion cell types in mouse retina. *Journal of Neuroscience*. https://doi.org/10.1523/JNEUROSCI.4554-15.2016

Nath, A., & Schwartz, G. W. (2017). Electrical synapses convey orientation selectivity in the mouse retina. *Nature Communications*. https://doi.org/10.1038/s41467-017-01980-9

Niell, C. M., & Stryker, M. P. (2008). Highly selective receptive fields in mouse visual cortex. *Journal of Neuroscience*. https://doi.org/10.1523/JNEUROSCI.0623-08.2008

Nikolaou, N., Lowe, A. S., Walker, A. S., Abbas, F., Hunter, P. R., Thompson, I. D., & Meyer,

M. P. (2012). Parametric Functional Maps of Visual Inputs to the Tectum. *Neuron*. https://doi.org/10.1016/j.neuron.2012.08.040

Nikolaou, N., & Meyer, M. P. (2012). Imaging circuit formation in zebrafish. *Developmental Neurobiology*. https://doi.org/10.1002/dneu.20874

Nikonov, S. S., Kholodenko, R., Lem, J., & Pugh, E. N. (2006). Physiological features of the S- and M-cone photoreceptors of wild-type mice from single-cell recordings. *Journal of General Physiology*. https://doi.org/10.1085/jgp.200609490

Nomura, A., Shigemoto, R., Nakamura, Y., Okamoto, N., Mizuno, N., & Nakanishi, S. (1994). Developmentally regulated postsynaptic localization of a metabotropic glutamate receptor in rat rod bipolar cells. *Cell*. https://doi.org/10.1016/0092-8674(94)90151-1

O'Malley, D. M., & Masland, R. H. (1989). Co-release of acetylcholine and γ-aminobutyric acid by a retinal neuron. *Proceedings of the National Academy of Sciences of the United States of America*. https://doi.org/10.1073/pnas.86.9.3414

O'Malley, D. M., Sandell, J. H., & Masland, R. H. (1992). Co-release of acetylcholine and GABA by the starburst amacrine cells. *Journal of Neuroscience*. https://doi.org/10.1523/jneurosci.12-04-01394.1992

Oesch, N., Euler, T., & Taylor, W. R. (2005). Direction-selective dendritic action potentials in rabbit retina. *Neuron*. https://doi.org/10.1016/j.neuron.2005.06.036

Oesch, N. W., & Taylor, W. R. (2010). Tetrodotoxin-resistant sodium channels contribute to directional responses in starburst amacrine cells. *PLoS ONE*. https://doi.org/10.1371/journal.pone.0012447

Ogasawara, K., McHaffie, J. G., & Stein, B. E. (1984). Two visual corticotectal systems in cat. *Journal of Neurophysiology*. https://doi.org/10.1152/jn.1984.52.6.1226

Okawa, H., Della Santina, L., Schwartz, G. W., Rieke, F., & Wong, R. O. L. (2014). Interplay of cell-autonomous and nonautonomous mechanisms tailors synaptic connectivity of converging axons in vivo. *Neuron*. https://doi.org/10.1016/j.neuron.2014.02.016

Oyster, C. W. (1968). The analysis of image motion by the rabbit retina. *The Journal of Physiology*. https://doi.org/10.1113/jphysiol.1968.sp008671

Oyster, Clyde W., & Barlow, H. B. (1967). Direction-selective units in rabbit retina: Distribution of preferred directions. *Science*. https://doi.org/10.1126/science.155.3764.841

Ozaita, A., Petit-Jacques, J., Völgyi, B., Ho, C. S., Joho, R. H., Bloomfield, S. A., & Rudy, B. (2004). A unique role for Kv3 voltage-gated potassium channels in starburst amacrine cell signaling in mouse retina. *Journal of Neuroscience*. https://doi.org/10.1523/JNEUROSCI.1275-04.2004

Park, S. J. H., Borghuis, B. G., Rahmani, P., Zeng, Q., Kim, I. J., & Demb, J. B. (2015). Function and circuitry of VIP+ interneurons in the mouse retina. *Journal of Neuroscience*. https://doi.org/10.1523/JNEUROSCI.0222-15.2015

Park, S. J. H., Kim, I. J., Looger, L. L., Demb, J. B., & Borghuis, B. G. (2014). Excitatory

synaptic inputs to mouse on-off direction- selective retinal ganglion cells lack direction tuning. *Journal of Neuroscience*. https://doi.org/10.1523/JNEUROSCI.5017-13.2014

Passaglia, C. L., Troy, J. B., Rüttiger, L., & Lee, B. B. (2002). Orientation sensitivity of ganglion cells in primate retina. *Vision Research*. https://doi.org/10.1016/S0042-6989(01)00312-1

Pearson, J. T., & Kerschensteiner, D. (2015). Ambient illumination switches contrast preference of specific retinal processing streams. *Journal of Neurophysiology*. https://doi.org/10.1152/jn.00360.2015

Pei, Z., Chen, Q., Koren, D., Giammarinaro, B., Ledesma, H. A., & Wei, W. (2015). Conditional knock-out of vesicular GABA transporter gene from starburst amacrine cells reveals the contributions of multiple synaptic mechanisms underlying direction selectivity in the retina. *Journal of Neuroscience*. https://doi.org/10.1523/JNEUROSCI.0933-15.2015

Percival, K. A., Venkataramani, S., Smith, R. G., & Taylor, W. R. (2019). Directional excitatory input to direction-selective ganglion cells in the rabbit retina. *Journal of Comparative Neurology*. https://doi.org/10.1002/cne.24207

Piscopo, D. M., El-Danaf, R. N., Huberman, A. D., & Niell, C. M. (2013). Diverse visual features encoded in mouse lateral geniculate nucleus. *Journal of Neuroscience*. https://doi.org/10.1523/JNEUROSCI.5187-12.2013

Pnevmatikakis, E. A., Soudry, D., Gao, Y., Machado, T. A., Merel, J., Pfau, D., Reardon, T., Mu, Y., Lacefield, C., Yang, W., Ahrens, M., Bruno, R., Jessell, T. M., Peterka, D. S., Yuste, R., & Paninski, L. (2016). Simultaneous Denoising, Deconvolution, and Demixing of Calcium Imaging Data. *Neuron*. https://doi.org/10.1016/j.neuron.2015.11.037

Poleg-Polsky, A., & Diamond, J. S. (2011). Imperfect space clamp permits electrotonic interactions between inhibitory and excitatory synaptic conductances, distorting voltage clamp recordings. *PLoS ONE*. https://doi.org/10.1371/journal.pone.0019463

Poleg-Polsky, A., Ding, H., & Diamond, J. S. (2018). Functional Compartmentalization within Starburst Amacrine Cell Dendrites in the Retina. *Cell Reports*. https://doi.org/10.1016/j.celrep.2018.02.064

Polsky, A., Mel, B. W., & Schiller, J. (2004). Computational subunits in thin dendrites of pyramidal cells. *Nature Neuroscience*. https://doi.org/10.1038/nn1253

Poznanski, R. R. (1992). Modelling the electrotonic structure of starburst amacrine cells in the rabbit retina: A functional interpretation of dendritic morphology. *Bulletin of Mathematical Biology*. https://doi.org/10.1007/BF02460658

Poznanski, R. R. (2005). Biophysical mechanisms and essential topography of directionally selective subunits in rabbit's retina. In *Journal of integrative neuroscience*. https://doi.org/10.1142/S0219635205000860

Priebe, N. J. (2016). Mechanisms of Orientation Selectivity in the Primary Visual Cortex. *Annual Review of Vision Science*. https://doi.org/10.1146/annurev-vision-111815-114456

Priebe, N. J., & Ferster, D. (2005). Direction selectivity of excitation and inhibition in simple cells of the cat primary visual cortex. *Neuron*. https://doi.org/10.1016/j.neuron.2004.12.024

Priebe, N. J., & Ferster, D. (2012). Mechanisms of Neuronal Computation in Mammalian Visual Cortex. In *Neuron*. https://doi.org/10.1016/j.neuron.2012.06.011

Priebe, N. J., Mechler, F., Carandini, M., & Ferster, D. (2004). The contribution of spike threshold to the dichotomy of cortical simple and complex cells. *Nature Neuroscience*. https://doi.org/10.1038/nn1310

Rall, W. (1964). Theoretical significance of dendritic trees for neuronal input-output relations. In *Reiss RF, editor. Neural theory and modeling. Palo Alto, CA: Stanford University Press.*

Ramón y Cajal, S. (2011). Histologie du système nerveux de l'homme & des vertébrés. In *Histologie du système nerveux de l'homme & des vertébrés.* https://doi.org/10.5962/bhl.title.48637

Rauen, T., Rothstein, J. D., & Wässle, H. (1996). Differential expression of three glutamate transporter subtypes in the rat retina. *Cell and Tissue Research*. https://doi.org/10.1007/s004410050702

Rhoades, R. W., & Chalupa, L. M. (1976). Directional selectivity in the superior colliculus of the golden hamster. *Brain Research*. https://doi.org/10.1016/0006-8993(76)90721-6

Robles, E., Filosa, A., & Baier, H. (2013). Precise lamination of retinal axons generates multiple parallel input pathways in the tectum. *Journal of Neuroscience*. https://doi.org/10.1523/JNEUROSCI.4990-12.2013

Rochefort, N. L., Narushima, M., Grienberger, C., Marandi, N., Hill, D. N., & Konnerth, A. (2011). Development of direction selectivity in mouse cortical neurons. *Neuron*. https://doi.org/10.1016/j.neuron.2011.06.013

Sabbah, S., Gemmer, J. A., Bhatia-Lin, A., Manoff, G., Castro, G., Siegel, J. K., Jeffery, N., & Berson, D. M. (2017). A retinal code for motion along the gravitational and body axes. *Nature*. https://doi.org/10.1038/nature22818

Sanes, J. R., & Masland, R. H. (2015). The Types of Retinal Ganglion Cells: Current Status and Implications for Neuronal Classification. *Annual Review of Neuroscience*. https://doi.org/10.1146/annurev-neuro-071714-034120

Saul, A. B., & Humphrey, A. L. (1992). Temporal-frequency tuning of direction selectivity in cat visual cortex. *Visual Neuroscience*. https://doi.org/10.1017/S0952523800005101

Schachter, M. J., Oesch, N., Smith, R. G., & Rowland Taylor, W. (2010). Dendritic spikes amplify the synaptic signal to enhance detection of motion in a simulation of the direction-selective ganglion cell. *PLoS Computational Biology*. https://doi.org/10.1371/journal.pcbi.1000899

Schubert, T., Hoon, M., Euler, T., Lukasiewicz, P. D., & Wong, R. O. L. (2013). Developmental regulation and activity-dependent maintenance of GABAergic presynaptic inhibition onto rod bipolar cell axonal terminals. *Neuron*, *78*(1), 124–137. https://doi.org/10.1016/j.neuron.2013.01.037

Sethuramanujam, S., Awatramani, G. B., & Slaughter, M. M. (2018). Cholinergic excitation complements glutamate in coding visual information in retinal ganglion cells. *Journal of*

Physiology. https://doi.org/10.1113/JP275073

Shen, Y., Heimel, J. A., Kamermans, M., Peachey, N. S., Gregg, R. G., & Nawy, S. (2009). A transient receptor potential-like channel mediates synaptic transmission in rod bipolar cells. *Journal of Neuroscience*. https://doi.org/10.1523/JNEUROSCI.0132-09.2009

Sherry, D. M., Wang, M. M., Bates, J., & Frishman, L. J. (2003). Expression of vesicular glutamate transporter 1 in the mouse retina reveals temporal ordering in development of rod vs. Cone and ON vs. OFF circuits. *Journal of Comparative Neurology*. https://doi.org/10.1002/cne.10838

Shi, X., Barchini, J., Ledesma, H. A., Koren, D., Jin, Y., Liu, X., Wei, W., & Cang, J. (2017). Retinal origin of direction selectivity in the superior colliculus. *Nature Neuroscience*. https://doi.org/10.1038/nn.4498

Sivyer, B., Taylor, W. R., & Vaney, D. I. (2010). Uniformity detector retinal ganglion cells fire complex spikes and receive only light-evoked inhibition. *Proceedings of the National Academy of Sciences of the United States of America*. https://doi.org/10.1073/pnas.0909621107

Sivyer, B., & Williams, S. R. (2013). Direction selectivity is computed by active dendritic integration in retinal ganglion cells. *Nature Neuroscience*. https://doi.org/10.1038/nn.3565

Skottun, B. C., De Valois, R. L., Grosof, D. H., Movshon, J. A., Albrecht, D. G., & Bonds, A. B. (1991). Classifying simple and complex cells on the basis of response modulation. *Vision Research*. https://doi.org/10.1016/0042-6989(91)90033-2

Stark, E., & Abeles, M. (2005). Applying resampling methods to neurophysiological data. *Journal of Neuroscience Methods*. https://doi.org/10.1016/j.jneumeth.2004.12.005

Steinmetz, N. A., Buetfering, C., Lecoq, J., Lee, C. R., Peters, A. J., Jacobs, E. A. K., Coen, P., Ollerenshaw, D. R., Valley, M. T., De Vries, S. E. J., Garrett, M., Zhuang, J., Groblewski, P. A., Manavi, S., Miles, J., White, C., Lee, E., Griffin, F., Larkin, J. D., … Harris, K. D. (2017). Aberrant cortical activity in multiple GCaMP6-expressing transgenic mouse lines. *ENeuro*. https://doi.org/10.1523/ENEURO.0207-17.2017

Sun, L., Han, X., & He, S. (2011). Direction-Selective Circuitry in Rat Retina Develops Independently of GABAergic, Cholinergic and Action Potential Activity. *PLoS ONE*, *6*(5), e19477. https://doi.org/10.1371/journal.pone.0019477

Sun, W., Deng, Q., Levick, W. R., & He, S. (2006). ON direction-selective ganglion cells in the mouse retina. *Journal of Physiology*. https://doi.org/10.1113/jphysiol.2006.115857

Sweeney, N. T., James, K. N., Nistorica, A., Lorig-Roach, R. M., & Feldheim, D. A. (2019). Expression of transcription factors divides retinal ganglion cells into distinct classes. *Journal of Comparative Neurology*. https://doi.org/10.1002/cne.24172

Sweeney, N. T., Tierney, H., & Feldheim, D. A. (2014). Tbr2 is required to generate a neural circuit mediating the pupillary light reflex. *Journal of Neuroscience*. https://doi.org/10.1523/JNEUROSCI.0035-14.2014

Taylor, W. R., & Vaney, D. I. (2002). Diverse synaptic mechanisms generate direction

selectivity in the rabbit retina. *Journal of Neuroscience*. https://doi.org/10.1523/jneurosci.22-17-07712.2002

Taylor, W. R., & Wässle, H. (1995). Receptive Field Properties of Starburst Cholinergic Amacrine Cells in the Rabbit Retina. *European Journal of Neuroscience*. https://doi.org/10.1111/j.1460-9568.1995.tb00652.x

Tian, N., & Copenhagen, D. R. (2003). Visual stimulation is required for refinement on ON and OFF pathways in postnatal retina. *Neuron*. https://doi.org/10.1016/S0896-6273(03)00389-1

Tien, N. W., Pearson, J. T., Heller, C. R., Demas, J., & Kerschensteiner, D. (2015). Genetically identified suppressed-by-contrast retinal ganglion cells reliably signal self-generated visual stimuli. *Journal of Neuroscience*. https://doi.org/10.1523/JNEUROSCI.1521-15.2015

Tikidji-Hamburyan, A., Reinhard, K., Seitter, H., Hovhannisyan, A., Procyk, C. A., Allen, A. E., Schenk, M., Lucas, R. J., & Münch, T. A. (2015). Retinal output changes qualitatively with every change in ambient illuminance. *Nature Neuroscience*. https://doi.org/10.1038/nn.3891

Tiriac, A., Smith, B. E., & Feller, M. B. (2018). Light Prior to Eye Opening Promotes Retinal Waves and Eye-Specific Segregation. *Neuron*. https://doi.org/10.1016/j.neuron.2018.10.011

Trenholm, S., Johnson, K., Li, X., Smith, R. G., & Awatramani, G. B. (2011). Parallel mechanisms encode direction in the retina. *Neuron*. https://doi.org/10.1016/j.neuron.2011.06.020

Trenholm, S., McLaughlin, A. J., Schwab, D. J., Turner, M. H., Smith, R. G., Rieke, F., & Awatramani, G. B. (2014). Nonlinear dendritic integration of electrical and chemical synaptic inputs drives fine-scale correlations. *Nature Neuroscience*. https://doi.org/10.1038/nn.3851

Triplett, J. W., Wei, W., Gonzalez, C., Sweeney, N. T., Huberman, A. D., Feller, M. B., & Feldheim, D. A. (2014). Dendritic and axonal targeting patterns of a genetically-specified class of retinal ganglion cells that participate in image-forming circuits. *Neural Development*. https://doi.org/10.1186/1749-8104-9-2

Tritsch, N. X., Ding, J. B., & Sabatini, B. L. (2012). Dopaminergic neurons inhibit striatal output through non-canonical release of GABA. *Nature*. https://doi.org/10.1038/nature11466

Tukker, J. J., Taylor, W. R., & Smith, R. G. (2004). Direction selectivity in a model of the starburst amacrine cell. *Visual Neuroscience*. https://doi.org/10.1017/S0952523804214109

Vaney, D. I., Sivyer, B., & Taylor, W. R. (2012). Direction selectivity in the retina: Symmetry and asymmetry in structure and function. In *Nature Reviews Neuroscience*. https://doi.org/10.1038/nrn3165

Vaney, D. I., & Young, H. M. (1988). GABA-like immunoreactivity in cholinergic amacrine cells of the rabbit retina. *Brain Research*. https://doi.org/10.1016/0006-8993(88)91366-2

Venkataramani, S., & Taylor, W. R. (2010). Orientation selectivity in rabbit retinal ganglion cells is mediated by presynaptic inhibition. *Journal of Neuroscience*. https://doi.org/10.1523/JNEUROSCI.2081-10.2010

Venkataramani, S., & Taylor, W. R. (2016). Synaptic mechanisms generating orientation selectivity in the on pathway of the rabbit retina. *Journal of Neuroscience*. https://doi.org/10.1523/JNEUROSCI.1432-15.2016

Villette, V., Chavarha, M., Dimov, I. K., Bradley, J., Pradhan, L., Mathieu, B., Evans, S. W., Chamberland, S., Shi, D., Yang, R., Kim, B. B., Ayon, A., Jalil, A., St-Pierre, F., Schnitzer, M. J., Bi, G., Toth, K., Ding, J., Dieudonné, S., & Lin, M. Z. (2019). Ultrafast Two-Photon Imaging of a High-Gain Voltage Indicator in Awake Behaving Mice. *Cell*. https://doi.org/10.1016/j.cell.2019.11.004

Vlasits, A. L., Bos, R., Morrie, R. D., Fortuny, C., Flannery, J. G., Feller, M. B., & Rivlin-Etzion, M. (2014). Visual Stimulation Switches the Polarity of Excitatory Input to Starburst Amacrine Cells. *Neuron*. https://doi.org/10.1016/j.neuron.2014.07.037

Vlasits, A. L., Morrie, R. D., Tran-Van-Minh, A., Bleckert, A., Gainer, C. F., DiGregorio, D. A., & Feller, M. B. (2016). A Role for Synaptic Input Distribution in a Dendritic Computation of Motion Direction in the Retina. *Neuron*. https://doi.org/10.1016/j.neuron.2016.02.020

Wang, L., Sarnaik, R., Rangarajan, K., Liu, X., & Cang, J. (2010). Visual receptive field properties of neurons in the superficial superior colliculus of the mouse. *Journal of Neuroscience*. https://doi.org/10.1523/JNEUROSCI.3305-10.2010

Wässle, H. (2001). Knock out of direction selectivity in the retina. In *Neuron*. https://doi.org/10.1016/S0896-6273(01)00335-X

Wässle, H., Regus-Leidig, H., & Haverkamp, S. (2006). Expression of the vesicular glutamate transporter vGluT2 in a subset of cones of the mouse retina. *Journal of Comparative Neurology*. https://doi.org/10.1002/cne.20942

Wei, W., Elstrott, J., & Feller, M. B. (2010). Two-photon targeted recording of GFP-expressing neurons for light responses and live-cell imaging in the mouse retina. *Nature Protocols*. https://doi.org/10.1038/nprot.2010.106

Wei, W., & Feller, M. B. (2011). Organization and development of direction-selective circuits in the retina. In *Trends in Neurosciences*. https://doi.org/10.1016/j.tins.2011.08.002

Wei, W., Hamby, A. M., Zhou, K., & Feller, M. B. (2011a). Development of asymmetric inhibition underlying direction selectivity in the retina. *Nature*. https://doi.org/10.1038/nature09600

Weng, S., Sun, W., & He, S. (2005). Identification of ON-OFF direction-selective ganglion cells in the mouse retina. *Journal of Physiology*. https://doi.org/10.1113/jphysiol.2004.076695

Wojcik, S. M., Katsurabayashi, S., Guillemin, I., Friauf, E., Rosenmund, C., Brose, N., & Rhee, J. S. (2006). A Shared Vesicular Carrier Allows Synaptic Corelease of GABA and Glycine. *Neuron*. https://doi.org/10.1016/j.neuron.2006.04.016

Wong, R. O., Meister, M., & Shatz, C. J. (1993). Transient period of correlated bursting activity during development of the mammalian retina. *Neuron*, *11*(5), 923–938. http://www.ncbi.nlm.nih.gov/pubmed/8240814

Yamagata, M., & Sanes, J. R. (2008). Dscam and Sidekick proteins direct lamina-specific

synaptic connections in vertebrate retina. *Nature*. https://doi.org/10.1038/nature06469

Yonehara, K., Balint, K., Noda, M., Nagel, G., Bamberg, E., & Roska, B. (2011). Spatially asymmetric reorganization of inhibition establishes a motion-sensitive circuit. *Nature*. https://doi.org/10.1038/nature09711

Yonehara, K., Farrow, K., Ghanem, A., Hillier, D., Balint, K., Teixeira, M., Jüttner, J., Noda, M., Neve, R. L., Conzelmann, K. K., & Roska, B. (2013). The first stage of cardinal direction selectivity is localized to the dendrites of retinal ganglion cells. *Neuron*. https://doi.org/10.1016/j.neuron.2013.08.005

Yonehara, K., Fiscella, M., Drinnenberg, A., Esposti, F., Trenholm, S., Krol, J., Franke, F., Scherf, B. G., Kusnyerik, A., Müller, J., Szabo, A., Jüttner, J., Cordoba, F., Reddy, A. P., Németh, J., Nagy, Z. Z., Munier, F., Hierlemann, A., & Roska, B. (2016). Congenital Nystagmus Gene FRMD7 Is Necessary for Establishing a Neuronal Circuit Asymmetry for Direction Selectivity. *Neuron*. https://doi.org/10.1016/j.neuron.2015.11.032

Yonehara, K., Ishikane, H., Sakuta, H., Shintani, T., Nakamura-Yonehara, K., Kamiji, N. L., Usui, S., & Noda, M. (2009). Identification of retinal ganglion cells and their projections involved in central transmission of information about upward and downward image motion. *PLoS ONE*. https://doi.org/10.1371/journal.pone.0004320

Yonehara, K., & Roska, B. (2014). Neuroscience: Retinal projectome reveals organizing principles of the visual system. In *Current Biology*. https://doi.org/10.1016/j.cub.2014.08.009

Yoshida, K., Watanabe, D., Ishikane, H., Tachibana, M., Pastan, I., & Nakanishi, S. (2001). A key role of starburst amacrine cells in originating retinal directional selectivity and optokinetic eye movement. *Neuron*. https://doi.org/10.1016/S0896-6273(01)00316-6

Zhao, X., Chen, H., Liu, X., & Cang, J. (2013). Orientation-selective responses in the mouse lateral geniculate nucleus. *Journal of Neuroscience*. https://doi.org/10.1523/JNEUROSCI.0095-13.2013

Zhao, X., Liu, M., & Cang, J. (2014). Visual cortex modulates the magnitude but not the selectivity of looming-evoked responses in the superior colliculus of awake mice. *Neuron*. https://doi.org/10.1016/j.neuron.2014.08.037

Part II

Expanding the materials toolbox for neural interrogation

Chapter 7

An atlas for nano-enabled neural interfaces

This chapter is a full reprint of Acarón Ledesma et al., *Nature Nanotechnology* (2019), in which I was the primary author. This work is included with permission from all authors.

Relevant Publication:

Acarón Ledesma, H., Li, X., Carvalho-de-Souza, J. L., Wei, W., Bezanilla, F., & Tian, B. (2019). An atlas of nano-enabled neural interfaces. *Nature Nanotechnology*, 14(7), 645-657.

Understanding the working principles of the nervous system has been a major goal of modern biomedical research. The brain is a high-dimensional functional network that accommodates around 100 billion neurons (in humans) which form local and long-range connections that drive processing of information in specialized brain centres and establish communication across systems, respectively. The complexity of the mammalian brain arises from three important phenomena. First, the high dimensionality of the vertebrate brain creates a 'big data problem' for neuroscience research. Second, neuronal subcellular structures span various length scales, such as tens of nanometres for synapses to centimetres for axonal projections, making it difficult to probe these components simultaneously with current technologies. Finally, approximately another 100 billion non-neuronal cells, called glia, reside in the brain and regulate neural activity through mechanisms that are still poorly understood.

Advances in microscopy and molecular strategies have allowed researchers to gain insight into the intricate organization of the mammalian brain and the roles that neurons play in processing

information. Despite vast progress, therapeutic strategies for neurological disorders remain limited, owing to a lack of biomaterials for sensing and modulating neuronal signalling *in vivo*. Therefore, there is a pressing need for developing material-based tools that can form seamless biointerfaces and interrogate the brain with unprecedented resolution.

7.1 Importance of nanoscale for neural interfaces

Historically, breakthroughs in neuroscience research have been tied to technological advances. For instance, bioelectric phenomena were first explored in the 1790s by Luigi Galvani, but it was not until the advent of electrophysiological recordings in the mid-twentieth century that theories of membrane excitability and ion channels were properly formulated. More recently, the design of new molecular tools for neuromodulation has provided scientists with the ability to control the activity of defined populations of neurons and to establish links between neural pathways and behaviour (Boyden et al., 2005). Nevertheless, our understanding of brain function remains poor, and our ability to prevent and treat neurological disorders is limited, in part because of the lack of minimally invasive tools capable of probing neuronal systems across the range of spatiotemporal scales. Currently, medical professionals rely on bulky implantable metal electrodes to pinpoint the origin of seizures, alleviate symptoms of Parkinson's disease and stimulate nerve growth following injury. The large size of these electrodes relative to individual cell bodies and nerve fibres leads to the activation of surrounding neurons during stimulation, creating unwanted side-effects (Benabid, 2003). Additionally, mechanical insertion of these bulky microelectrodes combined with micromotions within the skull (Terem et al., 2018) leads to immune activation and glial scar formation (Salatino et al., 2017), which encapsulates the electrode, causes displacement from

neurons of interest, decreases the overall device performance and even remodels the structure and function of the neural network surrounding the electrode.

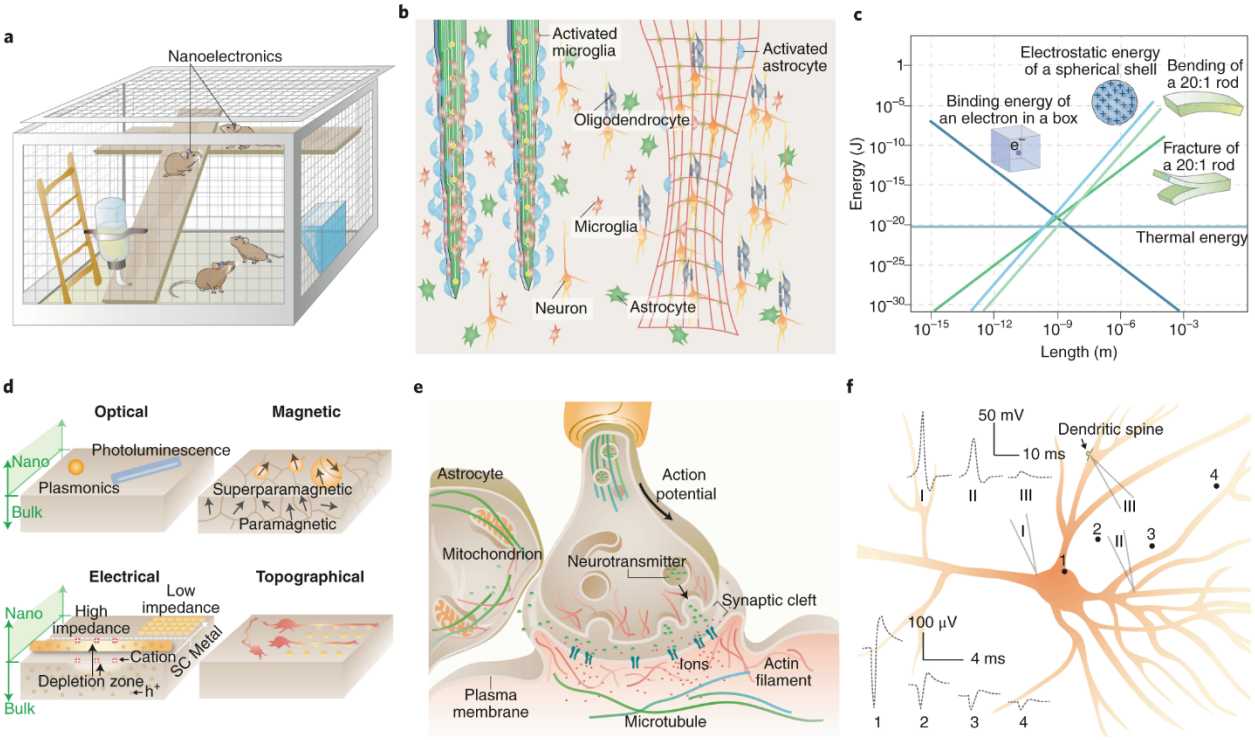

Figure 7.1: Nanoscale materials and devices can offer new opportunities in neural interfaces. **(A)** Nanodevices offer seamless biointegration with neural components, allowing for imperceptible, minimally invasive and wireless brain interrogation. **(B)** Compared with bulk implants (left), devices with nanoscale thicknesses and open framework are flexible, stretchable and can elicit less immune response (right). Many more astrocytes and microglial cells are recruited and activated at the bulk implant surfaces. **(C)** Many energy terms converge in amplitude at the nanoscale, suggesting that signal transduction at the neural interfaces can take multiple forms ("Cell Biology by the Numbers," 2016; R. Phillips & Quake, 2006). **(D)** New properties and capabilities emerge at the nanoscale. For example, as the size of metal or semiconductor shrinks, the plasmonic or photoluminescence properties exhibit size- and shape-dependency. Iron oxide switches from paramagnetic to superparamagnetic behaviour when the particle size is smaller than a single magnetic domain. FETs can be gated more easily with nanoscale channel geometries. Nanoscale protrusions or patterns can also yield a neural response that is absent for a planar neural substrate. SC, semiconductor; h^+, holes. **(E)** The synaptic junction and many other subcellular domains are highly crowded, dynamic and heterogeneous. Therefore, nanoscale electrophysiology and signal transduction can differ from those recorded in the bulk. **(F)** Electrical recordings show different signal shape and amplitude from different regions of a single neuron. The schematic traces 1–4 are extracellular electrical recordings from points 1–4; traces I–III are intracellular recordings from micropipettes I–III. Adapted from: c, (R. Phillips & Quake, 2006), AIP; ("Cell Biology by the Numbers," 2016), Taylor & Francis.

Motivated by increasing demand, academic, federal and private sectors have expanded their research efforts in neural technologies. For instance, the BRAIN Initiative (Insel et al., 2013) in the United States, the Human Brain Project (Amunts et al., 2016) in the European Union and the China Brain Project (Poo et al., 2016) are all multi-billion dollar projects that aim to develop new technologies, build seamlessly integrated neural interfaces for the interrogation of neural signals in freely moving and socially active subjects (**Fig. 7.1a**), and design personalized electronic medicine.

Nanoscale biomaterials can circumvent the limitations of current technologies, representing a potential imperceptible platform (**Fig. 7.1a**) for interfacing the nervous system at unprecedented spatiotemporal scales. First and foremost, the use of nanoscale building blocks means that electrodes can be packed together more densely, improving the resolution of current recording and neuromodulatory systems. Furthermore, given that bending stiffness scales with the cube of material thickness (Lacour et al., 2016), rigid materials become soft, flexible, stretchable and more biocompatible as their feature size reaches the nanoscale (**Fig. 7.1a–c**), reducing the mechanical mismatch between brain tissue and engineered materials. Therefore, although the overall size of implantable devices may remain at the macroscopic scale, nanoscale building blocks that mimic structural and mechanical properties of neural tissue can be seamlessly integrated with brain tissue, without being recognized by the immune system (X. Yang et al., 2019). Indeed, multiple lines of evidence have demonstrated that neural tissue exhibits negligible glial activation and scar formation when implanted with devices fabricated from nanoscale mechanically compliant subunits (Zhou et al., 2017) (**Fig. 7.1b**, right). Additionally, scaling down to the nanoscale can yield new physical properties and improved device capabilities, partially because the chemical,

mechanical, thermal and electrostatic energies all converge at the nanoscale (**Fig. 7.1c**), aiding signal transduction across different energy terms (R. Phillips & Quake, 2006). For instance, atomically thin nanoscale materials that can harvest electromagnetic radiation energy in the Wi-Fi band have been reported, making it possible to actuate neural implants by means of everyday electronics (X. Zhang et al., 2019). Also, nanostructures display size- and shape-dependent plasmonics and photoluminescence, superparamagnetism, enhanced electronic properties and bioactive topographical features, all of which are suitable for neural interrogation (**Fig. 7.1d**). The energy-matching phenomenon (**Fig. 7.1c**) and the emergence of new properties at the nanoscale (**Fig. 7.1d**) can lead to innovative modes of sensing and stimulation that would not be possible with bulky materials or devices.

Finally, nanoscale materials and devices enable localized neural probing. Neuronal membranes and subcellular compartments (**Table 1**) represent extremely crowded environments that use nanoscale molecular machinery to execute numerous tasks in parallel (**Fig. 7.1e**). For example, previous research has illustrated how cellular and biomolecular interactions along with the electrical properties of neuronal membranes formulate the classical description of synaptic transmission (**Fig. 7.1e**). However, how the surrounding local microenvironment, including intimately associated astrocytes, the extracellular matrix, and nearby neuronal processes, influences neural communication is a topic of active research that would benefit from tools with improved spatial resolution and cellular/subcellular targeting. Furthermore, neurons receive synaptic inputs across their dendritic trees, where the summation and integration of local excitatory and inhibitory inputs result in deviations from the resting potential; and, while in most neurons action potentials are generated at the axon hillock, their dendrites are also capable of nonlinear

transformations of electrical signals. In addition, biological membranes experience limited propagation of mechanical tension (Z. Shi et al., 2018) and can therefore elicit localized intracellular signalling in cellular subunits. Thus, nanoscale tools that depict a more accurate description of the multimodal signals experienced by cellular subunits would provide a better interpretation of neuronal input–output relationships and of electrical and mechanical heterogeneities (**Fig. 7.1f**). Moreover, if delivered intracellularly, nanoscale devices would be capable of real-time interrogation of signalling complexes and subcellular organelles — including the cytoskeleton, mitochondria and endoplasmic reticulum (**Fig. 7.1e**) — allowing scientists to explore their contributions to neural activity and determine protocols for rescuing neural phenotypes during disease.

Table 1: Representative numbers in neural systems that are relevant to nanoscale probing.

	Representative numbers	
Membrane	Size	• Thickness: ~5 nm • The membrane discs in photoreceptor rod cells (Selberg et al., 2018): disc spacing ~ 25 nm, disc number ~ 1000
	Rate	• The diffusion coefficient for membrane tension (Z. Shi et al., 2018): ~ 0.024 $\mu m^2/s$
	Physical properties	• Rupture of a membrane: ~ 300-400 mV (voltage (Selberg et al., 2018)), ~ 1-30 mN/m (stress (García-López et al., 2017)) • Peak membrane electric field during an action potential (Efros et al., 2018): ~250 kV cm^{-1}. • Membrane capacitance: 1 $\mu F/cm^2$ (unmyelinated membrane), 2 $\mu F/cm^2$ (node of myelinated membrane), 4.2 x 10^{-4} $\mu F/cm^2$ (internode of myelinated membrane), • Membrane resistance: 1.48 $k\Omega \cdot cm^2$ (unmyelinated membrane), 0.096 $k\Omega \cdot cm^2$ (node of myelinated membrane), 240 $k\Omega \cdot cm^2$ (internode of myelinated membrane)
Ion channels	Size	• ~ 10 x 10 x 10 nm^3 for a voltage-gated ion channel
	Rate	• ~ 10^6 - 10^8 ions per second
	Physical properties	• Time constants of activation/deactivation: sub-millisecond to a few milliseconds. • Time constant to inactivate: tens of milliseconds to seconds or minutes. • Temperature to activate TRPV1: >42 ^oC
Organelles	Size	• Synaptic vesicle volume (Selberg et al., 2018): ~ 10^{-5} μm^3 • Gap distances at the membrane contact sites ("Cell Biology by the Numbers," 2016): 3-15 nm (ER-endosome), 6-15 nm (ER-mitochondria)
	Rate	• Cytoskeletal transport (Kandel et al., 2000): ~ 0.3-1 μm/s (neurofilaments, anterograde), ~ 0.4 μm/s (mitochondria, bidirectional), ~0.3-0.4 μm/s (lysosomes, bidirectional)

Table 1 (cont.)

Organelles	Physical properties	• The stall forces for kinesin and dynein: ~ 7-8 pN (Steketee et al., 2011)
	Chemical properties	• Neurotransmitter concentration in synaptic vesicles (Selberg et al., 2018): ~ 100-200 mM • $[Ca^{2+}]$ in different organelles140: ~ 0.5 μM (early endosome), ~ 2.5 μM (late endosome), ~ 100 μM (peak concentration in inner mitochondrial matrix), ~ 60-500 μM (ER lumen), ~ 100 nM (nucleus)
Neurites and dendritic spines	Size	• Dendritic spines (Jayant et al., 2017): head (volume ~0.001–0.1 μm^3), neck (diameter ~0.1 μm, length ~1 μm) • Periodicity of actin rings in axon (Wang et al., 2018): ~ 190 nm • Node of Ranvier: ~ 1 μm
	Rate	• Growth cone motility of rat retinal ganglion cell *in vitro* (Steketee et al., 2011): ~ 30-60 μm/h.
	Physical properties	• EPSP attenuation in mouse hippocampal neuron (Jayant et al., 2017): from ~26 mV (spine head) to ~ 0.5-1 mV (soma) • Fracture strain and ultimate stress of nerves (Lacour et al., 2016): ~ 25% and ~ 10 MPa
Intercellular junctions	Size	• Chemical/electrical synaptic junction gap (Selberg et al., 2018): ~ 20-40 nm/~2-4 nm • Lumen diameter of electrical gap junction channel (Kandel et al., 2000): ~1.2-2 nm • The ratio of the axonal diameter divided by the diameter of the axon and its myelin sheath (g-ratio)(M. J. Phillips & Voeltz, 2016): 0.6-0.7
	Rate	• Chemical clearance at a synapse (Selberg et al., 2018): ~ 1 ms
	Physical properties	• Diameter requirement for cultured oligodendrocytes myelination (Seonok Lee et al., 2012): > 0.4 μm
Brain	Size	• Weight: ~2% of total body mass • Human brain blood vessels (Y. Chen & Liu, 2012; Millecamps & Julien, 2013): number ~ 100 billion, length ~ 650 km, surface area ~ 20 m^2 • The mean intercapillary distance in the human brain: ~ 40 μm • Volume of brain extracellular space (K. Xu et al., 2013): ~ 20 % of the brain tissue
	Rate	• Action potential speeds in humans: 10-100 m/s • Effective molecular diffusion coefficient in brain extracellular space (K. Xu et al., 2013): ~ 2/5 of that in a free solution
	Physical properties	• Elastic modulus (Lacour et al., 2016; Sherman & Brophy, 2005): 1.40 kPa (grey matter), 1.90 kPa (white matter), ~ 0.5-1.2 MPa (dura mater), ~10 GPa (cortical bone) • Elastic moduli that favour glial growth and migration (Lacour et al., 2016): ~ 700 Pa (oligodendrocytes), >10 kPa (microglia) • Intracranial pressure: 7-15 mmHg

7.2 Natural and cultured neural systems

During development, neurons assemble into functional networks through the concerted action of both molecular (Huberman et al., 2005) and activity-dependent (Dhande et al., 2011) mechanisms. The precise organization of excitatory and inhibitory synapses in local brain circuits coordinates the algorithmic functions involved in the execution of complex tasks such as information

processing. In the case of the vertebrate retina, the way in which neurons organize throughout development gives rise to its characteristic laminar structure (**Fig. 7.2a**), determines the direction of information flow (Hoon et al., 2014) and dictates the termination patterns of retinal axons onto downstream visual nuclei. Photoreceptors, bipolar cells and retinal ganglion cells form the main excitatory pathway in the retina and transmit information vertically (Hoon et al., 2014) (**Fig. 7.2a**), whereas horizontal cells and amacrine cells provide lateral inhibitory input to retinal neurons, helping to regulate the extent to which membranes become depolarized and thus modulate neuronal output. Because most circuit motifs observed throughout higher-order brain centres can be found in this simple tissue (three cellular layers and two synaptic layers), the retina has become a model system for testing developing neural technologies and for understanding how to restore sensation and proper neural function. For example, optoelectronic retinal prostheses, or devices capable of converting light into electrical currents that can activate the retinal network (Choi et al., 2017), are currently being explored as avenues for restoring vision. Although these have been effective as proof-of-concept, scaling down building block components to the nanoscale (Tang et al., 2018) (blue dots in **Fig. 7.2a**) may further enhance properties at the biointerface and even offer new interrogation capabilities. For example, injectable mesh nanoelectronics have enabled long-term *in vivo* recordings from individual retinal ganglion cells in awake animals (Dai et al., 2018), a capability previously inaccessible with conventional devices. More recently, injectable self-powered near-infrared (NIR) nanoantennae based on up-conversion nanoparticles (UCNPs) that bind to photoreceptors and transform NIR light into short-wavelength emissions have extended the mammalian visual spectrum into the NIR range (Ma et al., 2019). Lastly, besides subretinal and epiretinal implantation, nanoscale electrodes may interface subcellular structures in the inner

retina, such as dendritic shafts and individual varicosities, allowing compartmentalized signalling to be studied and shedding light on how information is processed by neuronal subunits.

Brain structures and neural signals (Table 1) are complex, multiscale and highly interconnected, and are regulated by many non-neuronal factors, including glial interactions and the extracellular matrix. For over a century, scientists have relied on cultured systems (**Fig. 7.2b–d**) to gain access to specific cell types and to simplify experimental studies. While primary cell cultures of hippocampal, cortical, and spinal cord neurons have been instrumental in elucidating mechanisms underlying neuronal development and cell polarization (Millet & Gillette, 2012), these cannot recapitulate many key extrinsic factors and signals that are known to coordinate neuronal organization, synaptogenesis and circuit development (Seabrook et al., 2017).

Advances in microfabrication and stem cell biology have led to the implementation of new *in vitro* model systems that can simplify and accelerate the characterization of nanoscale tools for neuroscience (blue dots in **Fig. 7.2b–d**). For example, immature neurons have been cultured in elastomeric polydimethylsiloxane (PDMS) microchips, in which channels and chambers provide spatiotemporal control of the extracellular chemical environment (Gonzales et al., 2017) (**Fig. 7.2b**). A similar approach can be used to study the formation of synapses between neuronal populations and the associations between neurons and glial cells (J. Park et al., 2009) (**Fig. 7.2b**). Nanoscale devices can be used in conjunction with these microfluidic systems to study axogenesis, myelination and synaptogenesis.

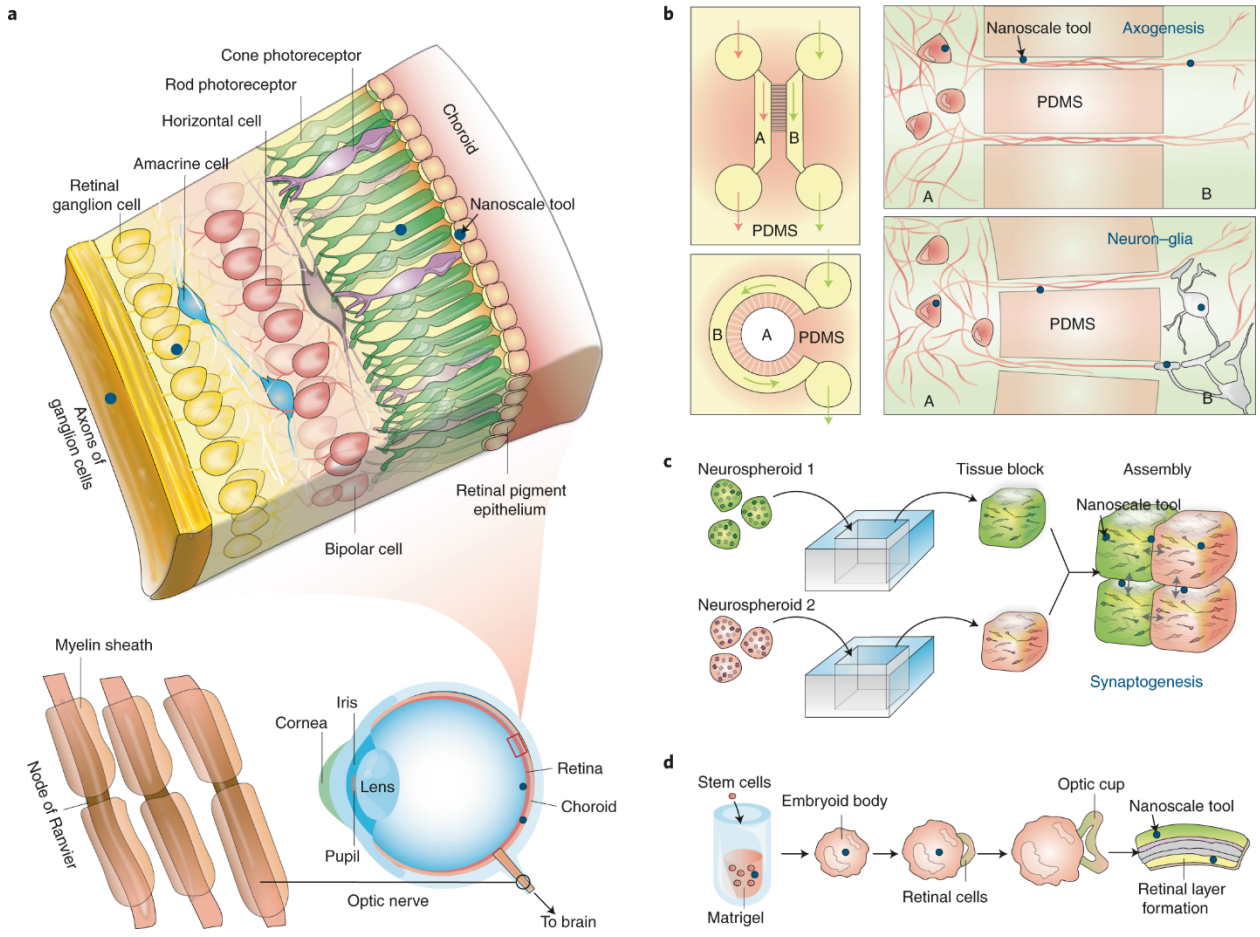

Figure 7.2: Naturally occurring and cultured neural systems provide plenty of room for nanoscale probing. (A) Layered structure of retinal tissue. Although epi- and subretinal spaces have been extensively explored for implants, nanoscale tools (blue dots) may access the retinal internal layers. **(B – D)** Neural cultures in 2D and 3D can enable bottom-up integration of devices with cells in a seamless manner. **(B)** Microfluidic systems with different compartments (for example, A and B) allow selective manipulation of neural cells, where nanoscale tools (blue dots) can be rationally positioned for studying axogenesis and neuron–glia interactions. **(C)** Neurospheroids can be assembled into 3D tissues, and nanoscale tools (blue dots) can be positioned at the tissue block interfaces for synaptogenesis and circuit studies. **(D)** Embryonic stem cells can develop into lab-grown retina, during which nanoscale tools may be used for growth control or for probing the functions of the final engineered tissues.

Recently, three-dimensional (3D) co-cultures and brain organoids have emerged as other *in vitro* alternatives that address some of the limitations experienced with 2D primary cell cultures (Quadrato et al., 2017; Sloan et al., 2018). For example, neurons assembled into cortical spheroids (**Fig. 7.2c**) display an enhanced level of self-organization reminiscent of a developing neocortex

and exhibit molecular expression of both deep and superficial cortical biomarkers (Pasca et al., 2015). Therefore, neurospheroids derived from human-induced pluripotent stem cells (hiPSCs) can more faithfully recapitulate human brain physiology (Birey et al., 2017; Pasca et al., 2015; Sloan et al., 2018) and have potential as neural models for studying the pathophysiology and progression of neuropsychiatric disorders. Stitching together blocks of tissue containing distinct neuronal populations (**Fig. 7.2c**) allows the study of attraction and repulsion of self and non-self neurites during synaptogenesis and of how they establish wiring specificity (Kato-Negishi et al., 2013). Nanoscale materials could probe the role played by local bioelectric signals during this process. Similarly, brain organoids grown from differentiated hiPSCs have become attractive models for studying brain development. As originally described by Eiraku et al., brain regions can spontaneously sprout from embryoid bodies, or clusters of embryonic stem cells, simply by modifying the conditions and local microenvironment in which cells are cultured (Eiraku et al., 2011). Further work on brain organoids has realized retina-like (Quadrato et al., 2017) and forebrain-like structures (Birey et al., 2017; Lancaster et al., 2017; Quadrato et al., 2017) with neurons becoming integrated into spontaneously active networks and photosensitive neurons in the optic cup enabling coordinated evoked activity upon light illumination (Quadrato et al., 2017). Nanoscale devices can interface brain organoids as they differentiate and develop into specialized brain regions, allowing scientists to understand how bioelectric signals emerge in the developing brain and how neural networks transition between activity states during development.

7.3 Nanoscale tools and building blocks

Current tools for neural interrogation include single-unit pulled glass micropipette electrodes or multi-electrode arrays, such as the Utah- and Michigan-style arrays. However, their mechanical

invasiveness and the decaying signal-to-noise ratio has pushed further research to focus on the miniaturization of these technologies and the innovation of platforms capable of seamless integration with brain tissue.

7.3.1 Substrate-bound transistors

Semiconductor nanostructures have emerged as promising materials for next-generation neural interfaces owing to their diverse physical properties, scalable fabrication and good biocompatibility (Jiang & Tian, 2018). In particular, nanoscale field-effect transistors (nanoFETs) represent a powerful alternative to traditional platforms because their performance does not depend on device impedance and can be experimentally scaled down to the sub-10-nm regime (Fu et al., 2014). Of particular relevance to neuroscience applications, carriers in the transistor channel of nanoFETs can be depleted (or modulated) by neural signals much more easily than in bulk, yielding higher voltage sensitivity (Mirza et al., 2017) (**Fig. 7.1d**). Additionally, the intrinsic delay time of a FET, as described either by equation (1) for conventional complementary metal–oxide semiconductor or by equation (2) for junctionless nanowire FETs

$$\tau = \frac{L^2}{\mu V_{DD}} \quad (1)$$

$$\tau = \frac{C_{ox} L^2}{q \mu N_D T_{si}} \quad (2)$$

(where C_{ox} is the gate oxide capacitance, L is the transistor gate length, μ the electron mobility, N_D the doping concentration, T_{Si} the thickness of silicon and V_{DD} the supply voltage) (Colinge et al., 2010) implies that with decreasing L, the device speed increases, potentially allowing nanoFETs to resolve faster neural events. Novel nanoFET configurations have been introduced in the past decade (**Fig. 7.3a**), including those based on kinked nanowires (Tian et al., 2010), bent nanowires (Y. Zhao et al., 2016), Si nanowire backbone/oxide nanotube branch structures (Duan et al., 2012;

Fu et al., 2014), Si nanotubes (Gao et al., 2012), ultra-short channel and etched nanowires (Cohen-Karni et al., 2012), nanomembranes (Kang et al., 2016), porous particles (Jiang et al., 2016), or graphene (Kuzum et al., 2014; D. W. Park et al., 2014), and those integrated into mesh-like nanoelectronics (J. Liu et al., 2015; Tian et al., 2012; Xie et al., 2015). Additionally, stretchable, high-mobility transistors have been realized by exploring nano-confinement in semiconducting polymers (J. Xu et al., 2017). Many of these nanoFETs act as point-like detectors capable of recording the dynamics of membrane voltages and extracellular field potentials. Furthermore, design principles have been developed for the future implementation of nanoFETs in either chronic (Fu et al., 2017; Zhou et al., 2017) or transient (Kang et al., 2016; Koo et al., 2018) applications.

7.3.2 Substrate-bound electrodes

A common strategy for reducing electrical impedance and improving charge injection capability is to enhance the surface area by introducing roughness, porosity or other nanostructured (Sunghoon Lee et al., 2019; Miyamoto et al., 2017) topographies to metal electrodes (**Fig. 7.1d**). Over the past decade, engineering approaches have been developed to expand the scope of miniaturized and nanostructured metal electrodes.

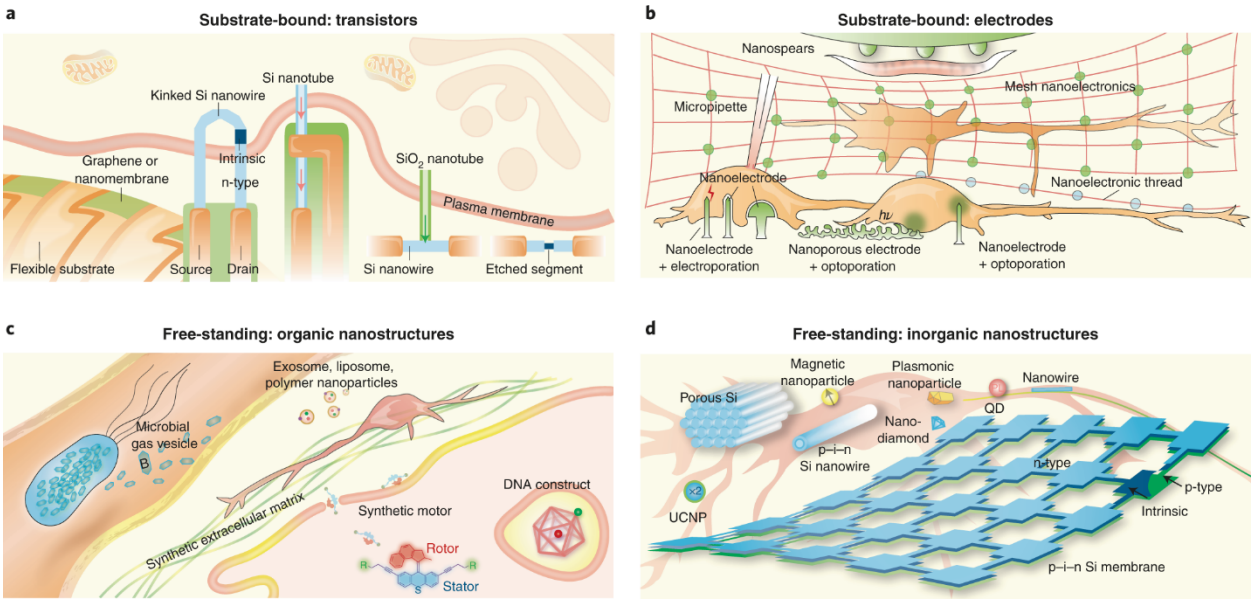

Figure 7.3: Nanoscale toolbox for neural interfaces. (A) Sharp protrusions formed by kinked *n–i–n* Si nanowires, Si nanotubes, or structures with SiO_2 nanotube branches and Si nanowire backbones have enabled transistor-based intracellular electrical recording. Selective etching of a segment in a Si nanowire FET promises localized extracellular recording. 2D nanomaterial-based FETs over flexible substrates can form compliant extracellular biointerfaces. The arrows highlight the entrance of cytosol into FET regions. **(B)** Gold mushroom-shaped nanoelectrodes, nanopillars/nanowires and nanospears yield high-resolution extracellular recording. With electroporation or optoporation, nanopillars/nanowires or nanoporous electrodes achieve intracellular recording. Metal films with nanoscale thicknesses allow brain tissue interfaces with mesh nanoelectronics or nanoelectronic-thread configurations. Nanospears represent an example of integration of a bioelectronics device with a microfluidic system. **(C)** DNA constructs can be used for intracellular delivery and sensing. Synthetic ECM can guide neural differentiation and growth. Exosome, liposome, polymer nanoparticles and synthetic motors may be used for drug delivery to neurons. Recently developed microbial gas vesicles hold promise for MRI and ultrasound imaging. **(D)** Mesoporous Si particles, *p–i–n* Si nanowires, superparamagnetic nanoparticles, plasmonics nanoparticles, UCNPs and *p–i–n* Si membranes have been developed for extracellular neuromodulation. The internalized Si nanowires permit intracellular modulation and cytoskeletal control. Quantum dots (QD) and nanodiamonds have been used for imaging or organelle tracking in neurons.

First, an important step has been the achievement of intracellular or intracellular-like recordings (**Fig. 7.3b**). For instance, mushroom-shaped noble-metal electrodes help in the detection of intracellular signals following engulfment through intrinsic phagocytic pathways (Hai et al., 2010; Hai & Spira, 2012). Similarly, vertical metal nanopillars (Xie et al., 2012), nanotubes (Lin et al., 2014) and metal-coated semiconductor nanowires (Robinson et al., 2012) have demonstrated the

capacity for intracellular recording and stimulation following electroporation. Gold nanotubes have also been used for localized poration (that is, pore formation in membranes) upon irradiation with near-infrared laser pulses, which allows for multiplexed intracellular recordings in neurons (Dipalo et al., 2017). Following this logic, nanoporous (50–200 nm) thin films of Pt metal have been used in the design of ultrasensitive electrodes for the recording and stimulation of excitable membranes following optoacoustic poration (Dipalo et al., 2018).

Second, considerable advances have been achieved in the fabrication of nanostructured electrode arrays over flexible or even macroporous polymer substrates (Fu et al., 2017; Tian et al., 2012; Xie et al., 2015) to create mechanically compliant 2D or 3D interfaces (**Figs. 7.1a, 3b**). Besides 3D mesh nanoelectronics, Xie and colleagues embedded Pt and Au electrodes in an ultraflexible polymer shank to create one of the smallest neural probes ever reported, the nanoelectronic thread (Luan et al., 2017).

Finally, integrated approaches have been developed to incorporate neural electrodes into other device platforms, such as microfluidic systems. For example, metal nanoelectrodes suspended from microfluidic channel walls (nanospears) have been used to study neuromuscular signal transduction (Gonzales et al., 2017) in intact small animals.

7.3.3 Free-standing organic nanostructures

Untethered operation of nanostructured platforms is attractive, as it allows these materials to act as free-standing devices and enables wireless interrogation of cellular activity through recording or localized stimulation (**Fig. 7.3c**). Nanostructured biological materials (Alvarez-Erviti et al.,

2011; Bhatia et al., 2016; Edelbrock et al., 2018; Leung et al., 2019; Prakash et al., 2016; Saha et al., 2015; Shapiro et al., 2014; Thubagere et al., 2017; Veetil et al., 2017) fabricated through rational design have ideal properties for subcellular interrogation, given their natural occurrence in biology, nanoscale feature size and self-assembly. For example, the incorporation of responsive domains and functional moieties into self-assembled DNA nanoconstructs provides a powerful approach for fabricating devices capable of sensing and actuation, as recently exemplified in sensors for ionic species (Prakash et al., 2016; Saha et al., 2015), in lysosome sensors based on fluorescence resonance energy transfer (Leung et al., 2019) and in drug-delivery vectors (Veetil et al., 2017). Other forms of nanostructured biological materials, such as peptide-presenting nanostructures (Edelbrock et al., 2018), exosomes (Alvarez-Erviti et al., 2011) and bacterial gas vesicles (Shapiro et al., 2014), are now beginning to be exploited as biological probes. In particular, gas vesicles —gas-filled protein-shelled compartments with typical widths of 45–250 nm and lengths of 100–600 nm — can help the cavitation centre to transduce acoustic energy into mechanical force or boost the functional ultrasound imaging resolution. Finally, besides polymer nanostructures (Sytnyk et al., 2017; Tortiglione et al., 2017), synthetic molecular machines (Berná et al., 2005) designed as rotors, walkers and cages have been used to transform optical energy into mechanical action causing reversible or irreversible openings in the lipid bilayer (García-López et al., 2017).

7.3.4 Free-standing inorganic nanostructures

Optical (Carvalho-de-Souza et al., 2018), acoustic (Kubanek et al., 2018) and magnetic stimulation (Hallett, 2000) represent non-invasive methods for neural stimulation. However, these strategies alone do not show optimal spatial resolution, lack ways of selective targeting and often require

high power densities potentially causing off-target effects. On the other hand, inorganic nanoscale materials are capable of harnessing energy, transducing it into physiologically relevant stimuli and focusing the site of action to localized subcellular compartments (**Fig. 7.3d**). For example, Au nanoparticles (Carvalho-de-Souza et al., 2015) and porous Si nanostructures (Y. Fang et al., 2018; Jiang et al., 2016) produce a photothermal effect that can be exploited for optocapacitive neuromodulation. Coaxial *p–i–n* Si nanowires (Parameswaran et al., 2018) or multi-layered Si membranes (Jiang et al., 2018) yield photoelectrochemical current for wireless activation of neural cultures or brain activity. UCNPs (Ma et al., 2019; Pliss et al., 2017) and fluorescent nanodiamonds (Haziza et al., 2017) have been used for NIR vision and neuromodulation, and for visualizing intraneuronal transport, respectively. Other examples of wireless stimulation and sensing include the use of heat-dissipating or force-generating superparamagnetic nanoparticles (H. Huang et al., 2010; Tay et al., 2016; Tay & Di Carlo, 2017) for ion channel modulation. These magnetic nanoparticles generate local force under a static magnetic field; however, in low-radiofrequency alternating magnetic fields, they can experience heat dissipation through relaxation processes (Roet et al., 2019). Finally, quantum dots have potential as optical indicators of membrane voltage through the quantum-confined Stark effect (Efros et al., 2018).

7.4 Neural interfaces at all length scales

7.4.1 Plasma membrane

At rest, the membrane potential sits at approximately −70 mV and, depending on the net excitatory drive, becomes depolarized by a few millivolts for subthreshold events or by 70–120 mV during action potential firing. These events are about 120 mV in amplitude at most; however, they generate large electric fields due to charge separation across a very thin geometry (Table 1).

Therefore, electric-field-sensitive nanoscale devices, such as photoluminescent quantum dots, are candidates for local readout of the membrane potential (Marshall & Schnitzer, 2013; Peterka et al., 2011). In the presence of an electric field, quantum dots experience a fast redshift in their emission spectra and a decrease in photoluminescence intensity (Efros et al., 2018) (**Fig. 7.4a**). Although embedding nanoparticles 60 nm or smaller in size within vesicle bilayers has been feasible (Bonnaud et al., 2014), the ability to accommodate quantum dots into neuronal membranes remains a challenge, limiting quantum dot applications for neuroscience. For electrical readout, kinked semiconductor nanowire FETs (**Fig. 7.4a**) have been proposed as local detectors of membrane potentials and have been configured onto flexible SU-8 substrates for 3D probing (Tian et al., 2010). To promote biomimetic intracellular entry, the surface of these nanowires can be modified with phospholipid coatings (Tian et al., 2010) and cell-penetrating peptides derived from HIV-1 (J. H. Lee et al., 2016). Additionally, synthetic molecular actuators (García-López et al., 2017) could provide the means to locally destabilize the membrane for device entry, as they can be designed with sensitivity to visible light, NIR, ultraviolet and radiofrequency (T. Xu et al., 2017).

Regarding neuronal modulation, millisecond infrared pulses can trigger action potentials in unmodified membranes through optocapacitive photothermal effects (Carvalho-de-Souza et al., 2018). In short, infrared irradiation results in local heating around the cell membrane, causing an increase in membrane capacitance (C) that generates an inward depolarizing capacitive current (I_{cap}). This technique explores the derivative of the capacitance that appears when one differentiates with respect to time the charge (Q) flowing to or from the membrane capacitor, as described by

$$I_{cap} = \frac{dQ}{dt} = C\frac{dV}{dt} + V\frac{dC}{dt} \quad (3)$$

Au nanorods (Carvalho-de-Souza et al., 2018) and porous Si nanostructures (Y. Fang et al., 2018; Jiang et al., 2016) can also show this phenomenon, as they experience heating upon irradiation with visible and NIR wavelengths and can be surface-modified with high-avidity neuronal ligands and antibodies (Carvalho-de-Souza et al., 2015). Therefore, nanostructured materials (**Fig. 7.4a**) offer a more targeted and localized photothermal stimulation, and can shift working wavelengths towards those commonly accessible in research laboratories and clinical settings (Carvalho-de-Souza et al., 2015). Alternatively, researchers have begun to explore the potential use of nanostructured photodiodes (Parameswaran et al., 2018) (as illustrated by the coaxial blue/green nanowire in **Fig. 7.4a**, top right) as free-standing, minimally invasive, and potentially more sensitive optoelectronic stimulators. Recently, Parameswaran et al. demonstrated that *p–i–n* Si nanowires doped with atomic Au on the surface exhibit photoelectrochemical current generation upon irradiation with visible light (Parameswaran et al., 2018) and can elicit single and trains of action potentials. The inclusion of Au and potentially other catalysts in these nanostructures enhances the Faradaic photoelectrochemical output (Jiang et al., 2018; Parameswaran et al., 2018) and results in wireless activation of neuronal membranes.

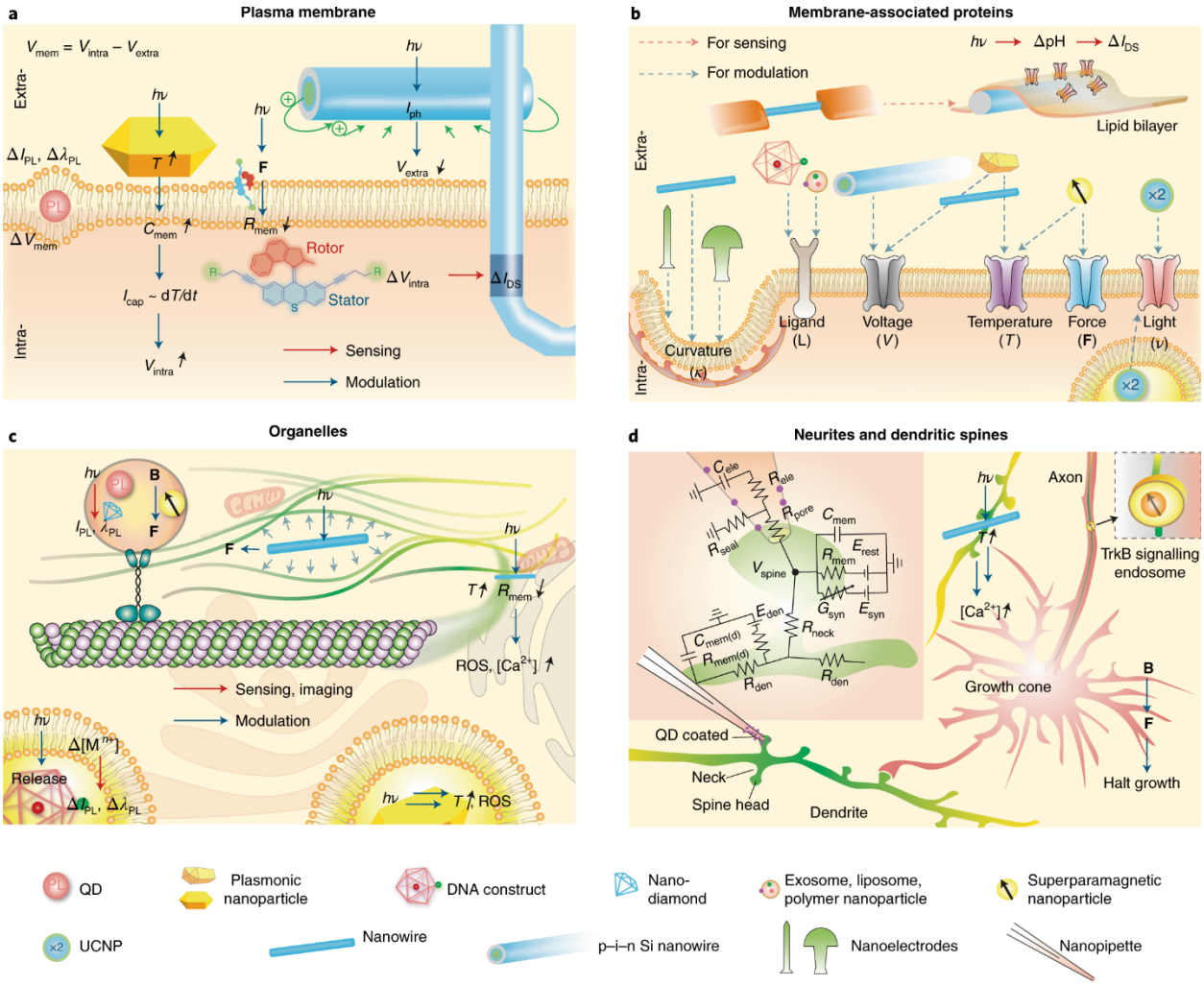

Figure 7.4: Nano-enabled subcellular neural interfaces. a, Interfacing plasma membranes: research labs have developed kinked nanowire FETs for intracellular electrical recording, Au nanorods for photothermal neuromodulation, coaxial Si nanowires for photoelectrochemical neuromodulation, synthetic molecular rotors for potential device entrance into neurons, and quantum dots for potential optical recording of membrane voltage. *hv*, photon energy; PL, photoluminescence; ΔI_{PL}, PL intensity change; $\Delta\lambda_{PL}$, PL wavelength change; T, temperature; F, force; I_{cap}, capacitive current; I_{ph}, photocurrent; ΔI_{DS}, FET source–drain current change; C_{mem}, membrane capacitance; R_{mem}, membrane resistance; V_{mem}, membrane voltage; V_{extra}, extracellular potential; V_{intra}, intracellular potential. **(B)** Interfacing membrane-associated proteins: exosomes, liposomes, polymer nanoparticles and DNA constructs present ligands for cellular targeting and induced endocytosis. Coaxial nanowire produces a photoelectrochemical effect to modulate the local extracellular potential and affects voltage-sensitive ion channels. A rapid photothermal effect from plasmonic nanoparticles or Si nanowires causes depolarization of plasma membrane and triggers activities in voltage-sensitive ion channels. The long-lasting photothermal effect and the magnetothermal effect from superparamagnetic nanoparticles can affect temperature-sensitive ion channels. Superparamagnetic nanoparticles can also actuate mechanical-sensitive ion channels. UCNPs have been used for ion channel modulation, possibly through both extra- and intracellular configuration. Other substrate-bound nanostructures can produce a response from curvature-sensing membrane proteins. Ion channels can also be reconstituted in vitro, producing electrical

Figure 7.4 (cont.) sensing signals in Si nanowire FET. **(C)** Interfacing organelles: quantum dots or nano-diamonds, plasmonic nanoparticles and superparamagnetic nanoparticles have been used for imaging or controlling cytoskeletal transport or polymerization. Intracellular Au may produce reactive oxygen species (ROS) and other cytotoxic effects upon light illumination. DNA constructs can be used for sensing of calcium or pH in the endosomes. Intracellular Si nanowire also allows for cytoskeletal control via the photoacoustic effect or calcium initiation via the photothermal effect. I_{PL}, PL intensity; λ_{PL}, PL wavelength; B, magnetic field; $[Mn^{+}]$, ion concentration. **(D)** Interfacing neuritis and dendritic spines: quantum-dot-coated nanopipette allowed the recording from the spine. Magnetic control of TrkB signalling can halt the neurite growth. A cross-junction between Si nanowire and filapodium produced localized calcium initiation. Inset, schematic diagram of the electrical equivalent circuit for the passive dendritic spine, adapted from (Jayant et al., 2017). R_{den}, dendritic resistance; R_{ele}, pipette resistance; R_{mem}, passive membrane resistance of spine head; $R_{mem(d)}$, dendrite passive membrane resistance; R_{neck}, neck resistance; R_{pore}, pore resistance; R_{seal}, seal resistance; C_{ele}, pipette capacitance; C_{mem}, passive membrane capacitance of spine head; $C_{mem(d)}$, dendrite passive membrane capacitance; E_{syn}, synaptic reversal potential; E_{rest}, leak reversal potential; E_{den}, dendritic reversal potential; G_{syn}, synaptic conductance. Adapted from: d, (Jayant et al., 2017), SNL.

7.4.2 Membrane-associated proteins

Currently, 60% of all pharmacological drugs target membrane-associated proteins, mainly G-protein-coupled receptors, ligand-gated ion channels and voltage-gated ion channels (Overington et al., 2006). Although the design of pharmaceuticals has been instrumental in improving human health, they can produce many off-target side effects as they access several tissues and organs. Therefore, nanoscale platforms (**Fig. 7.4b**) capable of targeting a wider array of molecular targets and modulating protein activity through a broader range of modalities could shape the future of medicine. For example, exosomes (Alvarez-Erviti et al., 2011), liposomes, polymeric nanoparticles (Kreuter, 2014) and DNA nanocages (Veetil et al., 2017) can present moieties for specific cell targeting (including the location of disease pathology) and induce endocytosis. Similarly, voltage-gated ion channels can be modulated by local changes in the membrane potential, through either photoelectrochemical process by coaxial nanowires (Parameswaran et al., 2018) or optocapacitive effect by Au nanoparticles (Carvalho-de-Souza et al., 2015, 2018) and porous nanostructures (Y. Fang et al., 2018; Jiang et al., 2016; Sytnyk et al., 2017). Under constant

illumination, Au nanostructures, instead of driving the optocapacitive effect, can induce suppression of spontaneous and potentially evoked correlated activity, through the activation of temperature-sensitive ion channels, such as TREK1 temperature-sensitive potassium channels (Yoo et al., 2014). Superparamagnetic nanoparticles can also have dual roles, as either local heat generators to target temperature-sensitive ion channels, such as TRPV1, or local force generators to target mechanosensitive channels. The ability to specifically target these ion channels will shed light on the mechanisms underlying touch perception, pain sensation and regulation of internal pressure.

Furthermore, cells cultured on vertically protruding nanostructures have revealed that local membrane curvature resulting from the settling of cell membranes around vertical electrodes promotes the recruitment of membrane curvature-sensing proteins and the engulfment of foreign particles (W. Zhao et al., 2017) (**Fig. 7.4b**). Lastly, nanoprobes can work in conjunction with optogenetic ion channels, allowing researchers to obtain a better understanding of their biophysical mechanisms and to further expand their potential use *in vivo*. For instance, bacterial opsins reconstituted in artificial lipid bilayers can be interfaced with Si nanowire FETs; on light illumination, the flow of ions across these channels will change the local pH around the nanoFET and yield a variation in device conductance (Tunuguntla et al., 2015). Moreover, in combination with UCNPs, optogenetic strategies (**Fig. 7.4b**) can be extended for deep brain stimulation, given that UCNPs can convert tissue-penetrating NIR laser pulses into visible light (S. Chen et al., 2018).

7.4.3 Subcellular organelles

In addition to biochemical signalling, mechanotransduction and charge-transfer phenomena are widespread throughout biological systems and across length scales. This is exemplified by subcellular organelles, but how these fundamental forces help coordinate subcellular processes and how they influence cell function and survival remain open ended questions in cell biology and require tools capable of visualizing and interrogating their interactions.

Nanostructures with physical features on the same order as organelles display negligible or low cytotoxicity and can enter cells through multiple internalization mechanisms (W. Zhao et al., 2017; Zimmerman et al., 2016). For example, internalized fluorescent nanodiamond (Haziza et al., 2017), photoluminescent quantum dots (Efros et al., 2018) and engulfed Au nanorods (Gu et al., 2012; Kaplan et al., 2018) become localized in endosomes and aid real-time imaging of axonal transport in cultured neurons (Haziza et al., 2017) (**Fig. 7.3c**). Nanoscale probes can help us to achieve a deeper understanding of biophysical mechanisms involved in molecular transport with the goal of potentially integrating these into biohybrid systems (Goel & Vogel, 2008). Organelles, such as the endoplasmic reticulum and mitochondria, may also be interfaced with photothermal Au nanoparticles (Carvalho-de-Souza et al., 2015) and nanostructured Si (Y. Fang et al., 2018; Jiang et al., 2018) for modulation of intracellular calcium levels and metabolic control over individual cells (**Fig. 7.3c**). However, it is important to note that the illumination condition during photothermal stimulation should be considered if reactive oxygen species and other cytotoxic effects need to be avoided (Johannsmeier et al., 2018). Additionally, in cases where a strong, non-damaging photothermal effect is induced, local shockwaves can be generated by the rapid increase in temperature, which have the potential for cytoskeletal manipulation and activation of mechanosensitive proteins inside cells (Jiang et al., 2018). Finally, DNA nanocages can locally

deliver molecular payload inside cells (Veetil et al., 2017) and report on intracellular and lumenal levels of calcium (Narayanaswamy et al., 2019), chloride (Leung et al., 2019; Prakash et al., 2016; Saha et al., 2015)**,** and pH (Leung et al., 2019) (**Fig. 7.3c**).

7.4.4 Neurites and dendritic spines

Advances in fluorescence (F. Chen et al., 2015; K. Chung & Deisseroth, 2013; B. Huang et al., 2008) and electron microscopy (Denk & Horstmann, 2004) have made it possible to map the connections of neuronal processes (or neurites) in 3D space, with nanometre resolution, across the entire nervous system of invertebrates (Zheng et al., 2018) and many mammalian brain regions (Gao et al., 2019; Martersteck et al., 2017). Nevertheless, how these anatomical substrates correlate to physiological function remains elusive in neuroscience, partly owing to the lack of tools able to interrogate local membrane dynamics.

Dendritic spines are membranous protrusions in dendrites, consisting of a spine head enriched in postsynaptic receptors and a narrow neck that compartmentalizes the spine from the rest of the dendrite (Beaulieu-Laroche & Harnett, 2018). Despite their extremely small size (Table 1), they play important roles in neuronal processes such as synaptic plasticity and have been recently targeted with quantum-dot-coated nanopipettes (Jayant et al., 2017) (**Fig. 7.4d**), revealing the dependency of somato-dendritic excitatory postsynaptic potentials on spine neck resistance. Therefore, as techniques for targeting dendrites and spines with nanoFETs and nanowire modulators (Y. Fang et al., 2018) (**Fig. 7.4d**) become more readily available, we expect that nanotechnology will open exciting opportunities to understand the electrical signals generated in dendritic structures and how they spread across neurons.

Axons also play important roles in bioelectric signalling, as action potentials generated at the axon hillock are conducted towards the axon terminal where they trigger neurotransmitter release. Nanoscale interfaces have aided in studies of axonal signal propagation using nanoFET arrays (Patolsky et al., 2006); however, nanostructures can also be used for studying axogenesis. For example, superparamagnetic nanoparticles functionalized with TrkB antibodies (**Fig. 7.4d**) have proven to be beneficial as they can initiate neurotrophic signalling and become engulfed into signalling endosomes (Steketee et al., 2011). Once located inside endosomes, these functionalized magnetic nanoparticles can help to visualize endosomes as they travel throughout neurons, and provide a means of manipulating endosome position and the neurite growth dynamics through the application of magnetic fields (Steketee et al., 2011).

7.4.5 Intercellular junctions

Neural communication is a fast and dynamic process coordinated by molecularly defined synaptic junctions, where the activity of a presynaptic neuron influences the activity of its postsynaptic neuron(s). During development, growth cones sense molecular guidance cues in the extracellular environment that direct their growth towards appropriate sublaminae where synaptic partners meet and form synapses. However, studies have recently demonstrated that nanowire topography (Gautam et al., 2017) also carries relevant information that helps guide neurite growth and coordinate synapse formation (**Fig. 7.5a**), suggesting that the nanoscale architecture of the extracellular environment works together with chemical cues to direct neurites to their proper destination. Further studies focusing on how nanoscale topography can be used to replicate neuronal organization seen *in vivo* will lead to advances in 3D neuron cultures and brain organoid

research (**Fig. 7.2c,d**). Moreover, techniques for interrogating and manipulating synapses are highly desirable in neuroscience research, as these can help to test functional connections between neurons and determine the contribution of specific synapses to neuronal output. Free-standing nanoscale devices, such as intracellular Si nanowires (Jiang et al., 2018) and extracellular Au particles (Carvalho-de-Souza et al., 2015; Yoo et al., 2014) are inorganic alternatives for intercellular neuromodulation (**Fig. 7.5a**) that can interface neurons and synapses inaccessible through genetic strategies.

In addition to synaptic junctions, neurons form intercellular junctions with multiple glial types (**Fig. 7.5a**), including astrocytes, oligodendrocytes in the central nervous system (CNS), and Schwann cells in the peripheral nervous system (PNS). Astrocytes form intimate associations with the synaptic structure (**Fig. 7.1e**) regulating neural activity through local ion buffering (Allen & Lyons, 2018) and neurotransmitter uptake (Deemyad et al., 2018). Therefore, by interfacing with astrocytic networks, nanoscale devices can potentially manipulate neural communication locally and over extended brain areas. On the other hand, myelin-forming glia — oligodendrocytes in the CNS and Schwann cells in the PNS — wrap around and insulate axons. These myelinated segments are interrupted by uninsulated hotspots highly concentrated in voltage-gated Na^+ channels called nodes of Ranvier (**Fig. 7.2a**), where action potentials are regenerated as they travel down the axon (Kandel et al., 2000). Myelination allows for faster conduction of electrical signals, minimizes energy consumption, and maintains the integrity and overall health of the axon (Nave, 2010). Understanding the precise mechanisms by which axons become myelinated is crucial to establishing strategies for promoting remyelination following injury, after onset of demyelinating diseases (such as multiple sclerosis), and for building new ‘myelinated’ bioelectronics. Earlier

work using electrospun nanofibre and micropillar arrays (**Fig. 7.5a**) demonstrated that axon diameter plays an important role in oligodendrocyte targeting and the initiation of myelin wrapping (Seonok Lee et al., 2012, 2013). Moreover, activity-dependent signalling between neurons and oligodendrocytes has been shown to contribute to the myelination process (Fields, 2015), opening the possibility for bioelectronic devices as therapeutic agents for remyelination.

7.4.6 Blood–brain barrier

A challenge in treating neurological disorders is the delivery of pharmaceutical drugs into the brain. Endothelial cells lining blood vessels passing through the brain, along with astrocytes and pericytes, form the blood–brain barrier (BBB), a collection of tight junctions that restrict the movement of large molecules from blood into neural tissue (**Fig. 7.5b**). Advanced drug delivery systems, such as polymer (Kreuter, 2014) and magnetic (Y. Chen & Liu, 2012) nanoparticles, can enhance transport across the BBB through receptor-mediated endocytosis. Exosomes, or secreted extracellular vesicles (Alvarez-Erviti et al., 2011; T. Yang et al., 2015), can also be prepared to carry therapeutic agents, and studies have shown that drug-loaded vesicles can cross the BBB through similar endocytic pathways. Other approaches have focused on strategies capable of reversibly permeabilizing the BBB without causing any permanent cell damage. For instance, local heat generation with magnetothermal nanoparticles (Y. Chen & Liu, 2012) and electroporation (Mohammad Bonakdar et al., 2016) can transiently increase BBB permeability and allow drugs to diffuse into the brain. Bioelectronic devices (**Fig. 7.5b**), such as mesh nanoelectronic scaffolds (J. Liu et al., 2015) and optoelectronic devices (Jiang et al., 2018), can be potentially used to deliver pulses of electrical current at the BBB interface for enhanced drug transport. Although animal studies are the ultimate goal when conducting tests on BBB permeability, *in vivo* experiments often

result in greater experimental complexity and species-specific effects. On the other hand, *in vitro* systems allow researchers to test the nano-enabled BBB permeabilization and neural control more rapidly, using, for example, organ-on-chip platforms (M. Bonakdar et al., 2017) (**Fig. 7.5b**). These configurations aim to create physiologically relevant microenvironments and eliminate species-specific variables. They also enable faster testing of drugs, drug delivery vehicles and devices capable of permeabilizing the BBB.

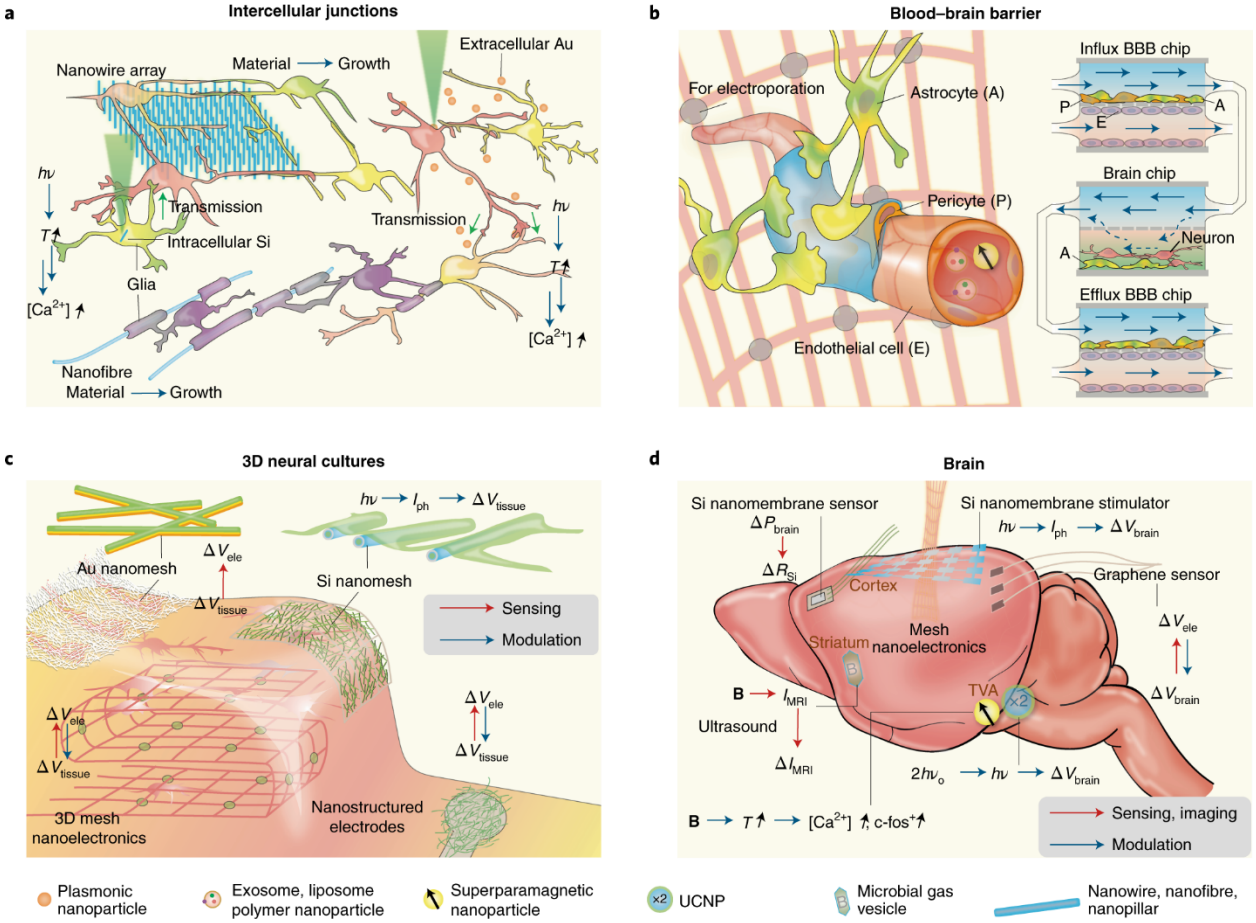

Figure 7.5: Nano-enabled cellular and tissue-scale neural interfaces. (A) Interfacing intercellular junctions. Nanowire arrays can guide neuronal processes and promote intercellular junctions and electrical synchronization. Intracellular Si or extracellular Au-based neural modulations may enable functional connection studies in neurons. Myelination of nano- and microfibres suggests future electrical or optoelectronic control of myelination through semiconductor or metallic nanowires. **(B)** Interfacing the blood–brain barrier. Exosomes, liposomes, polymer nanoparticles and magnetic nanoparticles have been suggested for enhanced delivery through BBB. Future opportunities include localized electroporation through mesh nanoelectronics, given in vitro electroporation studies for enhanced BBB passage. It is also promising to include nanomaterial or nanodevices with organ-on-a-chip model where the

Figure 7.5 (cont.) interactions among BBB, blood and neural systems can be evaluated together. **(C)** Interfacing 3D neural cultures. Macroporous nanoelectronics mesh can record from the inside of engineered tissues. Conducting nanofibre-coated recording electrodes have low impedance. Au nanomesh used for electrical recording of engineered cardiac tissues and Si nanomesh used for photoelectrochemical modulation of the heart could potentially be used for electrical interfaces with 3D neural cultures. V_{ele}, electrical potential recorded at the nanoelectronics surface; V_{tissue}, electrical potential from the tissue. **(D)** Interfacing the brain. Biodegradable Si nanomembrane can measure intracranial pressure (P_{brain}). Si photodiode nanomembranes produce photoelectrochemical modulation of the cortex and yield a field potential change (ΔV_{brain}). Semi-transparent graphene electrodes allow flexible electrical recording, and parallel imaging and optical stimulation. A microbial gas vesicle produces MRI signals (I_{MRI}) that can be modulated with ultrasound and allow multiplexed MRI imaging. Superparamagnetic nanoparticles and UCNPs yield deep-brain wireless neuromodulation, producing various effects such as the upregulation of *c-fos*, a proto-oncogene that is expressed within some neurons following depolarization.

7.4.7 3D neural cultures

The extracellular matrix (ECM) is composed of a wide variety of proteins and other bioactive molecules that regulate neuronal differentiation and growth. Recently, synthetic ECM or ECM-like devices (**Fig. 7.5c**) have been explored for regulating and interrogating 3D neuronal growth and function (Edelbrock et al., 2018; Mammadov et al., 2012). For example, peptide amphiphile nanofibres functionalized with bioactive components (Edelbrock et al., 2018; Mammadov et al., 2012), such as brain-derived neurotrophic factor, laminin and heparan sulfate epitopes, have been used to present growth factors to neurons. Interestingly, the effects of these factors on neuronal maturation and neurite growth were evident only when presented in peptide amphiphile nanofibre configurations (Edelbrock et al., 2018; Mammadov et al., 2012), suggesting that nanoscale architecture and topography work synergistically with the chemical nature of these molecules to initiate downstream signalling. For interrogating neural activity, folded macroporous nanoelectronic mesh devices (**Fig. 7.5c**) have generated interpenetrating recording networks with neurites, and have recorded the local field potentials and drug responses from engineered 3D neural cultures (Tian et al., 2012). Additionally, ECM-like nanoprobes (Sunghoon Lee et al., 2019;

Parameswaran et al., 2019) developed for engineered cardiac tissues (**Fig. 7.5c**) can be extended to neuronal preparations, since electrical properties across electrogenic cells follow similar fundamental principles. Recent examples include the ultra-light and movable nanogold–polyurethane mesh electronics (Sunghoon Lee et al., 2019; Miyamoto et al., 2017) used to monitor the electrical signals in cardiomyocytes (Sunghoon Lee et al., 2019), and the coaxial *p–i–n* Si nanowire network over the self-aligned SU-8 mesh for cardiac modulation (Parameswaran et al., 2019).

7.4.8 Neural systems and entire brain regions

As previously described, neurons exist within high-dimensional networks that extend over entire brain regions and perform specific tasks. Despite having individualized roles, neurons in specialized brain regions work in unity to generate, process and relay information. Therefore, the seamless interrogation of large ensembles of neurons is vital for understanding the information represented in neural systems, correlating signals to specific behaviours and monitoring how neural activity changes during disease progression. Additionally, the ability to modulate neural activity at the systems level can have multiple clinical implications, including terminating the spread of seizures, alleviating motor symptoms in Parkinson's disease patients and potentially slowing neurodegeneration in Alzheimer's disease. Advances in micro- and nanofabrication have led to the design and realization of new high-density transistor platforms for neural biointerfaces with the capability of resolving individual cells. For example, mesh nanoelectronics (Tian et al., 2012) (**Fig. 7.5d**) can be used for both modulation and recording of neural activity and their enhanced flexibility enables their packaging into small injection vehicles for subcortical brain delivery (J. Liu et al., 2015; Zhou et al., 2017). Following release, mesh nanoelectronics devices

can form intimate contacts with neuronal populations (J. Liu et al., 2015; X. Yang et al., 2019) and enable recordings in freely behaving animals (Hong et al., 2018; X. Yang et al., 2019) with single-cell resolution (**Fig. 7.1b**).

For certain applications, transient interfaces are favourable, as they eliminate the need for surgical removal when no longer needed. In particular, bioresorbable Si nanomembranes (**Fig. 7.5d**) have been designed as effective probes for temperature, pressure and electrical activity (Kang et al., 2016), enabling monitoring of post-surgery health and recovery. Other configurations include Au-decorated *p–i–n* Si nanomembranes (**Fig. 7.5d**) as *in vivo* optoelectronic devices for neural stimulation (Jiang et al., 2018). For use in combination with other optical methods, such as fluorescence imaging and optogenetics, graphene nanoelectronics (**Fig. 7.5d**) offer a transparent alternative to metals and semiconductors while maintaining suitable signal sensitivity (Choi et al., 2017; D. W. Park et al., 2014).

The 2D structure of Si nanomembranes and graphene microelectrodes limits their use to superficial cortical layers. However, deep brain interrogation can be achieved with superparamagnetic nanoparticles and UCNPs (**Fig. 7.5d**), because these can be wirelessly activated and can be delivered through injectable methods or potentially through the blood by transiently permeabilizing the BBB. Magnetic fields have excellent penetration through the skull and soft tissue, making magnetic nanoparticles extremely useful for deep brain magnetothermal stimulation (R. Chen et al., 2015; Munshi et al., 2017). Additionally, UCNPs can respond to NIR lasers, which also exhibit good tissue penetration. Upon NIR laser stimulation, UCNPs become excited and emit light in the visible range, which can modulate light-gated opsins (S. Chen et al., 2018) and

potentially other optoelectronic nanomaterials for deep brain stimulation. Lastly, acoustically modulated gas-filled protein vesicles have been used as high-contrast agents for deep-brain MRI (Lu et al., 2018; Shapiro et al., 2014), and rectennas (rectifying antennas) capable of harvesting high-frequency electromagnetic radiation can offer wireless control of implanted nanoprobes using Wi-Fi signals (X. Zhang et al., 2019).

7.5 Outlook

As illustrated throughout this chapter, advances in nanotechnology offer the capability of interfacing the brain with unprecedented resolution. The seamless integration of next-generation probes with the nervous system will shed light on many unanswered questions in neuroscience, re-evaluate some principles believed to be understood, and aid in therapeutics aiming to restore proper brain function. On the other hand, future rational design and implementation of nanoscale neural devices should be guided by the physical properties of neural components and their networks (Table 1). For example, to achieve 'myelinated' mesh nanoelectronic devices for modulating oligodendrocyte behaviour, the diameter/width of the mesh filament should not be less than 0.4 μm (Seonok Lee et al., 2012). Efforts in optimizing these devices are still ongoing, but successes in wireless interfacing (Parameswaran et al., 2018; Seo et al., 2016) and restoring or enhancing perceptual sensation (Ma et al., 2019; Tang et al., 2018) show that we are already at the initial stages of the nano-revolution in neuroscience.

The materials and devices described here minimize the mechanical and feature-size mismatch between probes and biological tissue. However, challenges remain for delivery and targeting, especially when precision electronic medicine (Tian & Lieber, 2019) is envisaged. In particular,

the skull represents a major obstacle for device implantation, often requiring invasive drilling or surgery. Interestingly, the presence of transcortical vessels that penetrate through the skull, connecting the bone marrow to the surface of the brain, has been recently reported (Herisson et al., 2018). These vessels could be exploited as avenues to enable deep brain interfaces for recording and modulation, although new engineering strategies will be necessary to target the desired brain regions with minimal harm. Furthermore, neural devices will require surface functionalization with cell- or subcellular-specific molecules that can enable tight junctions with molecularly defined populations. This will require close collaboration with molecular biologists researching transcriptomic and proteomic neural libraries and cell-type specific markers.

Nanoscale building blocks continue to be scaled down towards the order of organelles and protein complexes, blurring the distinction between neural interfaces and synthetic biology. At subcellular and molecular scales, bioelectronics could potentially enable real-time control of biological circuits involved in gene expression, regulatory networks and metabolism, among others (Selberg et al., 2018). Such biohybrid systems can be designed and engineered so that biological systems develop a symbiotic relationship with materials or implants, allowing them both to act as integral device components. This concept can be extended to neural systems for harnessing bio-energy and sustaining active neural interfaces. We envisage platforms in which the glial cells function together with the implanted materials as one hybrid system. In particular, gap-junction coupled astrocytes form networks that span large areas of the brain (Allen & Lyons, 2018; Deemyad et al., 2018) and are known to regulate synaptic transmission locally. Therefore, modulation of the astrocytic network through nanoscale tools would allow the simultaneous modulation of local circuits and large brain areas with minimal abiological components. Furthermore, such electrode–glia systems

could transform the generic excitatory stimulus coming from the inorganic electrode into a specific signal that recruits an intrinsic neuronal pathway.

Chapter 8

Texturing silicon nanowires for highly localized optical modulation of cellular dynamics

This chapter is a full reprint of Fang et al., *Nano Letters* (2018), in which I was a primary author. This work is included with permission from all authors.

Relevant Publication:
Fang, Y.*, Jiang, Y.*, Acaron Ledesma, H.*, Yi, J., Gao, X., Weiss, D. E., & Tian, B. (2018). Texturing silicon nanowires for highly localized optical modulation of cellular dynamics. *Nano letters*, 18(7), 4487-4492.

8.1 Abstract

Engineered silicon-based materials can display photoelectric and photo- thermal responses under light illumination, which may lead to further innovations at the silicon−biology interfaces. Silicon nanowires have small radial dimensions, promising as highly localized cellular modulators, however the single crystalline form typically has limited photothermal efficacy due to the poor light absorption and fast heat dissipation. In this work, we report strategies to improve the photothermal response from silicon nanowires by introducing nanoscale textures on the surface and in the bulk. We next demonstrate high- resolution extracellular modulation of calcium dynamics in a number of mammalian cells including glial cells, neurons, and cancer cells. The new materials may be broadly used in probing and modulating electrical and chemical signals at the

subcellular length scale, which is currently a challenge in the field of electrophysiology or cellular engineering.

8.2 Introduction

Modulating cellular dynamics can yield either direct or indirect outcome. For example, recent studies suggest the opportunity of using the control of nervous system as a way to enhance the body's natural defenses against infection and disease (Famm et al., 2013). In the past, researchers have interrogated the CNS using bulky electrodes (Hamill et al., 1981; Vetter et al., 2004), which have low spatial resolution and are not suitable for long-term probing due to their large-scale dimensions and mechanical mismatches with the targeted tissues (Biran et al., 2005). More recently, genetically encoded molecular actuators, such as channelrhodopsin (Boyden et al., 2005) and halorhodopsin (Gradinaru et al., 2010), have been used for light-gated modulation of neural activity; but their use in vivo is limited because genetic manipulation is required to express these opsins. On the other hand, silicon nanomaterials have emerged as promising materials for the development of next generation biomedical devices because of their unique mechanical (Zhu et al., 2009) and electronic (Cui et al., 2000) properties and are biocompatible (He et al., 2010). In particular, silicon nanowires (SiNWs) and silicon nanomembranes have been designed as field-effect transistors (Tian et al., 2010, 2012) and photoelectrochemical (Parameswaran et al., 2018) devices for the monitoring and modulation of neural activities and they can be configured into high density arrays (H. Fang et al., 2017; Viventi et al., 2011) or function as free- standing devices (Parameswaran et al., 2018; Zimmerman et al., 2015).

The composition (Gudiksen et al., 2002; Lauhon et al., 2002) and morphology (Tian et al., 2010; Y. Zhao et al., 2016; Zimmerman et al., 2015) of SiNWs synthesized through gold (Au) nanocluster-catalyzed vapor-liquid−solid (VLS) growth can be precisely controlled through doping (Cui et al., 2000) and modulation of other synthesis conditions, such as temperature (Ross et al., 2005) and pressure (Luo et al., 2015). Given the important role that surface topography plays in dictating the biointerfaces, rational design of new meso- and nanoscale features over SiNWs could significantly expand the current toolbox of Si-based bio- materials (Acaron Ledesma & Tian, 2017).

Here, we explore textured porous SiNWs for highly localized photothermal modulation of cellular activities. SiNWs have small radial dimensions, which is promising for highly localized cellular control. However, the single crystalline form typically has limited photothermal efficacy due to the poor light absorption and fast heat dissipation. Recently, through spontaneous instability at the Au−Si interface (Y. Fang et al., 2017) and pressure-dependent Au deposition and diffusion (Luo et al., 2015) on the Si surface, SiNWs with defined sidewall patterns have been prepared. Although SiNWs with increased surface area and roughness may experience enhanced interactions with cellular components (Jiang et al., 2016; Zimmerman et al., 2015, 2016), these structural features alone cannot modulate cell activities on demand. One potential strategy to achieve optical control of cellular dynamics with SiNWs is to further enhance the porosity or roughness throughout SiNW structures (i.e., not just at the sidewalls). Indeed, recent studies showed that mesoporous silicon particles (lateral dimension ∼2−5 μm) exhibit a strong photothermal property, which can be leveraged to elicit action potentials and other emergent output patterns in neurons (Jiang et al., 2016). In this current work, we present a new strategy to improve the photothermal effect in SiNWs

by texturing them with inclined channels from periodic Au deposits and demonstrate that this new material is effective in remotely modulating calcium dynamics in a number of mammalian cells (**Figure 8.1a**).

8.3 Results

To synthesize the textured SiNWs, we first used periodic pressure perturbations during the Au-catalyzed intrinsic SiNW (i-SiNW) growth to induce the Au deposition and diffusion at defined locations (Luo et al., 2015), followed by the metal-assisted chemical etching (MACE) (W. Chen et al., 2014; Den Hertog et al., 2008; Y. Fang et al., 2017; Gradinaru et al., 2010; Kim et al., 2017; Luo et al., 2015). In a typical synthesis, i-SiNWs were first grown at 470 °C under a constant pressure of 40 Torr for 1 min by setting the flow rates of SiH_4 and H_2 as 2 and 60 standard cubic centimeters per minute (sccm), respectively. After forming the base segment, periodic switches between 5 s of evacuation and 25 s of pressure ramping were performed to modulate the growth chamber pressure during the subsequent nanowire growth. Upon chamber evacuation, isolated Au nanoparticles are precipitated from the alloy droplet (Luo et al., 2015) and get deposited on the Si surfaces. Later on, Au species can diffuse on Si sidewalls to form patchy domains on the i-SiNW sidewalls (Luo et al., 2015) (**Figure 8.1b**). Once the pressure ramps up, the Au diffusion ceases and the SiNW resumes its elongation. The pressure switching cycles were iterated for 10 min after the base segment growth to yield the pressure modulated i-SiNWs with periodical Au bands on the surfaces. In the subsequent MACE experiment, the as-grown i-SiNWs on the growth substrates were dipped into a hydrogen peroxide (H_2O_2) and hydrofluoric acid (HF) aqueous mixture solution to etch Si.

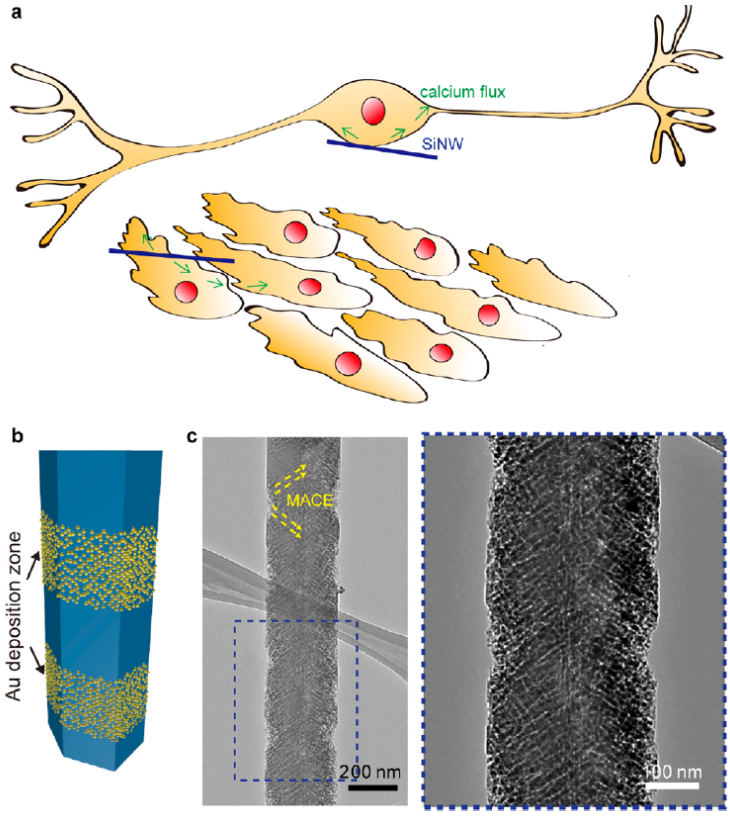

Figure 8.1: Textured Si nanowires by Au-catalyzed chemical etching allows highly localized optical modulation of cellular dynamics. (A) Photostimulation of extracellular junctions between textured SiNWs and various types of cells can elicit local calcium dynamics and subsequent intracellular and intercellular propagations. (B) A structural model illustrating Au bands on the i-SiNW surface after iterated pressure modulations during the nanowire growth. (C) TEM images highlighting the open networks of porous channels after the Au-catalyzed etching of i-SiNW. The dashed blue box on the left represents the region for a zoom-in view on the right.

After MACE, inclined open porous channels were formed that extended from the original surface locations of Au nanoparticles, yielding SiNWs with three-dimensional porous interior (**Figure 8.1c**, etched for 30 s). Despite the Si removal, TEM images and selected area electron diffraction (SAED) patterns show that the nanowires are still highly crystalline with the majority of SiNWs' growth direction following the ⟨112⟩ orientation (**Figure 8.2**). The depth of the textures and the corresponding SiNW porosity can be controlled by adjusting the etching duration (**Figure 8.3**). One unique aspect of this synthetic approach is that the locations of Au particles along SiNWs for MACE can be precisely programmed by the pressure modulation protocol.

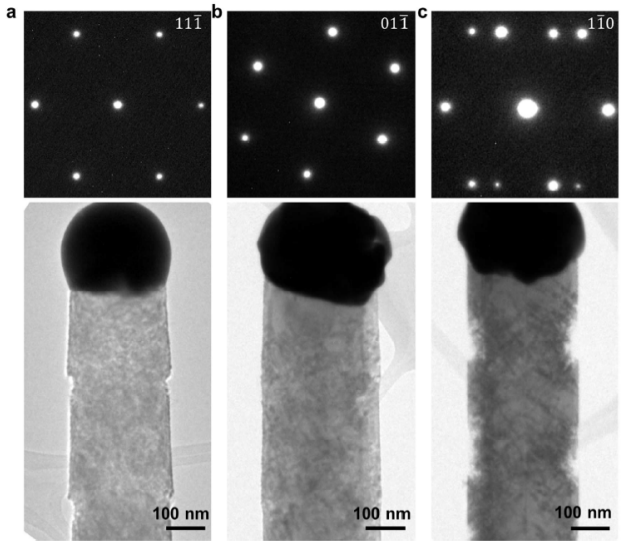

Figure 8.2: TEM images and corresponding SAED patterns of the textured i-SiNWs. Zone axes are labeled in individual panels as a) $11\bar{1}$, b) $01\bar{1}$, and c) $1\bar{1}0$.

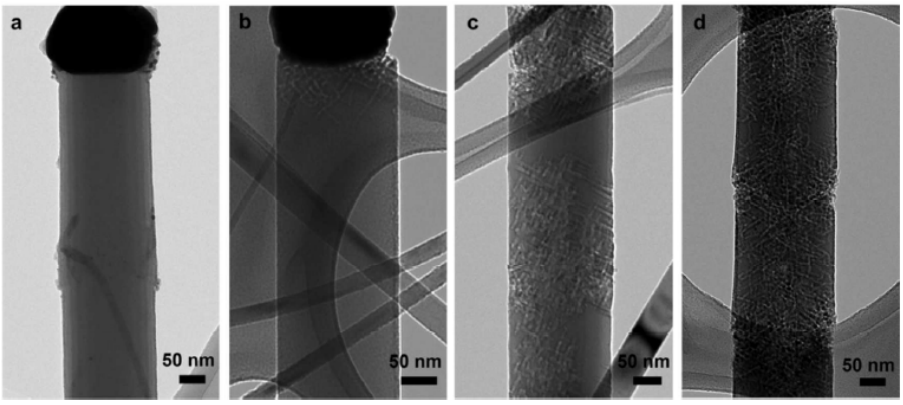

Figure 8.3: Comparison of TEM images of etched and unetched i-SiNWs (a) A TEM image of an unetched pressure modulated i-SiNW. (b-d) TEM images of textured i-SiNWs after etching in H_2O_2/HF solutions for different durations (b, 3 s; c, 10 s; d, 20 s).

To confirm the potential use of textured i-SiNWs for freestanding cellular modulation, we first assessed the physicochemical responses of these SiNWs to laser illumination in saline. We relieved SiNWs from the growth substrate through gentle sonication and drop-cast them in a phosphate buffered saline (PBS) solution. Using the patch-clamp system, we then positioned a micropipette electrode (~1 MΩ) within a ~ 2 μm proximity of a single SiNW. While in voltage-clamp mode, we monitored the current flowing through the pipet tip before, during, and after delivering short

pulses (1 ms duration) of a 532 nm focused laser (~47.1 mW) (Figure 8.4a). On one hand, SiNWs could display photoelectric effect upon light illumination, where light-generated carriers accumulate at the Si interface and attract counterions in the solution to compensate the charge imbalance at the interface. The photoelectrically induced current is only a function of carrier dynamics at the Si surface so the amplitude of the current is independent of the pipet holding level. On the other hand, SiNWs could yield photothermal effect which elevates the local temperature of the electrolyte and increases the ion mobilities, yielding a reduced pipet resistance. In this photothermal scenario, even under the same holding potential, the amplitude of ionic current through the pipet tip will increase during the light illumination period, as governed by Ohm's law. Given the different dependence on the holding level of photoelectrically and photothermally induced currents, multiple recordings performed at different pipet holding levels can be used to decouple the light-induced thermal and electrical effects of SiNWs. At a given time point t during the light illumination period, the recorded current, $I_0 + \Delta I_{light}(t)$, excluding the photoelectrically induced current part $\Delta I_{electric}(t)$, and the pipet tip resistance $R(t)$ should follow the Ohm's law as long as the holding potential V_p is fixed, $V_p = I_0 \times R_0 = (I_0 + \Delta I_{light}(t) - \Delta I_{electric}(t)) \times R(t)$, where I_0 and R_0 are the holding current and pipet resistance in dark, respectively. Rearranging the equation gives the relationship between the light-induced current $\Delta I_{light}(t)$ and the holding current I_0 that $\Delta I_{light}(t) = \left(\frac{R_0}{R(t)} - 1\right) \times I_0 + \Delta I_{electric}(t)$. From this equation, the photoelectric effect is explicitly manifested as the intercept of the $\Delta I_{light}(t) - I_0$ curve while the photothermal effect is implicitly embedded in the fitted slope as the pipet resistance is a function of temperature (Jiang et al., 2018). Individual photo responses can then be extrapolated from all the measurements and compared between textured and smooth nanowires; the smooth SiNWs were

synthesized under a similar condition as that of the textured ones except that neither pressure modulation nor etching were used (**Figure 8.4b,c**).

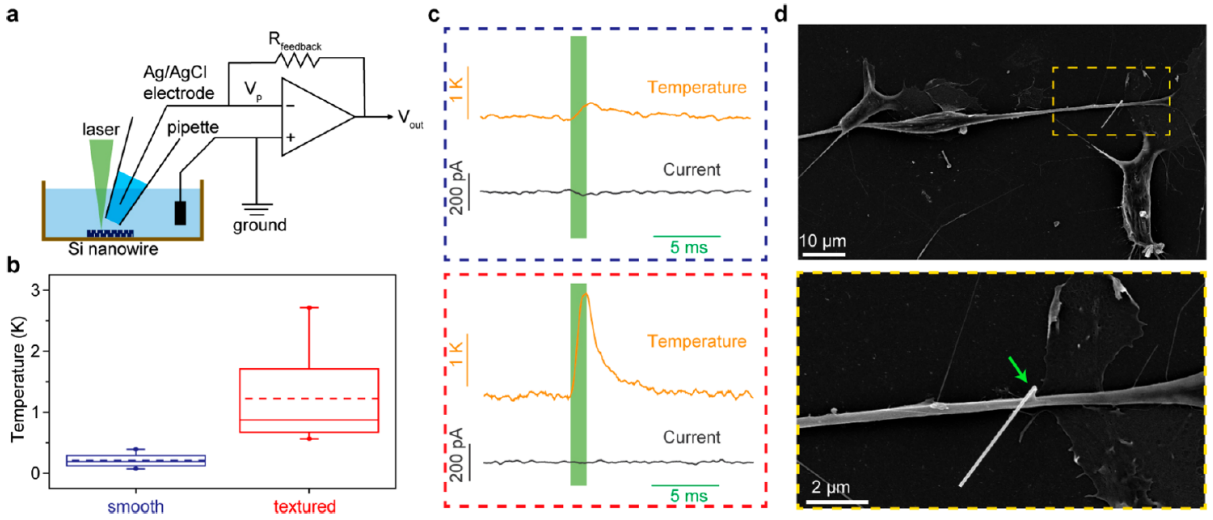

Figure 8.4: Textured nanowires show a strong photothermal response to light and can interface with cell membranes. (a) A schematic diagram of the experimental setup for the photoresponse measurement of Si nanowires. 532 nm laser pulses are delivered onto the Si nanowires immersed in a PBS solution. (b) Textured Si nanowires (red) show significantly larger photothermal effects compared to smooth nanowires (blue) under illumination with 532 nm laser for 1 ms (n = 8). (c) Representative traces of local temperature dynamics (yellow) and photocurrents (gray) after laser illumination (532 nm, 47.1 mW for 1 ms) of smooth (blue dashed box) and textured (red dashed box) Si nanowires. (d) SEM images of a typical glial cell/textured nanowire interface showing a strong interaction between Si and the cell membrane (marked by the green arrow). The yellow dashed box in upper panel marks the region for a zoom-in view in the lower panel.

From the recorded ionic current dynamics from both textured and smooth SiNWs, the fitted intercept values of the $\Delta I_{light}(t) - I_0$ curves stay nearly zero throughout the entire illumination period, indicating minimal contributions from the photoelectric effect of i-SiNWs (**Figure 8.4c**, orange traces). Nevertheless, both SiNWs induce local temperature elevations upon laser illumination as derived from the fitted slope values of the $\Delta I_{light}(t) - I_0$ curves in conjunction with the temperature-resistance calibration (**Figure 8.4c**, black traces). On average, the textured i-SiNWs demonstrate larger photo- thermal responses (~2 °C) than the smooth i-SiNWs (~0.2°C) over the 1 ms illumination (**Figure 8.4b**). Consistent with the prior work of mesoporous Si

particles, the porosity in the textured SiNWs likely contributes to the enhanced thermal output due to reduced thermal conductivity, heat capacity, and enhanced light absorption (Jiang et al., 2016). Nevertheless, it should be noted that the laser power density used in the present study is still ~1 order of magnitude higher than that applied for the mesoporous Si particles in order to yield similar thermal response, because the size of a single textured SiNW (one- dimensional wire with ~200 nm in diameter) is significantly smaller than that of a mesoporous Si particle (three-dimensional quasi-spherical object with ~2−5 μm in diameter).

One important feature offered by SiNWs is that they can be readily dispersible in aqueous solution and can be administered to biological systems in a drug-like fashion. Additionally, the rough surfaces of the textured i-SiNWs may promote robust biointerfaces versus the smooth counterparts (Jiang et al., 2016; Luo et al., 2015). Indeed, high-yield extracellular junctions can be observed between textured i-SiNWs and the filamentous membrane protrusions of satellite glia from a rat dorsal root ganglia (DRG) culture after a short coculture (**Figs. 8.4d and 8.5**), frequently forming cross-bars. The ease of highly localized extracellular junction formation, along with the enhanced photothermal effect described above, suggest that textured i-SiNWs can be used for freestanding photothermal modulation of cellular dynamics through the artificial synapse-like interfaces.

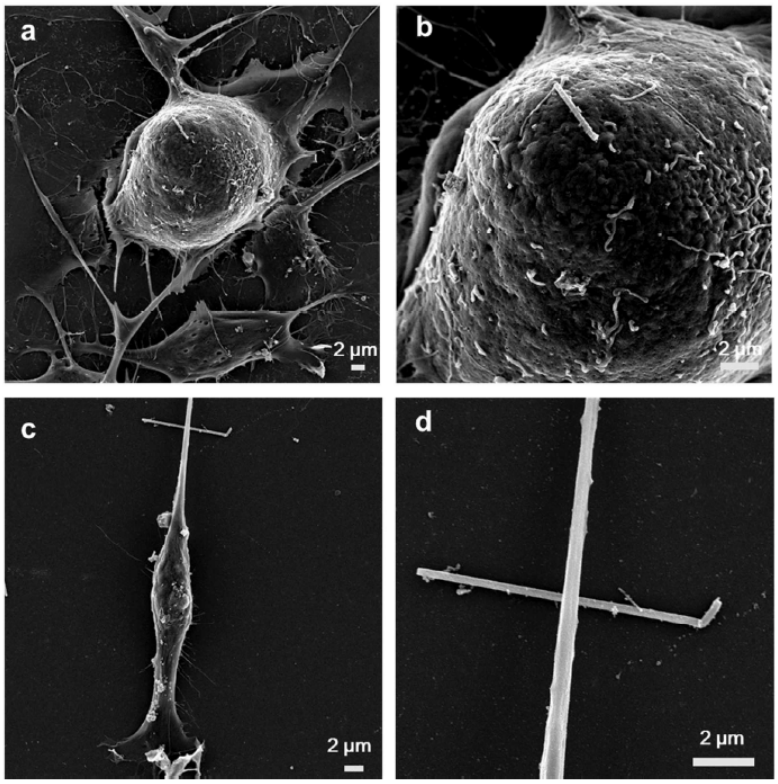

Figure 8.5: Cellular interfaces with textured SiNWs. (a-b) SEM images of a neuron/textured SiNW interface at the soma. (c-d) SEM images of a glia/textured SiNW interface at the protrusion forming a crossbar junction.

Laser illumination of a textured i-SiNW in close contact with a glial cell protrusion elicits rapid calcium surges initiated right at the stimulation site, likely related to a series of coupled biophysical processes (**Figs. 8.6a and 8.7**). Briefly, the strong photothermal effect of the nanowire with porous channels upon illumination can rapidly elevate the local temperature and subsequently increase the capacitance of the interfacing cell membrane, which depolarizes of the membrane (Jiang et al., 2016). Calcium dynamics can then be triggered due to the existence of voltage-gated calcium channels on glial cell membranes (Sontheimer, 1994). Additionally, shock waves can also be initiated by the photothermal−acoustic effect that can activate mechano-sensitive ion channels of the cell (M. Shi et al., 2013). The locally generated calcium concentration gradient can drive the propagation of the signal inside the cell by going through the cell body and then to other branches

of protrusions (**Figure 8.6a,b**). Besides glial cells, SiNWs can also interface with DRG neurons for direct neuromodulations. Upon laser illumination of the Si/neuron junction, calcium dynamics can be evoked in a similar manner through either voltage (Simms & Zamponi, 2014) or mechano-sensitive (Ranade et al., 2015) calcium channels expressed on the neuron membrane (**Fig. 8.6c,d**).

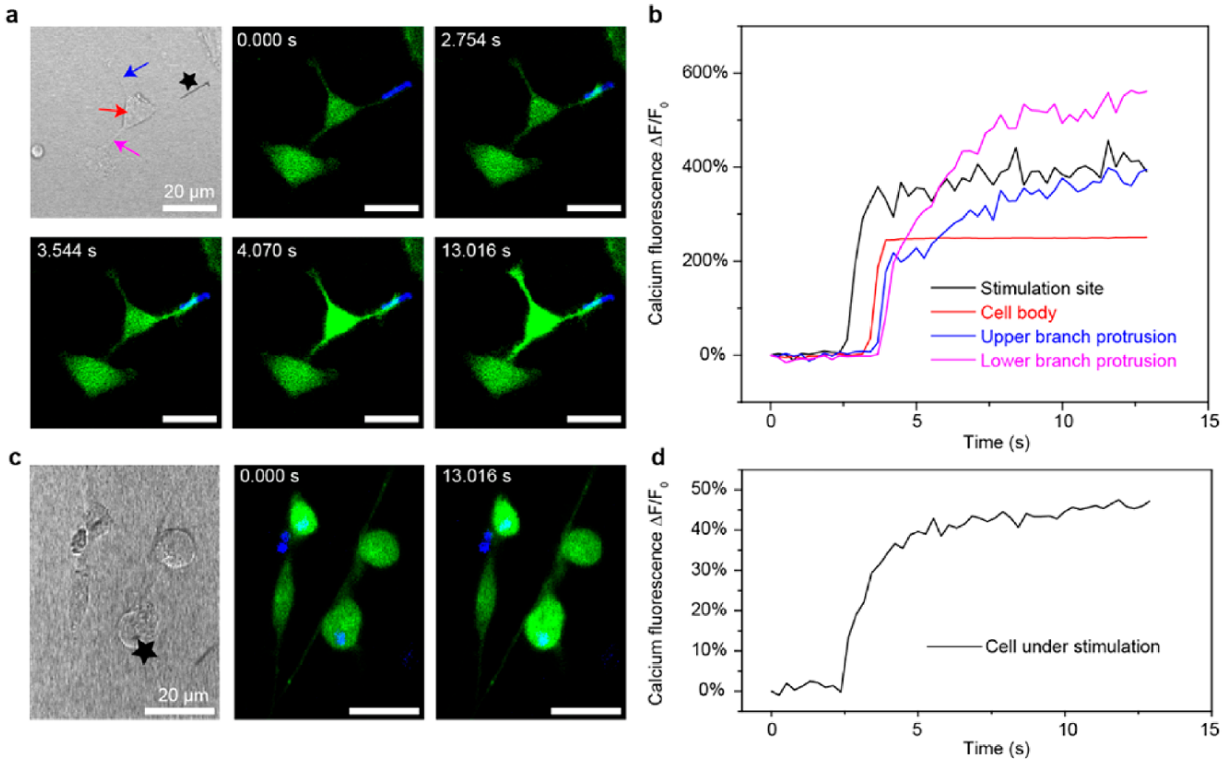

Figure 8.6: Calcium dynamics can be elicited in DRG cultures with textured Si nanowires. (a) Confocal microscope time series images (green, calcium; blue, Si nanowires) showing an intracellular calcium wave propagation. The glial cell calcium was locally elevated right after the illumination of a textured Si nanowire. The black star marks the illumination site. A 1 ms laser pulse (592 nm, ~22.3 mW) was delivered right before the 2.754 s time point. (b) Quantitative analysis of calcium fluorescence intensities over time from four regions of interest show calcium dynamics at different locations marked in (a) black, the stimulation site; red, glial cell body; blue, upper branch protrusion; pink, lower branch protrusion. (c) Confocal microscope time series images of a neuron interfacing with a textured nanowire and (d) the corresponding quantitative analysis of the calcium fluorescence intensity over time showing the stimulation effect of the neuron. A 1 ms laser pulse (592 nm, ~22.3 mW) was delivered right before the 2.754 s time point.

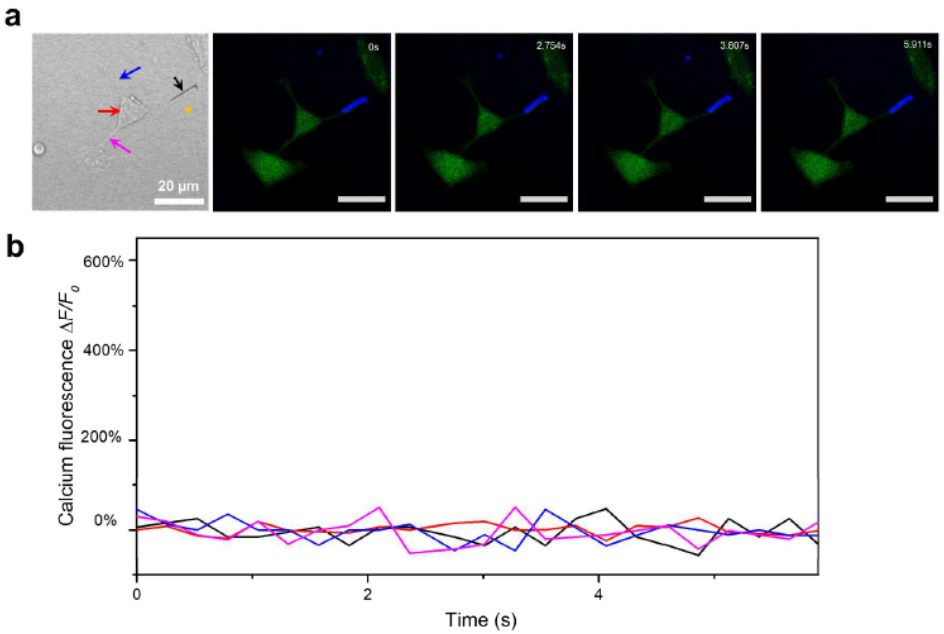

Figure 8.7: Control experiment with an off-target illumination does not yield significant calcium dynamics. (A) Confocal microscope time series images and (B) quantitative analysis of the fluorescence intensities from the same cell in Figure 8.3A show no obvious calcium wave propagations. The glial cell can only be photostimulated when the laser is hitting right at the Si/cell interface. The orange star marks the laser spot location.

Moving forward, highly localized modulations of both neuron and glial cell activities at subcellular resolution with programmed temporal patterns allow precise probing of natural neural-glial interactions as well as reinforcing intra- cellular and intercellular signaling networks for cellular engineering applications. In our work, the spatial resolution of extracellular modulation depends on the exact configuration of the junction. Indeed, the overlapped area between the nanowire, the cell, and the laser spot will determine the final resolution. If the nanowire is aligned with the cell protrusion or lies on top of the cell body, the resolution would be the projected area of the nanowire under the laser spot, which is the nanowire diameter (~200 nm) times either the nanowire length (if the nanowire length is smaller than the laser spot size) or the laser spot size (if the nanowire length is larger than the laser spot size). On the other hand, when the nanowire and the cell protrusion form a cross-bar junction (**Figure 8.4d, Figure 8.6**), the resolution is the nanowire

diameter (~200 nm) times the protrusion width (down to submicron scales). With a finely focused laser spot (down to the diffraction limit), one can generate highly localized heating of the nanowire right at the illumination spot. Therefore, even if the nanowire has a couple of microns in its length, the ultimate resolution will be determined by the laser spot size and the nanowire diameter. Furthermore, the photostimulation protocol adopted in this work is minimally invasive to cells. For example, the same cell can be stimulated repetitively to induce calcium elevations following each stimulus, suggesting that cellular functions are preserved after the calcium cycles (**Figure 8.8**). LIVE/DEAD assays (**Figure 8.9**) indicate that the cell cannot be killed unless a laser pulse of ~2.5-fold of the threshold value for eliciting calcium dynamics was delivered, allowing a large dynamic range to manipulate cellular activities. At higher laser intensity, only the cell under stimulation instead of a large population of cells was killed, suggesting that the cell death was likely mediated through the apoptosis pathway (Elmore, 2007).

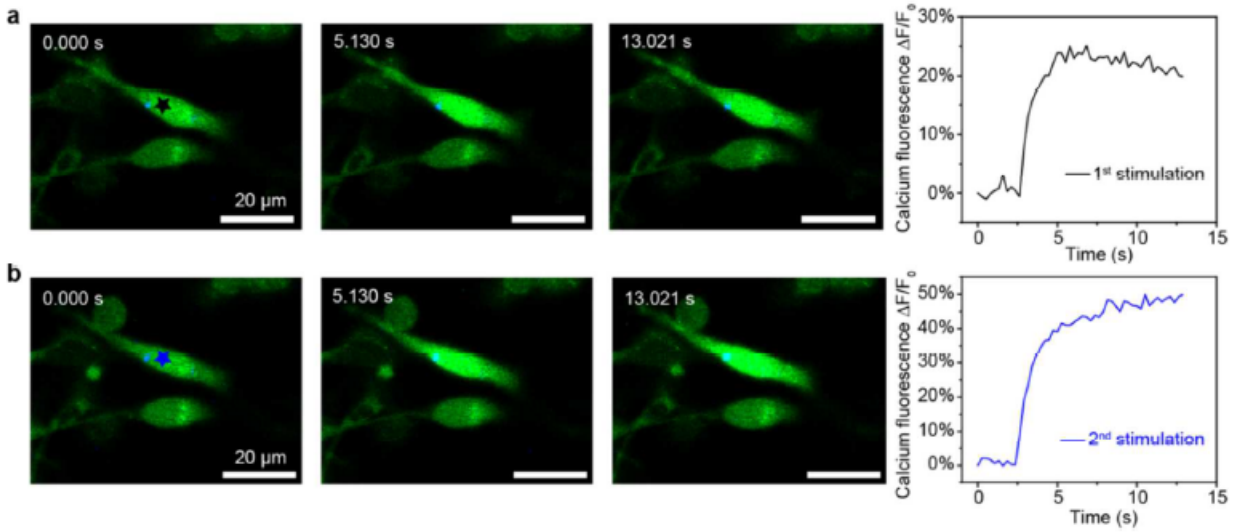

Figure 8.8: Extracellular photostimulation of same glial cell by a textured SiNW can be performed for multiple times. (a) and (b), The same glial cell was stimulated repetitively without being killed. 1-ms laser pulses (592 nm, ~ 22.3 mW) were delivered right before the 2.754 s time points in both trials. Black and blue stars mark the stimulation sites.

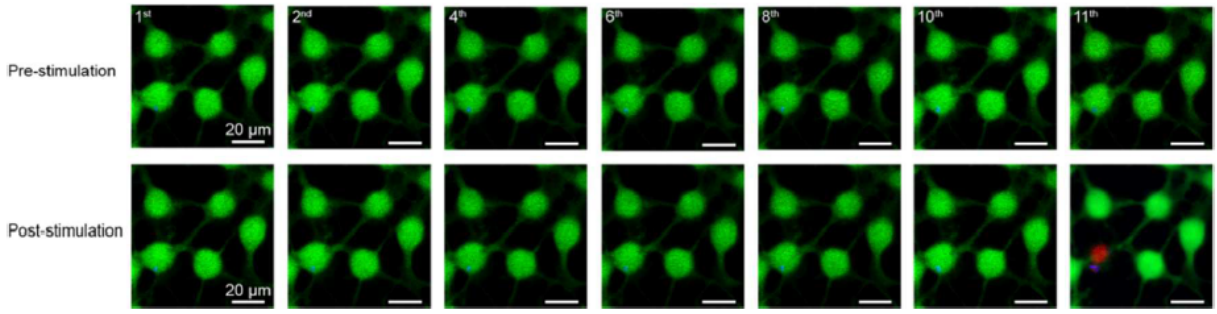

Figure 8.9: LIVE/DEAD assay shows that the nanowire-enabled extracellular photostimulation is minimally invasive. The same cell (green, calcein AM; blue, SiNWs) was stimulated extracellularly for ten consecutive times without being killed (592 nm, 32.2 mW for 1 ms). The cell can be killed (red, ethidium homodimer-1; blue, SiNWs) with a 1-ms pulse of laser with ~ 54.1 mW power. White arrows denote the stimulation sites.

Finally, we showed that textured nanowire-enabled and optically controlled cellular modulation can be extended to cell types directly involved in disease, such as cancer cells. We focused on U2OS, a human bone osteosarcoma epithelial cell line, and added a textured SiNW suspension to the cell culture in a druglike fashion. Focused laser pulses were delivered as described above onto individual nanowires interfacing with U2OS cell membranes. Our calcium imaging data shows that calcium dynamics can be elicited from the stimulation site immediately following the light illumination likely involving the contributions of voltage-sensitive (Jacquemet et al., 2016) and/or mechanosensitive (Y. W. Huang et al., 2015) calcium channels (**Figures 8.10a and 8.11**). Rapid intracellular calcium wave propagation was then observed inside the cell under stimulation with a speed of ∼15 μm/s driven by the large calcium concentration gradient established through the local influx of extracellular calcium ions (**Figure 8.10b**). For nonexcitable cells, such as U2OS, action potentials cannot be fired and the cell membrane would just be depolarized more with a higher light intensity within a dynamic range. The cell membrane depolarization would lead to an elevated level of inositol 1,4,5-trisphosphate (IP3, lipid signaling molecule) in the cell under stimulation, which induces a calcium signal. Besides intracellular waves, calcium signals can also propagate to

neighbor cells, likely due to the diffusion of IP3 through gap junctions to adjacent cells, which has been reported in certain cancer cell lines (Leybaert & Sanderson, 2012). Therefore, although the optical modulation method itself only input highly localized stimulus, this platform may still be adapted for large scale manipulation of cell populations or even small tissues. The fact that nonexcitable cancer cell cultures can be photostimulated demonstrates the broad applicability of the nanowire-enabled optical modulation to a variety of biological targets and suggests potential new areas for future bioelectric studies.

In this work, we found that textured i-SiNWs show enhanced photothermal response to laser illumination compared to smooth nanowires. These textured nanostructures can establish synapse-like interfaces with cell membranes and can be used to elicit calcium wave propagations both intracellularly and intercellularly. The modulation mechanism mediated by this device platform relies on photothermally (Sytnyk et al., 2017) induced membrane capacitance change, a biophysical mecha- nism that can be generally applied to a variety of cell types including nonexcitable cells. Additionally, with the high spatial resolution of the wireless cellular modulation textured SiNWs provide a means for further exploration of biophysical processes across multiple spatiotemporal scales, such as intercellular communications, cell motility, intracellular trans- port, and disease progression. Moreover, Si-based materials have a bandgap (∼1.1 eV) which allows light absorption over a brand range that includes one near-infrared (NIR) window. Therefore, instead of being limited by visible light stimulation, textured Si may be further adapted for NIR light-based in vivo stimulation. Overall, our results present textured SiNWs as a new platform for nongenetic optically controlled modulations of cellular signaling dynamics.

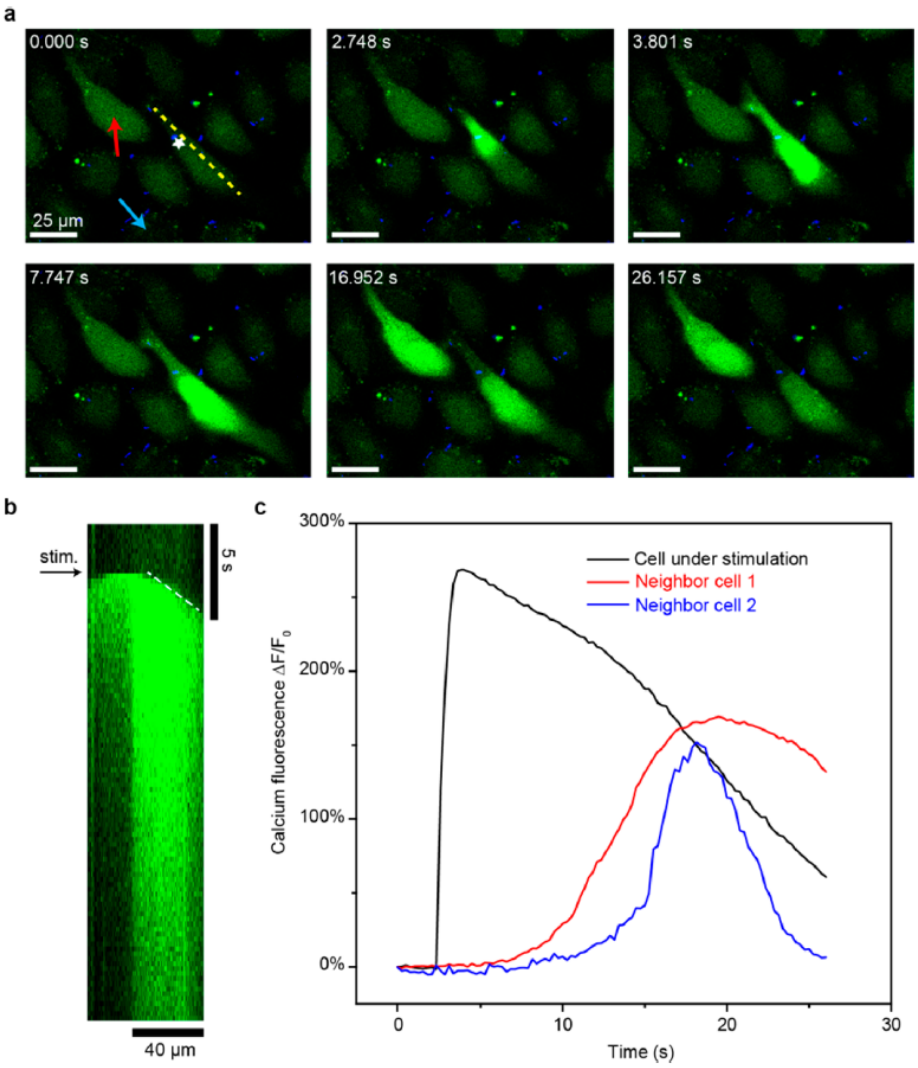

Figure 8.10: Extracellular stimulation of calcium dynamics can be extended to other cell lines. (a) Confocal microscope time series images of a U2OS cell culture being photostimulated by a textured Si nanowire (green, calcium; blue, Si nanowires). Intracellular calcium elevation was triggered at the stimulation site and caused subsequent intercellular calcium wave propagations to neighbor cells. A 1 ms laser pulse (592 nm, ~22.3 mW) was delivered right before the 2.748 s time point. The white star marks the illumination site. (b) A kymograph taken along the cell body shows the evolution of intracellular calcium gradient. (c) Quantitative analysis of the fluorescence intensities over time show the stimulation effect of the cell under stimulation and two neighboring cells: black, the cell under stimulation; red and blue, neighbor cells.

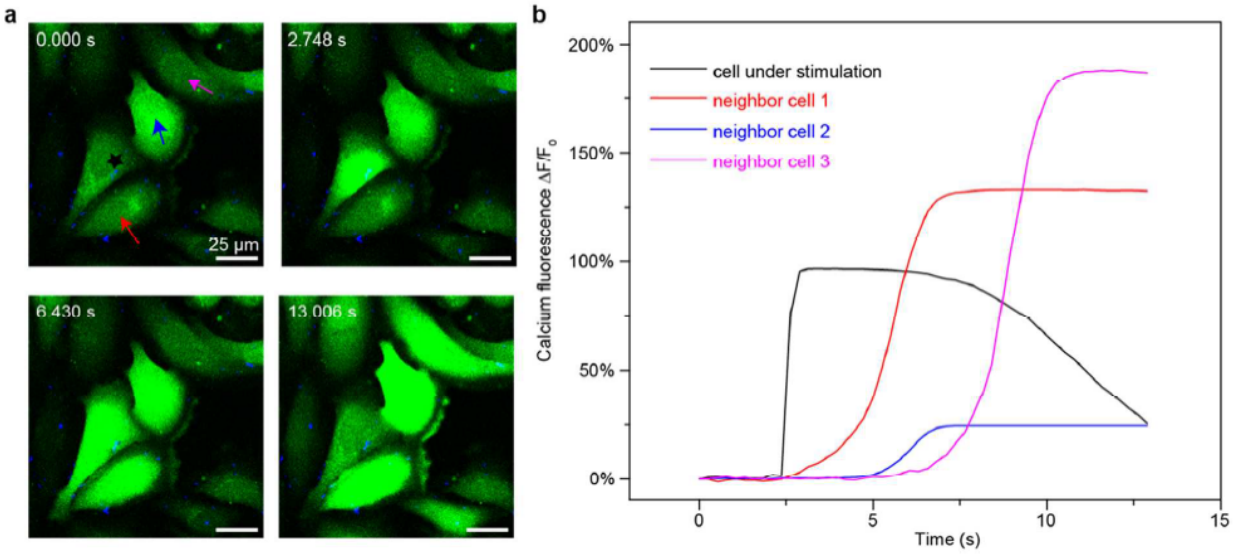

Figure 8.11: Photostimulation of U2OS cells. (a) Confocal microscope time series images of U2OS cells being photostimulated. Both intracellular calcium elevation and subsequent intercellular calcium wave propagations to neighbor cells can be extracellularly stimulated by a textured SiNW. A 1-ms laser pulse (592 nm, ~ 22.3 mW) was delivered right before the 2.748s time point. The black star marks the stimulation site. (b) Corresponding quantitative analysis of the fluorescence intensities over time (black, cell under stimulation; red, blue, and pink, neighbor cells).

8.3 Experimental Procedures

Synthesis of silicon nanowires (SiNWs)

SiNWs were synthesized using a gold (Au) nanoparticle-catalyzed chemical vapor deposition (CVD) method. The native oxide layers on the Si substrates were first removed with hydrofluoric acid (HF) (Sigma-Aldrich, USA) to yield hydrogen-terminated surfaces. The citrate-stabilized Au colloidal nanoparticles (Ted Pella, USA, 200 nm) were then deposited onto Si (100) substrates (Nova Electronic Materials, USA, n-type, 0.001~0.005 Ω cm) as catalysts. For a typical growth of pressure modulated SiNWs, intrinsic Si nanowires (i-SiNWs) were grown under 470 ^{o}C by setting the flow rates of silane (SiH_4) and hydrogen (H_2) as 2 and 60 standard cubic centimeters per minute (sccm), respectively. The first segment was grown under a constant pressure of 40 Torr for 1 min. Later on, periodic switches between 5 s of evacuation and 25 s of pressure ramping were performed

to modulate the growth chamber pressure during the SiNW growth. The pressure switching cycles were iterated for 10 min after the base segment growth to yield the pressure modulated SiNWs.

Metal assisted etching of SiNWs

An etching system consisting of HF and hydrogen peroxide (H_2O_2) was applied for the metal assisted etching of SiNWs. In a typical etching experiment, the as-grown pressure modulated i-SiNWs on Si wafers were dipped into a 10.85 wt% H_2O_2 (Fisher Scientific, USA) and 10.37 wt% HF aqueous mixture solution at 10 °C for 3~45 s. Then the etched samples were rinsed with deionized (DI) water for 5 times and blow dried by nitrogen (N_2).

Transmission electron microscopy

For electron microscopy of textured i-SiNWs after etching, they were gently sonicated in IPA and dispersed onto lacey carbon copper grids. A FEI transmission electron microscope (TEM) (Tecnai F30, FEI, USA) was used to characterize the morphology of the SiNWs. Crystallography of the SiNWs was studied by analyzing TEM images and corresponding selected area electron diffraction (SAED) patterns taken by a JEOL TEM operated at 300 keV (JEM-3010, JEOL, Japan).

Si photo-response measurements

For the photo-response measurements, a standard patchclamp setup was employed. In particular, an upright microscope (Olympus, Japan, BX61WI) with a 20×/0.5 NA water immersion objective was used to deliver light pulses from a laser source (Laserglow, Canada, 532 nm, diode-pumped solid-state laser, ~ 5 μm spot size). The light pulses were controlled by transistor-transistor logic (TTL) signals (1 ms) delivered from a digitizer (Molecular Devices, USA, Digidata 1550).

Voltage-clamp protocols were done by an Axopatch 200B amplifier (Molecular Devices, USA), controlled by pClamp software (Molecular Devices, USA). Glass pipettes were pulled in a flaming/brown type micropipette puller (Sutter Instrument, USA, P-97) for a final resistance of ~1 MΩ when filled with 1× phosphate buffered saline (PBS, Fisher Scientific, USA) solutions. In a typical measurement, a SiNW was immersed in the same PBS solution where the pipette tip was positioned in close proximity to the Si surface (~ 2 μm). Ionic currents across the pipette tip and the resistance of the pipette were recorded in the voltage-clamp mode. After the photo-response measurement, the same micropipette was placed into another dish of pre-heated PBS with an initial temperature of about 50 ^{o}C. A thermocouple was positioned close to the pipette tip during the temperature measurement. A calibration curve was created, based on the pipette resistance changes in the range between 50 ^{o}C and 20 ^{o}C, which was then used to estimate the local temperature increase.

Cell culture protocols.

(1) DRG were excised from P1–P3 neonatal rats into DMEM-F12 (Life Technologies, USA) on ice. They were then digested in 2.5 mg/ml trypsin (Worthington, USA) in EBSS (Life Technologies, USA) for 20 min in a 37 °C shaker. Following trypsinization, digested DRGs were resuspended into EBSS + 10% FBS (ATCC, USA) to inhibit further digestion by any remaining trypsin. Digested ganglia were then mechanically triturated via three glass pipettes decreasing in size. The resulting dispersed DRG cells were then resuspended into DMEM + 5% FBS + 100 U/mL penicillin (SigmaAldrich, USA) + 100 μg/mL streptomycin (Sigma-Aldrich, USA) and seeded onto glassbottom dishes previously treated with 0.01% poly-L-lysine.

(2) U2OS cells (ATCC, USA) were cultured on glass-bottomed Petri dishes and passaged following standard procedures from the vendor.

(3) Interfacing cells with textured SiNWs. SiNW suspensions in different cell culture media were prepared by extensively sonicating small pieces of the SiNW growth substrates (~ 2 mm × 2 mm) in culture media for 30 sec. The as-made nanowire suspensions were added to the cultures in a drug-like fashion (~ 10 μL of suspension per 1 mL of medium) and cocultured for ~ 2 hours before photostimulation experiments.

Calcium imaging

Cells were stained with 2 μM of Fluo-4 AM (Life Technologies, USA) for 30 min at 37 oC and gently washed with dye-free culture media before imaging. The asstained cells were imaged using a confocal laser scanning microscope (Leica, Germany, SP5 II STED-CW) with SiNWs being imaged simultaneously with the scattered light. In a typical experiment, a laser pulse (1 ms, 592 nm) was delivered to the SiNW of interest in the middle of a calcium imaging time series. The calcium fluorescence intensity over time was then analyzed offline using the ImageJ software (National Institutes of Health, USA).

Chapter 9

Micelle-enabled preparation of hierarchical micro-supercapacitor for bioelectric modulation

Manuscript under review
Yin Fang*, Menahem Y. Rotenberg*, Hector Acaron Ledesma*, Lingyuan Meng, Yingying Lv, Junyoung Jeong, Naomi Yamamoto, Yuanwen Jiang, Erik Schaumann, Benayahu Elbaz, Wei Wei, Bozhi Tian

9.1 Abstract

Real-world bioelectronics applications, including drug delivery systems, biosensing, and electrical modulation of tissues and organs, largely require biointerfaces at the macroscopic level. However, macroscale bioelectronics devices usually exhibit invasive and power-inefficient architectures, poor spatial resolution, and faradaic reactions at the biointerfaces. Here, we develop a micelle-enabled self-assembly fabrication method for a binder-free, carbon-based micro-supercapacitor device aimed at large-scale bioelectric modulation. Our device incorporates a multi-scale porous material architecture, interdigitated electrode layout, and a micro-supercapacitor working mechanism. In cell training processes, we use the device to modulate the contraction rate of primary cardiomyocytes to target frequency *in vitro*. We also achieve capacitive control of electrophysiology in isolated heart and retinal tissues *ex vivo*, and sciatic nerves *in vivo*. Our results support the exploration of device platforms already used in energy research to identify new opportunities in bioelectronics and biointerfaces.

9.2 Introduction

Modern bioelectronics with multi-scale structures are used extensively for drug delivery, biosensing, and biological modulation applications (Berggren & Richter-Dahlfors, 2007; G. Liu et al., 2016; Moon et al., 2018; A. Zhang & Lieber, 2016) . By allowing macro-scale modulation of biological activity, these bioelectronics have contributed to the transformative understanding of biological dynamics and function. Moreover, they hold great therapeutic potential for treating many biological disorders, such as Parkinson's disease, congenital heart defects, and paralysis (Someya et al., 2016) . However, macroscopic electronic devices generally require high charge injection to interact with biological systems, not only producing deep-penetrating electrical fields, which yield unintended side effects to other tissues and organs, but also displaying faradaic reactions at the biointerfaces, which generate toxic reactive species and cause corrosion of electrodes and permanent damage to adjacent tissues (Zhirnov & Cavin, 2011).

While reducing the size of electrodes for minimally invasive biointerfaces and spatially confined electric fields compromises the charge injection limit, functional coating layer with carbon materials, such as graphene and carbon nanotubes (CNTs), are widely used on traditional electrodes to reduce the electrode junction impedance and increase the charge transfer rate(N. Chen et al., 2017; Rastogi et al., 2018; W. Yang et al., 2007). However, the polymer binding process associated with the functional coating of graphene or CNTs can result in problematic ‘dead’ volumes or surfaces, increased device total thickness, and a reduced bendability at the bio-interfaces (Alkire et al., 2011). Moreover, the production of freestanding CNTs can potentially result in the formation of toxic isolated carbon nanostructures in vivo (Ema et al., 2016; Pietroiusti et al., 2011; Rittinghausen et al., 2014). Although conductive polymer-based hydrogel bioelectronics are widely used for biological modulation as well, they are not as electrochemically

stable as inorganic ones, especially in terms of degradation and swelling upon repetitive charge injections and long-term soaking in liquid solution (Lyu & Untereker, 2009; Ratner et al., 2004).

In this study, we demonstrate micelle-enabled self-assembly of a binder-free and carbon-based micro-supercapacitor device for large-scale bioelectric modulation. Micelle-enabled preparation of nanoporous monolithic carbon does not produce isolated CNTs, which eliminates the potential for in vivo toxicity associated with free carbon nanostructures. Using conventional lithography, we construct hierarchical porous carbon in the form of a micro-supercapacitor with interdigitated electrodes, thereby extending the utility of carbon from functional coating to complete electrode in bioelectronics devices. We demonstrate the electrochemical performance, including high spatial resolution and low power consumption, of the device under physiological conditions. Thereafter, we show its utility from cellular to organ levels, including in vitro cardiomyocytes (CMs), ex vivo isolated heart and retinal tissues, and in vivo sciatic nerves modulations. Overall, the micro-supercapacitor device is flexible, biocompatible, and capable of low current bioelectric modulation.

9.3 Results

9.3.1 Carbon membrane synthesis and characterization

We adopted a bottom-up approach for the direct preparation of monolithic (*i.e.*, binder-free) and hierarchical carbon membranes. Nanoscale micelles were prepared through biphasic interaction between triblock copolymer Pluronic F127 (template) and resin (precursor) in ethanol. Following solvent evaporation-induced self-assembly (**Fig. 9.1a, panel 1)**, the micelles were carbonized into mesoporous carbon membranes (**Fig. 9.S1**). This led to highly ordered mesostructures with a

uniform pore size of 7 nm, as shown in transmission electron microscopy (TEM) and scanning electron microscopy (SEM) (**Figs. 9.1b**, **S2)**. Addition of ~200 nm-sized silica (SiO_2) spheres into the Pluronic F127 and resin mixture during the membrane preparation introduced macroporous (*i.e.*, pore size of >50 nm) structures (**Fig. 9.1a**, **panels 2-3; Fig. 9.1c; Figs. 9.S3-S4**). The fabrication scheme permitted layer-by-layer assembly of mesoporous carbon by spin coating, where the thickness and porosity for individual layers could be controlled (**Fig. 9.1c**). While the mesoporous film had a Young's modulus and hardness of 25.30 GPa and 3.82 GPa, respectively, addition of ~700 nm of macroporous layer reduced these values to 4.20 GPa (modulus) and 0.69 GPa (hardness) (**Fig. 9.1d**). The large surface area of the mesoporous structure should provide greater surface contact with cells when forming biointerfaces (**Fig. 9.1e**), leading us to hypothesize that this will result in efficient ion transport during charging and discharging, which can be exploited for biological modulation.

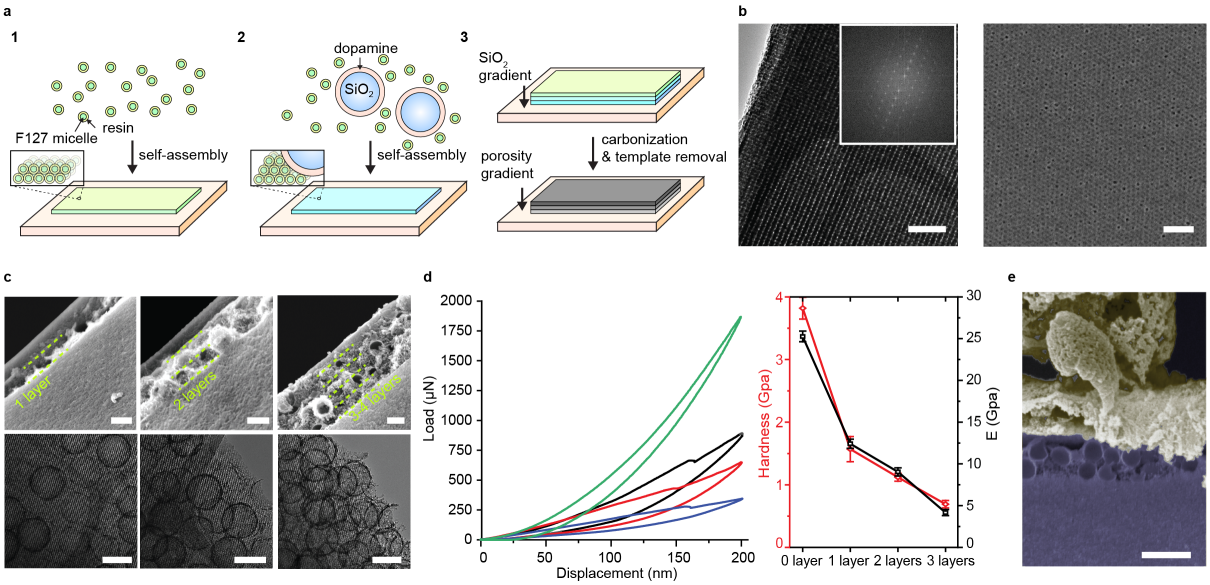

Figure 9.1. (**a**) Illustration of the hierarchical mesoporous materials which mimic the structures and functions of chemical synapses. (**b**) Transmission electron microscopy (TEM; left panel; scale bar, 100 nm), corresponding fast Fourier transform (FFT) diffraction pattern (left panel inset) and scanning electron microscopy (SEM) images of mesoporous materials, showing the highly ordered mesostructures (right panel; scale bar, 200 nm). (**c**) Cross-sectional view (upper panels) and associated top view (lower panels) of the hierarchical porous material. The hierarchical structures display two components: the bottom layer constructed from ordered mesoporous structure and the

Figure 9.1 (cont.) top porous vesicles assembled into multiple layers (1, 2, and 3-4 layers, from left to right). Scale bar, 200 nm. (**d**) Load versus displacement plots (left panel) of the hierarchical mesoporous thin film measured with a nano-indenter (with 0, 1, 2 and 3-4 vesicle layers, from top to bottom, green color). Young's modulus and hardness calculated from the load versus displacement plots (right panel). As layer number increases, Young's modulus and hardness decrease, indicating the film becomes softer. (**e**) Cross-sectional (false color) SEM image of cardiomyocytes (CMs) cultured on the hierarchical mesoporous film, implying that soft-hard hybrid interfaces can form between the film and cells. Scale bar, 100 nm.

9.3.2 Micro-supercapacitor fabrication and characterization

We designed and fabricated a micro-supercapacitor-like device to achieve rapid ion modulation (**Figs. 9.2a**, **S5-S6**). Photo-patternable, flexible SU-8 film was utilized as the substrate. The device was designed such that the microfabricated porous carbon electrodes displayed an interdigitated pattern on top of a ~10 μm thick SU-8 mesh substrate (**Fig. 9.2a**). Raman spectroscopy showed carbon peaks at 1330 and 1590 cm^{-1} only in the patterned region (**Fig. 9.2b**), confirming the presence of carbon membrane. Finite element simulations of the electrolyte potentials between two comb-like electrodes revealed ion transport gradients (**Fig. 9.2c, top panel; Fig. 9.S7**). Electric field distributions at the cross-section of the interdigitated comb-like micro-supercapacitor were compared with a simple two-electrode model of the same electrode area (**Fig. 9.2c, bottom panel; Fig. 9.S8)**. A smaller field distribution height at on the z-axis for the micro-supercapacitor signified a more localized and refined electrical field with much less penetration depth than with the simple two-electrode model. The micro-supercapacitor was then used directly in electrochemical tests using culture media as electrolyte without any binder or additives. The electrochemical performance of the micro-supercapacitor was calculated by cyclic voltammogram (CV) analysis using three electrode measurements. Capacitive behavior of the micro-supercapacitor was also measured by galvanostatic charge/discharge method at varied current density and time. CV was performed over a wide range of scan rates (2-100 mV/s) in multiple

electrolytes (**Fig. 9.2d; Figs. 9.S9-S12**). In Na_2SO_4 electrolyte solution, the micro-supercapacitor showed rectangular CV profiles up to a scan rate of 100 mV/s (**Figs. 9.S9a, b**), indicating that the device acted as an electrostatic double-layer capacitor. Notably, the micro-supercapacitor also showed a near-rectangular CV profile in DMEM up to a scan rate of 100 mV/s, demonstrating that the capacitor behavior is maintained even in cell culture medium (**Figs. 9.2d**, **S11**). Stack volumetric capacitances calculated from the CV profiles (**Fig. 9.S9c**) were comparable to those of other micro-supercapacitors (G. Lee et al., 2014; Pech et al., 2010; Song et al., 2015), indicating a low ion transport resistance at the interfaces. The low equivalent resistance of about 680 Ω and 715 Ω were obtained in PBS and DMEM solutions, respectively, by electrochemical impedance spectroscopy (EIS) tests (**Fig. 9.S13**), suggesting the excellent capacitive behaviors and ion transport properties. Device stability in biological environments was tested by submerging the device in 37°C PBS solution for one month, during which no obvious change in capacitance rate was observed (**Fig. 9.2e**). The device also showed perfect cycling stability; after 10,000 cycles, the device capacity maintained its initial rate (**Fig. 9.2f**). The live-dead assay showed that CMs cultured over the micro-supercapacitor devices have nearly 100% live rate after a 3-day culture (**Fig. 9.S14**), suggesting good biocompatibility. Together, these results demonstrate that the device has promise for biological modulation applications.

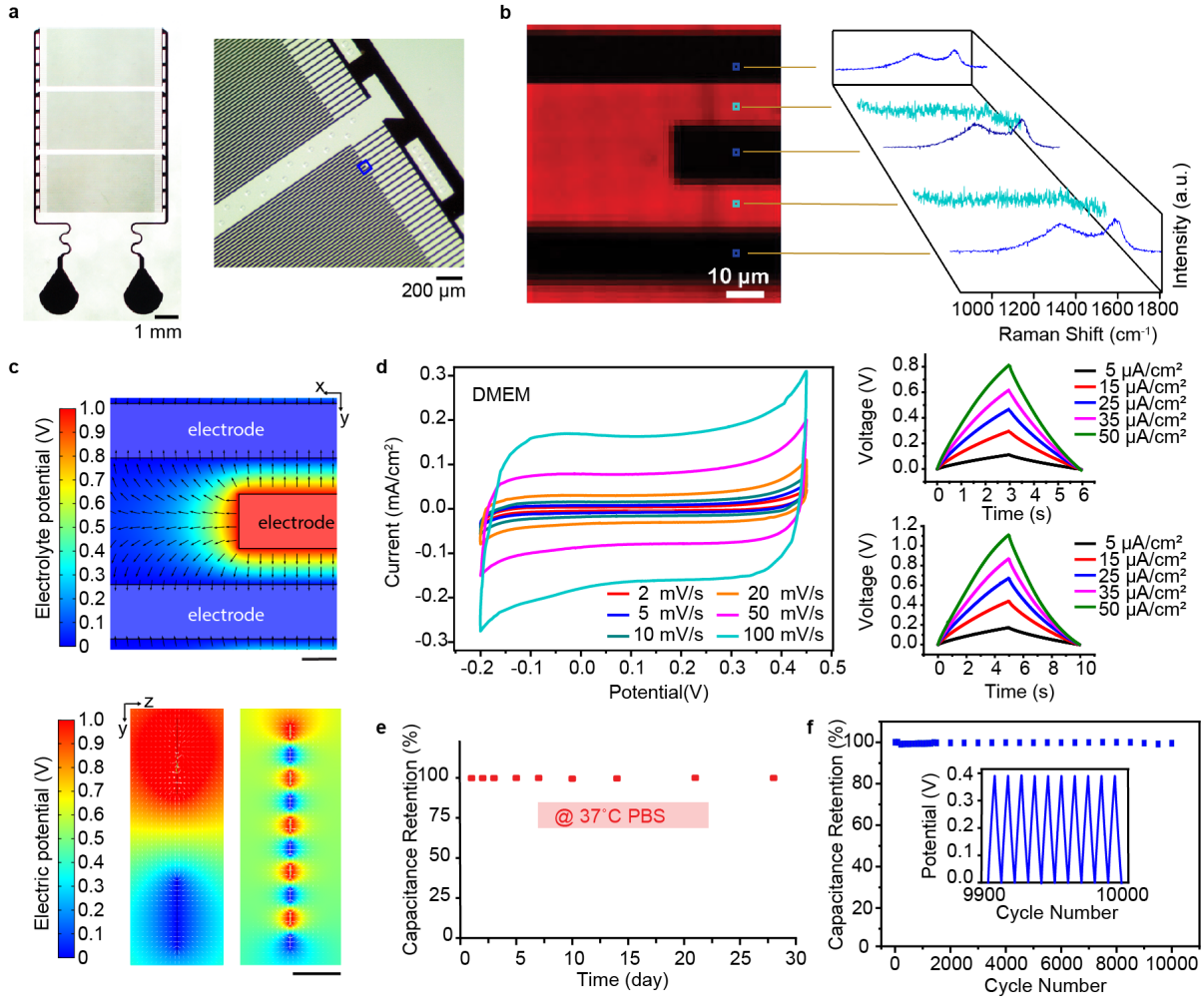

Figure 9.2. (**a**) Optical images of the micro-supercapacitor device fabricated using the hierarchical mesoporous carbon film. The SU-8 mesh-structured substrate is designed to improve flexibility and permeability of the device. (**b**) Raman spectra mapping for the micro-supercapacitor device (left panel), corresponding to the blue box marked in (a), indicating the same pattern shown in (a). Raman spectra show typical carbon peaks at around 1330 cm^{-1} and 1590 cm^{-1}, which were only found in the designed pattern region. (**c**) COMSOL simulation of the electrolyte potentials in the gap between the two comb-like electrodes, corresponding to the blue box marked in (a). Scale bar, 10 μm (top panel). COMSOL simulation of cross-section electric potential distributions using a model of two five-prong comb-like electrodes, compared with two-electrode model of same area. The comb-like micro-supercapacitor shows a more refined and localized electrical field with much less penetration depth. Scale bar, 50 μm (bottom panel). (**d**) CV profiles for the micro-supercapacitor device at different scan rates in cell culture medium DMEM (left panel). Charge-discharge curves in DMEM medium (right panels) of the micro-supercapacitor device at different current densities for same time window (6 s and 10 s). (**e**) Cycling stability of the device in buffer solution (PBS) at 37°C. (**f**) Cycling stability of the device tested over 10,000 cycles and the charge-discharge curve during last 10 cycles is shown in the insert.

9.3.3 Biological training in vitro

The ability of the hierarchical micro-supercapacitor device to modulate ion flow with applied voltage is reminiscent of the regulation of ions and molecules at nerve synaptic junctions and cardia field coupling (**Fig. 9.3a**) (Copene & Keener, 2008; Sperelakis & McConnell, 2002). To study the ability of the micro-supercapacitor to modify signal transduction, we established a biointerface between the device and CMs. We first seeded CMs on the device and verified cell adhesion and expression of typical cardiac markers, such as cardiac troponin and connexin-43 (**Figs. 9.3b, S15**). To determine whether ion manipulation by the micro-supercapacitor device could modulate cellular activity, we applied low input electrical potentials to CM-interfacing devices and performed simultaneous calcium imaging to monitor electrical activity (**Figs. 9.S16-S22**). Prior to stimulation, CMs were synchronized to one another with a baseline rate of ~0.67 Hz. Upon application of input electrical potential (~0.8 V) (**Figs. 9.3c, S21, S22**), overdrive pacing was achieved, and the contraction rate immediately synchronized to the stimulation rate (1 Hz in **Fig. 9.3c** and **Fig. 9.S22**, and 0.5 Hz in **Fig. 9.S21**). The ability to perform overdrive pacing of CMs may have promising therapeutic applications. However, we also wanted to demonstrate the utility of the device for in vitro cellular manipulation that will allow basic mechanistic investigations. To this end, we applied ionic manipulation with subthreshold amplitude, which did not elicit a direct overdrive pacing response. **Figure 9.3d** (pre-training traces) illustrates low spontaneous activity (~0.2 Hz and 0 Hz at two stimulation sites) of CMs prior to stimulation. When low amplitude charge/discharge cycles were applied (0-0.23 V, 1 Hz, ~4 times lower than for overdrive pacing), the CMs did not show an immediate response. However, when the stimulation was applied for a longer duration, a gradual increase in contraction was observed. After ~1500 s of stimulation, the cells were 'trained' by the ionic manipulation and their contraction rate

increased to the target stimulation rate of 1 Hz (**Fig. 9.3e**). This observation resembles the gradual increase of CMs electrical activity rate upon subthreshold optical stimulation (Parameswaran et al., 2019). We postulate that the repetitive stimulation of the cells alters the resting membrane potential of the CM to the point that the cells are sufficiently depolarized to elicit action potentials, reminiscent of the 'memory effect' (referring to how pacing history alters the excitability of a cell) (Hund & Rudy, 2000). Because of the unique mechanism of our micro-supercapacitor, where ions are manipulated without generating current injection and high junctional electric fields, we were able to pace or train the CMs with a biocompatible voltage lower than many previously reported ones (Agarwal et al., 2013; Baumgartner et al., 2015; C. Chung et al., 2012; Eng et al., 2016). Moreover, the lack of anodic and cathodic reactions on the surface of the micro-supercapacitor will prevent complications due to electrode hydrolysis, which would result in an increase in resistance over time, and in severe cases, device failure.

To better understand the biomimetic cardiac training dynamics, we established a Markov model using computational methods to assess cell behavior upon modulation input (**Figs. 9.S17-S22**). Based on the observation that CMs tend to alter their spontaneous contraction rate in vitro, we hypothesized that these frequency changes follow a stochastic mechanism, in which the cells can transition between three different states: (i) increasing, (ii) decreasing, and (iii) constant frequency. Under this assumption, we analyzed the stimulated cultures and, according to their observed frequencies, we determined the state of the cell state. We generated a transition matrix, describing the transition between the three states, to best fit the observed data by randomly generating simulated trials, and selected the trial that minimized the square errors. Given each initial state, the transition matrix was used to calculate the probability distribution of the next

state:$[Transition\ Matrix]^n[Initial\ State] = [Distribution\ of\ State\ n]$. **Figures 9.3f and Fig. 9.S23a** show the observed and calculated transitions states which we used to build our Markov model. Our observed data fit well within the expected range of variation generated by the model (**Figs. 9.3g, S23 b**), which suggests an underlying cell regulation process that results in a fluctuating, rather than smooth, training curve. As our model takes into account the internal fluctuating behavior of the cells, as well as the externally applied ionic manipulation, it should perform better (lower error) than a standard linear regression. These results demonstrate that our micro-supercapacitor generates an ionic manipulation, thus allowing for a subthreshold stimulation that does not override the inherent electrical activity of the cells, but still allows the gradual training effect to take place. Although this proof of concept is based on small data sets, we believe that this approach for electrically modulating and analyzing the cellular activity will enable investigations of how internal fluctuations of CM rates determine their reaction to external electrical inputs, and their contribution to the cellular 'memory effect' in a way that has been thus far overlooked.

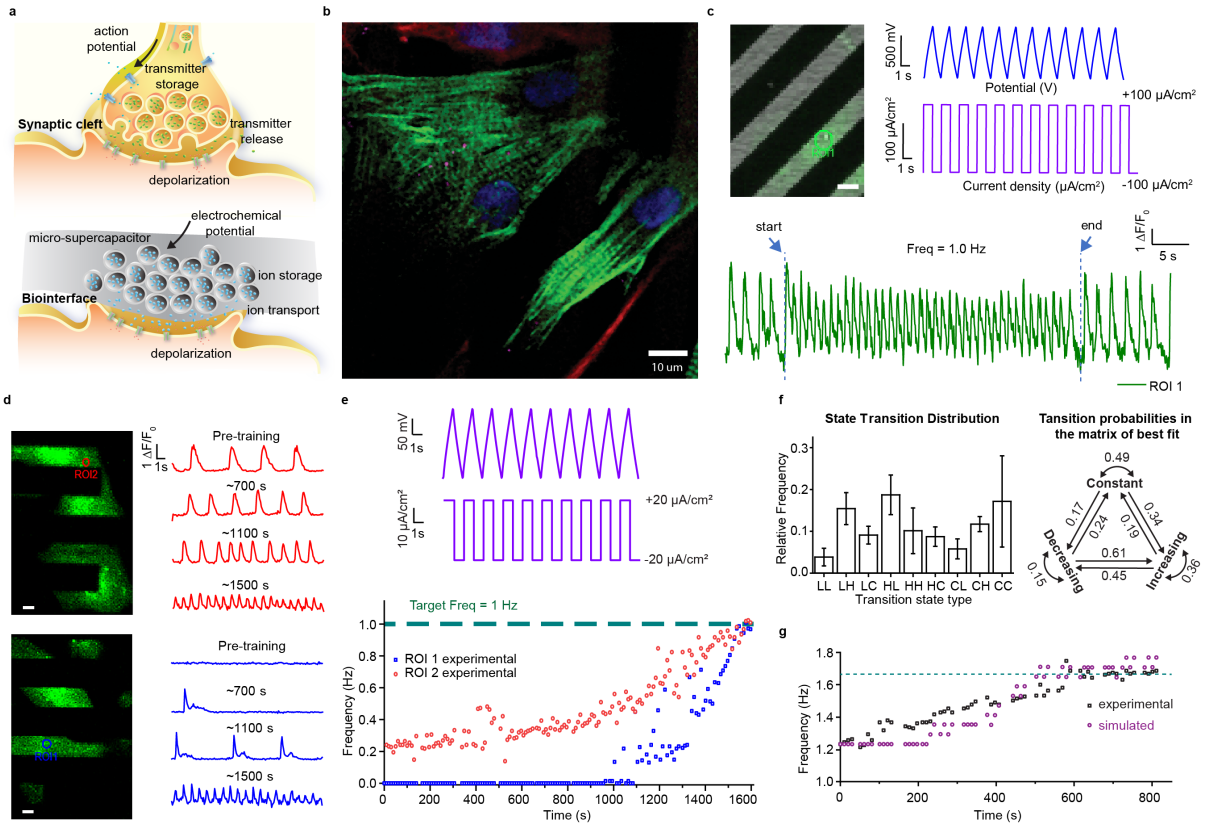

Figure 9.3. (**a**) Top: illustration of action potential-driven neurotransmitter (including ions) release from a chemical synapse. Bottom: reminiscent of neurotransmitter release from nerve fibers, an electric field can control ion release in the micro-supercapacitor. (**b**) Immunohistochemistry images for cardiac cells cultured on the micro-supercapacitor device. Cells were stained for cardiac troponin (CMs, green), connexin-43 (magenta), vimentin (fibroblasts, red) and DAPI (blue). (**c**) Upper left: representative image of CMs loaded with calcium sensitive dye; transmitted light shows the micro-supercapacitor (appeared in black). Scale bar, 10 μm. Upper right: device input voltage (top) and current (bottom) during the stimulation. Bottom: cell contraction rate illustrated by plotting the intensity profile of the region of interest (ROI, highlighted by green circle in the image). (**d**) Representative images of CMs loaded with calcium sensitive dye recorded during stimulation for 1600 s (left; scale bar, 5μm), and intensity profiles of the blue and red ROIs marked on the images (right). Graphs show representative intensity at 20 s intervals before and after 700, 1100, and 1500 s of stimulation. (**e**) Input signaling of the devices during a training process (upper panel) showing the voltage (top) and current (bottom) applied to the cells. Frequency analysis (lower panel) of two different ROIs from (d) shows a gradual and fluctuating increase in contracting rate which eventually reaches the target stimulation frequency of 1 Hz. (**f**) Each observation in our data was assigned a state transition (L, low; H, high; C, constant), and the graph shows the distribution and standard error of the observations (left). Transition matrices were randomly generated then tested. Transition probabilities for the matrix that best fit the data (with OLS error) are shown here (right). (**g**) Example comparing simulated trials with observed data.

9.3.4 Biological modulation at the tissue and organ level

We tested the efficacy of our device as a bio-modulator in both intact excitable tissues and ex vivo organs. Intact neural tissues represent highly crowded environments with non-neuronal factors, such as the extracellular matrix and glial interactions, that can influence neuronal activation. To determine whether the micro-supercapacitor device can modulate activity in intact neural circuits, we performed stimulation experiments on isolated mouse retinas **(Fig. 9.4a)**. The laminated organization of the retina and its diverse neural circuit motifs make the retina an accessible model system to study brain circuit function. Additionally, the use of retinal tissue allows us to stimulate physiologically relevant "input neurons", the photoreceptors, and record activity from the "output neurons", the retinal ganglion cells (RGCs) of a well-defined sensory circuit. In these experiments, we utilized retinas isolated from transgenic mice (*Slc17a6*$^{tm2(cre)Lowl}$*/Gt(ROSA)26Sor*$^{tm95.1(CAG-GCaMP6f)Hze}$) expressing GCaMP6 in all RGCs (Ellis et al., 2016; Martersteck et al., 2017). This enabled simultaneous monitoring of neural activity via multiple neurons. Micro-supercapacitor devices and interconnects were fixed on glass coverslips using glue and PDMS and used as bottoms for the retina perfusion chamber. All prongs in one device were used as an end of the two-electrode stimulating system. Dissected retinas were then positioned with the photoreceptor layer facing the micro-supercapacitor device and the RGC layer pointing upward. Using two-photon (2PT) laser scanning microscopy, we recorded calcium transients from RGCs while stimulating the photoreceptor layer with micro-supercapacitor modulation. We used an input electrical potential from 0 to 0.78 V to control the ion flows on the mesoporous carbon surface and modulate the neural activity of the ganglion cell layer. Ion flow direction was periodically switched by alternating the current direction every 3.5 s. During micro-supercapacitor stimulation, large periodic transients could be observed across several RGCs following the stimulation protocol.

During the stimulation, when the device was charged, RGCs exhibited large calcium transients suggesting that they had become depolarized; when the device was discharged, the calcium levels in RGCs returned to resting levels **(Fig. 9.4b)**. To corroborate that the micro-supercapacitor stimulation observed was due to activation of the glutamatergic pathway from photoreceptors to bipolar cells to RGCs, we applied a cocktail of glutamate receptor antagonists, including AP-5, L-AP4, and DNQX, to silence glutamate transmission in the retina. Upon glutamate receptor blockade, the large calcium transients could no longer be observed in RGCs during micro-supercapacitor stimulation (**Fig. 9.4c**). These results demonstrated that the charging and discharging patterned stimulation at the supercapacitor-photoreceptor interface evoked changes in glutamate release from photoreceptor neurons and could therefore activate the retinal network.

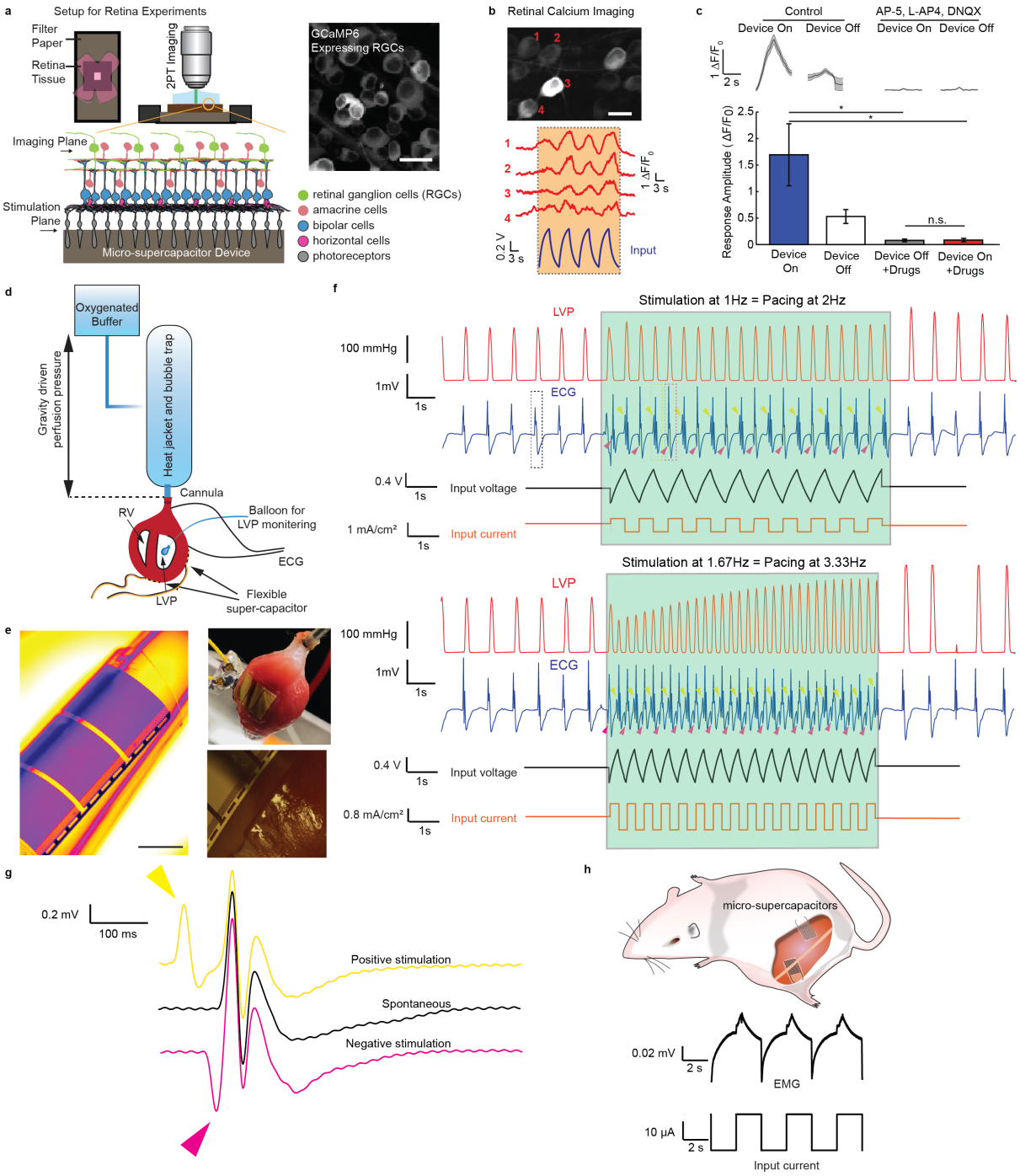

Figure 9.4. (**a**) Top left: experimental setup for retinal stimulation with a micro-supercapacitor. Top right: max-intensity projection of RGCs expressing GCaMP6. Scale bar, 25 µm. Bottom: schematic of the retina-device interface highlighting the location of GCaMP6-expressing neurons and the location of the photoreceptors stimulated by the micro-supercapacitor device. (**b**) Max-intensity projection of RGCs expressing GCaMP6. Scale bar, 25 µm (top panel). Representative calcium traces from RGCs upon micro-supercapacitor stimulation. Results for individual cells are indicated by numbers in red (bottom panel). (**c**) Calcium transient traces represented as average ± standard error for stimulation and no stimulation in both control and glutamate antagonist conditions (top panel) and quantification of response amplitude of calcium transients (bottom

Figure 9.4 (cont.) panel). (**d**) Schematics of the Langendorff perfusion system. Heart perfusion pressure was constantly monitored and kept stable using gravity perfusion. Electrocardiogram (ECG) and left ventricular (LV) pressure were monitored to show the effect of micro-supercapacitor stimulation on the heart rate. (**e**) Images of the flexible device conforming around a cylindrical holder (left; scale bar, 2 mm) and around the curvilinear and contractile tissue (right). (**f**) Representative LV pressure (LVP) profiles and ECG recordings of the isolated heart stimulated at two different frequencies of 2 and 3.33 Hz. Input stimulation of the devices (top, voltage; bottom, current) is synchronized to the corresponding stimulated portions of the LVP and ECG recordings. (**g**) Closer look at an ECG recording of a spontaneous AP (black line) and APs that follow positive (yellow) and negative (pink) artifacts. These enlarged APs are highlighted by a dashed square and corresponding color in **Fig. 9.4f.** (**h**) Top: schematic illustration of the experimental setup, where the sciatic nerve was exposed, and the poles of the device were places under the nerve and on the skin. Bottom: representative EMG recording of the stimulated limb, with the corresponding device's current input.

For ex vivo whole heart experiments, a micro-supercapacitor was placed on the apex and another was placed on the left ventricular (LV) wall of a rat heart (**Fig. 9.4d, Fig. 9.S24**). The flexibility of our device allowed it to conform around the heart, minimizing the mechanical mismatch (**Fig. 9.4e**). The rat heart contained ~75 μm thick epicardium, separating the CMs and the device (Jenkins et al., 2013). Therefore, a single micro-supercapacitor, with just 10 μm spacing between the leads, was not sufficient to accumulate the depolarizing charge. The thickness of the epicardium, which is much larger than the distance between the leads, would prevent the CMs from sensing the electrical input with our initial device dimensions, as the positive and negative leads cancel one another, resulting in a zero charge at the CMs. Thus, we used two micro-supercapacitors, one on the apex and one on the LV wall. Electrocardiogram (ECG) electrodes were placed on the aorta and the LV. By separating the charge/discharge cycles, we were able to perform overdrive pacing of the heart. It is important to mention that every cycle contained two charging and two discharging inputs (one on each opposite lead); each input gave rise to an action potential, the result being a pacing frequency double that of the device frequency. To stimulate the isolated heart, we applied charge/discharge cycles with different frequencies (1 Hz, ±0.8 mA/cm^2

and 1.67 Hz, ±1 mA/cm^2, **Fig. 9.4f**). To lower the spontaneous heart rate, we removed the sinoatrial node along with the atriums, which resulted in a slow atrioventricular node pace (~1 Hz). Upon micro-supercapacitor stimulation, the heart immediately contracted at double the stimulation rate, i.e. 1 and 1.67 Hz stimulation frequencies corresponded to 2 and 3.33 Hz pacing frequencies, respectively (**Fig. 9.4f**). Due to the capacitive nature of our device and lack of current injection, we believe that the mechanism governing the electrical stimulation of our device is similar to field coupling (Copene & Keener, 2008; Sperelakis & McConnell, 2002). As current is not injected into the cells, the charging capacitor attracts counter ions to its surface. This manipulation results in a charge accumulation that eventually depolarizes the CMs to their threshold excitation, i.e. eliciting an AP. We also noticed a large difference in the stimulation threshold (over an order of magnitude) between the in vitro and in vivo models. This fits well with the fact that native CMs functioning as a syncytium have a much lower input resistance and higher capacitance (De Mello, 1975; Weidmann & Hodgkin, 1966). Although the pacing can be easily observed with a LV pressure balloon, the ECG recording of the heart gave more insight by showing the artifact associated with the charge/discharge cycle. **Figure 9.4g** provides a closer look at a representative ECG recording of three different APs. While no artifact was associated with the spontaneous AP, we observed a positive/negative alternating artifact during the stimulation (**Fig. 9.4f, g,** yellow and pink arrowheads, respectively). As the ECG was recorded from the aorta and the LV, the observed artifact may be attributed to the stimulating micro-supercapacitor positioned on the LV, and not on the apex. This explains the alternating positive/negative artifact which corresponds to charge/discharge cycle. Moreover, it seems that the negative artifact is the one that depolarizes the tissue, thus resulting in an immediate AP. The positive artifact, on the other hand, hyperpolarizes the tissue and has no immediate effect. However, at the same time, the micro-supercapacitor placed

at the apex depolarized the tissue and generated an AP. The 45 ms time gap between the positive artifact and the AP may be attributed to the time of AP propagation from the apex to the LV. Overall, the stable, flexible and successful modulation of the heart activity ex vivo could be implemented for long term in vivo heart pacing.

To demonstrate its utility for in vivo neuro-modulation applications, we interfaced the micro-supercapacitor with sciatic nerves. We used an acute setting in which the micro-supercapacitor was interfaced with the exposed nerve. **Figure 9.4h** shows that application of charge/discharge cycles using two separate devices resulted in bioelectrical modulation of the nerve. When one device was interfaced with the sciatic nerve and the other device was interfaced with the rat's body, we observed that the associated limb was clearly moving with every discharge of the associated micro-supercapacitor. This was further validated by electromyography (EMG) recordings from the rat foot, which showed an AP that was synchronized to the discharge cycle **(Fig. 9.4h, bottom**). Thereafter, we exposed the second sciatic nerve and connected the two devices to the two nerves. As every discharge in each device corresponds to the charge of the other device, the two limbs were stimulated with a discharge intermittently. Consequently, the limbs moved in turn, triggered by each discharge portion of the cycle which resulted in depolarization of the nerve. Overall, we show here that our micro-supercapacitor device may be employed for in vivo applications. It can allow precise control of neuronal modulation, which will open many avenues for long term, non-faradaic electrical modulation.

In summary, we have developed a micro-supercapacitor device capable of biological modulation. The hierarchical carbon membrane composition is effective in stimulating chemical synapses and

allows control over ion flow via electrical potential inputs. The micro-supercapacitor device shows long-term stability and good biocompatibility, increasing its capacity for use in clinical settings. We have shown that our device can modulate the contraction of primary CMs from a slow beating rate to a specified target frequency in a minimally invasive manner via a cell training process. Our system also successfully modulated electrical activity at tissue and organ scale. In addition to expanding our available toolkits for investigating fundamental biological modulation mechanisms, we anticipate that our findings will promote the use of such carbon-based micro-supercapacitor devices as clinical therapeutics.

9.4 Experimental Procedures

Materials preparation and device fabrication

Hierarchical mesoporous carbon films were synthesized by the following method. Resol precursors (low-molecular) were prepared by crosslinking of phenol and formaldehyde, using methods from the literature (Meng et al., 2005). Pluronic block copolymer F127 (template) and phenolic resol (carbon source) were mixed at ratio of 1:2 into an ethanol solution. The solution was stirred for 1 hour before use and named Solution A. Vesicle structures were constructed using silica nanosphere templates. 200 nm-diameter silica nanospheres (NanoComposix, 10 mg/ml) were surface modified with a dopamine layer, according to a literature method (R. Liu et al., 2011). The modified nanospheres were then added into Solution A and mixed until a homogeneous mixture formed. This new solution was named Solution B. Silicon wafer (Nova Electronic Materials, p-type, 600 nm thermal oxide SiO_2) was cut into small pieces with suitable sizes (e.g. 2 cm × 4 cm) and cleaned by O_2 plasma (Plasma Etcher, PE100) at 100 w for 2 minutes. Solution B was spin-coated (Laurell, WS-650 spin coater) onto the surface-cleaned silicon at 1500 rpm for 45

s. Multiple layers were formed by leaving the silicon wafer at room temperature for 10 minutes and then repeating the spin-coating. Then Solution A was spin-coated onto the substrate at 3000 rpm for 45 s. The wafers were kept immobile for 4-6 h at 25°C, then baked in an oven for 24 h at 100°C. After baking, the wafers were transferred into inert argon atmosphere and heated at 500°C (temperature rise rate at 5°C/min) for 30 min. The wafers were cooled to room temperature and then spin-coated in a thin protective layer of polymethyl methacrylate. The thin film was etched off the silicon wafer and nanospheres were etched by submerging the wafers in buffered hydrofluoric acid (HF) for 8 h. The thin film was rinsed with deionized (DI) water 3-4 times, then carefully transferred onto a new silicon wafer and dried slowly at room temperature. The wafers were transferred into inert argon atmosphere and calcined at 700°C for 30 min. After cooling, a standard photolithography procedure was applied to make the desired pattern on the hierarchical mesoporous carbon. An 80 nm thick Au layer was evaporated on the pattern surface using an e-beam evaporator (AJA, ATC-Orion) and extra carbon parts were removed by reactive-ion etching (Oxford Instruments PlasmaPro, NGP80) in O_2 flow (100 sccm, 4 mins). The supporting SU-8 layer with designed mesh patterns was made following a standard photolithography procedure using a double side mask aligner (EVG, EVG620). The pattern on the SU-8 layer was etched from the substrate by buffered HF and transferred into DI water for 1 day. After washing the device with DI water 6 times, the patterns on SU-8 were carefully transferred onto the cover glasses or culture dishes. Wire bonding on the desired pattern led to final device fabrication.

Electron microscopy

Transmission electron microscopy (TEM, Tecnai F30, FEI) and scanning electron microscopy (SEM, Carl Zeiss, Merlin) were used to characterize the hierarchical mesoporous materials and

material/cell interfaces. CMs on the materials were fixed in 5% glutaraldehyde phosphate-buffered saline (PBS) solution for 30 min, washed in DI water, and then dehydrated with an increasing ethanol gradient from 30% to 98%. The samples were dried in a critical point dryer (Leica EM CPD300) and observed on the same SEM after coating with an 8 nm Pt/Pd metal layer on a sputter coater (Ted Pella, Inc.). SEM was operated at 2 kV.

Mechanical test

Indentation modulus and hardness were measured by performing nanoindentation using a Hysitron 950 Tribolndenter in ambient environment with a Berkovich indenter (three-sided pyramid-shaped diamond tip, tip radius ~100 nm). All measurements were kept at a constant displacement of 200 nm. The data were analyzed using standard Oliver and Pharr (1) analysis to extract the reduced modulus (E_r) and hardness by selecting upper fit at 95% and lower fit at 20%. The Young's modulus E of the samples were extracted based on Eq. (1) (Oliver & Pharr, 2004), a general relation that applies to any axisymmetric indenter. The diamond tip has a Young's modulus E_i = 1141 GPa and a Poisson's ratio ν_i = 0.07 (Li & Bhushan, 2002). Here, we assume the Poisson's ratio of the samples ν = 0.25, which has been widely used for amorphous carbon (Suk et al., 2012).

$$\frac{1}{E_r} = \frac{1-\nu^2}{E} + \frac{1-\nu_i^2}{E_i} \qquad (1)$$

Finite element analysis of the electric field distribution

The finite element analysis of the electric field distribution through electrodes was performed using AC/DC Module of COMSOL Multiphysics software. For 2D electrolyte potential, the device geometry was uploaded from an autoCAD file and was consistent with the experimental setup. Each electrode had a length of 5000 μm and a width of 15 μm. Voltages of 1V were applied to the prongs of one comb and ground (0V) was applied to the prongs of the opposite comb. A heat map

was colored according to the electrolyte potentials (V) with arrows indicating the electrolyte current density vectors. The boundaries were defined as $\emptyset_I = \emptyset_{I,bnd}$, while the insulations were defined as $-n \cdot i_I = 0$ and $-n \cdot i_s = 0$, and the electrolyte was defined with $\nabla \cdot i_I = Q_I$ and $i_I = -\sigma_I \nabla \emptyset_I$. Secondary current distributions were also taken into account in simulating the electric field potential. For 3D electric field distribution at the cross-section of the micro-supercapacitor, the electric scalar potential, V, satisfies Poisson's equation, $-\nabla \cdot (\varepsilon_0 \varepsilon_r \nabla V) = \rho$, where ε_0 is the permittivity of free space, ε_r is the relative permittivity, and ρ is the space charge density. The electric fields are obtained from the gradient of V: $\mathbf{E} = -\nabla V$, and the displacement is defined as $\mathbf{D} = \varepsilon_0 \varepsilon_r \mathbf{E}$. To simplify the simulation (versus actual device with three hundred prongs), a five-prong comb-like electrode model pair was built with a gap of 10 μm and prongs of 200 μm length and 15μm width. Prong width and gap width were consistent with the experimental setup. Voltages of 1V were applied to the prongs of one comb and ground (0V) was applied to the prongs of the opposite comb. For comparison, the electric field distribution of two planar electrodes was also calculated. The area of each electrode was equal to the total area of a single comb, and the gap width between the two planar electrodes was equal to the summation of the gaps in each comb-like electrode; as such, each electrode was of 75 μm width and 200 μm length with a gap of 50 μm between the two. A heat map was colored according to the surface electric potentials (V) with arrows indicating the electric field direction and strength.

Cell culture

All animal procedures were conducted in complete compliance with and approval from the University of Chicago Institutional Animal Care and Use Committee (IACUC) Animal Care and Use Protocol. Hearts were excised from P0-5 neonatal rats into ice cold HBSS (without Ca^{2+} or

Mg^{2+}). The hearts were cut to small <1 mm pieces, and then rinsed with HBSS to remove blood. Pierce™ primary cardiomyocyte isolation kit (Thermo Fisher Scientific) was used for digesting the tissue according to manufacturer protocol. After isolation, the suspended cells (mainly CMs contaminated with cardiac fibroblasts) were pre-plated for 2 h, allowing fibroblasts to adhere to the tissue culture plate. Then the enriched CMs population was seeded onto the micro-supercapacitor device pre-treated with fibronectin (Sigma). The cells were allowed to sit in culture media (DMEM high glucose + 10% FBS, 1% Glutamax and 1% penicillin–streptomycin) for 24 h, then the media was changed to CM-specific media (DMEM high glucose + 10% FBS, 1% penicillin–streptomycin, and 0.1% growth supplement from isolation kit). This media prevented fibroblasts from proliferating and taking over the culture.

Calcium sensitive dye

CMs were treated with calcium sensitive dye (2μM Fluo-4, AM, cell permeant, Thermo Fisher Scientific) for 30 min at 37°C. Cells were rinsed and incubated for 30 min to allow complete de-esterification. The treated cells were then visualized with a Leica SP5, STED-CW Super-resolution Laser Scanning Confocal.

Retina slice

Vglut2-IRES-Cre mice (016963-*Slc17a6*$^{tm2(cre)Lowl}$*/J*) and floxed *Ai95(RCL-GCaMP6f)-D* mice (028865-*Gt(ROSA)26Sor*$^{tm95.1(CAG-GCaMP6f)Hze}$*/J*) were acquired from The Jackson Laboratory and were crossed to each other in the laboratory of Dr. Wei to obtain hybrid *Vglut2-IRES-Cre/GCaMP6f* transgenic mice. Mice of both sexes (postnatal days 21-35) were used for retinal calcium imaging experiments. All procedures were in accordance with the University of Chicago Institutional Animal Care and Use Committee, the National Institutes of Health's *Guide for the*

Care and Use of Laboratory Animals, and the Public Health Service Policy. Mice were anesthetized with isoflurane and decapitated after dark adaptation. Under infrared illumination, retinas were isolated from the pigment epithelium in oxygenated Ames' medium (Sigma-Aldrich, A1420), cut into dorsal and ventral halves, and mounted on filter papers as described in the literature (Wei et al., 2010). Retinas were kept in the dark at room temperature in Ames' medium bubbled with 95% O_2/5% CO_2 until use (0–7 h). Glass coverslips with adhered micro-supercapacitor devices were used as the bottoms of the imaging chamber. During imaging, retinas were placed on top of micro-supercapacitor devices and gently pressed against the surface using a platinum (Pt) wire weight and perfused with oxygenated Ames at 32–33°C. Cells were visualized with infrared light (> 900 nm) and an IR-sensitive video camera (Watec). Calcium transients from GCaMP6f expressing retinal ganglion cells were recorded by a custom-built two-photon microscope (Bruker) equipped with a Ti:sapphire laser (Chameleon Ultra II; Coherent Technologies) tuned to 920 nm. Data were acquired using PrairieView software from a 100 μm × 100 μm field of view with an acquisition rate of ~15 Hz. Raw frames were uploaded onto ImageJ software in which ROIs were manually drawn to enclose the soma of each GCaMP6f-expressing cell and a background region where there was no detectable GCaMP6s expression. Using custom MATLAB scripts, we calculated the average intensity over time for all ROIs and subtracted the background trace from light-responsive somatic traces to remove noise. The calcium traces were resampled to 75 Hz and smoothed using a moving average sliding window of 25 data points (~333 ms). For each stimulation protocol, the average $\Delta F/F_0$ was calculated for every cell.

Isolated heart

An adult rat was heparinized (1,000 IU/kg IP) and anesthetized using open-drop exposure of isoflurane in a bell jar configuration. The heart was removed and placed in ice cold HBSS buffer, and the aorta was cannulated in preparation for use in a Langendorff setup. Oxygenated Hepes-buffered Tyrode's solution (containing, in mM, NaCl 126, KCl 5.4, Glucose 10, Hepes 10, $MgCl_2$ 1, $CaCl_2$ 2, $MgSO_4$ 1.2, NaH_2PO_4 0.39; bubbled with 99.5% O_2; pH 7.3) was perfused through the cannulated aorta. The perfusion was passed through a heating coil and bubble trap (Radnoti), and the heart was placed in a water-jacketed beaker (Fisher Scientific) to maintain a temperature of 37°C. The perfusion pressure was maintained at 80–100 mmHg by adjusting the height of the I.V. bag containing the perfusion buffer. The perfusion and left ventricular (LV) pressures were monitored using a BP-100 probe (iWorx) connected to the perfusion line and a water filled balloon inserted to the LV, respectively. For ECG recordings, needle electrodes were positioned on the apex and aorta and connected to a C-ISO-256 preamplifier (iWorx). All signals (perfusion, LV pressure and ECG) were amplified using an IA-400D amplifier (iWorx) and interfaced with a PC using a DigiData 1550 digitizer with pClamp software (Molecular Devices). Two devices were placed on the heart; one below the heart's apex, and the other covering the LV wall. Charge/discharge cycles were applied to the devices, while the clear ECG artifacts were used to time the stimulation with the recording. To avoid the electrical noise introduced by the devices, we recorded the LV pressure to monitor the contraction rate of the heart during stimulation.

In vivo rat nerve stimulation

Seven-week-old rats were deeply anesthetized with ketamine (100 mg/kg) and xylazine (10 mg/kg) via intraperitoneal injection. The fur was removed from the hindquarters using a surgical clippers and hair removal cream. A semi-circular incision across the midline was made in the skin, and the fascial plane was opened between the gluteus maximus and the anterior head of the

biceps femoris, thereby exposing the sciatic nerve. In this setting, two devices were used. One device was placed under the sciatic nerve and the other under the rat's skin. For intermittent limb stimulation, the two devices were paced under the two sciatic nerves. All animals were housed under pathogen-free conditions and all animal procedures were approved by the Institutional Animal Care and Use Committees of the University of Chicago (IACUC).

9.5 Supporting Information

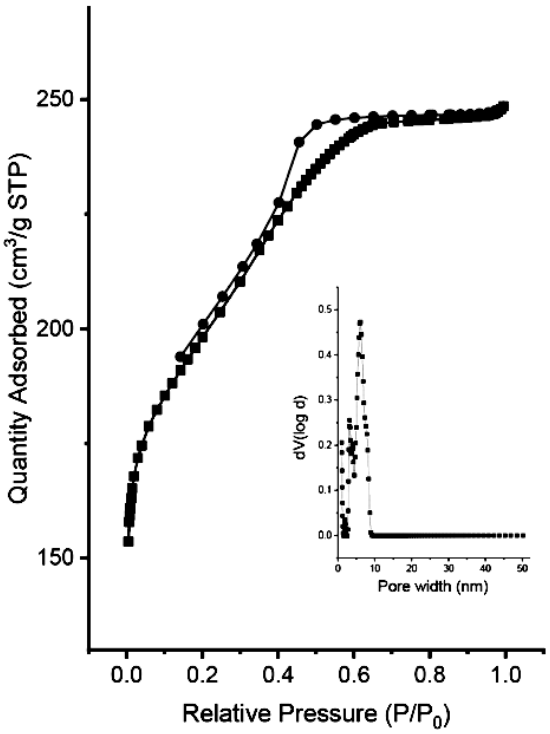

Figure 9.S1. Nitrogen adsorption and desorption curves of mesoporous carbon film, with corresponding pore size distributions.

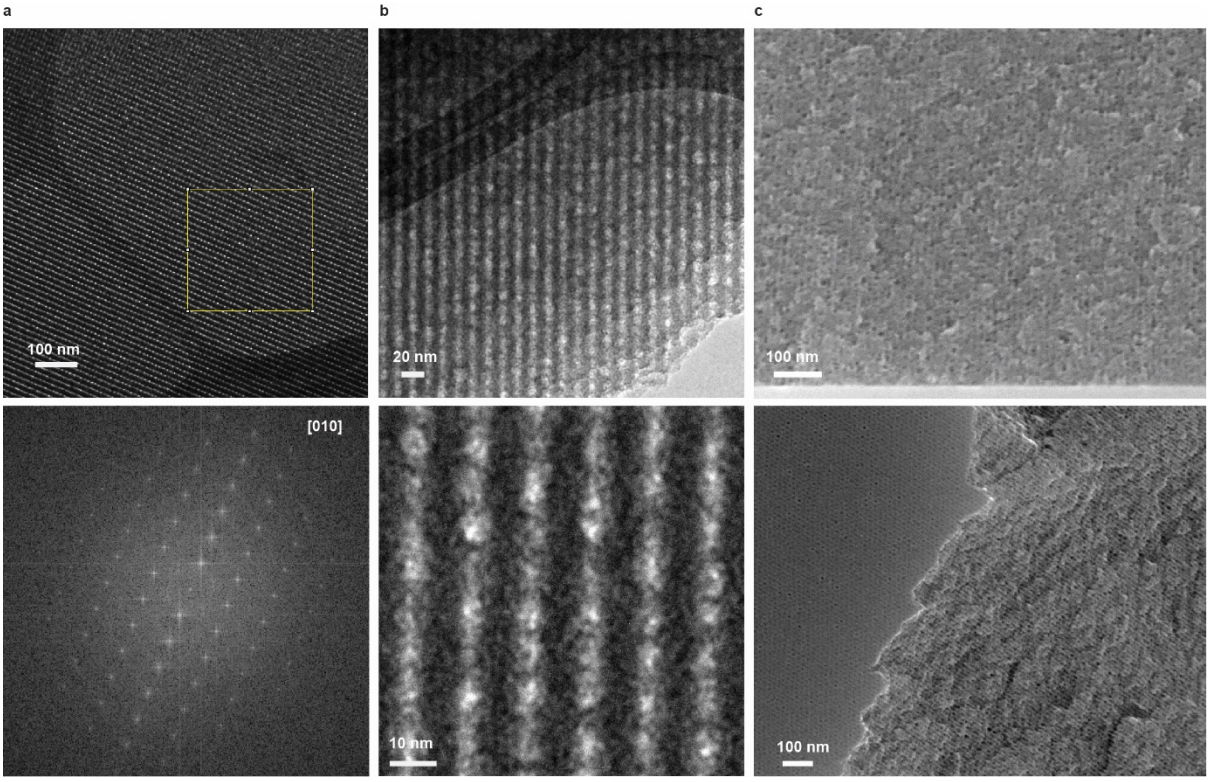

Figure 9.S2. (a) TEM and corresponding FFT (lower panel), (b) High-resolution TEM, and (c) SEM images of a pure mesoporous film, showing the highly ordered mesostructures.

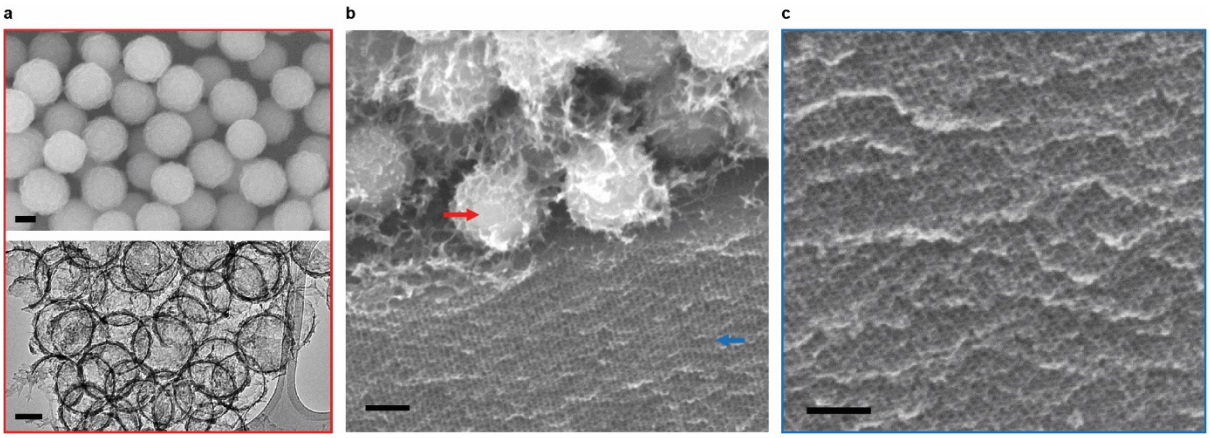

Figure 9.S3. (a) SEM images (upper panel) of the building blocks used to construct the hierarchical mesoporous film. SiO_2-C nanospheres show diameters around 200 nm and are very uniform. TEM images (lower panel) show the hollow spherical structures after the SiO_2 is etched. Scale bar, 100 nm. (b) SEM images showing the junction parts of the hierarchical mesoporous film, in which a two-layer structure is found. Nanospherical building blocks are indicated by the red arrow, and ordered mesoporous structures are indicated by the blue arrow. Scale bar, 100 nm. (c) SEM images of the mesostructures in the hierarchical mesoporous film, which is displayed in (b). Scale bar, 100 nm.

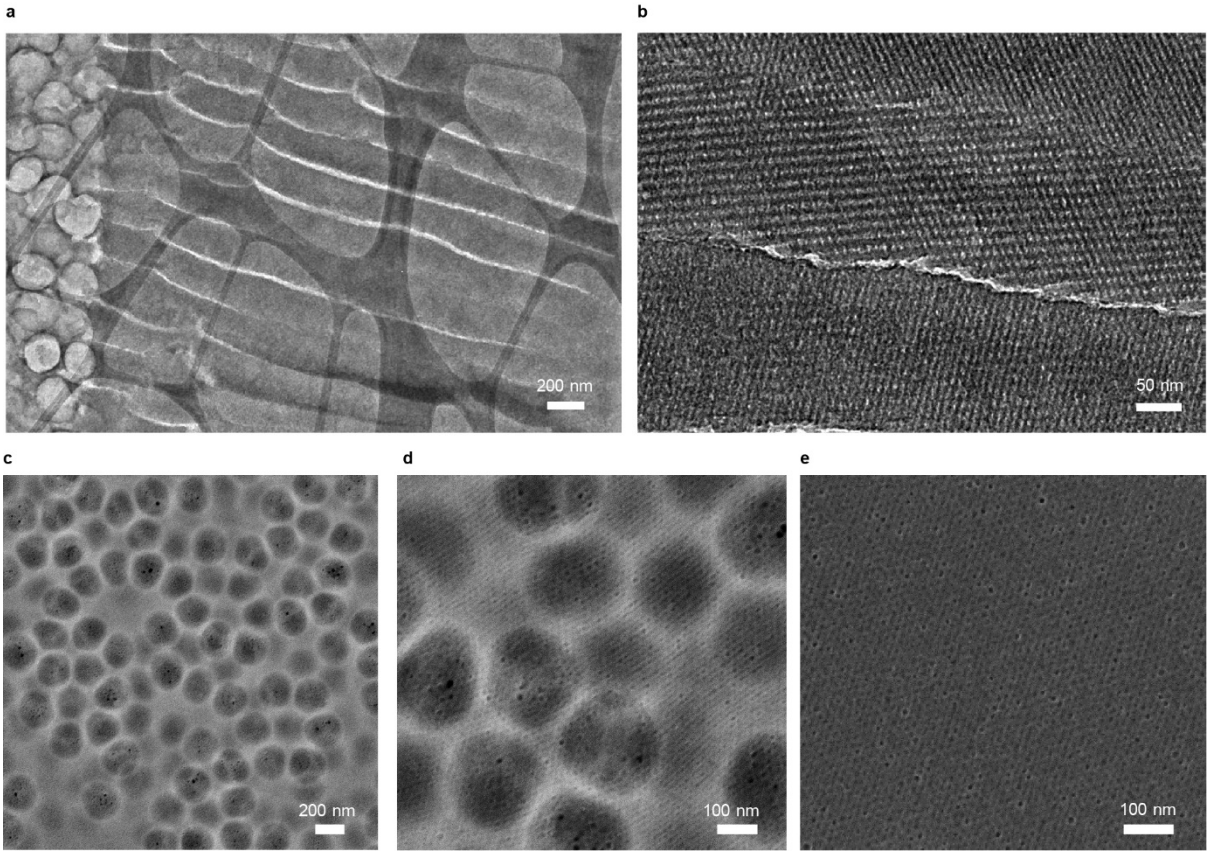

Figure 9.S4. (a-b) TEM images of the cross-sectional view for the thin film, demonstrating the hierarchical porous structures. The cracks are due to the microtome process. (c-d) SEM images of the thin film from the macroporous side, showing the continuous ordered mesostructures. The darker parts indicate the regions of hollow structures. (e) SEM images of the thin film from the mesoporous side, showing a flat thin film surface.

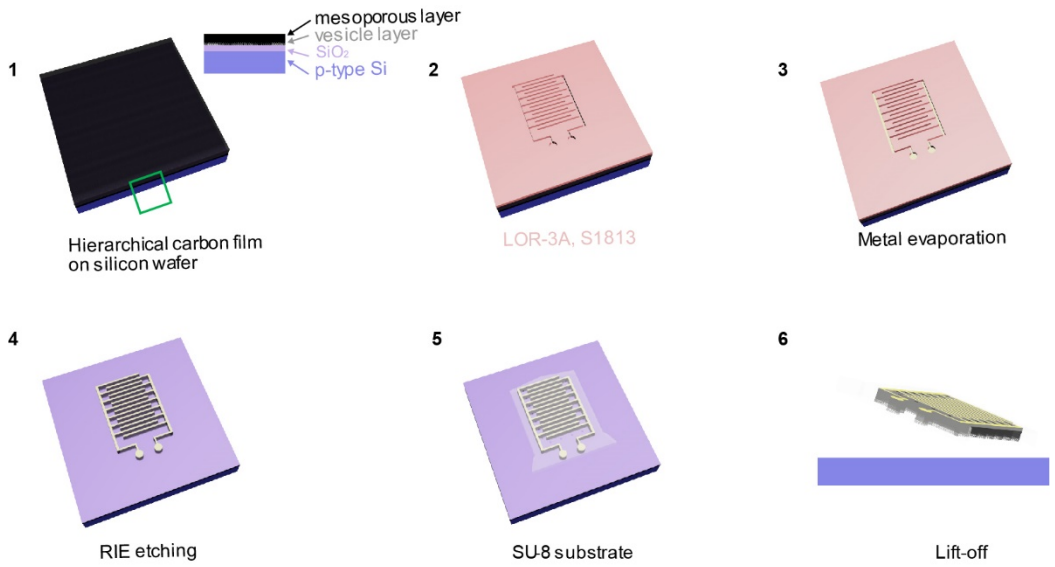

Figure 9.S5. Scheme for the device fabrication.

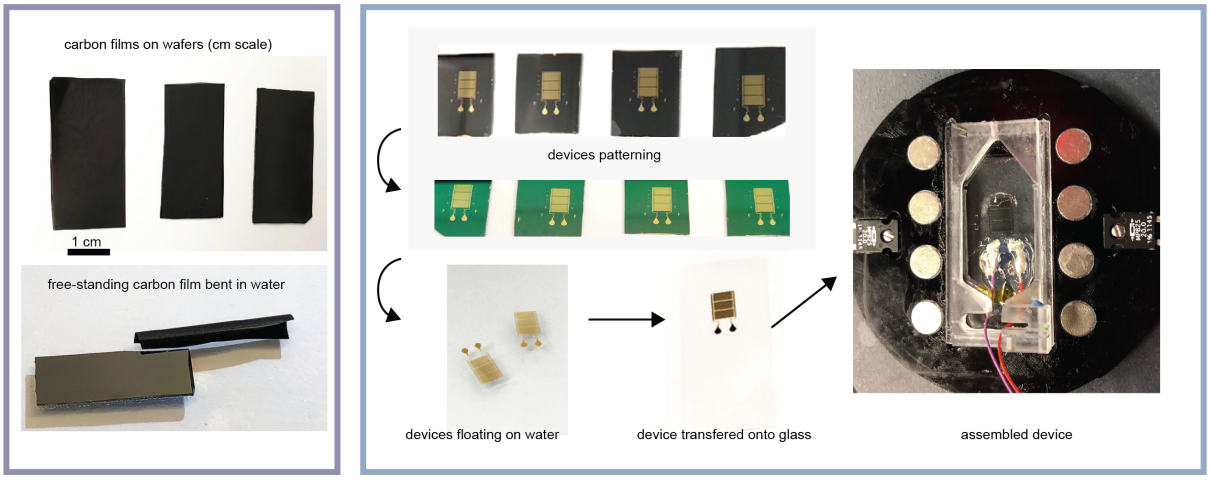

Figure 9.S6. Optical images of the carbon films materials, devices during fabrication process, and a final assembled device.

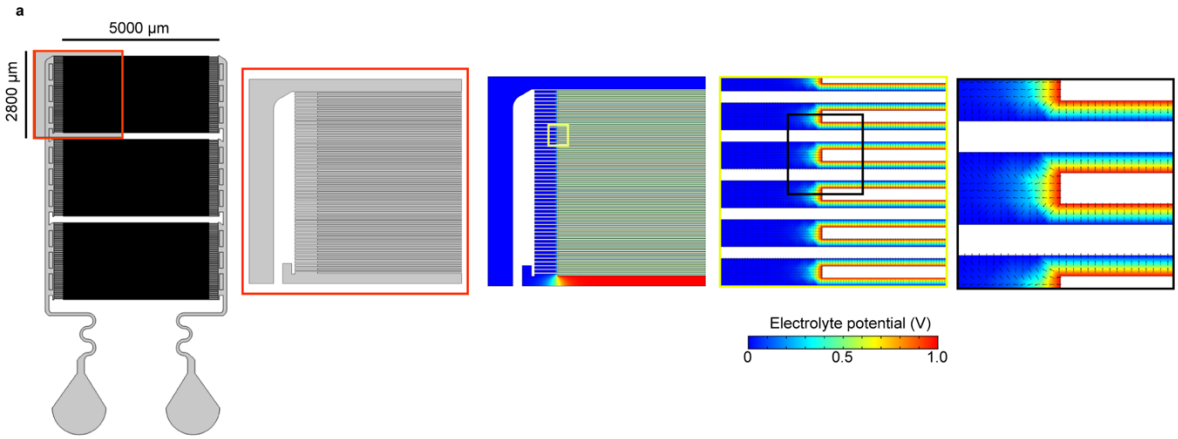

Figure 9.S7. (a) COMSOL simulation for 2D electrolyte potential distribution of the micro-supercapacitor. The rainbow color indicates the electrolyte potential between the two comb-like electrodes.

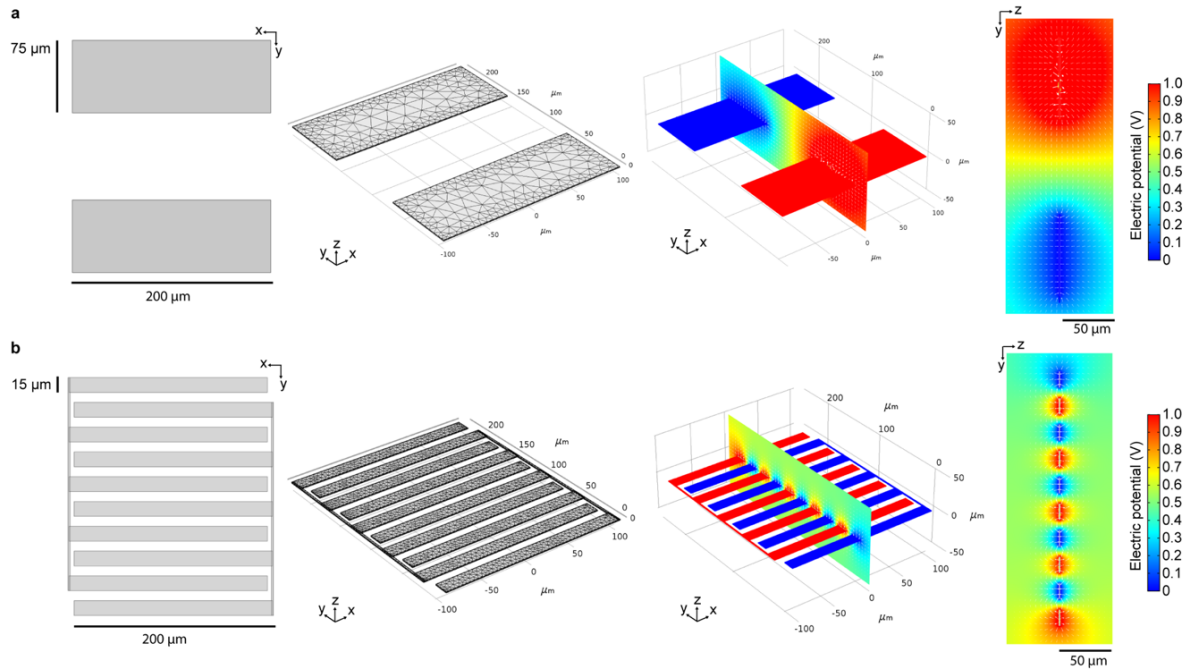

Figure 9.S8. (a) COMSOL simulation for 3D electric potential distribution of a simplified two planar electrode system. The rainbow color indicates the electric potential at the cross section, which spreads up to more than 50 µm space. (b) COMSOL simulation for 3D electric potential distribution of a micro-supercapacitor model with a pair of five-prong comb-like electrodes. The rainbow color indicates the electric potential at the cross section, which shows a much refined and localized field.

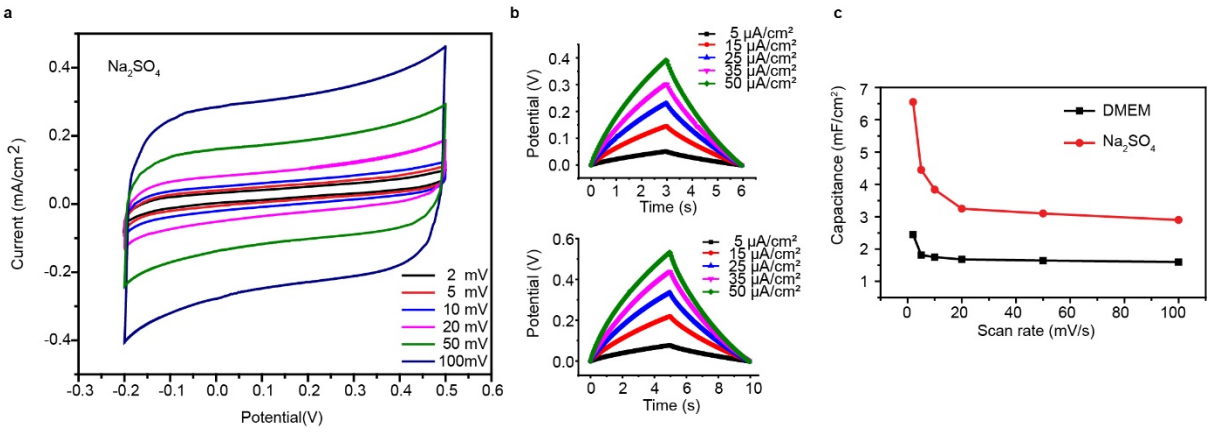

Figure 9.S9. (a) CV profiles for the micro-supercapacitor device at different scan rates in Na_2SO_4 solution. (b) Charge-discharge curves for the micro-supercapacitor device at different current densities for the same time windows (6 s and 10 s). (c) The stack volumetric capacitance with DMEM and Na_2SO_4 electrolytes of hierarchical mesoporous carbon micro-supercapacitor as a function of scan rate.

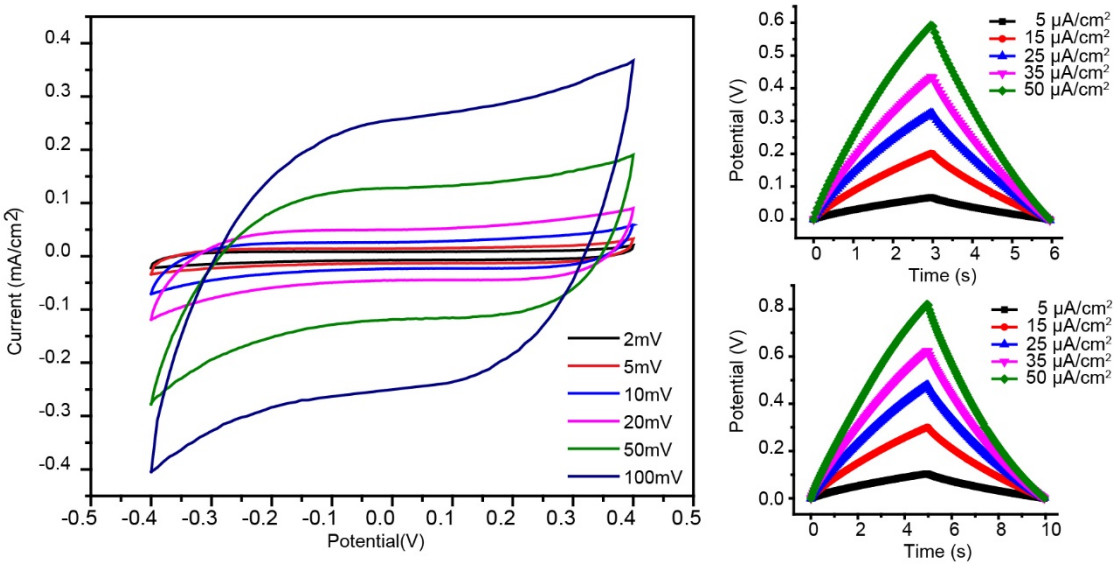

Figure 9.S10. CV profiles for the micro-supercapacitor device at different scan rates in PBS solution (left) and charge-discharge curves of the micro-supercapacitor device at different current densities for the same time windows (right, 6 s and 10 s).

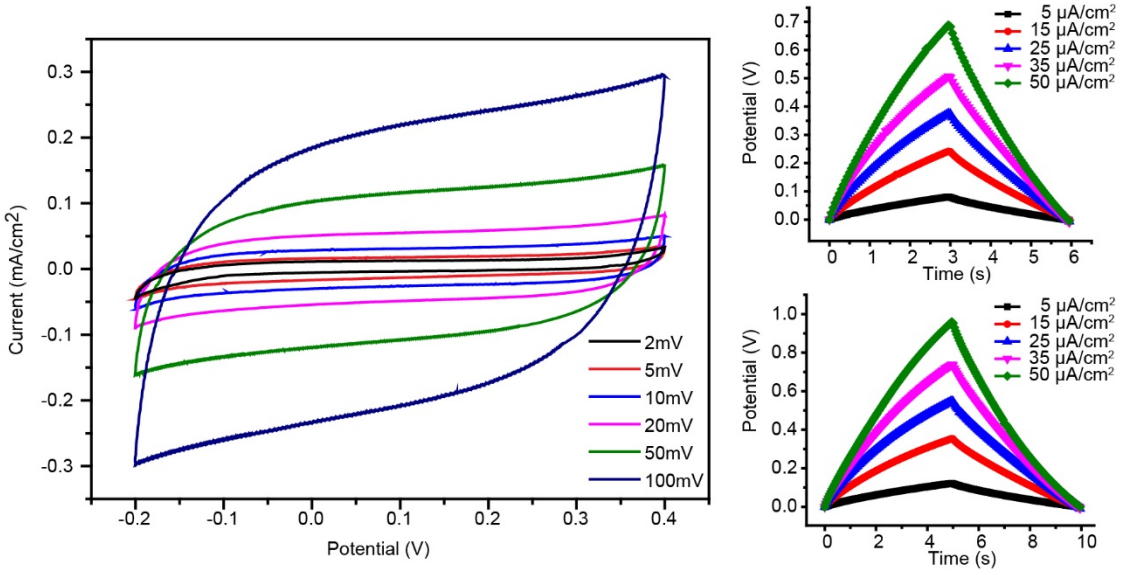

Figure 9.S11. CV profiles for the micro-supercapacitor device at different scan rates in culture medium ACSF solution (left) and charge-discharge curves for the micro-supercapacitor device at different current densities for the same time windows (right, 6 s and 10 s).

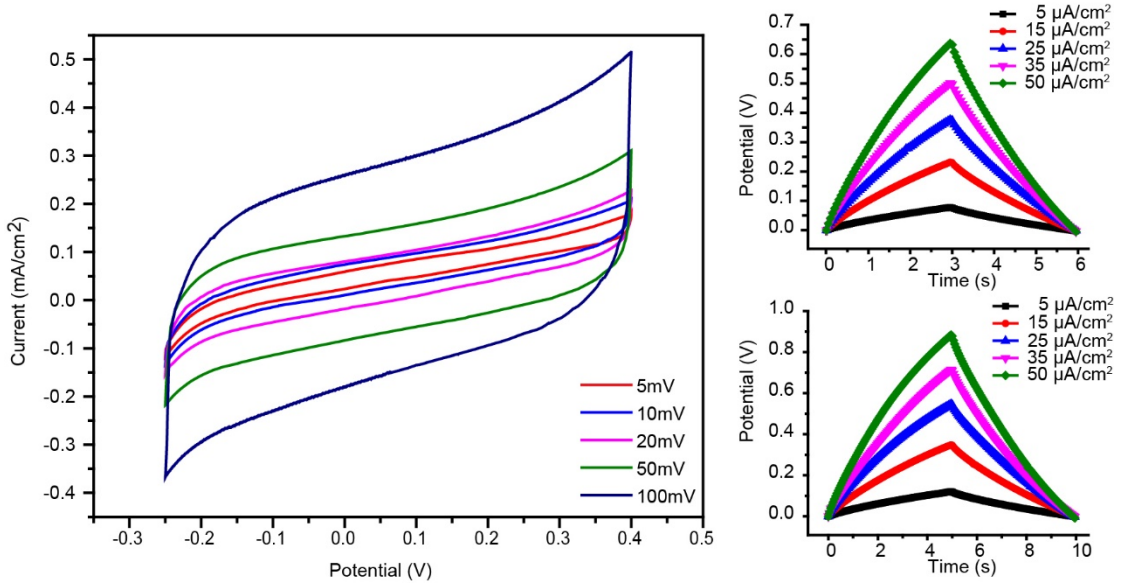

Figure 9.S12. (a) CV profiles for the micro-supercapacitor device at different scan rates in Hepes-buffered Tyrode's solution (left) and charge-discharge curves for the micro-supercapacitor device at different current densities for the same time windows (right, 6 s and 10 s).

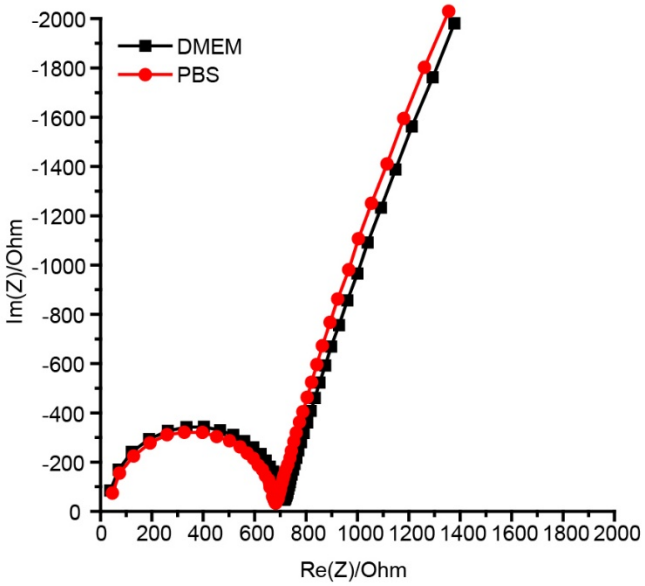

Figure 9.S13. Impedance measurements of the micro-supercapacitor device in DMEM culture medium and PBS.

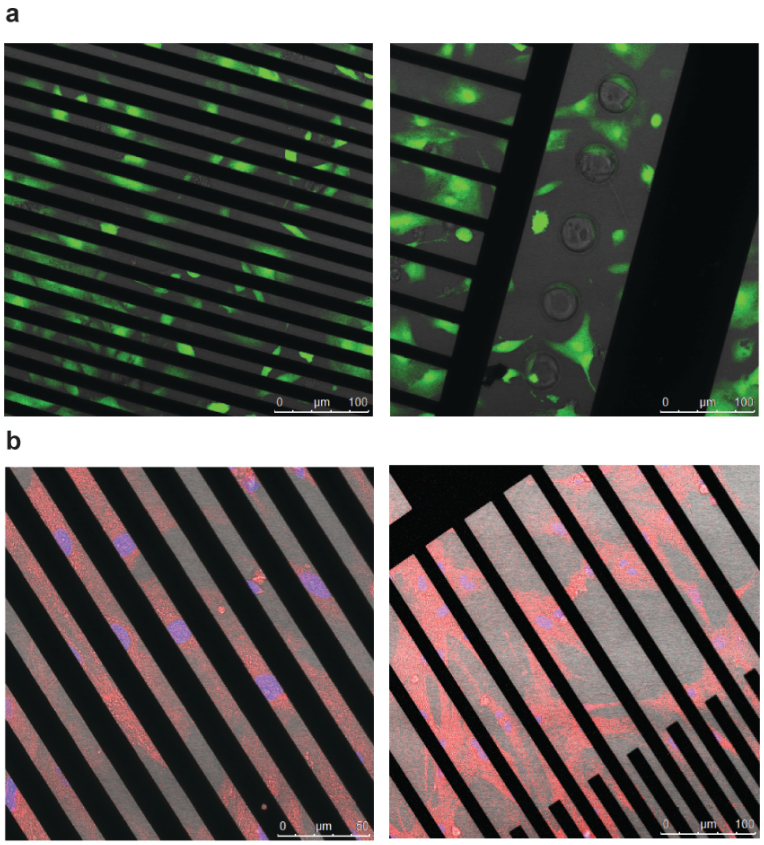

Figure 9.S14. (a) LIVE/DEAD assay shows that almost all cells cultured on the device for 3 days survive, demonstrating the good biocompatibility of our device. (b) In the positive control experiments, the cells are almost dead after treated with 100% ETOH for 20 minutes.

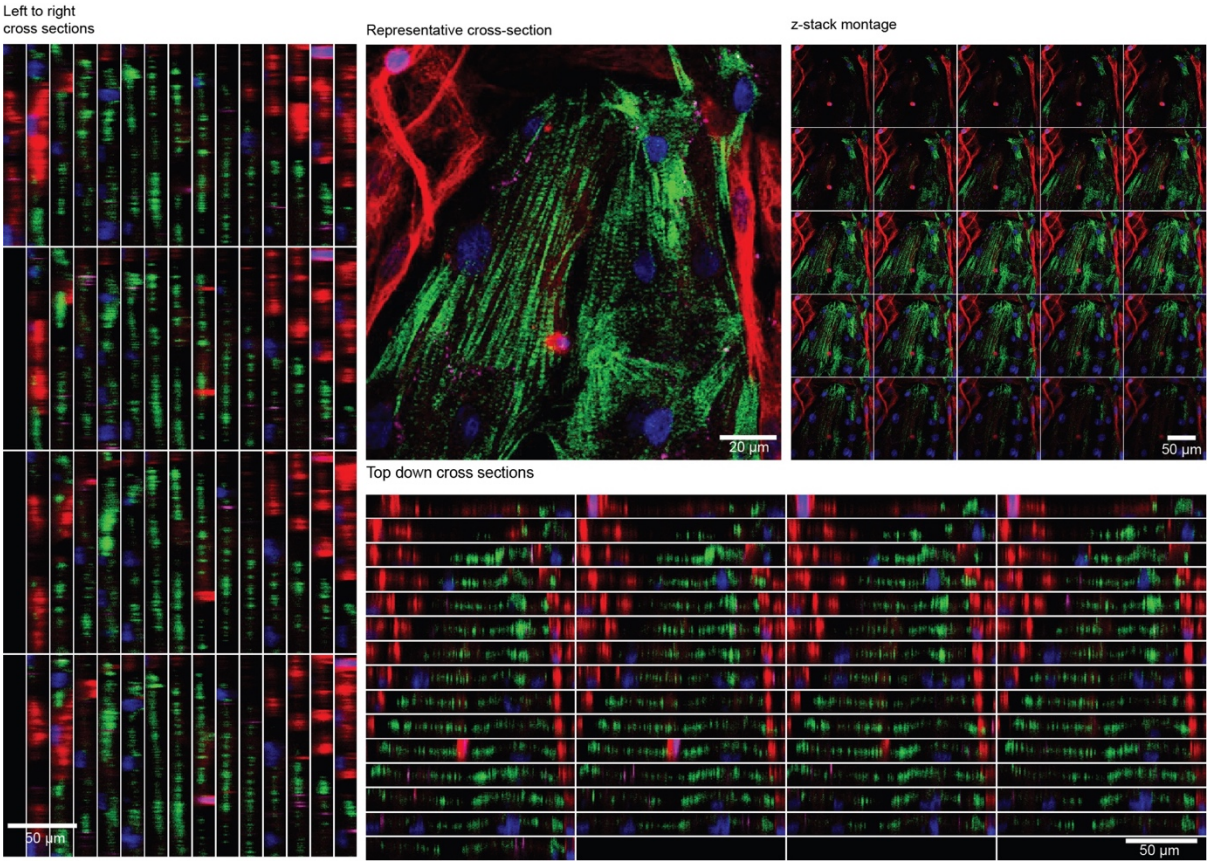

Figure 9.S15. Cross section (left to right and top down) and Z-stack montage views for images of the cardiac cells cultured on the device. Cells stained for cardiac troponin (CMs, green), connexin-43 (magenta), vimentin (fibroblasts, red) and DAPI (blue).

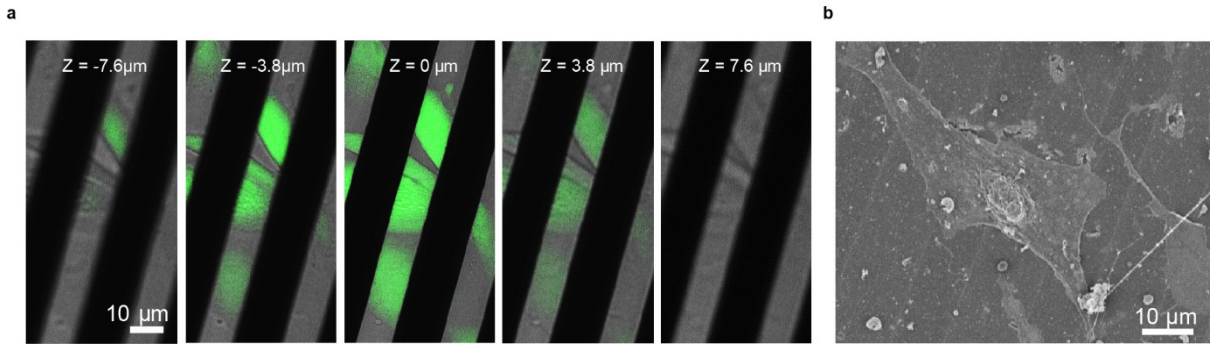

Figure 9.S16. (a) Z stacks images of the cells loaded with fluo-4 dye adhered to the device. The device was completely opaque, as represented by dark lines. (b) SEM image shows adhered cells on the device. In both images, the cells alignment does not follow device directionality.

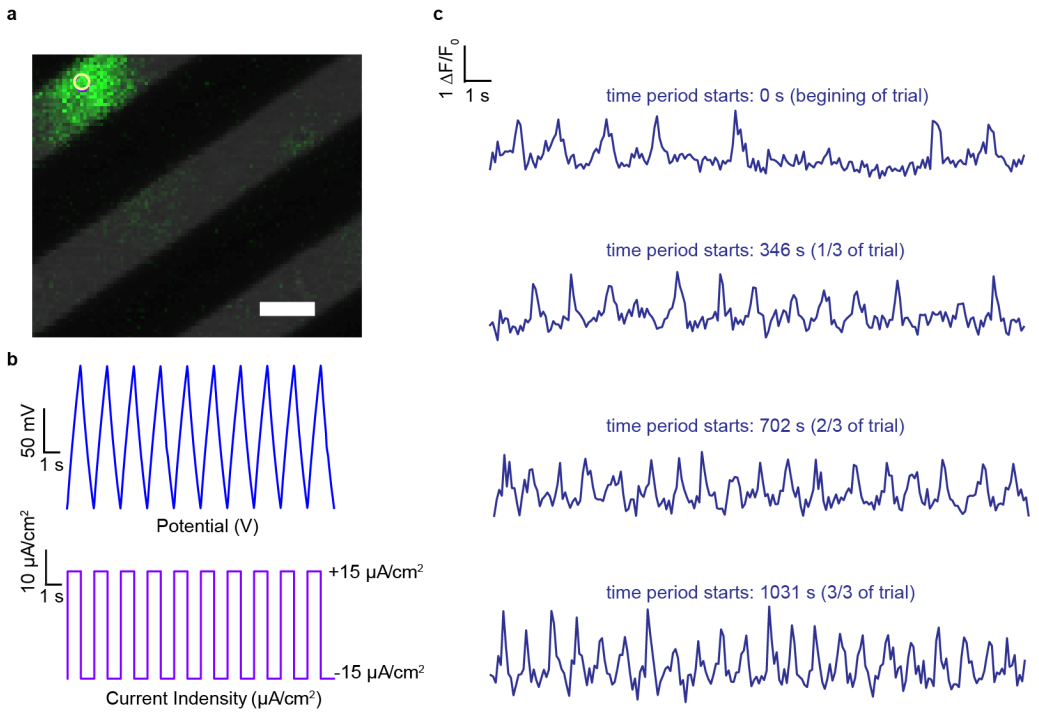

Figure 9.S17. (a) Representative images of the cells recorded during training with ROI region marked in yellow. Scale bar, 10 µm. (b) Typical input signal of the devices during a training process showing the voltage (top) and current (bottom) applied to the cells. Input signaling frequency is 1.1 Hz (1/0.9 s). (c) Intensity profiles for the marked ROI. Graphs are representative of results at 20 s intervals before and after 346 s, 702 s, and 1031 s of training. The intensity profile eventually reaches the target frequency of 1.1 Hz.

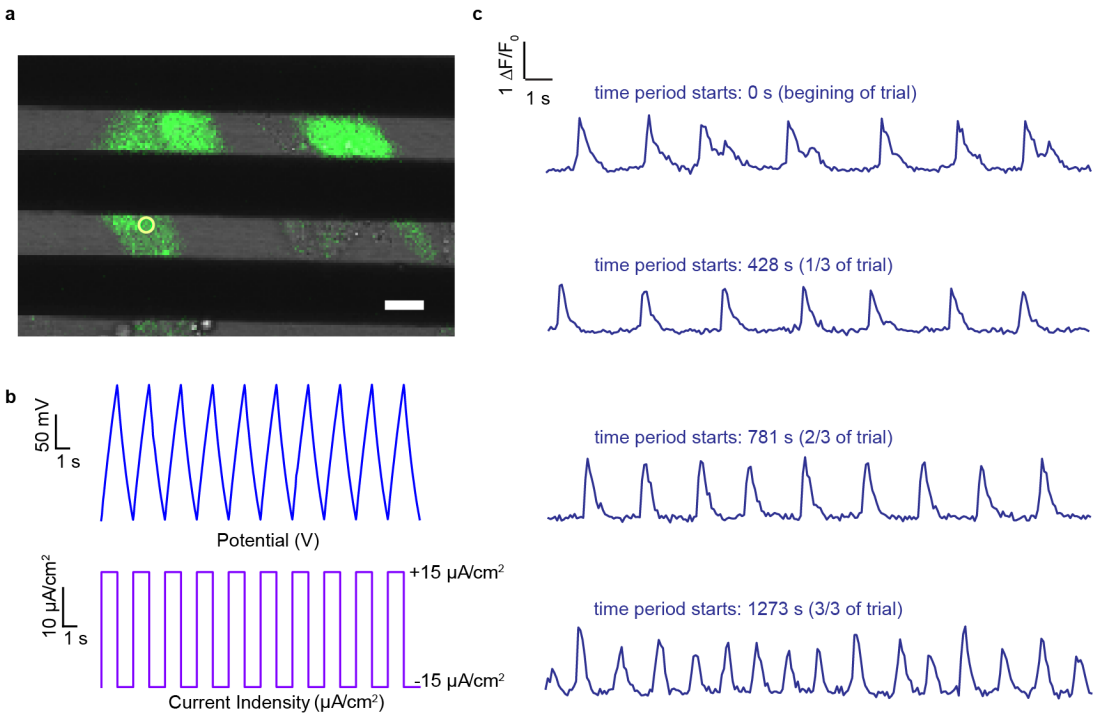

Figure 9.S18. (a) Representative images of the cells recorded during training with ROI region marked in yellow. Scale bar, 10 μm. (b) Typical input signal of the devices during a training process showing the voltage (top) and current (bottom) applied to the cells. Input signaling frequency is 0.83 Hz (1/1.2 s). (c) Intensity profiles of the marked ROIs are plotted. Graphs are representative of results at 20 s intervals before and after 428 s, 781 s, and 1273 s of training. The intensity profile eventually reaches the target frequency of 0.83 Hz.

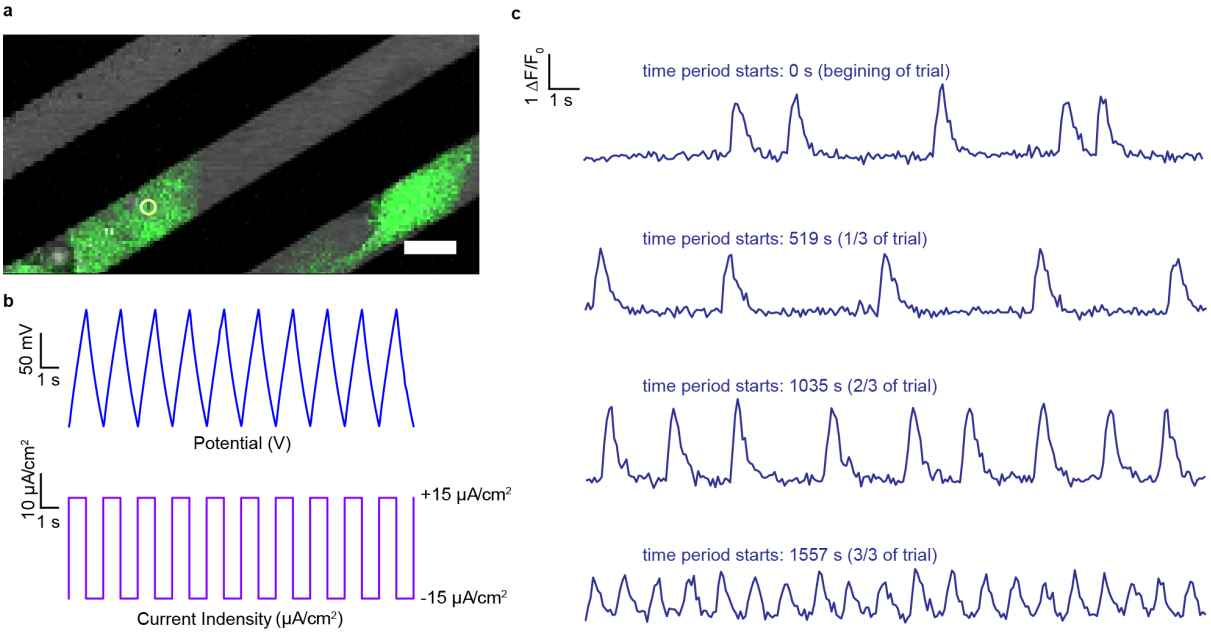

Figure 9.S19. (a) Representative images of the cells recorded during training with ROI region marked in yellow. Scale bar, 10 μm. (b) Typical input signal of the devices during a training process showing voltage (top) and current (bottom) applied to the cells. Input signaling frequency is 1.0 Hz (1/1.0 s). (c) Intensity profiles of the marked ROIs are plotted. Graphs are representative of results at 20 s intervals before and after 519 s, 1035 s, and 1557 s of training. The intensity profile eventually reaches the target frequency of 1.0 Hz.

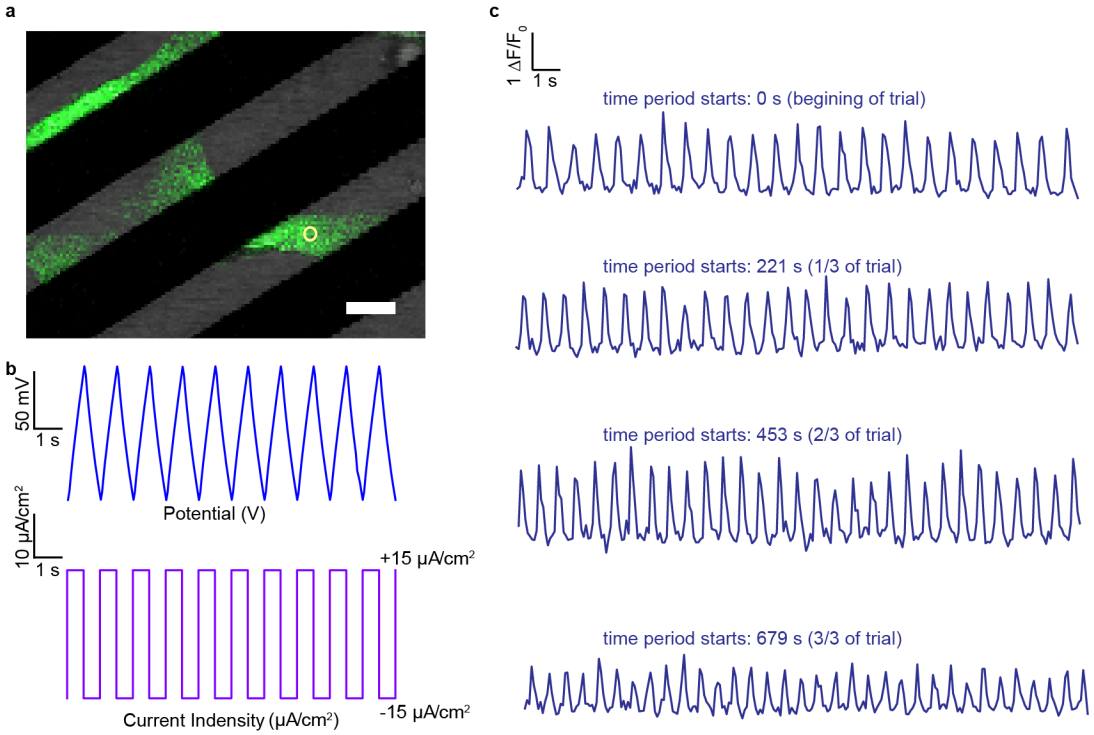

Figure 9.S20. (a) Representative images of the cells recorded during training with ROI region marked in yellow. Scale bar, 10 μm. (b) Typical input signal of the devices during a training process showing voltage (top) and current (bottom) applied to the cells. Input signaling frequency is 1.66 Hz (1/0.6 s). (c) Intensity profiles of the marked ROIs are plotted. Graphs are representative of results at 20 s intervals before and after 221 s, 453 s, and 679 s of training. The intensity profile eventually reaches the target frequency of 1.66 Hz.

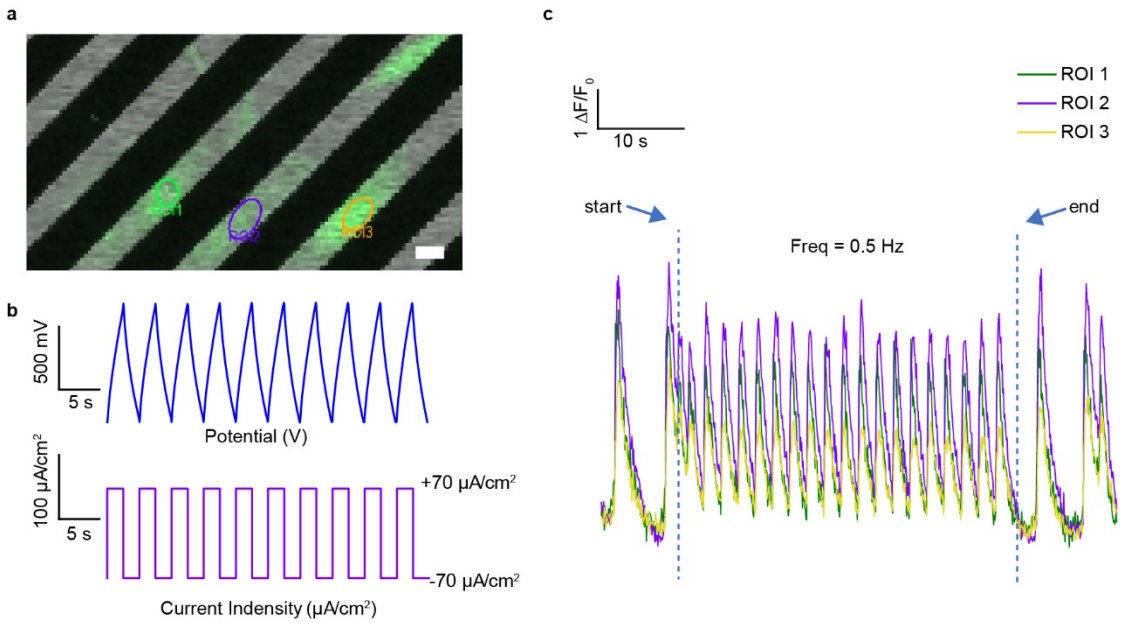

Figure 9.S21. (a) Representative images of the cells recorded during stimulation with ROI regions (green, purple and yellow). Scale bar, 10 μm. (b) Typical input signal of the devices during a stimulation process showing voltage (top) and current (bottom) applied to the cells. Input signaling frequency is 0.5 Hz (1/2.0 s), the stimulation time is ~40 s. (c) Intensity profiles of the marked ROIs, during the stimulation process for ~40 s; the intensity profile immediately follows the target frequency of 0.5 Hz.

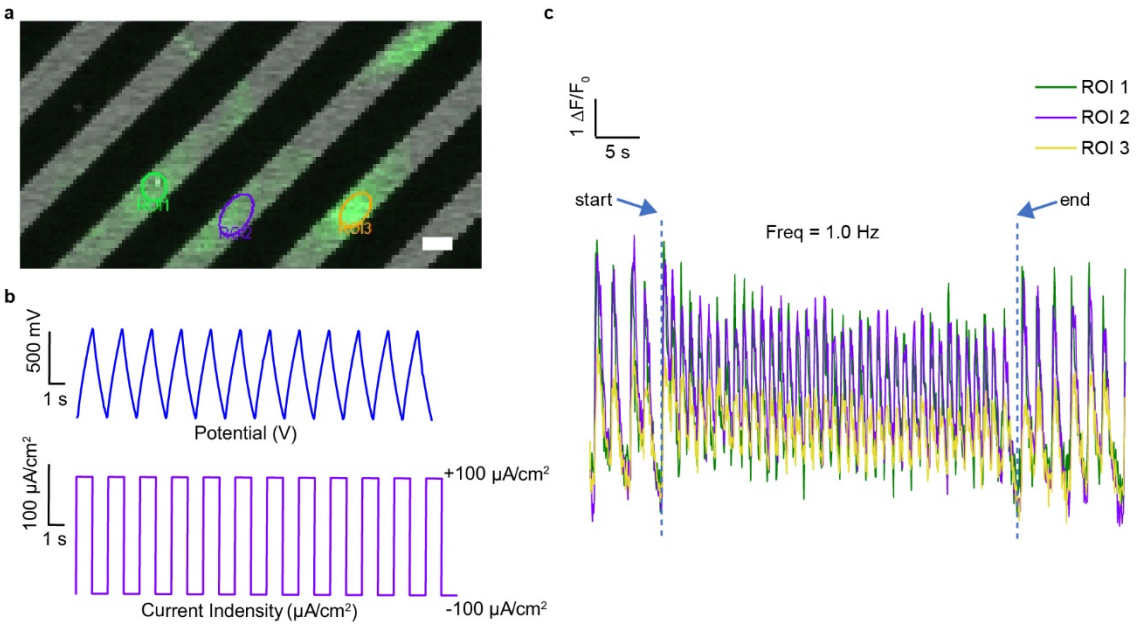

Figure 9.S22. (a) Representative images of the cells recorded during stimulation with ROI regions (green, purple and yellow). Scale bar, 10 µm. (b) Typical input signal of the devices during a stimulation process showing voltage (top) and current (bottom) applied to the cells. Input signaling frequency is 1.0 Hz (1/1.0 s), the stimulation time is ~40 s. (c) Intensity profiles of the marked ROIs, during the stimulation process for ~40 s; the intensity profile immediately follows the target frequency of 1.0 Hz.

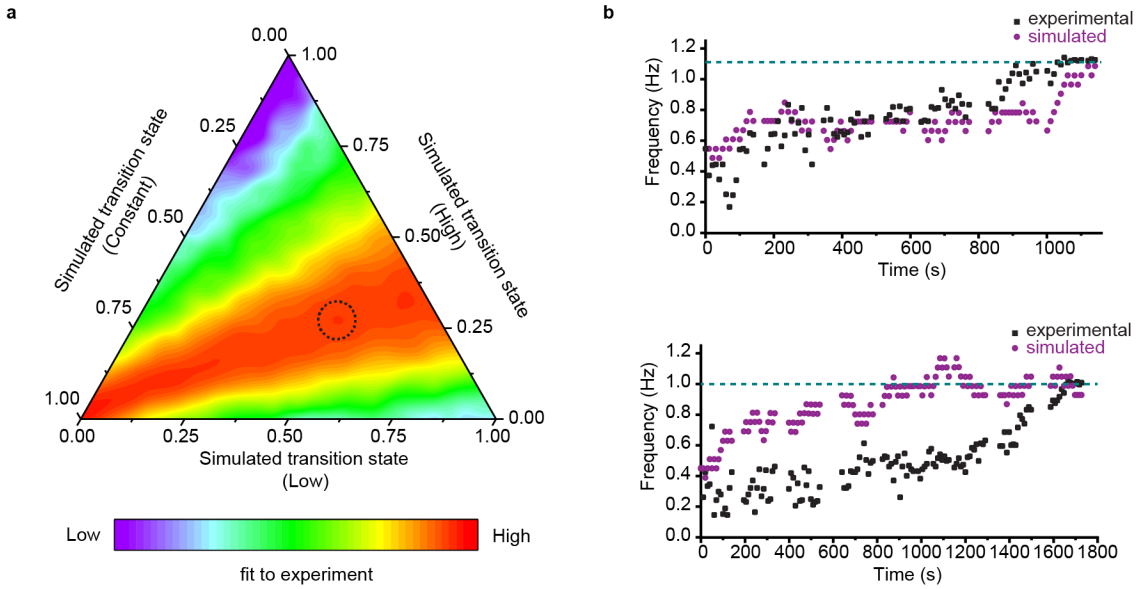

Figure 9.S23. (a) The heat map of a projection of the transition matrix space that maintains the proportions of final high and low states (b) Examples of simulated trials compared to observed data.

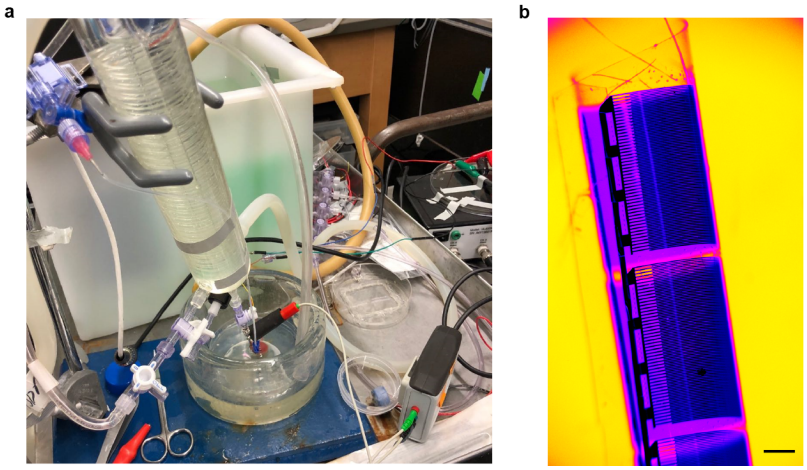

Figure 9.S24. (a) Optical images for the Langendorff perfusion system. (b) The device could be easily bent, demonstrating the excellent flexibility. Scale bar, 500 µm.

References

Acaron Ledesma, H., & Tian, B. (2017). Nanoscale silicon for subcellular biointerfaces. In *Journal of Materials Chemistry B*. https://doi.org/10.1039/c7tb00151g

Agarwal, A., Goss, J. A., Cho, A., McCain, M. L., & Parker, K. K. (2013). Microfluidic heart on a chip for higher throughput pharmacological studies. *Lab on a Chip*. https://doi.org/10.1039/c3lc50350j

Alkire, R. C., Kolb, D. M., Lipkowski, J., & Ross, P. N. (2011). Chemically Modified Electrodes. In *Chemically Modified Electrodes*. https://doi.org/10.1002/9783527627059

Allen, N. J., & Lyons, D. A. (2018). Glia as architects of central nervous system formation and function. In *Science*. https://doi.org/10.1126/science.aat0473

Alvarez-Erviti, L., Seow, Y., Yin, H., Betts, C., Lakhal, S., & Wood, M. J. A. (2011). Delivery of siRNA to the mouse brain by systemic injection of targeted exosomes. *Nature Biotechnology*. https://doi.org/10.1038/nbt.1807

Amunts, K., Ebell, C., Muller, J., Telefont, M., Knoll, A., & Lippert, T. (2016). The Human Brain Project: Creating a European Research Infrastructure to Decode the Human Brain. In *Neuron*. https://doi.org/10.1016/j.neuron.2016.10.046

Baumgartner, S., Halbach, M., Krausgrill, B., Maass, M., Srinivasan, S. P., Sahito, R. G. A., Peinkofer, G., Nguemo, F., Müller-Ehmsen, J., & Hescheler, J. (2015). Electrophysiological and morphological maturation of murine fetal cardiomyocytes during electrical stimulation in vitro. *Journal of Cardiovascular Pharmacology and Therapeutics*. https://doi.org/10.1177/1074248414536273

Beaulieu-Laroche, L., & Harnett, M. T. (2018). Dendritic Spines Prevent Synaptic Voltage Clamp. *Neuron*. https://doi.org/10.1016/j.neuron.2017.11.016

Benabid, A. L. (2003). Deep brain stimulation for Parkinson's disease. In *Current Opinion in Neurobiology*. https://doi.org/10.1016/j.conb.2003.11.001

Berggren, M., & Richter-Dahlfors, A. (2007). Organic bioelectronics. *Advanced Materials*. https://doi.org/10.1002/adma.200700419

Berná, J., Leigh, D. A., Lubomska, M., Mendoza, S. M., Pérez, E. M., Rudolf, P., Teobaldi, G., & Zerbetto, F. (2005). Macroscopic transport by synthetic molecular machines. *Nature Materials*. https://doi.org/10.1038/nmat1455

Bhatia, D., Arumugam, S., Nasilowski, M., Joshi, H., Wunder, C., Chambon, V., Prakash, V., Grazon, C., Nadal, B., Maiti, P. K., Johannes, L., Dubertret, B., & Krishnan, Y. (2016). Quantum dot-loaded monofunctionalized DNA icosahedra for single-particle tracking of endocytic pathways. *Nature Nanotechnology*. https://doi.org/10.1038/nnano.2016.150

Biran, R., Martin, D. C., & Tresco, P. A. (2005). Neuronal cell loss accompanies the brain tissue response to chronically implanted silicon microelectrode arrays. *Experimental Neurology*. https://doi.org/10.1016/j.expneurol.2005.04.020

Birey, F., Andersen, J., Makinson, C. D., Islam, S., Wei, W., Huber, N., Fan, H. C., Metzler, K.

R. C., Panagiotakos, G., Thom, N., O'Rourke, N. A., Steinmetz, L. M., Bernstein, J. A., Hallmayer, J., Huguenard, J. R., & Pasca, S. P. (2017). Assembly of functionally integrated human forebrain spheroids. *Nature*. https://doi.org/10.1038/nature22330

Bonakdar, M., Graybill, P. M., & Davalos, R. V. (2017). A microfluidic model of the blood-brain barrier to study permeabilization by pulsed electric fields. *RSC Advances*. https://doi.org/10.1039/c7ra07603g

Bonakdar, Mohammad, Wasson, E. M., Lee, Y. W., & Davalos, R. V. (2016). Electroporation of Brain Endothelial Cells on Chip toward Permeabilizing the Blood-Brain Barrier. *Biophysical Journal*. https://doi.org/10.1016/j.bpj.2015.11.3517

Bonnaud, C., Monnier, C. A., Demurtas, D., Jud, C., Vanhecke, D., Montet, X., Hovius, R., Lattuada, M., Rothen-Rutishauser, B., & Petri-Fink, A. (2014). Insertion of nanoparticle clusters into vesicle bilayers. *ACS Nano*. https://doi.org/10.1021/nn406349z

Boyden, E. S., Zhang, F., Bamberg, E., Nagel, G., & Deisseroth, K. (2005). Millisecond-timescale, genetically targeted optical control of neural activity. *Nature Neuroscience*. https://doi.org/10.1038/nn1525

Carvalho-de-Souza, J. L., Pinto, B. I., Pepperberg, D. R., & Bezanilla, F. (2018). Optocapacitive Generation of Action Potentials by Microsecond Laser Pulses of Nanojoule Energy. *Biophysical Journal*. https://doi.org/10.1016/j.bpj.2017.11.018

Carvalho-de-Souza, J. L., Treger, J. S., Dang, B., Kent, S. B. H., Pepperberg, D. R., & Bezanilla, F. (2015). Photosensitivity of neurons enabled by cell-targeted gold nanoparticles. *Neuron*. https://doi.org/10.1016/j.neuron.2015.02.033

Cell biology by the numbers. (2016). *Choice Reviews Online*. https://doi.org/10.5860/choice.196525

Chen, F., Tillberg, P. W., & Boyden, E. S. (2015). Optical imaging. Expansion microscopy. *Science (New York, N.Y.)*. https://doi.org/10.1126/science.1260088

Chen, N., Tian, L., Patil, A. C., Peng, S., Yang, I. H., Thakor, N. V., & Ramakrishna, S. (2017). Neural interfaces engineered via micro- and nanostructured coatings. In *Nano Today*. https://doi.org/10.1016/j.nantod.2017.04.007

Chen, R., Romero, G., Christiansen, M. G., Mohr, A., & Anikeeva, P. (2015). Wireless magnetothermal deep brain stimulation. *Science*. https://doi.org/10.1126/science.1261821

Chen, S., Weitemier, A. Z., Zeng, X., He, L., Wang, X., Tao, Y., Huang, A. J. Y., Hashimotodani, Y., Kano, M., Iwasaki, H., Parajuli, L. K., Okabe, S., Loong Teh, D. B., All, A. H., Tsutsui-Kimura, I., Tanaka, K. F., Liu, X., & McHugh, T. J. (2018). Near-infrared deep brain stimulation via upconversion nanoparticle–mediated optogenetics. *Science*. https://doi.org/10.1126/science.aaq1144

Chen, W., Yu, L., Misra, S., Fan, Z., Pareige, P., Patriarche, G., Bouchoule, S., & Cabarrocas, P. R. I. (2014). Incorporation and redistribution of impurities into silicon nanowires during metal-particle-assisted growth. *Nature Communications*. https://doi.org/10.1038/ncomms5134

Chen, Y., & Liu, L. (2012). Modern methods for delivery of drugs across the blood-brain barrier. In *Advanced Drug Delivery Reviews*. https://doi.org/10.1016/j.addr.2011.11.010

Choi, C., Choi, M. K., Liu, S., Kim, M. S., Park, O. K., Im, C., Kim, J., Qin, X., Lee, G. J., Cho, K. W., Kim, M., Joh, E., Lee, J., Son, D., Kwon, S. H., Jeon, N. L., Song, Y. M., Lu, N., & Kim, D. H. (2017). Human eye-inspired soft optoelectronic device using high-density MoS2-graphene curved image sensor array. *Nature Communications*. https://doi.org/10.1038/s41467-017-01824-6

Chung, C., Anderson, E., Pera, R. R., Pruitt, B. L., & Heilshorn, S. C. (2012). Hydrogel crosslinking density regulates temporal contractility of human embryonic stem cell-derived cardiomyocytes in 3D cultures. *Soft Matter*. https://doi.org/10.1039/c2sm26082d

Chung, K., & Deisseroth, K. (2013). CLARITY for mapping the nervous system. *Nature Methods*. https://doi.org/10.1038/nmeth.2481

Cohen-Karni, T., Casanova, D., Cahoon, J. F., Qing, Q., Bell, D. C., & Lieber, C. M. (2012). Synthetically encoded ultrashort-channel nanowire transistors for fast, pointlike cellular signal detection. *Nano Letters*. https://doi.org/10.1021/nl3011337

Colinge, J. P., Lee, C. W., Afzalian, A., Akhavan, N. D., Yan, R., Ferain, I., Razavi, P., O'Neill, B., Blake, A., White, M., Kelleher, A. M., McCarthy, B., & Murphy, R. (2010). Nanowire transistors without junctions. *Nature Nanotechnology*. https://doi.org/10.1038/nnano.2010.15

Copene, E. D., & Keener, J. P. (2008). Ephaptic coupling of cardiac cells through the junctional electric potential. *Journal of Mathematical Biology*. https://doi.org/10.1007/s00285-008-0157-3

Cui, Y., Duan, X., Hu, J., & Lieber, C. M. (2000). Doping and electrical transport in silicon nanowires. *Journal of Physical Chemistry B*. https://doi.org/10.1021/jp0009305

Dai, X., Hong, G., Gao, T., & Lieber, C. M. (2018). Mesh Nanoelectronics: Seamless Integration of Electronics with Tissues. *Accounts of Chemical Research*. https://doi.org/10.1021/acs.accounts.7b00547

De Mello, W. C. (1975). Effect of intracellular injection of calcium and strontium on cell communication in heart. *The Journal of Physiology*. https://doi.org/10.1113/jphysiol.1975.sp011051

Deemyad, T., Lüthi, J., & Spruston, N. (2018). Astrocytes integrate and drive action potential firing in inhibitory subnetworks. *Nature Communications*. https://doi.org/10.1038/s41467-018-06338-3

Den Hertog, M. I., Rouviere, J. L., Dhalluin, F., Desré, P. J., Gentile, P., Ferret, P., Oehler, F., & Baron, T. (2008). Control of gold surface diffusion on Si nanowires. *Nano Letters*. https://doi.org/10.1021/nl073356i

Denk, W., & Horstmann, H. (2004). Serial block-face scanning electron microscopy to reconstruct three-dimensional tissue nanostructure. *PLoS Biology*. https://doi.org/10.1371/journal.pbio.0020329

Dhande, O. S., Hua, E. W., Guh, E., Yeh, J., Bhatt, S., Zhang, Y., Ruthazer, E. S., Feller, M. B., & Crair, M. C. (2011). Development of single retinofugal axon arbors in normal and β2 knock-out mice. *Journal of Neuroscience*. https://doi.org/10.1523/JNEUROSCI.4899-10.2011

Dipalo, M., Amin, H., Lovato, L., Moia, F., Caprettini, V., Messina, G. C., Tantussi, F., Berdondini, L., & De Angelis, F. (2017). Intracellular and Extracellular Recording of Spontaneous Action Potentials in Mammalian Neurons and Cardiac Cells with 3D Plasmonic Nanoelectrodes. *Nano Letters*. https://doi.org/10.1021/acs.nanolett.7b01523

Dipalo, M., Melle, G., Lovato, L., Jacassi, A., Santoro, F., Caprettini, V., Schirato, A., Alabastri, A., Garoli, D., Bruno, G., Tantussi, F., & De Angelis, F. (2018). Plasmonic meta-electrodes allow intracellular recordings at network level on high-density CMOS-multi-electrode arrays. *Nature Nanotechnology*. https://doi.org/10.1038/s41565-018-0222-z

Duan, X., Gao, R., Xie, P., Cohen-Karni, T., Qing, Q., Choe, H. S., Tian, B., Jiang, X., & Lieber, C. M. (2012). Intracellular recordings of action potentials by an extracellular nanoscale field-effect transistor. *Nature Nanotechnology*. https://doi.org/10.1038/nnano.2011.223

Edelbrock, A. N., Àlvarez, Z., Simkin, D., Fyrner, T., Chin, S. M., Sato, K., Kiskinis, E., & Stupp, S. I. (2018). Supramolecular Nanostructure Activates TrkB Receptor Signaling of Neuronal Cells by Mimicking Brain-Derived Neurotrophic Factor. *Nano Letters*. https://doi.org/10.1021/acs.nanolett.8b02317

Efros, A. L., Delehanty, J. B., Huston, A. L., Medintz, I. L., Barbic, M., & Harris, T. D. (2018). Evaluating the potential of using quantum dots for monitoring electrical signals in neurons. In *Nature Nanotechnology*. https://doi.org/10.1038/s41565-018-0107-1

Eiraku, M., Takata, N., Ishibashi, H., Kawada, M., Sakakura, E., Okuda, S., Sekiguchi, K., Adachi, T., & Sasai, Y. (2011). Self-organizing optic-cup morphogenesis in three-dimensional culture. *Nature*. https://doi.org/10.1038/nature09941

Ellis, E. M., Gauvain, G., Sivyer, B., & Murphy, G. J. (2016). Shared and distinct retinal input to the mouse superior colliculus and dorsal lateral geniculate nucleus. *Journal of Neurophysiology*. https://doi.org/10.1152/jn.00227.2016

Elmore, S. (2007). Apoptosis: A Review of Programmed Cell Death. In *Toxicologic Pathology*. https://doi.org/10.1080/01926230701320337

Ema, M., Hougaard, K. S., Kishimoto, A., & Honda, K. (2016). Reproductive and developmental toxicity of carbon-based nanomaterials: A literature review. *Nanotoxicology*. https://doi.org/10.3109/17435390.2015.1073811

Eng, G., Lee, B. W., Protas, L., Gagliardi, M., Brown, K., Kass, R. S., Keller, G., Robinson, R. B., & Vunjak-Novakovic, G. (2016). Autonomous beating rate adaptation in human stem cell-derived cardiomyocytes. *Nature Communications*. https://doi.org/10.1038/ncomms10312

Famm, K., Litt, B., Tracey, K. J., Boyden, E. S., & Slaoui, M. (2013). Drug discovery: A jump-start for electroceuticals. In *Nature*. https://doi.org/10.1038/496159a

Fang, H., Yu, K. J., Gloschat, C., Yang, Z., Song, E., Chiang, C. H., Zhao, J., Won, S. M., Xu,

S., Trumpis, M., Zhong, Y., Han, S. W., Xue, Y., Xu, D., Choi, S. W., Cauwenberghs, G., Kay, M., Huang, Y., Viventi, J., … Rogers, J. A. (2017). Capacitively coupled arrays of multiplexed flexible silicon transistors for long-term cardiac electrophysiology. *Nature Biomedical Engineering*. https://doi.org/10.1038/s41551-017-0038

Fang, Y., Jiang, Y., Acaron Ledesma, H., Yi, J., Gao, X., Weiss, D. E., Shi, F., & Tian, B. (2018). Texturing Silicon Nanowires for Highly Localized Optical Modulation of Cellular Dynamics. *Nano Letters*. https://doi.org/10.1021/acs.nanolett.8b01626

Fang, Y., Jiang, Y., Cherukara, M. J., Shi, F., Koehler, K., Freyermuth, G., Isheim, D., Narayanan, B., Nicholls, A. W., Seidman, D. N., Sankaranarayanan, S. K. R. S., & Tian, B. (2017). Alloy-assisted deposition of three-dimensional arrays of atomic gold catalyst for crystal growth studies. *Nature Communications*. https://doi.org/10.1038/s41467-017-02025-x

Fields, R. D. (2015). A new mechanism of nervous system plasticity: Activity-dependent myelination. In *Nature Reviews Neuroscience*. https://doi.org/10.1038/nrn4023

Fu, T. M., Duan, X., Jiang, Z., Dai, X., Xie, P., Cheng, Z., & Lieber, C. M. (2014). Sub-10-nm intracellular bioelectronic probes from nanowire-nanotube heterostructures. *Proceedings of the National Academy of Sciences of the United States of America*. https://doi.org/10.1073/pnas.1323389111

Fu, T. M., Hong, G., Viveros, R. D., Zhou, T., & Lieber, C. M. (2017). Highly scalable multichannel mesh electronics for stable chronic brain electrophysiology. *Proceedings of the National Academy of Sciences of the United States of America*. https://doi.org/10.1073/pnas.1717695114

Gao, R., Asano, S. M., Upadhyayula, S., Pisarev, I., Milkie, D. E., Liu, T. L., Singh, V., Graves, A., Huynh, G. H., Zhao, Y., Bogovic, J., Colonell, J., Ott, C. M., Zugates, C., Tappan, S., Rodriguez, A., Mosaliganti, K. R., Sheu, S. H., Pasolli, H. A., … Betzig, E. (2019). Cortical column and whole-brain imaging with molecular contrast and nanoscale resolution. *Science*. https://doi.org/10.1126/science.aau8302

Gao, R., Strehle, S., Tian, B., Cohen-Karni, T., Xie, P., Duan, X., Qing, Q., & Lieber, C. M. (2012). Outside looking in: Nanotube transistor intracellular sensors. *Nano Letters*. https://doi.org/10.1021/nl301623p

García-López, V., Chen, F., Nilewski, L. G., Duret, G., Aliyan, A., Kolomeisky, A. B., Robinson, J. T., Wang, G., Pal, R., & Tour, J. M. (2017). Molecular machines open cell membranes. *Nature*. https://doi.org/10.1038/nature23657

Gautam, V., Naureen, S., Shahid, N., Gao, Q., Wang, Y., Nisbet, D., Jagadish, C., & Daria, V. R. (2017). Engineering Highly Interconnected Neuronal Networks on Nanowire Scaffolds. *Nano Letters*. https://doi.org/10.1021/acs.nanolett.6b05288

Goel, A., & Vogel, V. (2008). Harnessing biological motors to engineer systems for nanoscale transport and assembly. In *Nature Nanotechnology*. https://doi.org/10.1038/nnano.2008.190

Gonzales, D. L., Badhiwala, K. N., Vercosa, D. G., Avants, B. W., Liu, Z., Zhong, W., & Robinson, J. T. (2017). Scalable electrophysiology in intact small animals with nanoscale

suspended electrode arrays. *Nature Nanotechnology*. https://doi.org/10.1038/nnano.2017.55

Gradinaru, V., Zhang, F., Ramakrishnan, C., Mattis, J., Prakash, R., Diester, I., Goshen, I., Thompson, K. R., & Deisseroth, K. (2010). Molecular and Cellular Approaches for Diversifying and Extending Optogenetics. *Cell*. https://doi.org/10.1016/j.cell.2010.02.037

Gu, Y., Sun, W., Wang, G., Jeftinija, K., Jeftinija, S., & Fang, N. (2012). Rotational dynamics of cargos at pauses during axonal transport. *Nature Communications*. https://doi.org/10.1038/ncomms2037

Gudiksen, M. S., Lauhon, L. J., Wang, J., Smith, D. C., & Lieber, C. M. (2002). Growth of nanowire superlattice structures for nanoscale photonics and electronics. *Nature*. https://doi.org/10.1038/415617a

Hai, A., Shappir, J., & Spira, M. E. (2010). In-cell recordings by extracellular microelectrodes. *Nature Methods*. https://doi.org/10.1038/nmeth.1420

Hai, A., & Spira, M. E. (2012). On-chip electroporation, membrane repair dynamics and transient in-cell recordings by arrays of gold mushroom-shaped microelectrodes. *Lab on a Chip*. https://doi.org/10.1039/c2lc40091j

Hallett, M. (2000). Transcranial magnetic stimulation and the human brain. In *Nature*. https://doi.org/10.1038/35018000

Hamill, O. P., Marty, A., Neher, E., Sakmann, B., & Sigworth, F. J. (1981). Improved patch-clamp techniques for high-resolution current recording from cells and cell-free membrane patches. *Pflügers Archiv European Journal of Physiology*. https://doi.org/10.1007/BF00656997

Haziza, S., Mohan, N., Loe-Mie, Y., Lepagnol-Bestel, A. M., Massou, S., Adam, M. P., Le, X. L., Viard, J., Plancon, C., Daudin, R., Koebel, P., Dorard, E., Rose, C., Hsieh, F. J., Wu, C. C., Potier, B., Herault, Y., Sala, C., Corvin, A., … Simonneau, M. (2017). Fluorescent nanodiamond tracking reveals intraneuronal transport abnormalities induced by brain-disease-related genetic risk factors. *Nature Nanotechnology*. https://doi.org/10.1038/nnano.2016.260

He, Y., Fan, C., & Lee, S. T. (2010). Silicon nanostructures for bioapplications. In *Nano Today*. https://doi.org/10.1016/j.nantod.2010.06.008

Herisson, F., Frodermann, V., Courties, G., Rohde, D., Sun, Y., Vandoorne, K., Wojtkiewicz, G. R., Masson, G. S., Vinegoni, C., Kim, J., Kim, D. E., Weissleder, R., Swirski, F. K., Moskowitz, M. A., & Nahrendorf, M. (2018). Direct vascular channels connect skull bone marrow and the brain surface enabling myeloid cell migration. *Nature Neuroscience*. https://doi.org/10.1038/s41593-018-0213-2

Hong, G., Fu, T. M., Qiao, M., Viveros, R. D., Yang, X., Zhou, T., Lee, J. M., Park, H. G., Sanes, J. R., & Lieber, C. M. (2018). A method for single-neuron chronic recording from the retina in awake mice. *Science*. https://doi.org/10.1126/science.aas9160

Hoon, M., Okawa, H., Della Santina, L., & Wong, R. O. L. (2014). Functional architecture of the retina: Development and disease. In *Progress in Retinal and Eye Research*. https://doi.org/10.1016/j.preteyeres.2014.06.003

Huang, B., Wang, W., Bates, M., & Zhuang, X. (2008). Three-dimensional super-resolution imaging by stochastic optical reconstruction microscopy. *Science*. https://doi.org/10.1126/science.1153529

Huang, H., Delikanli, S., Zeng, H., Ferkey, D. M., & Pralle, A. (2010). Remote control of ion channels and neurons through magnetic-field heating of nanoparticles. *Nature Nanotechnology*. https://doi.org/10.1038/nnano.2010.125

Huang, Y. W., Chang, S. J., I-Chen Harn, H., Huang, H. T., Lin, H. H., Shen, M. R., Tang, M. J., & Chiu, W. T. (2015). Mechanosensitive store-operated calcium entry regulates the formation of cell polarity. *Journal of Cellular Physiology*. https://doi.org/10.1002/jcp.24936

Huberman, A. D., Murray, K. D., Warland, D. K., Feldheim, D. A., & Chapman, B. (2005). Ephrin-As mediate targeting of eye-specific projections to the lateral geniculate nucleus. *Nature Neuroscience*. https://doi.org/10.1038/nn1505

Hund, T. J., & Rudy, Y. (2000). Determinants of excitability in cardiac myocytes: Mechanistic investigation of memory effect. *Biophysical Journal*. https://doi.org/10.1016/S0006-3495(00)76544-1

Insel, T. R., Landis, S. C., & Collins, F. S. (2013). Research priorities. The NIH BRAIN Initiative. *Science (New York, N.Y.)*. https://doi.org/10.1126/science.1239276

Jacquemet, G., Baghirov, H., Georgiadou, M., Sihto, H., Peuhu, E., Cettour-Janet, P., He, T., Perälä, M., Kronqvist, P., Joensuu, H., & Ivaska, J. (2016). L-type calcium channels regulate filopodia stability and cancer cell invasion downstream of integrin signalling. *Nature Communications*. https://doi.org/10.1038/ncomms13297

Jayant, K., Hirtz, J. J., Plante, I. J. La, Tsai, D. M., De Boer, W. D. A. M., Semonche, A., Peterka, D. S., Owen, J. S., Sahin, O., Shepard, K. L., & Yuste, R. (2017). Targeted intracellular voltage recordings from dendritic spines using quantum-dot-coated nanopipettes. *Nature Nanotechnology*. https://doi.org/10.1038/nnano.2016.268

Jenkins, M. W., Wang, Y. T., Doughman, Y. Q., Watanabe, M., Cheng, Y., & Rollins, A. M. (2013). Optical pacing of the adult rabbit heart. *Biomedical Optics Express*. https://doi.org/10.1364/boe.4.001626

Jiang, Y., Carvalho-De-Souza, J. L., Wong, R. C. S., Luo, Z., Isheim, D., Zuo, X., Nicholls, A. W., Jung, I. W., Yue, J., Liu, D. J., Wang, Y., De Andrade, V., Xiao, X., Navrazhnykh, L., Weiss, D. E., Wu, X., Seidman, D. N., Bezanilla, F., & Tian, B. (2016). Heterogeneous silicon mesostructures for lipid-supported bioelectric interfaces. *Nature Materials*. https://doi.org/10.1038/nmat4673

Jiang, Y., Li, X., Liu, B., Yi, J., Fang, Y., Shi, F., Gao, X., Sudzilovsky, E., Parameswaran, R., Koehler, K., Nair, V., Yue, J., Guo, K. H., Fang, Y., Tsai, H. M., Freyermuth, G., Wong, R. C. S., Kao, C. M., Chen, C. T., … Tian, B. (2018). Rational design of silicon structures for optically controlled multiscale biointerfaces. *Nature Biomedical Engineering*. https://doi.org/10.1038/s41551-018-0230-1

Jiang, Y., & Tian, B. (2018). Inorganic semiconductor biointerfaces. In *Nature Reviews Materials*. https://doi.org/10.1038/s41578-018-0062-3

Johannsmeier, S., Heeger, P., Terakawa, M., Kalies, S., Heisterkamp, A., Ripken, T., & Heinemann, D. (2018). Gold nanoparticle-mediated laser stimulation induces a complex stress response in neuronal cells. *Scientific Reports*. https://doi.org/10.1038/s41598-018-24908-9

Kandel, E. R., Schwartz, J. H., & Jessell, T. M. (2000). Principles of Neural Science, fourth addition. In *McGraw-Hill Companies*. https://doi.org/10.1036/0838577016

Kang, S. K., Murphy, R. K. J., Hwang, S. W., Lee, S. M., Harburg, D. V., Krueger, N. A., Shin, J., Gamble, P., Cheng, H., Yu, S., Liu, Z., McCall, J. G., Stephen, M., Ying, H., Kim, J., Park, G., Webb, R. C., Lee, C. H., Chung, S., … Rogers, J. A. (2016). Bioresorbable silicon electronic sensors for the brain. *Nature*. https://doi.org/10.1038/nature16492

Kaplan, L., Ierokomos, A., Chowdary, P., Bryant, Z., & Cui, B. (2018). Rotation of endosomes demonstrates coordination of molecular motors during axonal transport. *Science Advances*. https://doi.org/10.1126/sciadv.1602170

Kato-Negishi, M., Morimoto, Y., Onoe, H., & Takeuchi, S. (2013). Millimeter-Sized Neural Building Blocks for 3D Heterogeneous Neural Network Assembly. *Advanced Healthcare Materials*. https://doi.org/10.1002/adhm.201300052

Kim, S., Hill, D. J., Pinion, C. W., Christesen, J. D., McBride, J. R., & Cahoon, J. F. (2017). Designing Morphology in Epitaxial Silicon Nanowires: The Role of Gold, Surface Chemistry, and Phosphorus Doping. *ACS Nano*. https://doi.org/10.1021/acsnano.7b00457

Koo, J., MacEwan, M. R., Kang, S. K., Won, S. M., Stephen, M., Gamble, P., Xie, Z., Yan, Y., Chen, Y. Y., Shin, J., Birenbaum, N., Chung, S., Kim, S. B., Khalifeh, J., Harburg, D. V., Bean, K., Paskett, M., Kim, J., Zohny, Z. S., … Rogers, J. A. (2018). Wireless bioresorbable electronic system enables sustained nonpharmacological neuroregenerative therapy. *Nature Medicine*. https://doi.org/10.1038/s41591-018-0196-2

Kreuter, J. (2014). Drug delivery to the central nervous system by polymeric nanoparticles: What do we know? In *Advanced Drug Delivery Reviews*. https://doi.org/10.1016/j.addr.2013.08.008

Kubanek, J., Shukla, P., Das, A., Baccus, S. A., & Goodman, M. B. (2018). Ultrasound elicits behavioral responses through mechanical effects on neurons and ion channels in a simple nervous system. *Journal of Neuroscience*. https://doi.org/10.1523/JNEUROSCI.1458-17.2018

Kuzum, D., Takano, H., Shim, E., Reed, J. C., Juul, H., Richardson, A. G., De Vries, J., Bink, H., Dichter, M. A., Lucas, T. H., Coulter, D. A., Cubukcu, E., & Litt, B. (2014). Transparent and flexible low noise graphene electrodes for simultaneous electrophysiology and neuroimaging. *Nature Communications*. https://doi.org/10.1038/ncomms6259

Lacour, S. P., Courtine, G., & Guck, J. (2016). Materials and technologies for soft implantable neuroprostheses. In *Nature Reviews Materials*. https://doi.org/10.1038/natrevmats.2016.63

Lancaster, M. A., Corsini, N. S., Wolfinger, S., Gustafson, E. H., Phillips, A. W., Burkard, T. R., Otani, T., Livesey, F. J., & Knoblich, J. A. (2017). Guided self-organization and cortical plate formation in human brain organoids. *Nature Biotechnology*.

https://doi.org/10.1038/nbt.3906

Lauhon, L. J., Gudlksen, M. S., Wang, D., & Lieber, C. M. (2002). Epitaxial core-shell and core-multishell nanowire heterostructures. *Nature*. https://doi.org/10.1038/nature01141

Lee, G., Kim, D., Yun, J., Ko, Y., Cho, J., & Ha, J. S. (2014). High-performance all-solid-state flexible micro-supercapacitor arrays with layer-by-layer assembled MWNT/MnOx nanocomposite electrodes. *Nanoscale*. https://doi.org/10.1039/c4nr02035a

Lee, J. H., Zhang, A., You, S. S., & Lieber, C. M. (2016). Spontaneous Internalization of Cell Penetrating Peptide-Modified Nanowires into Primary Neurons. *Nano Letters*. https://doi.org/10.1021/acs.nanolett.6b00020

Lee, Seonok, Christin Chong, S. Y., Tuck, S. J., Corey, J. M., & Chan, J. R. (2013). A rapid and reproducible assay for modeling myelination by oligodendrocytes using engineered nanofibers. *Nature Protocols*. https://doi.org/10.1038/nprot.2013.039

Lee, Seonok, Leach, M. K., Redmond, S. A., Chong, S. Y. C., Mellon, S. H., Tuck, S. J., Feng, Z. Q., Corey, J. M., & Chan, J. R. (2012). A culture system to study oligodendrocyte myelination processes using engineered nanofibers. *Nature Methods*. https://doi.org/10.1038/nmeth.2105

Lee, Sunghoon, Sasaki, D., Kim, D., Mori, M., Yokota, T., Lee, H., Park, S., Fukuda, K., Sekino, M., Matsuura, K., Shimizu, T., & Someya, T. (2019). Ultrasoft electronics to monitor dynamically pulsing cardiomyocytes. *Nature Nanotechnology*. https://doi.org/10.1038/s41565-018-0331-8

Leung, K. H., Chakraborty, K., Saminathan, A., & Krishnan, Y. (2019). A DNA nanomachine chemically resolves lysosomes in live cells. *Nature Nanotechnology*. https://doi.org/10.1038/s41565-018-0318-5

Leybaert, L., & Sanderson, M. J. (2012). Intercellular Ca2+ waves: Mechanisms and function. In *Physiological Reviews*. https://doi.org/10.1152/physrev.00029.2011

Li, X., & Bhushan, B. (2002). A review of nanoindentation continuous stiffness measurement technique and its applications. *Materials Characterization*. https://doi.org/10.1016/S1044-5803(02)00192-4

Lin, Z. C., Xie, C., Osakada, Y., Cui, Y., & Cui, B. (2014). Iridium oxide nanotube electrodes for sensitive and prolonged intracellular measurement of action potentials. *Nature Communications*. https://doi.org/10.1038/ncomms4206

Liu, G., Qi, M., Hutchinson, M. R., Yang, G., & Goldys, E. M. (2016). Recent advances in cytokine detection by immunosensing. In *Biosensors and Bioelectronics*. https://doi.org/10.1016/j.bios.2016.01.020

Liu, J., Fu, T. M., Cheng, Z., Hong, G., Zhou, T., Jin, L., Duvvuri, M., Jiang, Z., Kruskal, P., Xie, C., Suo, Z., Fang, Y., & Lieber, C. M. (2015). Syringe-injectable electronics. *Nature Nanotechnology*. https://doi.org/10.1038/nnano.2015.115

Liu, R., Mahurin, S. M., Li, C., Unocic, R. R., Idrobo, J. C., Gao, H., Pennycook, S. J., & Dai, S. (2011). Dopamine as a carbon source: The controlled synthesis of hollow carbon spheres

and yolk-structured carbon nanocomposites. *Angewandte Chemie - International Edition*. https://doi.org/10.1002/anie.201102070

Lu, G. J., Farhadi, A., Szablowski, J. O., Lee-Gosselin, A., Barnes, S. R., Lakshmanan, A., Bourdeau, R. W., & Shapiro, M. G. (2018). Acoustically modulated magnetic resonance imaging of gas-filled protein nanostructures. *Nature Materials*. https://doi.org/10.1038/s41563-018-0023-7

Luan, L., Wei, X., Zhao, Z., Siegel, J. J., Potnis, O., Tuppen, C. A., Lin, S., Kazmi, S., Fowler, R. A., Holloway, S., Dunn, A. K., Chitwood, R. A., & Xie, C. (2017). Ultraflexible nanoelectronic probes form reliable, glial scar–free neural integration. *Science Advances*. https://doi.org/10.1126/sciadv.1601966

Luo, Z., Jiang, Y., Myers, B. D., Isheim, D., Wu, J., Zimmerman, J. F., Wang, Z., Li, Q., Wang, Y., Chen, X., Dravid, V. P., Seidman, D. N., & Tian, B. (2015). Atomic gold-enabled three-dimensional lithography for silicon mesostructures. *Science*. https://doi.org/10.1126/science.1257278

Lyu, S. P., & Untereker, D. (2009). Degradability of polymers for implantable biomedical devices. In *International Journal of Molecular Sciences*. https://doi.org/10.3390/ijms10094033

Ma, Y., Bao, J., Zhang, Y., Li, Z., Zhou, X., Wan, C., Huang, L., Zhao, Y., Han, G., & Xue, T. (2019). Mammalian Near-Infrared Image Vision through Injectable and Self-Powered Retinal Nanoantennae. *Cell*. https://doi.org/10.1016/j.cell.2019.01.038

Mammadov, B., Mammadov, R., Guler, M. O., & Tekinay, A. B. (2012). Cooperative effect of heparan sulfate and laminin mimetic peptide nanofibers on the promotion of neurite outgrowth. *Acta Biomaterialia*. https://doi.org/10.1016/j.actbio.2012.02.006

Marshall, J. D., & Schnitzer, M. J. (2013). Optical strategies for sensing neuronal voltage using quantum dots and other semiconductor nanocrystals. *ACS Nano*. https://doi.org/10.1021/nn401410k

Martersteck, E. M., Hirokawa, K. E., Evarts, M., Bernard, A., Duan, X., Li, Y., Ng, L., Oh, S. W., Ouellette, B., Royall, J. J., Stoecklin, M., Wang, Q., Zeng, H., Sanes, J. R., & Harris, J. A. (2017). Diverse Central Projection Patterns of Retinal Ganglion Cells. *Cell Reports*. https://doi.org/10.1016/j.celrep.2017.01.075

Meng, Y., Gu, D., Zhang, F., Shi, Y., Yang, H., Li, Z., Yu, C., Tu, B., & Zhao, D. (2005). Ordered mesoporous polymers and homologous carbon frameworks: Amphiphilic surfactant templating and direct transformation. *Angewandte Chemie - International Edition*. https://doi.org/10.1002/anie.200501561

Millecamps, S., & Julien, J. P. (2013). Axonal transport deficits and neurodegenerative diseases. In *Nature Reviews Neuroscience*. https://doi.org/10.1038/nrn3380

Millet, L. J., & Gillette, M. U. (2012). Over a century of neuron culture: From the hanging drop to microfluidic devices. *Yale Journal of Biology and Medicine*.

Mirza, M. M., Schupp, F. J., Mol, J. A., MacLaren, D. A., Briggs, G. A. D., & Paul, D. J. (2017). One dimensional transport in silicon nanowire junction-less field effect transistors.

Scientific Reports. https://doi.org/10.1038/s41598-017-03138-5

Miyamoto, A., Lee, S., Cooray, N. F., Lee, S., Mori, M., Matsuhisa, N., Jin, H., Yoda, L., Yokota, T., Itoh, A., Sekino, M., Kawasaki, H., Ebihara, T., Amagai, M., & Someya, T. (2017). Inflammation-free, gas-permeable, lightweight, stretchable on-skin electronics with nanomeshes. *Nature Nanotechnology*. https://doi.org/10.1038/nnano.2017.125

Moon, J. M., Thapliyal, N., Hussain, K. K., Goyal, R. N., & Shim, Y. B. (2018). Conducting polymer-based electrochemical biosensors for neurotransmitters: A review. In *Biosensors and Bioelectronics*. https://doi.org/10.1016/j.bios.2017.11.069

Munshi, R., Qadri, S. M., Zhang, Q., Rubio, I. C., del Pino, P., & Pralle, A. (2017). Magnetothermal genetic deep brain stimulation of motor behaviors in awake, freely moving mice. *ELife*. https://doi.org/10.7554/eLife.27069

Narayanaswamy, N., Chakraborty, K., Saminathan, A., Zeichner, E., Leung, K. H., Devany, J., & Krishnan, Y. (2019). A pH-correctable, DNA-based fluorescent reporter for organellar calcium. *Nature Methods*. https://doi.org/10.1038/s41592-018-0232-7

Nave, K. A. (2010). Myelination and support of axonal integrity by glia. In *Nature*. https://doi.org/10.1038/nature09614

Oliver, W. C., & Pharr, G. M. (2004). Measurement of hardness and elastic modulus by instrumented indentation: Advances in understanding and refinements to methodology. *Journal of Materials Research*. https://doi.org/10.1557/jmr.2004.19.1.3

Overington, J. P., Al-Lazikani, B., & Hopkins, A. L. (2006). How many drug targets are there? *Nature Reviews Drug Discovery*. https://doi.org/10.1038/nrd2199

Parameswaran, R., Carvalho-De-Souza, J. L., Jiang, Y., Burke, M. J., Zimmerman, J. F., Koehler, K., Phillips, A. W., Yi, J., Adams, E. J., Bezanilla, F., & Tian, B. (2018). Photoelectrochemical modulation of neuronal activity with free-standing coaxial silicon nanowires. *Nature Nanotechnology*. https://doi.org/10.1038/s41565-017-0041-7

Parameswaran, R., Koehler, K., Rotenberg, M. Y., Burke, M. J., Kim, J., Jeong, K. Y., Hissa, B., Paul, M. D., Moreno, K., Sarma, N., Hayes, T., Sudzilovsky, E., Park, H. G., & Tian, B. (2019). Optical stimulation of cardiac cells with a polymer-supported silicon nanowire matrix. *Proceedings of the National Academy of Sciences of the United States of America*. https://doi.org/10.1073/pnas.1816428115

Park, D. W., Schendel, A. A., Mikael, S., Brodnick, S. K., Richner, T. J., Ness, J. P., Hayat, M. R., Atry, F., Frye, S. T., Pashaie, R., Thongpang, S., Ma, Z., & Williams, J. C. (2014). Graphene-based carbon-layered electrode array technology for neural imaging and optogenetic applications. *Nature Communications*. https://doi.org/10.1038/ncomms6258

Park, J., Koito, H., Li, J., & Han, A. (2009). Microfluidic compartmentalized co-culture platform for CNS axon myelination research. *Biomedical Microdevices*. https://doi.org/10.1007/s10544-009-9331-7

Pasca, A. M., Sloan, S. A., Clarke, L. E., Tian, Y., Makinson, C. D., Huber, N., Kim, C. H., Park, J. Y., O'Rourke, N. A., Nguyen, K. D., Smith, S. J., Huguenard, J. R., Geschwind, D. H., Barres, B. A., & Pasca, S. P. (2015). Functional cortical neurons and astrocytes from human

pluripotent stem cells in 3D culture. *Nature Methods*. https://doi.org/10.1038/nmeth.3415

Patolsky, F., Timko, B. P., Yu, G., Fang, Y., Greytak, A. B., Zheng, G., & Lieber, C. M. (2006). Detection, stimulation, and inhibition of neuronal signals with high-density nanowire transistor arrays. *Science*. https://doi.org/10.1126/science.1128640

Pech, D., Brunet, M., Durou, H., Huang, P., Mochalin, V., Gogotsi, Y., Taberna, P. L., & Simon, P. (2010). Ultrahigh-power micrometre-sized supercapacitors based on onion-like carbon. *Nature Nanotechnology*. https://doi.org/10.1038/nnano.2010.162

Peterka, D. S., Takahashi, H., & Yuste, R. (2011). Imaging Voltage in Neurons. In *Neuron*. https://doi.org/10.1016/j.neuron.2010.12.010

Phillips, M. J., & Voeltz, G. K. (2016). Structure and function of ER membrane contact sites with other organelles. In *Nature Reviews Molecular Cell Biology*. https://doi.org/10.1038/nrm.2015.8

Phillips, R., & Quake, S. R. (2006). The biological frontier of physics. *Physics Today*. https://doi.org/10.1063/1.2216960

Pietroiusti, A., Massimiani, M., Fenoglio, I., Colonna, M., Valentini, F., Palleschi, G., Camaioni, A., Magrini, A., Siracusa, G., Bergamaschi, A., Sgambato, A., & Campagnolo, L. (2011). Low doses of pristine and oxidized single-wall carbon nanotubes affect mammalian embryonic development. *ACS Nano*. https://doi.org/10.1021/nn200372g

Pliss, A., Ohulchanskyy, T. Y., Chen, G., Damasco, J., Bass, C. E., & Prasad, P. N. (2017). Subcellular Optogenetics Enacted by Targeted Nanotransformers of Near-Infrared Light. *ACS Photonics*. https://doi.org/10.1021/acsphotonics.6b00475

Poo, M. ming, Du, J. lin, Ip, N. Y., Xiong, Z. Q., Xu, B., & Tan, T. (2016). China Brain Project: Basic Neuroscience, Brain Diseases, and Brain-Inspired Computing. In *Neuron*. https://doi.org/10.1016/j.neuron.2016.10.050

Prakash, V., Saha, S., Chakraborty, K., & Krishnan, Y. (2016). Rational design of a quantitative, pH-insensitive, nucleic acid based fluorescent chloride reporter. *Chemical Science*. https://doi.org/10.1039/c5sc04002g

Quadrato, G., Nguyen, T., Macosko, E. Z., Sherwood, J. L., Yang, S. M., Berger, D. R., Maria, N., Scholvin, J., Goldman, M., Kinney, J. P., Boyden, E. S., Lichtman, J. W., Williams, Z. M., McCarroll, S. A., & Arlotta, P. (2017). Cell diversity and network dynamics in photosensitive human brain organoids. *Nature*. https://doi.org/10.1038/nature22047

Ranade, S. S., Syeda, R., & Patapoutian, A. (2015). Mechanically Activated Ion Channels. In *Neuron*. https://doi.org/10.1016/j.neuron.2015.08.032

Rastogi, S. K., Kalmykov, A., Johnson, N., & Cohen-Karni, T. (2018). Bioelectronics with nanocarbons. In *Journal of Materials Chemistry B*. https://doi.org/10.1039/C8TB01600C

Ratner, B. D., Hoffman, A. S., Schoen, F. J., & Lemons, J. E. (2004). Biomaterials science: an introduction to materials in medicine. In *Chemical Engineering*.

Rittinghausen, S., Hackbarth, A., Creutzenberg, O., Ernst, H., Heinrich, U., Leonhardt, A., &

Schaudien, D. (2014). The carcinogenic effect of various multi-walled carbon nanotubes (MWCNTs) after intraperitoneal injection in rats. *Particle and Fibre Toxicology*. https://doi.org/10.1186/s12989-014-0059-z

Robinson, J. T., Jorgolli, M., Shalek, A. K., Yoon, M. H., Gertner, R. S., & Park, H. (2012). Vertical nanowire electrode arrays as a scalable platform for intracellular interfacing to neuronal circuits. *Nature Nanotechnology*. https://doi.org/10.1038/nnano.2011.249

Roet, M., Hescham, S. A., Jahanshahi, A., Rutten, B. P. F., Anikeeva, P. O., & Temel, Y. (2019). Progress in neuromodulation of the brain: A role for magnetic nanoparticles? In *Progress in Neurobiology*. https://doi.org/10.1016/j.pneurobio.2019.03.002

Ross, F. M., Tersoff, J., & Reuter, M. C. (2005). Sawtooth faceting in silicon nanowires. *Physical Review Letters*. https://doi.org/10.1103/PhysRevLett.95.146104

Saha, S., Prakash, V., Halder, S., Chakraborty, K., & Krishnan, Y. (2015). A pH-independent DNA nanodevice for quantifying chloride transport in organelles of living cells. *Nature Nanotechnology*. https://doi.org/10.1038/nnano.2015.130

Salatino, J. W., Ludwig, K. A., Kozai, T. D. Y., & Purcell, E. K. (2017). Glial responses to implanted electrodes in the brain. *Nature Biomedical Engineering*. https://doi.org/10.1038/s41551-017-0154-1

Seabrook, T. A., Burbridge, T. J., Crair, M. C., & Huberman, A. D. (2017). Architecture, Function, and Assembly of the Mouse Visual System. *Annual Review of Neuroscience*. https://doi.org/10.1146/annurev-neuro-071714-033842

Selberg, J., Gomez, M., & Rolandi, M. (2018). The Potential for Convergence between Synthetic Biology and Bioelectronics. In *Cell Systems*. https://doi.org/10.1016/j.cels.2018.08.007

Seo, D., Neely, R. M., Shen, K., Singhal, U., Alon, E., Rabaey, J. M., Carmena, J. M., & Maharbiz, M. M. (2016). Wireless Recording in the Peripheral Nervous System with Ultrasonic Neural Dust. *Neuron*. https://doi.org/10.1016/j.neuron.2016.06.034

Shapiro, M. G., Goodwill, P. W., Neogy, A., Yin, M., Foster, F. S., Schaffer, D. V., & Conolly, S. M. (2014). Biogenic gas nanostructures as ultrasonic molecular reporters. *Nature Nanotechnology*. https://doi.org/10.1038/nnano.2014.32

Sherman, D. L., & Brophy, P. J. (2005). Mechanisms of axon ensheathment and myelin growth. In *Nature Reviews Neuroscience*. https://doi.org/10.1038/nrn1743

Shi, M., Du, F., Liu, Y., Li, L., Cai, J., Zhang, G. F., Xu, X. F., Lin, T., Cheng, H. R., Liu, X. D., Xiong, L. Z., & Zhao, G. (2013). Glial cell-expressed mechanosensitive channel TRPV4 mediates infrasound-induced neuronal impairment. *Acta Neuropathologica*. https://doi.org/10.1007/s00401-013-1166-x

Shi, Z., Graber, Z. T., Baumgart, T., Stone, H. A., & Cohen, A. E. (2018). Cell Membranes Resist Flow. *Cell*. https://doi.org/10.1016/j.cell.2018.09.054

Simms, B. A., & Zamponi, G. W. (2014). Neuronal voltage-gated calcium channels: Structure, function, and dysfunction. In *Neuron*. https://doi.org/10.1016/j.neuron.2014.03.016

Sloan, S. A., Andersen, J., Paşca, A. M., Birey, F., & Paşca, S. P. (2018). Generation and assembly of human brain region–specific three-dimensional cultures. *Nature Protocols*. https://doi.org/10.1038/s41596-018-0032-7

Someya, T., Bao, Z., & Malliaras, G. G. (2016). The rise of plastic bioelectronics. In *Nature*. https://doi.org/10.1038/nature21004

Song, B., Li, L., Wu, Z., Moon, K. S., Wu, J., & Wong, C. P. (2015). Solution-processed flexible solid-state micro-supercapacitors for on-chip energy storage devices. *Proceedings - Electronic Components and Technology Conference*. https://doi.org/10.1109/ECTC.2015.7159793

Sontheimer, H. (1994). Voltage-dependent ion channels in glial cells. *Glia*. https://doi.org/10.1002/glia.440110210

Sperelakis, N., & McConnell, K. (2002). Electric field interactions between closely abutting excitable cells. *IEEE Engineering in Medicine and Biology Magazine*. https://doi.org/10.1109/51.993199

Steketee, M. B., Moysidis, S. N., Jin, X. L., Weinstein, J. E., Pita-Thomas, W., Raju, H. B., Iqbal, S., & Goldberg, J. L. (2011). Nanoparticle-mediated signaling endosome localization regulates growth cone motility and neurite growth. *Proceedings of the National Academy of Sciences of the United States of America*. https://doi.org/10.1073/pnas.1019624108

Suk, J. W., Murali, S., An, J., & Ruoff, R. S. (2012). Mechanical measurements of ultra-thin amorphous carbon membranes using scanning atomic force microscopy. *Carbon*. https://doi.org/10.1016/j.carbon.2012.01.037

Sytnyk, M., Jakešová, M., Litviňuková, M., Mashkov, O., Kriegner, D., Stangl, J., Nebesářová, J., Fecher, F. W., Schöfberger, W., Sariciftci, N. S., Schindl, R., Heiss, W., & Głowacki, E. D. (2017). Cellular interfaces with hydrogen-bonded organic semiconductor hierarchical nanocrystals. *Nature Communications*. https://doi.org/10.1038/s41467-017-00135-0

Tang, J., Qin, N., Chong, Y., Diao, Y., Yiliguma, Wang, Z., Xue, T., Jiang, M., Zhang, J., & Zheng, G. (2018). Nanowire arrays restore vision in blind mice. *Nature Communications*. https://doi.org/10.1038/s41467-018-03212-0

Tay, A., & Di Carlo, D. (2017). Magnetic Nanoparticle-Based Mechanical Stimulation for Restoration of Mechano-Sensitive Ion Channel Equilibrium in Neural Networks. *Nano Letters*. https://doi.org/10.1021/acs.nanolett.6b04200

Tay, A., Kunze, A., Murray, C., & Di Carlo, D. (2016). Induction of Calcium Influx in Cortical Neural Networks by Nanomagnetic Forces. *ACS Nano*. https://doi.org/10.1021/acsnano.5b07118

Terem, I., Ni, W. W., Goubran, M., Rahimi, M. S., Zaharchuk, G., Yeom, K. W., Moseley, M. E., Kurt, M., & Holdsworth, S. J. (2018). Revealing sub-voxel motions of brain tissue using phase-based amplified MRI (aMRI). *Magnetic Resonance in Medicine*. https://doi.org/10.1002/mrm.27236

Thubagere, A. J., Li, W., Johnson, R. F., Chen, Z., Doroudi, S., Lee, Y. L., Izatt, G., Wittman, S.,

Srinivas, N., Woods, D., Winfree, E., & Qian, L. (2017). A cargo-sorting DNA robot. *Science*. https://doi.org/10.1126/science.aan6558

Tian, B., Cohen-Karni, T., Qing, Q., Duan, X., Xie, P., & Lieber, C. M. (2010). Three-dimensional, flexible nanoscale field-effect transistors as localized bioprobes. *Science*. https://doi.org/10.1126/science.1192033

Tian, B., & Lieber, C. M. (2019). Nanowired Bioelectric Interfaces. In *Chemical Reviews*. https://doi.org/10.1021/acs.chemrev.8b00795

Tian, B., Liu, J., Dvir, T., Jin, L., Tsui, J. H., Qing, Q., Suo, Z., Langer, R., Kohane, D. S., & Lieber, C. M. (2012). Macroporous nanowire nanoelectronic scaffolds for synthetic tissues. *Nature Materials*. https://doi.org/10.1038/nmat3404

Tortiglione, C., Antognazza, M. R., Tino, A., Bossio, C., Marchesano, V., Bauduin, A., Zangoli, M., Morata, S. V., & Lanzani, G. (2017). Semiconducting polymers are light nanotransducers in eyeless animals. *Science Advances*. https://doi.org/10.1126/sciadv.1601699

Tunuguntla, R. H., Bangar, M. A., Kim, K., Stroeve, P., Grigoropoulos, C., Ajo-Franklin, C. M., & Noy, A. (2015). Bioelectronic light-gated transistors with biologically tunable performance. *Advanced Materials*. https://doi.org/10.1002/adma.201403988

Veetil, A. T., Chakraborty, K., Xiao, K., Minter, M. R., Sisodia, S. S., & Krishnan, Y. (2017). Cell-targetable DNA nanocapsules for spatiotemporal release of caged bioactive small molecules. *Nature Nanotechnology*. https://doi.org/10.1038/NNANO.2017.159

Vetter, R. J., Williams, J. C., Hetke, J. F., Nunamaker, E. A., & Kipke, D. R. (2004). Chronic neural recording using silicon-substrate microelectrode arrays implanted in cerebral cortex. *IEEE Transactions on Biomedical Engineering*. https://doi.org/10.1109/TBME.2004.826680

Viventi, J., Kim, D. H., Vigeland, L., Frechette, E. S., Blanco, J. A., Kim, Y. S., Avrin, A. E., Tiruvadi, V. R., Hwang, S. W., Vanleer, A. C., Wulsin, D. F., Davis, K., Gelber, C. E., Palmer, L., Van Der Spiegel, J., Wu, J., Xiao, J., Huang, Y., Contreras, D., … Litt, B. (2011). Flexible, foldable, actively multiplexed, high-density electrode array for mapping brain activity in vivo. *Nature Neuroscience*. https://doi.org/10.1038/nn.2973

Wang, B., Grill, W. M., & Peterchev, A. V. (2018). Coupling Magnetically Induced Electric Fields to Neurons: Longitudinal and Transverse Activation. *Biophysical Journal*. https://doi.org/10.1016/j.bpj.2018.06.004

Wei, W., Elstrott, J., & Feller, M. B. (2010). Two-photon targeted recording of GFP-expressing neurons for light responses and live-cell imaging in the mouse retina. *Nature Protocols*. https://doi.org/10.1038/nprot.2010.106

Weidmann, S., & Hodgkin, A. L. (1966). The diffusion of radiopotassium across intercalated disks of mammalian cardiac muscle. *The Journal of Physiology*. https://doi.org/10.1113/jphysiol.1966.sp008092

Xie, C., Lin, Z., Hanson, L., Cui, Y., & Cui, B. (2012). Intracellular recording of action potentials by nanopillar electroporation. *Nature Nanotechnology*.

https://doi.org/10.1038/nnano.2012.8

Xie, C., Liu, J., Fu, T. M., Dai, X., Zhou, W., & Lieber, C. M. (2015). Three-dimensional macroporous nanoelectronic networks as minimally invasive brain probes. *Nature Materials*. https://doi.org/10.1038/nmat4427

Xu, J., Wang, S., Wang, G. J. N., Zhu, C., Luo, S., Jin, L., Gu, X., Chen, S., Feig, V. R., To, J. W. F., Rondeau-Gagné, S., Park, J., Schroeder, B. C., Lu, C., Oh, J. Y., Wang, Y., Kim, Y. H., Yan, H., Sinclair, R., … Bao, Z. (2017). Highly stretchable polymer semiconductor films through the nanoconfinement effect. *Science*. https://doi.org/10.1126/science.aah4496

Xu, K., Zhong, G., & Zhuang, X. (2013). Actin, spectrin, and associated proteins form a periodic cytoskeletal structure in axons. *Science*. https://doi.org/10.1126/science.1232251

Xu, T., Gao, W., Xu, L. P., Zhang, X., & Wang, S. (2017). Fuel-Free Synthetic Micro-/Nanomachines. In *Advanced Materials*. https://doi.org/10.1002/adma.201603250

Yang, T., Martin, P., Fogarty, B., Brown, A., Schurman, K., Phipps, R., Yin, V. P., Lockman, P., & Bai, S. (2015). Exosome delivered anticancer drugs across the blood-brain barrier for brain cancer therapy in Danio Rerio. *Pharmaceutical Research*. https://doi.org/10.1007/s11095-014-1593-y

Yang, W., Thordarson, P., Gooding, J. J., Ringer, S. P., & Braet, F. (2007). Carbon nanotubes for biological and biomedical applications. In *Nanotechnology*. https://doi.org/10.1088/0957-4484/18/41/412001

Yang, X., Zhou, T., Zwang, T. J., Hong, G., Zhao, Y., Viveros, R. D., Fu, T. M., Gao, T., & Lieber, C. M. (2019). Bioinspired neuron-like electronics. *Nature Materials*. https://doi.org/10.1038/s41563-019-0292-9

Yoo, S., Hong, S., Choi, Y., Park, J. H., & Nam, Y. (2014). Photothermal inhibition of neural activity with near-infrared-sensitive nanotransducers. *ACS Nano*. https://doi.org/10.1021/nn5020775

Zhang, A., & Lieber, C. M. (2016). Nano-Bioelectronics. In *Chemical Reviews*. https://doi.org/10.1021/acs.chemrev.5b00608

Zhang, X., Grajal, J., Vazquez-Roy, J. L., Radhakrishna, U., Wang, X., Chern, W., Zhou, L., Lin, Y., Shen, P. C., Ji, X., Ling, X., Zubair, A., Zhang, Y., Wang, H., Dubey, M., Kong, J., Dresselhaus, M., & Palacios, T. (2019). Two-dimensional MoS2-enabled flexible rectenna for Wi-Fi-band wireless energy harvesting. *Nature*. https://doi.org/10.1038/s41586-019-0892-1

Zhao, W., Hanson, L., Lou, H. Y., Akamatsu, M., Chowdary, P. D., Santoro, F., Marks, J. R., Grassart, A., Drubin, D. G., Cui, Y., & Cui, B. (2017). Nanoscale manipulation of membrane curvature for probing endocytosis in live cells. *Nature Nanotechnology*. https://doi.org/10.1038/nnano.2017.98

Zhao, Y., Yao, J., Xu, L., Mankin, M. N., Zhu, Y., Wu, H., Mai, L., Zhang, Q., & Lieber, C. M. (2016). Shape-Controlled Deterministic Assembly of Nanowires. *Nano Letters*. https://doi.org/10.1021/acs.nanolett.6b00292

Zheng, Z., Lauritzen, J. S., Perlman, E., Robinson, C. G., Nichols, M., Milkie, D., Torrens, O., Price, J., Fisher, C. B., Sharifi, N., Calle-Schuler, S. A., Kmecova, L., Ali, I. J., Karsh, B., Trautman, E. T., Bogovic, J. A., Hanslovsky, P., Jefferis, G. S. X. E., Kazhdan, M., … Bock, D. D. (2018). A Complete Electron Microscopy Volume of the Brain of Adult Drosophila melanogaster. *Cell*. https://doi.org/10.1016/j.cell.2018.06.019

Zhirnov, V. V., & Cavin, R. K. (2011). Microsystems for Bioelectronics. In *Microsystems for Bioelectronics*. https://doi.org/10.1016/C2009-0-20467-3

Zhou, T., Hong, G., Fu, T. M., Yang, X., Schuhmann, T. G., Viveros, R. D., & Lieber, C. M. (2017). Syringe-injectable mesh electronics integrate seamlessly with minimal chronic immune response in the brain. *Proceedings of the National Academy of Sciences of the United States of America*. https://doi.org/10.1073/pnas.1705509114

Zhu, Y., Xu, F., Qin, G., Fung, W. Y., & Lu, W. (2009). Mechanical properties of vapor - Liquid - Solid synthesized silicon nanowires. *Nano Letters*. https://doi.org/10.1021/nl902132w

Zimmerman, J. F., Murray, G. F., Wang, Y., Jumper, J. M., Austin, J. R., & Tian, B. (2015). Free-Standing Kinked Silicon Nanowires for Probing Inter- and Intracellular Force Dynamics. *Nano Letters*. https://doi.org/10.1021/acs.nanolett.5b01963

Zimmerman, J. F., Parameswaran, R., Murray, G., Wang, Y., Burke, M., & Tian, B. (2016). Cellular uptake and dynamics of unlabeled freestanding silicon nanowires. *Science Advances*. https://doi.org/10.1126/sciadv.1601039

Conclusions & Future Directions

Part I

The first part of this dissertation focused on two neural computations in the mammalian retina: direction and orientation selectivity. Starburst amacrine cells (SACs) are the primary interneuron of the retinal direction selective circuit and are responsible for relaying direction selective signals to the output neurons of the circuit through dendro-dendritic synapses. The dendrites of SACs are the first site along the visual pathway where direction selectivity is observed. Results from this dissertation show that centrifugal direction selectivity in the tips of SAC dendrites relies on intact mGluR2 signaling and Kv3-mediated currents. In particular, Chapter 2 demonstrates that mGluR2 gates interactions between SAC dendritic subdomains by regulating availability of voltage-gated calcium channels (VGCCs). Furthermore, Kv3 in the dendrites of SACs restricts the propagation of postsynaptic potentials, further compartmentalizing individual dendritic sectors.

Further studies focusing on how endogenous glutamate activates mGluR2 are necessary in order to understand whether mGluR2-mediated regulation of compartmentalized signaling in SACs is dependent on visual-evoked activity. We suspect that tonic levels of glutamate activate mGluR2 to some extent but we cannot rule out the possibility that it can be further modulated by visual evoked glutamate release from bipolar cells. If so, we would expect that recruitment of mGluR2 signaling would be dependent on visual conditions including as contrast, luminance, and spatial frequency.

Furthermore, the onset of mGluR2 and Kv3 expression throughout retinal development coincides with the downregulation of stage II cholinergic waves and initiation of stage III glutamatergic waves. The influence of mGluR2 or Kv3 in the transition of SACs from spontaneously active to primarily inhibitory interneurons has not been studied. As bipolar cell terminals begin releasing glutamate and reach their postsynaptic sites between P8-9, activated mGluR2 could play an important role in restricting acetylcholine release from SAC varicosities. Additionally, the upregulation of Kv3 could shunt the propagation of activity through the SAC network. It would be interesting to study the effects of mGluR2 agonists during stage II cholinergic waves and the persistence of cholinergic retinal waves in transgenic mice lacking mGluR2.

In Chapters 3 – 5, we presented the Vgat KO mouse model in which SAC GABA release is disrupted affecting asymmetric inhibition onto DSGCs and mutual inhibition between neighboring SACs. Using this transgenic mouse model, we demonstrate that direction selective cholinergic excitation contributes to the encoding of motion direction in DSGCs (Chapter 3); however further work is needed to achieve a mechanistic understanding of cholinergic transmission in the direction selective circuit. Despite parallel mechanisms contributing to direction selectivity, asymmetric inhibition between SACs and DSGCs is a central mechanism for retinal motion detection and it is necessary for optimal tuning of the DSGC population and proper clustering of DSGC preferred directions (Chapter 4).

Our collaboration with the Cang lab demonstrated the direction selectivity in the superior colliculus of the mouse is inherited from the retina through converging inputs from similarly tuned

DSGC inputs onto collicular neurons. On-Off DSGCs project to the shell of the dorsal lateral geniculate nucleus (dLGN); however, the retinogeniculate synapse appears to follow a diversity of integration modes compared to the superior colliculus. For instance, clusters of RGC boutons encoding for similar polarity and direction have been observed to converge onto the same thalamic dendrite; but, convergence of oppositely tuned and tuned versus untuned boutons has also been observed. Axial-selective and direction selective visual responses in the mouse dLGN have been reported, but whether these are computed de novo or arise from convergence of tuned retinal inputs remains to be explored. These experiments are integral for understanding how visual responses are transformed along the retino-geniculo-cortical pathway and for establishing a link between cortical selectivity and retinal receptive fields.

In Chapters 4 and 6, I employed transgenic methods for expressing GCaMP6 in RGCs, which enabled the use of ultrasensitive optical probes to interrogate retinal visual responses across development. Using this strategy, I identified On-Off orientation sensitive receptive fields in the mouse retina that are developmentally regulated during the first week after eye-opening. Although their maturation is independent of visual experience, these RGCs represent a major output channel of the mouse retina and can influence visual processing in downstream visual nuclei. Further studies are necessary to uncover their underlying synaptic mechanisms, developmental regulations, and their retinofugal projections.

Part II

The second part of this dissertation focused on technology development for neural interrogation. Current strategies for interrogation of neural circuits utilize metal electrodes (single-unit or multi-electrode arrays) or molecular tools, such as optical sensors and actuators. However, advances in nanotechnology offer the capability of interfacing the brain with unprecedented resolution. As described in Chapter 7, devices fabricated from building blocks with nanoscale dimensions minimize the mechanical and feature-size mismatch between probes and biological tissue and facilitate the formation of seamless biointerfaces.

In Chapter 8 and 9, together with collaborators from the Tian lab I demonstrated that both organic and inorganic materials can be fabricated that are capable of interfacing neurons at the nanoscale. These devices represent next-generation injectable and implantable platforms for neural stimulation. Future experiments will focus on strategies to target these to proper brain regions and to molecularly-defined neuronal populations. This will require close collaboration with molecular biologists researching transcriptomic and proteomic neural libraries and cell-type specific markers. Additionally, further tests are necessary to determine the potential of these devices to the treatment of neurological disorders.